UNIVERSIDAD COMPLUTENSE DE MADRID
FACULTAD DE CIENCIAS QUÍMICAS
Departamento de Química Orgánica

TESIS DOCTORAL

Turning the optoelectronic properties of graphene and carbon nanodots-based materials

Modulación de propiedades optoelectrónicas de materiales basados en grafeno y nanopuntos de carbono

MEMORIA PARA OPTAR AL GRADO DE DOCTOR

PRESENTADA POR

Andrés Ferrer Ruiz

Directores

Nazario Martín León
Mª Ángeles Herranz Astudillo

Madrid
Ed. electrónica 2019

UNIVERSIDAD COMPLUTENSE DE MADRID
FACULTAD DE CIENCIAS QUÍMICAS
Departamento de Química Orgánica

Tuning the optoelectronic properties of graphene and carbon nanodots-based materials

Modulación de propiedades optoelectrónicas de materiales basados en grafeno y nanopuntos de carbono

TESIS DOCTORAL

Andrés Ferrer Ruiz

Madrid, 2019

Tuning the optoelectronic properties of graphene and carbon nanodots-based materials

Modulación de propiedades optoelectrónicas de materiales basados en grafeno y nanopuntos de carbono

Directores:
Dr. Nazario Martín León
Dr. Mª Ángeles Herranz Astudillo

Memoria que para optar al grado de
DOCTOR EN CIENCIAS QUÍMICAS
presenta
Andrés Ferrer Ruiz

MADRID
Abril, 2019

Dª. Mª Ángeles Herranz Astudillo, Profesora Titular del Departamento de Química Orgánica de la Universidad Complutense de Madrid y **D. Nazario Martín León**, Catedrático de Universidad del Departamento de Química Orgánica de la Universidad Complutense de Madrid,

CERTIFICAN:

Que la presente Memoria titulada: *Tuning the optoelectronic properties of graphene and carbon nanodots-based materials (Modulación de propiedades optoelectrónicas de materiales basados en grafeno y nanopuntos de carbono),* se ha realizado bajo su dirección en el Departamento de Química Orgánica de la Facultad de Ciencias Químicas de la Universidad Complutense de Madrid por el Licenciado en Ciencias Químicas D. Andrés Ferrer Ruiz y autorizan su presentación para ser calificada como Tesis Doctoral.

Y para que conste firman el presente certificado en Madrid, a 30 de Abril de 2019.

Fdo. Dra. Mª Ángeles Herranz Astudillo Fdo. Dr. Nazario Martín León

A mis padres

Agradecimientos

Esta Tesis se ha realizado en el Departamento de Química Orgánica de la Universidad Complutense de Madrid bajo la dirección de los Profesores Mª Ángeles Herranz y Nazario Martín.

En primer lugar me gustaría dar las gracias a mis directores de Tesis, Nazario y Mª Ángeles. Nazario, muchísimas gracias por haberme dado la oportunidad de formar parte de tu grupo de investigación, por tu confianza y por haberme transmitido tú pasión y dedicación por la ciencia. Mª Ángeles, me gustaría agradecerte tu ayuda e interés por mi trabajo a lo largo de la tesis. Además te agradezco lo mucho que me has ayudado a crecer como profesional y persona más allá de lo estrictamente académico.

Ahora me gustaría hacer mención a la Dra. Laura Rodríguez. Muchísimas gracias por haberme enseñado tantas cosas a lo largo de estos años, sobre todo en mis comienzos donde fuiste esencial para mi crecimiento en el campo. Has sido una pieza fundamental para el desarrollo de esta Tesis. Gracias.

En la realización de este trabajo han participado otros grupos de investigación, a los que agradezco su contribución:

Al grupo del Prof. Dirk M. Guldi de la Universidad Friedrich-Alexander de Erlangen/Nürnberg (Alemania) por los estudios fotofísicos realizados a lo largo de esta Tesis, además de haberme dado la oportunidad de realizar una estancia en su grupo.

Al Prof. Juan Casado de la Universidad de Málaga, por los análisis Raman para el estudio de grafitización de nanopuntos de carbono.

También quiero agradecer al personal de los diferentes CAI de la Facultad de Ciencias Químicas por su apoyo para la caracterización incluida en este trabajo: a Ana Soubrié por la realización de las imágenes de microscopía de AFM. A Ángel Sánchez y a las Dras. Dolores Molero y Elena Sáez del CAI de RMN por su ayuda y disponibilidad a la hora de realizar los distintos experimentos de RMN. Finalmente a Emilio por su ayuda a la hora de realizar experimentos XRD.

A los técnicos de laboratorio Laura García, Francisco Javier García y Javier Cornejo por su ayuda y disposición en todo momento.

A continuación, quiero dar las gracias a todos los compañeros y amigos del departamento y, en especial, del laboratorio.

A toda la gente del departamento por los grandes momentos tanto dentro como fuera de la Facultad. En especial a: Paula, Alberto, Dani, Elena, Yago, Mayka, Sergio, Paloma. Me llevo un gran recuerdo de todas las cosas que he vivido con vosotros.

Al grupo de Luis Sánchez, Julia, Elisa y Yeray muchas gracias por los buenos momentos a lo largo de estos años. Mención especial para mi viejo amigo Jorge que no ha parado de regalarme buenos momentos desde que le conocí en el máster. Ha sido un placer.

Beti, Carmen, Ángel, Andreas, Luis, David, muchísimas gracias por estar siempre dispuestos a ayudar. Salvo, muchas gracias por darle vidilla a los pasillos y por tus conversaciones futboleras. Virginia, gracias por tu simpatía y Ana, muchas gracias por tu constante ayuda para resolver cualquier problema.

Al resto de mis compañeros del grupo, Rosa, Alfonso, Javi Sevilla, Mikiko, Antonio, muchas gracias por vuestra compañía y amabilidad en el día a día. Paul y Chus gracias por todas las risas con buena música de fondo que nos hemos echado en los últimos años. Mención también para la gente de IMDEA, Agus, José, Javi y Eider gracias por recibirnos siempre con lo brazos abiertos. Ahora me gustaría agradecer a todos aquellos que abandonaron el grupo hace poco pero que he disfrutado mucho de su compañía: Inés, Rafa, Marina, Sonia, Marta y Valentina. Y aquellos que se fueron hace más tiempo: Toni, Luismo, Carmen, Javi, Silvia, Jaime, María, Mateo, Johannes.

A todas las personas que he tenido a mi cargo cuyas investigaciones han sido una contribución muy grande para esta Tesis. Adrián, Álvaro y Juanma muchas gracias por vuestra aportación y por los buenos momentos que me habéis regalado. Os deseo mucha suerte para vuestro futuro.

Finalmente, me gustaría agradecer a dos personas que aunque estuvieron a punto de dejarme sordo, han sido esenciales para mí. Marta y Sara, muchísimas gracias por haber estado a mi lado durante estos años, vuestro apoyo y compañía han sido fundamentales. Me llevo dos grandes amigas de estos años, sois geniales. Gracias.

Ahora es turno para mis grupos de amigos.

En primer lugar, a mis compañeros de la carrera, a mis Quimicefos, muchísimas gracias por vuestro continuo apoyo. La verdad que habéis sido de gran ayuda a lo largo de estos años, vuestro interés y admiración han sido una gran motivación para mí. Gracias a cada uno de vosotros por todos los buenos momentos que hemos pasado en estos cuatro años.

Ahora les toca a mis amigos del barrio, más conocidos como "La Familia". La verdad que me faltan palabras para describir lo esencial que habéis sido para mi en estos años. Vuestra continua preocupación e interés sobre mis investigaciones aun sin saber mucho del tema me han dado mucha fuerza y motivación para afrontar estos años de Tesis. Muchísimas gracias a todos.

Por supuesto, no puedo olvidarme de todos los miembros de mi Familia: Todos mis tíos y mis primos que han confiado en mi durante estos años. Y por supuesto a mis abuelos, que aunque se fueron hace un tiempo, han sido todo un referente y ejemplo a lo largo de mi vida, estando muy presentes durante estos años.

Es momento de hablar de la persona que sin duda me ha regalado los mejores momentos durante mi Tesis. Alicia, eres lo mejor que me llevo de mi Tesis. Eres una persona increíble y te doy miles de gracias por tu ayuda y confianza en mi, así como por haberme hecho las cosas más fáciles. Mención especial por tu paciencia durante mi escritura y darte mucho ánimo para tu recta final que, conociéndote, sé que no tendrás problema alguno.

Si hay una persona que siempre ha estado ahí cuando la he necesitado capaz de sacarme una sonrisa incluso en los peores momentos esa es mi hermana. Natalia, has sido y eres mi gran compañera a lo largo de mi vida, sin duda una de las personas que mejor me entiende. No hace falta decir que tenerte cerca durante mi Tesis ha sido vital para mí. Muchísimas gracias, no puedo ser más afortunado de tener una hermana como tú.

Sin duda este agradecimiento final va dirigido a las personas a las que debo todo lo que soy, mis padres. Papá, gracias por todas las oportunidades que me has ofrecido así como por haberme apoyado en todas las decisiones que he tomado. Mamá muchas gracias por toda la paciencia, dedicación y fe absoluta que siempre has tenido en mí, sin ti jamás hubiera llegado tan lejos. Sois unos padres ejemplares, y os agradezco de corazón todo vuestro cariño y dedicación.

ABBREVIATIONS AND ACRONYMS

Bibliographic citations have been placed as footnotes in the pages where they were first cited in the section and at the end of this manuscript.

In addition to the standard abbreviations and acronyms in organic chemistry (as defined in the Journal of Organic Chemistry author guidelines, http://pubs.acs.org/paragonplus/submission/joceah/joceah_abbreviations.pdf) the following terms have been used in this manuscript:

AFM	Atomic force microscopy
ATRP	Atom transfer radical polymerization
ca.	Circa (“around”, “about”)
CND	Carbon nanodots
CNT	Carbon nanotubes
CQD	Carbon quantum dots
CTAB	Cetyltrimethylammonium bromide
CVD	Chemical vapor deposition
CVs	Cyclic voltammograms
Cy	Cyanines
D-A	Donor–acceptor systems
DLS	Dynamic light scattering
DPV	Differential pulse voltammetry
DXR	Doxorubicin hydrochloride
ECL	Electrochemiluminescence
EDC	1-ethyl-3-(3-dimethylaminopropyl)-carbodiimide
EDC·HCl	N-ethylcarbodiimide hydrochloride
exTTF	π-extended tetrathiafulvalene

FRET	Fluorescence resonance energy transfer
FWHM	Full-width half-maximum
GO	Graphene oxide
GQD	Graphene quantum dots
GR	Pristine graphene
HATU	2-(7-aza-1H-benzotriazole-1-yl)-1,1,3,3-tetramethyluronium hexafluorophosphate
HOBT	Hydroxybenzotriazole
HRTEM	High-resolution transmission electron microscopy
IL	Ionic liquids
MAS	Magic angle spinning NMR spectroscopy
MWCNT	Multi-walled carbon nanotube
NHS	N-hydroxysuccinimide
NIRF	Near-infrared fluorescence
P	Porphyrin
P3HT	Poly(3-hexylthiophene)
PAHs	Polycyclic aromatic hydrocarbons
PBI	Perylene bisimides
PCBM	Phenyl-C_{61}-butyric-methyl-ester
pCND	Pressure-synthesized carbon nanodots
PDI	Perylenediimides
PDMAEMA	Poly-(2-(dimethylamino)ethyl methacrylate)

PMMA	Poly(methyl methacrylate)
PTFE	Poly(tetrafluoroethylene)
PVP	Polyvinylpyrrolidone
rGO	Reduced graphene oxide
SDBS	Sodium dodecylbenzene sulfonate
SQD	Metal-based semiconductor quantum dots
SWCNT	Single-walled carbon nanotubes
$TBAClO_4$	Tetrabutylammonium perchlorate
TCAQ	11,11,12,12-tetracyano-9,10-anthra-*p*-quinodimethane
TCF	Tricyanofurane
TEM	Transmission electron microscopy
TGA	Thermogravimetric analysis
TTF	Tetrathiafulvalene
vs.	Versus (“against”)
WS_2	Tungsten disulfide
XPS	X-ray photoelectron spectroscopy
XRD	X-ray Powder diffraction

Table of contents

SUMMARY **1**

RESUMEN **9**

INTRODUCTION **19**

Chapter 1 ..... **31**

1.1. BACKGROUND **33**

1.1.1. Graphene structure definitions 35

1.1.2. Pristine graphene production methods 38

1.1.3. Graphene oxide and reduced graphene oxide production methods 45

1.1.4. Techniques involved in the characterization of graphene-based materials 48

1.1.5. Graphene functionalization 49

1.1.5.1. Pristine graphene covalent functionalization 50

1.1.5.2. Pristine graphene non-covalent functionalization 55

1.1.5.3. Graphene oxide functionalization 57

1.1.6. Donor-acceptor interactions in graphene-based hybrids 61

1.1.7. Cyanine dyes 66

1.2. OBJECTIVES **71**

1.3. RESULTS AND DISCUSSION **77**

1.3.1. Production of few-layer graphene and graphene oxide 79

1.3.2. Anionic heptamethine cyanine dyes 90

1.3.2.1. Synthesis of the cyanine-pyrene (CyPyr) dye 91

1.3.3. Supramolecular complexes of GR and SWCNT with CyPyr 98

1.3.3.1. Optical and electronic properties of CyPyr 98

1.3.3.2. Synthesis and characterization of GR-CyPyr and SWCNT-CyPyr hybrids 101

1.3.4. Synthesis of GR and GO imidazolium salts and Cy hybrids 114

1.3.4.1. Synthesis of GO imidazolium salts and Cy hybrids 114

1.3.4.2. Synthesis of GR imidazolium salts and Cy hybrids 120
1.4. EXPERIMENTAL SECTION 129
1.4.1. Synthesis of cyanine dyes and molecular precursors 133
1.4.2. Synthesis and preparation of nanocarbon hybrids 141
Chapter 2 151
2.1. BACKGROUND 153
2.1.1. Types of carbon-based fluorescents nanodots 155
2.1.2. Synthesis of fluorescent carbon-based dots 158
2.1.2.1. Top-down synthesis 160
2.1.2.2. Bottom-up synthesis 164
2.1.3. Purification and isolation of carbon-based dots 170
2.1.4. Optical properties 171
2.1.5. Characterization techniques 174
2.1.6. Surface functionalization 176
2.2. OBJECTIVES 185
2.3. RESULTS AND DISCUSSION 191
2.3.1. Synthesis and characterization of GQD 193
2.3.2. Synthesis and characterization of CND 198
2.3.3. Functionalization of GQD and pCND with exTTF molecules 221
2.3.3.1. Synthesis of exTTF electron donor units 222
2.3.3.2. Synthesis and characterization of pCND-exTTF hybrids 225
2.3.3.3. Synthesis and characterization of GQD-exTTF hybrids 231
2.3.3.4. Photophysical properties of pCND-exTTF and GQD-exTTF hybrids 234
2.3.4. Synthesis and characterization of pCND-TCAQ hybrids 238
2.3.4.1. Synthesis of TCAQ electron-acceptor units 239
2.3.4.2. Synthesis and characterization of pCND-TCAQ hybrids 240
2.3.4.3. Photophysical properties of pCND-TCAQ hybrids 244

2.3.5. Synthesis and characterization of pCND-C_{60} and pCND-C_{70} hybrids 245
2.3.5.1. Synthesis of $PC_{60}BM$-OH and $PC_{70}BM$-OH derivatives 247
2.3.5.2. Synthesis and characterization of pCND-$PC_{60}BM$ and pCND-$C_{70}BM$ hybrids 249
2.4. EXPERIMENTAL SECTION 259
2.4.1. Synthesis of molecular precursors 261
2.4.2. Synthesis of carbon-based nanodots 269
CONCLUSIONS 279
BIBLIOGRAPHY AND NOTES 287

SUMMARY

Tuning the optoelectronic properties of graphene and carbon nanodots-based materials

Introduction

Nowadays, the degradation of the environment and the climate change are some of the main concerns of our society. Therefore, a lot of effort has been invested in the search for new alternatives to fossil fuels. One interesting solution to this problem is to use solar energy as a renewable supply. In nature, it is well-known that solar energy can be transformed into chemical energy by means of photosynthetic processes. This concept has inspired a lot of efforts in the development of new artificial photosynthetic systems composed by donor-acceptor (D-A) assemblies. Specifically, in recent years, the combination of carbon nanoforms and light-harvesting dyes using covalent and supramolecular approaches has been widely studied. In this sense, the improvement in the formation methodology of new D-A assemblies, as well as the understanding of the charge transfer processes involved in these systems, are the main keys to create new artificial systems with a potential applicability.

Objectives

In this context, the aim of this thesis was the production of different carbon nanoforms –few layer graphene (GR), graphene oxide (GO), graphene quantum dots (GQD) and carbon nanodots (CND)– and their further use as scaffolds for the formation of donor-acceptor assemblies in combination with electroactive molecules. The incorporation of the latter was carried out using different synthetic methodologies which involved both, covalent and supramolecular approaches. Moreover, most of the as-formed hybrids were subjected to photophysical investigations in order to study the charge transfer process between the carbon materials and the electroactive units of organic nature. Therefore, the main goal of this thesis was to develop covalent and supramolecular methodologies for the preparation of different D-A systems. In order to get a better understanding of the photochemically induced charge transfer processes and further evaluating of the applicability of these systems in artificial photosynthesis, an exhaustive characterization of structures and properties, has been carried out.

Results and Discussion

1. Pristine graphene and graphene oxide production

GR was produced by mechanical exfoliation of graphite in liquid phase. For that task, the exfoliation of graphite was carried out employing two different solvents, NMP and *o*-DCB. The obtained results pointed to higher quality GR dispersions when NMP was used as a solvent, obtaining more homogeneous aggregates with only a few layers. Turning to the production of graphene oxide (GO), this was carried out by the treatment of graphite with $KClO_4$ in a mixture of H_2SO_4 and HNO_3. First insights in GO formation came from the observation of the hydrophilic character of the material which, in contrast with the starting graphite, could be perfectly dispersed in aqueous media. Moreover, the new oxygenated species formed in the sp^2 network were detected by different techniques such as TGA and FTIR and XPS spectroscopies.

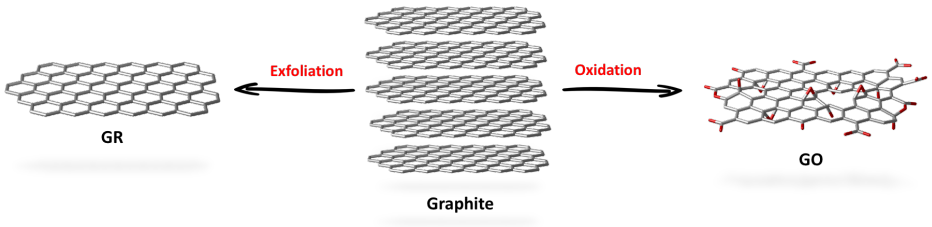

2. Chemical functionalization of single-wall carbon nanotubes (SWCNT) and graphene-based materials with anionic heptamethine cyanines (Cy)

In the first part of Chapter 1, SWCNT and GR were decorated with an anionic heptamethine cyanine covalently linked to pyrene (CyPyr). The pyrene fragments present in the structure allowed the formation of stable assemblies by π-π stacking forces. After the complex formation, the electron-donating character of the CyPyr when combined with both SWCNT and GR, was corroborated by Raman and transient absorption spectroscopies. Results from the electronic interaction were the observed shift in charge density from CyPyr to SWCNT or GR in the electronically dark state and a noticeable charge transfer upon photoexcitation.

In the second part of Chapter 1, it was employed a different strategy for the incorporation of cyanines in graphene-based materials, which consisted in the

covalent attachment of imidazoulim salts onto GR and GO. These structural units are present in ionic liquids (IL), and they have been used in combination with carbon nanostructures since they can improve the hydrophobicity/hydrophilicity of the carbon materials by the exchange of the counter anion of the imidazolium salt. Regarding the attachment of the IL on the graphene sheets, it was performed by two different synthetic strategies depending on the substrate. In the case of GO the IL was incorporated through an amidation reaction, and for the case of GR by a radical addition on the sp^2 lattice. Finally, the bromide anions were exchanged by the cyanine dyes (Cy and CyC_{60}) resulting in four different materials: GO^{IL}-Cy, GO^{IL}-CyC_{60}, GR^{IL}-Cy and GR^{IL}-CyC_{60}. The course of the different synthetic steps was followed by using different techniques such as absorption spectroscopy (UV-Vis-NIR), FTIR, TGA and XPS.

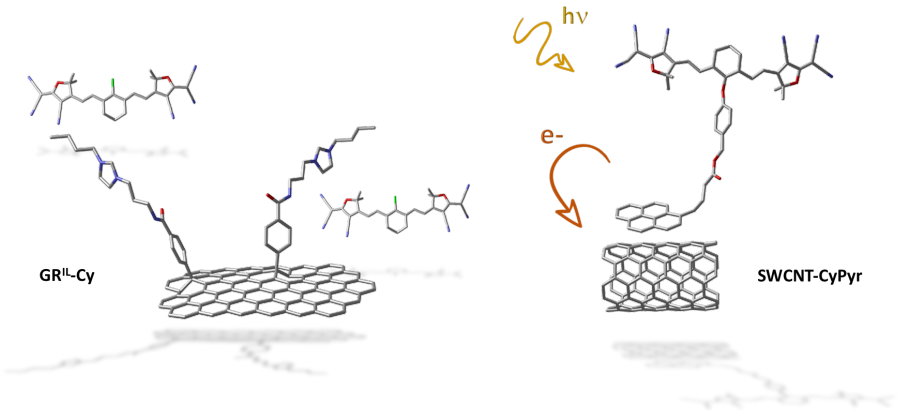

3. Graphene quantum dots and carbon nanodots production

In Chapter 2 is described the production and characterization of GQD and CND, with the aim of determining their structures and to understand their properties. On the one hand, GQD were synthesized following a top-down strategy which involves an oxidative treatment of GO in H_2SO_4/HNO_3 to assure the cutting of GO layers in small GQD. The formation of GQD was confirmed by the presence of nanoparticles with sizes around 1-10 nm, which presented new properties such as yellow fluorescent emission under UV light illumination.

On the other hand, CND were produced by bottom-up strategies. Firstly, CND were produced by a single source precursor strategy, using *L*-glutamic acid as

starting material (CND_{aGlu}). This strategy consists in the pyrolysis of *L*-glutamic acid in a solvent-free microwave-assisted synthesis which led to the formation of spherical nanoparticles with medium heights around 2 nm. Furthermore, CND_{aGlu} exhibited a blue and narrower emission under UV irradiation in comparison with that observed in GQD. The structural characterization of CND_{aGlu} revealed a polymer-like nature which motivated the investigation of additional graphitization experiments. From these experiments it was concluded that the thermal annealing with temperatures above 160 ºC lead to the graphitization of CND_{aGlu} structures, accompanied by changes in their optical properties.

An alternative to the monocomponent CND synthesis was a strategy that involves the production from several precursors, using citric acid and urea as starting materials (pCND). This method consisted in the microwave heating of an aqueous solution of citric acid and urea maintaining the pressure constant at 15 bar for 5 min. Therefore, these conditions gave rise to pCND which presented higher content of graphitic domains than CND_{aGlu}, without the need to perform other additional annealing treatments. Moreover, pCND presented enhanced optical properties with a narrow emission band and excitation-independent emission.

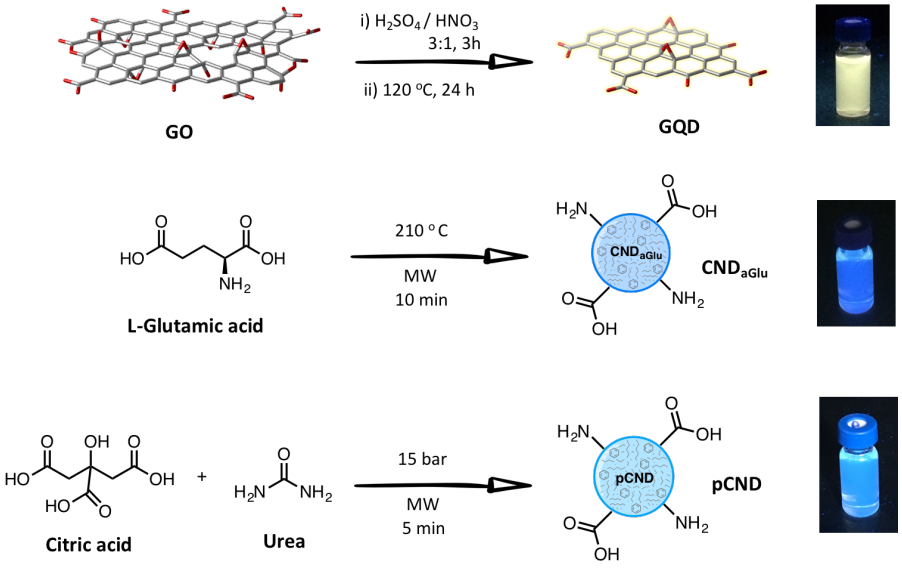

4. Functionalization of GQD and CND with electroactive molecules

In the second part of Chapter 2 is described the development of an efficient synthetic methodology for the covalent incorporation of electroactive molecules onto CND and GQD. In both cases, the strategy was the same, the activation of the carboxylic acids present in both systems and the further incorporation of different molecules by esterification reactions.

Firstly, electron-donor derivatives of 9,10-bis(1,3-dithiol-2-ylidene)-9,10-dihydroanthracene (exTTF) were incorporated in both, pCND and GQD surfaces, according with this methodology. The next step was the complete structural characterization of the pCND-exTTF and GQD-exTTF hybrids by different techniques. By means of TEM and AFM microscopies it was observed an increase of the size upon the incorporation of the exTTF, whose presence was also confirmed by XPS, NMR and electrochemistry experiments.

Moreover, upon the attachment of exTTF units, it was observed an almost quantitative quenching of the pCND and GQD fluorescence, which is indicative of electronic interactions between the carbon nanodots and the exTTF molecules in the excited state. Additional photophysical experiments confirmed the formation of a charge separated state where the exTTF was oxidized to the cation-radical and pCND or GQD are reduced to the anion-radical species. The observed lifetime for the charge recombination in $GQD^{\bullet-}$-$exTTF^{\bullet+}$ (54 ps) was slower than that observed in $pCND^{\bullet-}$-$exTTF^{\bullet+}$ (13 ps) as a result of the difference structures of pCND and GQD.

Secondly, pCND were decorated with electron-acceptor molecules derived from 9,10-bis(dicyanomethylene)-9,10-dihydroanthracene (TCAQ). The pCND-TCAQ hybrids were characterized by FTIR and XPS spectroscopies among other techniques. Further experiments in the excited state revealed the electron-donating behavior of pCND in combination with the acceptor TCAQ. Herein, a charge separated state $pCND^{\bullet+}$-$TCAQ^{\bullet-}$ was observed, where the TCAQ was reduced and the pCND oxidized. Up to now, this is the first example where CND act as electron-donors in covalent D-A systems.

Finally, we performed the incorporation of the acceptors derived of [6,6]-phenyl-fullerene-methyl butyrate ($PC_{60}BM$ and $PC_{70}BM$) onto pCND. These functionalization processes were more difficult than those carried out for the synthesis of the above-mentioned hybrids due to the different solubilities

between the fullerenes and pCND. Therefore, it was employed a mixture of chlorobenzene/DMSO in the reaction conditions unlike pCND-exTTF and pCND-TCAQ, where only DMSO was used as solvent. By means of electrochemical experiments, AFM microscopy and FTIR, UV-Vis and XPS spectroscopies, the characterization of the pCND-$PC_{60}BM$ and pCND-$PC_{70}BM$ hybrids was accomplished.

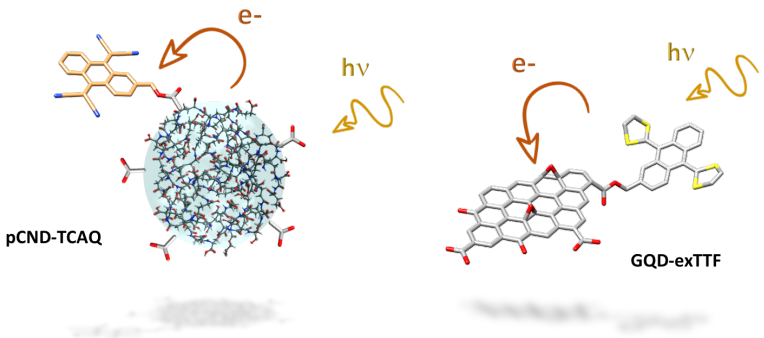

Conclusions

Throughout this thesis, the synthesis and characterization of different carbon nanoforms have been carried out. Herein, most of the carbon species were graphene-based materials (GR and GO) and carbon dots (CND and GQD). Once studied their properties and their structures, the next step was the development of different methodologies for their combination with different electroactive molecules. These methodologies involved both covalent and supramolecular strategies for the formation of new D-A assemblies, which were characterized by different techniques. Moreover, besides the structural characterization and the spectroscopic analysis of these hybrids in the excited state, further experiments in the excited state were performed. These experiments revelaed the different charge transfer processes that happened upon photoexcitation between the carbon structures and the organic electroactive molecule.

RESUMEN

Modulación de propiedades optoelectrónicas de materiales basados en grafeno y nanopuntos de carbono

Introducción

Actualmente, unas de las mayores preocupaciones de nuestra sociedad son la degradación del medio ambiente y el cambio climático. Debido a esto, se ha invertido mucho esfuerzo en la búsqueda de nuevas alternativas a los combustibles fósiles. Una solución interesante a este problema es el uso de la energía solar como fuente de energía renovable. Como bien sabemos, los procesos fotosintéticos observados en la naturaleza son capaces de transformar la energía solar en energía química. Buscando inspiración en este concepto, se ha puesto mucho esfuerzo en el desarrollo de nuevos sistemas fotosintéticos artificiales basados en complejos de tipo dador-aceptor (D-A). Concretamente, en los últimos años, ha sido muy estudiada la formación de sistemas basados en nanoformas de carbono y colorantes con gran capacidad de absorción de luz, a través de estrategias covalentes y supramoleculares. En este sentido, las claves para la creación de sistemas artificiales con una potencial aplicabilidad son la mejora de las metodologías para la formación de los sistemas D-A, así como la comprensión de los procesos de trasferencia de carga que operan en este tipo de sistemas.

Objetivos

En este contexto, el principal objetivo de esta tesis ha sido la producción de diversas nanoformas de carbono –grafeno de pocas capas (GR), óxido de grafeno (GO), puntos cuánticos de grafeno (GQD) y nanopuntos de carbono (CND)– para ser utilizadas en la formación de sistemas D-A con diferentes moléculas electroactivas. La incorporación de estas últimas sobre las nanoformas de carbono se ha llevado a cabo a través de diferentes aproximaciones sintéticas utilizando tanto estrategias de funcionalización de tipo covalente como de tipo supramolecular. Además, la mayoría de los híbridos D-A sintetizados, fueron considerados en estudios fotofisicos con el objetivo de investigar los procesos de trasferencia de carga entre las nanoformas de carbono y las unidades electroactivas de naturaleza orgánica. Por lo tanto, el principal objetivo de esta tesis ha sido la puesta a punto de metodologías tanto covalentes como supramoleculares para la preparación de

diferentes sistemas D-A, el llevar a cabo una exhaustiva caracterización estructural y de propiedades, y el entender los procesos electrónicos que se inducen fotoquímicamente. Este estudio permitirá evaluar la aplicabilidad de estos sistemas en fotosíntesis artificial.

Resultados y discusión

1. Producción de grafeno y óxido de grafeno

El GR se produjo siguiendo un método de exfoliación mecánica de grafito en fase líquida. Dicha exfoliación se llevo a cabo utilizando dos disolventes diferentes, NMP y *o*-DCB. Los resultados obtenidos indicaron que utilizando NMP como disolvente se obtienen dispersiones de GR de mayor calidad, presentando agregados más homogéneos compuestos por pocas láminas. Respecto a la producción de óxido de grafeno (GO), esta se llevo a cabo mediante el tratamiento de grafito con $KClO_4$ en una mezcla de H_2SO_4 y HNO_3. La primera evidencia de la formación de GO fue la observación del carácter hidrófilo que presentó el nuevo material, el cual se dispersa perfectamente en medio acuoso, al contrario que el grafito de partida. Además, los nuevos grupos oxigenados generados en la red sp^2 se identificaron por diferentes técnicas como TGA, FTIR y XPS.

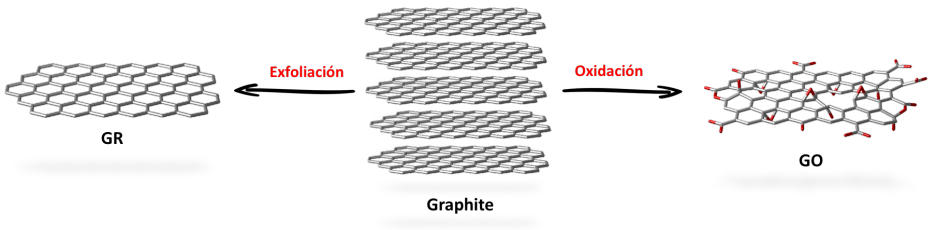

2. Funcionalización química de nanotubos de carbono de pared sencilla (SWCNT) y materiales basados en grafeno derivados de heptametilen-cianinas aniónicas (Cy)

En la primera parte del Capítulo 1, tanto SWCNT como GR se funcionalizaron con una heptametilen-cianina aniónica unida covalentemente a pireno (CyPyr). Gracias al fragmento de pireno que presenta la estructura de CyPyr, se pudieron formar complejos estables mediante fuerzas de empaquetamiento de tipo π–π. Tras la formación de dichos complejos, se demostró el carácter electro-dador de la molécula de CyPyr mediante espectroscopias Raman y de

absorción transitoria. Además, se detectó un desplazamiento de la densidad electrónica de CyPyr hacia GR o SWCNT en el estado fundamental, y un proceso de transferencia de carga en el estado excitado.

En la segunda parte del Capítulo 1, se siguió una estrategia diferente para incorporar cianinas en la superficie de materiales basados en grafeno, la cual consitió en la incorporación de manera covalente de sales de imidazolio sobre GR y GO. Estas unidades estructurales están presentes en líquidos iónicos (IL), y han sido usadas en combinación con nanoestructuras de carbono con el fin de modular el carácter hidrófilo/hidrofóbico de éstas mediante el intercambio del anión presente en la sal de imidazolio. La incorporación de IL sobre las láminas de grafeno se realizó de manera diferente dependiendo del tipo de sustrato. En el caso de GO se llevo a cabo mediante una reacción de amidación, y en el caso de GR mediante una adición radicalaria sobre la superficie sp^2. Finalmente, el anión bromuro de IL fue intercambiado por diferentes cianinas (Cy y CyC_{60}), obteniéndose un total de cuatro materiales diferentes: GO^{IL}-Cy, GO^{IL}-CyC_{60}, GR^{IL}-Cy y GR^{IL}-CyC_{60}. Las diferentes etapas sintéticas fueron monitorizadas por diversas técnicas como TGA y espectroscopias UV-vis-NIR, FTIR y XPS.

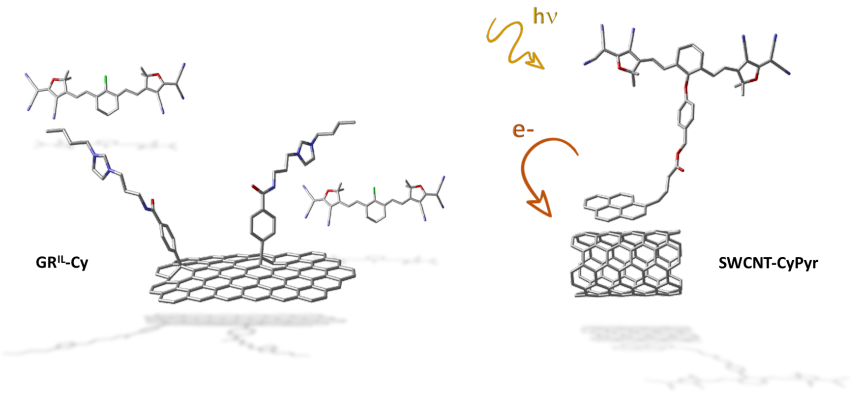

3. Producción de puntos cuánticos de grafeno y nanopuntos de carbono

En el Capítulo 2 se describe en primer lugar la producción y caracterización de GQD y CND con el fin de determinar sus estructuras y comprender sus propiedades. Por un lado, se ha llevado a cabo la síntesis de GQD mediante una estrategia de tipo descendente (*top-down*) que implica la oxidación de GO en una mezcla H_2SO_4/HNO_3, con el fin de fragmentar las láminas de GO en

pequeños GQD. La formación de estos últimos se confirmó mediante la detección de nanopartículas con tamaños de 1 a 10 nm, las cuales además presentaron nuevas propiedades como una emisión fluorescente de color amarillo al ser irradiadas con luz UV.

Por otro lado, los CND fueron producidos mediante estrategias de tipo ascendente (*bottom-up*). En primer lugar, se empleó un solo precursor para la formación de CND, concretamente ácido L-glutámico como material de partida (CND_{aGlu}). Esta estrategia consistió en la pirolisis en microondas del ácido L-glutámico en ausencia de disolvente, generando nanoparticulas esféricas con una altura media de alrededor de 2 nm. Estos CND_{aGlu} se caracterizaron por presentar una emisión de color azul al ser irradiados con luz UV, además de por mostrar una banda de emisión más estrecha que la observada para GQD. La caracterización estructural de estas nanoparticulas reveló una naturaleza polimérica, lo cual motivó la realización de experimentos de grafitización adicionales. Estos experimentos permitieron concluir que tratamientos térmicos por encima de 160 ºC dan lugar a la grafitización de CND_{aGlu}, además de llevar asociados cambios en las propiedades ópticas.

Una alternativa a la síntesis monocomponente fue el uso de una estrategia de producción con varios precursores, utilizando como materiales de partida ácido cítrico y urea (pCND). Este método consistió en el calentamiento en microondas de una disolución acuosa de ácido cítrico y urea manteniendo la presión constante a 15 bar durante 5 min. Bajo estas condiciones se formaron pCND, los cuales mostraron tener un mayor contenido de dominios grafiticos que CND_{aGlu}, sin la necesidad de tener que realizar tratamientos térmicos adicionales. Además, los pCND presentaron mejores propiedades ópticas, con una banda de emisión estrecha y que no se desplaza con la variación de la longitud de onda de excitación.

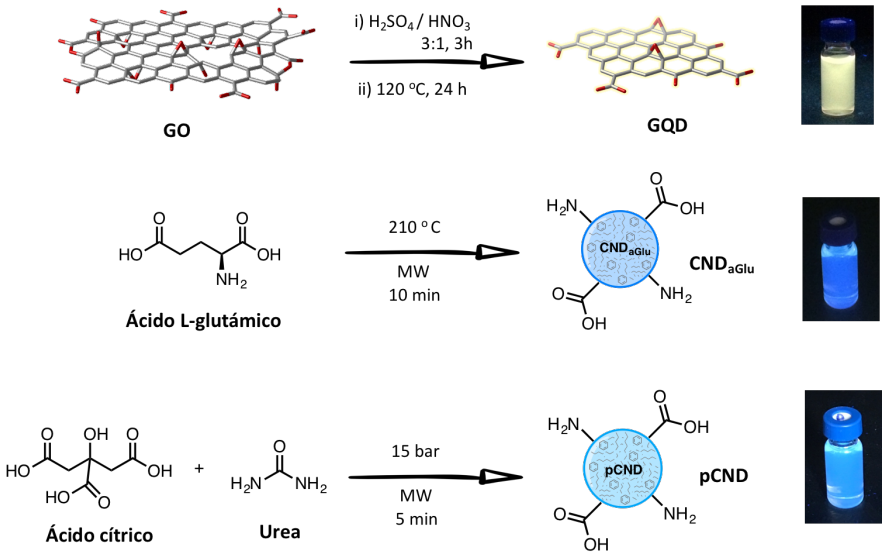

4. Funcionalización de GQD y pCND con moléculas electroactivas

En la segunda parte del Capítulo 2, se describe el desarrollo de una metodología sintética para la incorporación covalente de moléculas electroactivas a CND y GQD. En ambos casos la estrategia fue la misma, la activación de los ácidos carboxílicos presentes en ambos sistemas, seguida de la incorporación de las diferentes moléculas mediante reacciones de esterificación.

En primer lugar, de acuerdo con esta metodología se introdujo un electro-dador derivado de 9,10-bis(1,3-ditiol-2-iliden)-9,10-dihidroantraceno (exTTF) sobre la superficie de pCND y GQD. El siguiente paso fue la caracterización estructural completa de los híbridos pCND-exTTF y GQD-exTTF mediante diferentes técnicas. Por medio de microscopia TEM y AFM se observó un aumento del tamaño tras la incorporación del exTTF, cuya presencia también fue confirmada por XPS, RMN y experimentos de electroquímica.

Además, tras la incorporación de las unidades de exTTF, se observó una disminución casi cuantitativa de la fluorescencia de pCND y GQD, lo que fue indicativo de interacciones electrónicas en el estado excitado entre las nanopartículas de carbono y las moléculas de exTTF.

Experimentos fotofísicos adicionales confirmaron la formación de un estado con separación de carga donde el exTTF es oxidado al catión-radical y pCND o GQD son reducidos a las especies anión-radical. El tiempo de vida de la recombinación de carga en GQD$^{\bullet-}$-exTTF$^{\bullet+}$ (54 ps) fue más lento que el observado en pCND$^{\bullet-}$-exTTF$^{\bullet+}$ (13 ps) como consecuencia de las diferencias estructurales entre pCND y GQD.

En segundo lugar, los pCND se funcionalizaron con moléculas electro-aceptoras derivadas de 9,10-bis(dicianometilen)-9,10-dihidroantraceno (TCAQ). Los híbridos pCND-TCAQ fueron caracterizados mediante espectroscopias FTIR y XPS, entre otras técnicas. De manera complementaria, experimentos en el estado excitado revelaron el carácter dador de electrones de los pCND cuando se combinan con el electro-aceptor TCAQ. Concretamente, se observó un estado de separación de cargas pCND$^{\bullet+}$-TCAQ$^{\bullet-}$, donde se reduce el TCAQ y se oxida el pCND. Hasta ahora, es el primer ejemplo en el que los CND actúan como dadores de electrones en sistemas D-A covalentes.

Finalmente, se realizó la incorporación de los aceptores derivados de [6,6]-fenil-fullereno-butirato de metilo ($PC_{60}BM$ y $PC_{70}BM$) sobre los pCND. Estos procesos de funcionalización fueron más difíciles que para los híbridos mencionados anteriormente debido a las diferentes solubilidades de los fullerenos y los pCND. En este caso, fue preciso emplear una mezcla de clorobenceno/DMSO en las condiciones de reacción, a diferencia de la preparación de los híbridos de pCND-exTTF y pCND-TCAQ, para la que se empleó sólo DMSO. Los híbridos pCND-$PC_{60}BM$ y pCND-$PC_{70}BM$ se caracterizaron mediante experimentos electroquímicos, microscopia AFM y espectroscopias FTIR, UV-Vis y XPS.

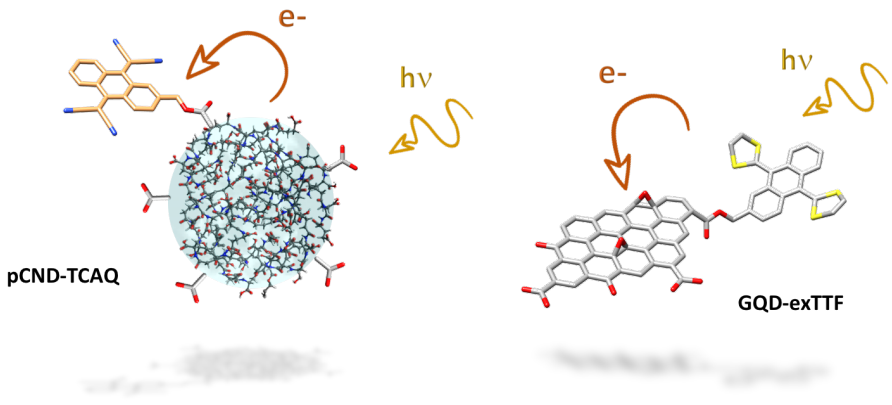

Conclusiones

A lo largo esta tesis se ha llevado a cabo la síntesis y caracterización de diferentes nanoformas de carbono. La mayoría de estas especies fueron materiales basados en grafeno (GR y GO) así como puntos de carbono (CND y GQD). Una vez estudiadas sus propiedades y estructuras, el siguiente paso fue el desarrollo de nuevas metodologías para su combinación con moléculas electroactivas. Aquí se usaron estrategias covalentes y supramoleculares para la formación de los complejos D-A, los cuales fueron posteriormente caracterizados a través de diferentes técnicas. Además de estudios espectroscópicos de estos híbridos en el estado fundamental, también se llevaron a cabo estudios en el estado excitado. Estos estudios revelaron los diferentes procesos de trasferencia de carga entre las formas de carbono y las moléculas electroactivas tras fotoexcitar los sistemas D-A.

INTRODUCTION

INTRODUCTION

There is an important debate nowadays about the lack of alternatives to fossil fuels, which are the main source of energy in our society in spite of being a non-renewable source. In many daily aspects of our lives, we strongly rely on fuels or chemicals, population growth and technological advances in the last decades have caused a large increase in the energy consumption.[1] This dependence has increasingly triggered the degradation of the environment as consequence of the greenhouse effect, global warming or the accumulated concentration of toxic pollutants in the atmosphere.

In order to maintain the sustainability of our society, one promising alternative is the use of solar energy as a renewable supply. However, at the moment, has not reach the expected development.[2] In energy terms, the solar radiation that reaches the Earth every day has a power of the order of terawatts,[3] which can be transformed in other forms of energy or can be used to convert raw materials in useful chemicals.[4] Today, two main approaches are known to use sunlight to harness the light and to transform it in energy: i) direct conversion of solar energy into electrical energy (photovoltaic processes), with their corresponding problems of light harvesting yield and storage, or ii) conversion to chemical energy, as it occurs in nature, through photosynthetic processes.

The great potential of the second approach is demonstrated in the context of photosynthesis, taking into account the high performance of this process in the natural environment through photo-induced charge separation processes. The human being, following the vital instinct to understand and imitate this natural environment, has been progressively approaching the molecular functioning of photosynthetic processes, enabling the creation of simple artificial photosynthetic systems composed of molecular and supramolecular architectures (Figure 1).[5]

---

[1] U.S. Energy Information Administration, International Energy Outlook, **2018**. https://www.eia.gov/analysis/

[2] I. McConnell, G. Li, W. G. Brudvig, *Chem. Biol.* **2010**, *17*, 434.

[3] K. Kalyasundaram, M. Graetzel, *Curr. Opin. Biotechnol.* **2010**, *21*, 298.

[4] C. Liu, N. P. Dasgupta, P. Yang, *Chem. Mater.* **2013**, *25*, 415.

[5] M. El-Khouly, E. El-Mohsnawy, S. Fukuzumi, *J. Photochem. Photobiol. C: Photochem. Rev*. **2017**, *31*, 36.

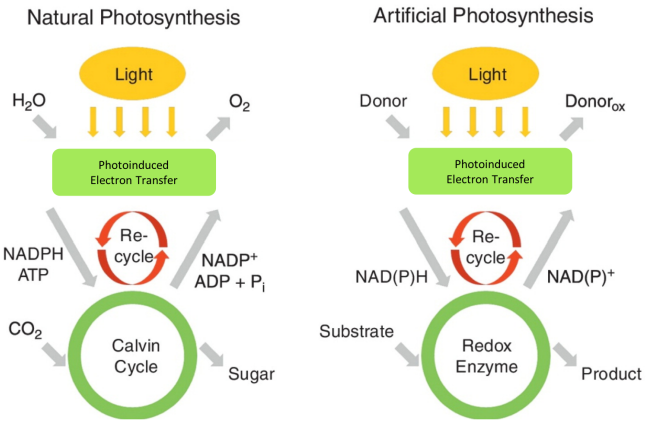

Figure 1. Natural photosynthesis *vs*. artificial photosynthesis.

Natural photosynthesis. In general terms, photosynthesis is the process where plants, some bacteria and protoctists manage to reduce CO_2 molecules to more complex organic structures. However, under standard conditions, carbon dioxide is the most thermodynamically stable form in which this element can be found. In fact, this process of reduction requires energy, which in the case of photosynthesis comes from the solar radiation. This process is usually described by the following equation:

$$CO_2 + H_2O + \text{light} \rightarrow \text{organic compounds} + O_2$$

There are different photosynthetic systems in nature, however, despite seeming quite unalike at first, the main stages are quite similar from one to another. Two main phases are distinguished: a first phase of light absorption and a series of electron transfer reactions in which the H_2O molecule is oxidized to O_2 (in aerobic photosynthesis), and a second phase called dark phase in which, through reactions independent of light, the CO_2 is reduced to organic matter.

In nature, the photosynthetic process works as follows: a photon is captured by a complex antenna and transferred as a coherent superposition of excited states, called excitons, to a reaction center.[6] Once the different excitons have reached the reaction center, their energy is used to generate a primary charge separation

[6] H. Van Amerongen, *Photosynthetic Excitons*, Singapore: World Scientific Publishing Co. Pte. Ltd. **2000**.

reaction in a molecular pair within the reaction center. Reaction centers are usually trans-membrane proteins oriented perpendicularly in a lipid bilayer. In this way, by producing charge separation, each charge is held on one side of the membrane, thus generating an electrical gradient or membrane potential that can be used for the synthesis of organic compounds. Therefore, the main mission of the reaction center is to produce the above-mentioned gradient quickly and without losses.[2]

On the other hand, the reaction center has a high quantum efficiency since it traps the energy of the exciton, rapidly exciting itself to a state of separation of long-lived charges (generally of the order of ms[7]) that leaves behind any other possible form of de-excitation to the fundamental state. Therefore, the state of charge separation must be much more stable than any intermediate electronic state involved in the charge transfer process to allow much slower electronic and protonic transfers to occur.

The as-generated electrical gradient or membrane potential it is employed to form nicotinamide adenine dinucleotide phosphate (NADPH) and adenosine-5'-triphosphate (ATP) which will be further consumed in the dark phase to convert CO_2 into other organic molecules.

Artificial photosynthesis. In non-natural models are found examples where the light collection unit is the center of the reaction itself, so the problem is simplified but the efficiency is reduced. Light-harvesting antennas include, among others, porphyrins and phthalocyanines, which are very close in chemical structure to natural chlorophylls.[2]

Actually, most of the receiving antennas used today have been built using multiporphyrin series with various chromophores to achieve photonic absorption in wider bands of the visible spectrum. However, it should be noted that the introduction of chromophores is not always beneficial since, in order to be beneficial, the process of charge separation must be coupled on time and energy scales, preventing the excited state from decaying by different radiative and non-radiative unimolecular processes.

On the other hand, the next step is to accumulate the energy for a sufficient time in an excited state of charge separation of the donor-acceptor type in the

[7] W. Zynth, J. Wachtveilt, *Chem.Phys.Chem.* **2005***,* 6, 871.

molecule of the reaction center. Among all the possible models tested at laboratory level, the simplest of them use porphyrin as a donor, acting also as a photon capture antenna, and a quinone molecule as an electron acceptor. Other molecules have also been employed as antenna such as cyanine dyes, which can present a strong absorption in the UV range as well as in the near-infrared.

In recent years, there has been much interest in the preparation and study of donor-acceptor assemblies by combining light-harvesting dyes with carbon nanostructures. The formation of these hybrids has been carried out using both, covalent and supramolecular approaches, and the combination has resulted in particulary noteworthy photophysical events.

Carbon nanostructures. The position of carbon, midway in the periodic table, makes it equally prone to interact with electropositive or electronegative elements to form different carbon compounds. Besides, carbon forms different allotropes.[8] In addition to diamond and graphite, the newest allotropic forms of carbon exist in a wide variety of nanostructures with an ample distribution of shapes and sizes (Figure 2).

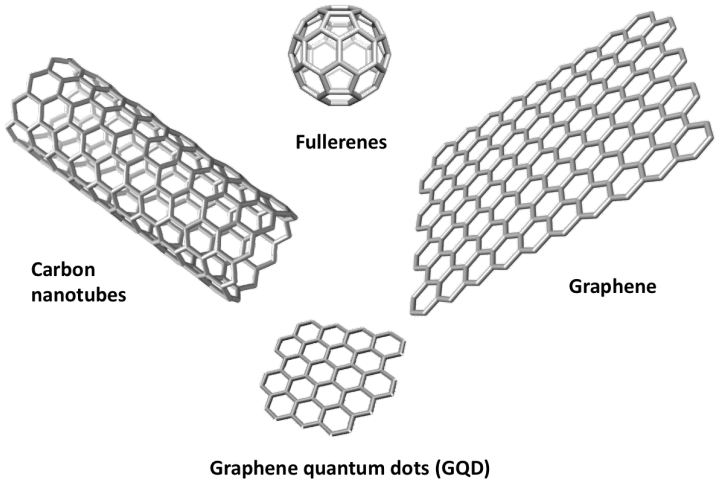

Figure 2. Representation of different carbon nanoforms.

[8] a) E. H. L. Falcao, F. Wudl, *J. Chem. Technol. Biotechnol*. **2007**, *82*, 524. b) J. L. Delgado, M. A. Herranz, N. Martín, *J. Mater. Chem*. **2008**, *18*, 1417.

Regarding the different structures in which carbon can be presented, in 1985 arose a complete revolution in the field. Up to this date, only two different allotropes of this element were known: diamond (sp^3 hybridization) and graphite (sp^2 hybridization). In that year, [60]fullerene was discovered during the simulation of the conditions under which carbon nucleates in the atmosphere of red giant stars.[9] This molecule was considered the third allotropic form of carbon and consisted in 60 carbon atoms linked together spherically shaped with a sp^2 hybridization. There are two main properties of C_{60} particulary relevant for artificial photosynthesis: i) its relatively low energy LUMO, with a t_{1u} symmetry,[10] allowing fullerene to have excellent charge-accepting properties, accepting up to 6 electrons reversibly; and ii) the low reorganization energy that it exhibits ($\lambda \approx 0.23$ eV), [11] providing long-lived charge transfer states. Both characteristics, together with the high symmetry of the molecule, make [60]fullerene a potential component of future photosynthetic cells.

Moreover, the great electron withdrawing ability of C_{60} is a fundamental key to understand the chemistry of fullerenes, undergoing typical reactions of poorly-conjugated and electron-defficient alkenes and reacting readily with nucleophiles.[12] The chemical functionalization by both, covalent and supramolecular approaches, is essential for the design of donor-acceptor systems based on fullerenes for further applications.

It was in 1991 when carbon nanotubes (CNT) were discovered by Sumio Iijima, who reported the production of a new carbon nanoform with needle shape. By means of transmission electron microscopy, it was found that each needle was constituted by several concentric tubes of graphitic sheets,[13] giving rise to multi-walled carbon nanotubes (MWCNT). Two years later, in 1993, Iijima reported, under catalytic conditions, the production of single-walled carbon nanotubes (SWCNT) which consist in only one tube formed by one

[9] a) H. W. Kroto, J. R. Heath, S. C. O'Brien, R. F. Curl, R. E. Smalley, *Nature* **1985**, *318*, 162. b) J. R. Heath, R. F. Curl, R. E. Smalley, *J. Chem. Phys.* **1987**, *87*, 4236.
[10] N. Martín, L. Sánchez, B. Illescas, I. Pérez, *Chem. Rev.* **1998**, *7*, 2527.
[11] H. Imahori, N. V. Tkachenko, V. Vehmanen, K. Tamaki, H. Lemmetyinen, Y. Sakata, S. Fukuzumi, *J. Chem. Phys. A*. **2001**, *105*, 1750.
[12] R. Taylor, D. R. M. Walton, *Nature* **1993**, *363*, 685.
[13] S. Iijima, *Nature* **1991**, *354*, 56.

layer of sp^2 carbons.[14] The attribution of this breakthrough arose some controversy and discussion due to the considerable amount of work between the 1950-1970 decades on these filamentous carbon structures.

A decade after CNT, in 2004, Alexander Geim and Konstantin Novoselov reported the isolation of a single layer of graphite, resulting in what today is called graphene.[15] This is one of the most interesting and studied nanomaterials in recent years. It consists in a bidimensional sheet of sp^2-hybridized carbon atoms localized following a hexagonal pattern and resulting in the thinnest and the strongest material ever known. Graphene films were initially obtained by mechanical exfoliation using sticky tape to peel atomically thin layers of graphite. In 2010 both, Geim and Novoselov, were laureated with the Nobel Prize in Physics.

The great attention in CNT and graphene is related to their attractive properties. Both CNT and graphene are nanostructured materials which present improved mechanical and thermal properties in comparison to fullerenes.[16] Some of them exhibit high current density, ballistic transport, ultrahigh thermal conductivity and extremely high mechanical strength,[17] which make them appealing for different applications.[18] Graphene presents similar features to that of CNT but with a better performance (Table 1).

[14] a) S. Iijima, T. Ichihashi, *Nature* **1993**, *363*, 603. b) D. S. Bethune, C. H. Klang, M. S. de Vries, G. Gorman, R. Savoy, J. Vazquez, R. Beyers, *Nature* **1993**, *363*, 605.

[15] K. S. Novoselov, A. K. Geim, S. V. Morozov, D. Jiang, Y. Zhang, S. V. Dubonos, I. V. Grigorieva, A. A. Firsov, *Science* **2004**, *306*, 666.

[16] D. M. Guldi, N. Martín, *Carbon Nanotubes and Related Structures*, Wiley-VCH, Weinheim, **2010**.

[17] R. H. Baughman, A. A. Zakhidov, W. A. d. Heer, *Science* **2002**, *297*, 787.

[18] M. F. L. De Volder, S. H. Tawfick, R. H. Baughman, A. J. Hart, *Science* **2013**, *339*, 535.

Table 1. Graphene and CNT properties.

Properties	Graphene	CNT
Fracture strength (GPa)	≈ 124 (Modulus ≈ 1100 GPa)	45
Density (g/cm^3)	> 1	1.33
Thermal conductivity (W/m·k)	≈ 5000	3000
Electrical conductivity (S/cm)	10^6	5000
Charge mobility (cm^2/V·s)	200000	100000
Specific surface area (m^2/g)	2630	400 (for nanotube "paper")

The electronic features of graphene are particulary remarkable. Thus, it is a zero band-gap semiconductor where the conduction band touches the valence band at the Brillouin zone corners (Figure 3a).[19] For many electronic applications, it is necessary to open this band gap. To carry out this opening there are four strategies: heteroatom doping,[20] electrostatic field tuning,[21] cutting graphene into nanoribbons[22] and chemical modification[23] (Figure 3b).

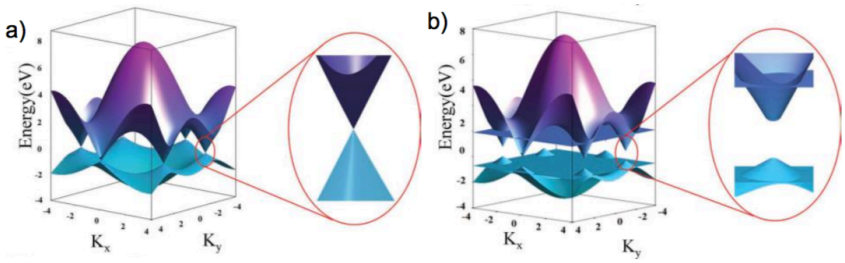

Figure 3. a) Zero band-gap of graphene, b) Band-gap opening by chemical modification.

[19] a) K. S. Kim, Y. Zhao, H. Jang, S. Y. Lee, J. M. Kim, K. S. Kim, J.-H. Ahn, P. Kim, J.-Y. Choi, B. H. Hong, *Nature* **2009**, *457*, 706. b) A. H. Castro Neto, F. Guinea, N. M. R. Peres, K. S. Novoselov, A. K. Geim, *Rev. Mod. Phys*. **2009**, *81*, 109.
[20] M. L. Mueller, X. Yan, B. Dragnea, L. S. Li, *Nano Lett*. **2011**, *11*, 56.
[21] T. Ohta, A. Bostwick, T. Seyller, K. Horn, E. Rotenberg, *Science* **2006**, *313*, 951.
[22] L. Jiao, L. Zhang, X. Wang, G. Diankov, H. Dai, *Nature* **2009**, *458*, 877.
[23] H. Liu, Y. Liu, D. Zhu, *J. Mater. Chem.* **2011**, *21*, 3335.

From these approaches, chemical modification (covalent or supramolecular) is essential to improve the processability for any practical applications of all carbon nanostructures. In this regard, the combination of them with electroactive molecules attracts considerable attention for their potential as electron donor-acceptor systems for artificial photosynthesis,[24] and photovoltaics.[25] Herein, it is important to mention that, unlike fullerenes, graphene and CNT have an ambipolar nature and they can act as donors or acceptors depending on what type of electroactive molecule is used in the hybrid formation.

More recently, new carbon nanostructures have caught the attention of the scientific community. On one hand, graphene quantum dots (GQD) are nanomaterials derived from different carbon sources (graphite, carbon fibers, CNT, coal,…) by fragmentation. Thus, as a consequence of its size (<20 nm) the so-called quantum confinement effect appears.[26] This quantum effect allows GQD to exhibit photoluminiscent properties such as fluorescence. These properties depend on the size, shape and fraction of sp^2 domains, so that emission and absorption range may be tuned by several processes and a wide variety of photoluminescent GQD can be obtained.[27]

On the other hand, another possible approach is using easy to access low-cost and biocompatible organic molecules (for instance aminoacids or carbohydrates) as a carbon source and build up photoluminiscent materials. These new materials are known as carbon nanonots (CND). Regarding structural concerns, CND are different from GQD, having the former a carbon core containing sp^2 and sp^3 domains intermingled and presenting, the latter, a well-defined structure predominantly consisting of sp^2 carbon layers (Figure 4).[28]

[24] a) X. Huang, Z. Yin, S. Wu, X. Qi, Q. He, Q. Zhang, Q. Yan, F. Boey, H. Zhang, *Small*. **2011**, *7*, 1876. b) X. Wan, Y. Huang, Y. Chen, *Acc. Chem. Res*. **2012**, *45*, 598.
[25] a) L. Dai, *Acc. Chem. Res*. **2013**, *46*, 31. b) N. Martín, *Adv. Energy Mater*. **2017**, 7, 1601102.
[26] R. Sekiya, Y. Uemura, H. Murakami, T. Haino, *Angew. Chem. Int. Ed.* **2014**, *53*, 5619.
[27] K. P. Loh, Q. Bao, G. Eda, M. Chhowalla, *Nat. Chem.* **2010**, *2,* 1015.
[28] M. Shamsipur, A. Barati, S. Karami, *Carbon* **2017**, *124*, 429.

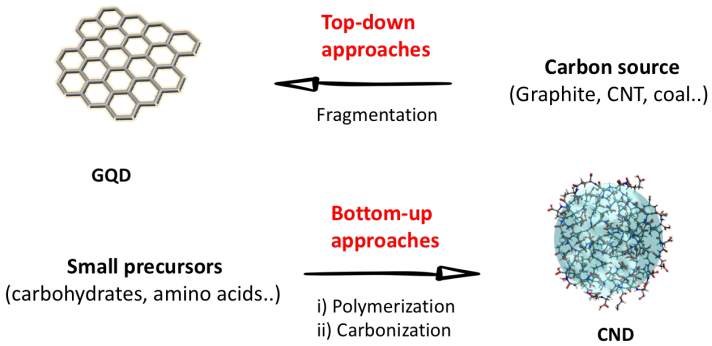

Figure 4. Scheme representing the general methods for obtaining GQD (top) and CND (bottom).

The main advantages of these two systems are: low cytotoxicity, excellent solubility in water, chemical inertness, stable photoluminescence and better surface grafting than graphene, making them promising for development of optoelectronic devices, sensors or IR bioimaging probes, among other applications.[26,28] Furthermore, chemical modification of CND appears at this moment as a pretty intriguing field when considering artificial photosynthesis. The reason is that CND are able to undergo charge transfer reactions both, as a donor and acceptor in the excited state, suffering, thereby, a quenching in their photoluminescence.[28]

In this context, we have explored the chemical reactivity of different carbon nanoforms, (graphene, CNT, GQD and CND) using both covalent and supramolecular approaches, for the incorporation of electroactive units. Furthermore, in most cases the newly formed hybrids have been subjected to photophysical investigations in order to study the charge transfer process between the carbon materials and the electroactive units. These experiments aimed to establish the bases to understand the charge transfer processes between carbon-nanoforms and electroactive molecules, with the intention of further use these systems for application in artificial photosynthesis.

Chapter 1

1.1. BACKGROUND

1.1. BACKGROUND

1.1.1. Graphene structure definitions

Graphite is the most abundant and stable form of carbon under standard conditions which can be of natural origin or synthetically generated[29]. Graphite presents a layered planar structure, where each single layer (graphene) is constituted by sp^2 carbon atoms arranged in a honeycomb lattice. Hence, each atom is bonded to other three, forming hexagons that are fused throughout the layer. The 3D layers organization can lead to a hexagonal (AB) or rhombohedral (ABC) stacking, or may be turbostratic with no regularities within the layer sequence.[30] Layers are separated by a distance of 3.35 Å and linked by van der Waals interactions generated by the delocalization of π-orbitals (Figure 1.1). This delocalization generates conjugated π-electrons that are responsible of the electronic properties of graphite. Graphite is an anisotropic material because of the nature of these binding forces, presenting good electrical and thermal conductivity through the layers but poor in the perpendicular direction.[31]

As it was mentioned above, graphene is a single layer of graphite formed by sp^2 hybridized carbon atoms arranged into a two-dimensional honeycomb structure. Because of its atomic thickness, graphene is the thinnest known material which, in addition, presents outstanding mechanical, thermal and electronic properties.[32] In 2004 graphene was reported by A. Geim and K. Novoselov as the first two-dimensional material ever isolated.[15,33] Until that moment, it was supposed that two dimensional materials could not exist because they were thermodynamically unstable.[34,35] Nevertheless, these materials are stabilized by deformations in the third dimension. Although it

[29] N. V. Kozhemyakina, S. Eigler, R. E. Dinnebier, A. Inayat, W. Schwieger, A. Hirsch, *Fullerenes*, *Nanotubes and Carbon Nanostructures* **2013**, *21*, 804.
[30] H. Lipson, A. R. Stokes, *Nature* **1942**, *149*, 328.
[31] D. D. L. Chung, *J. Mater. Sci*. **2002**, *37*, 1475.
[32] A. K. Geim, *Science* **2009**, *324*, 1530.
[33] K. S. Novoselov, A. K. Geim, S. V. Morozov, D. Jiang, M. I. Katsnelson, I. V. Grigorieva, S. V. Dubonos, A. A. Firsov, *Science* **2005**, *438*, 197.
[34] R. Peierls, *Ann. Inst. Henri Poincare* **1935**, *5*, 177.
[35] J. Tolédano, P. Tolédano, *The Landau theory of phase transitions,* World Scientific Lecture Notes in Physics, **1987**.

was expected that graphene was perfectly flat, A. Geim and K. Novoselov reported that graphene layers present intrinsic corrugations and can exist without a substrate.[36] Real graphene exhibits edges that have either a zig-zag or an armchair arrangement (Figure 1.1b). The high-resolution transmission electron microscopy (HRTEM) image of graphene in Figure 1.1c shows a graphene layer with a typical edge.[37]

The ideal concept of two-dimensional material refers to materials composed of a single atomic layer, but graphene is usually considered a two-dimensional material until it reaches a 10 layers thickness. Furthermore, the singular electronic properties of single layer, bilayer and few-layer graphene allows the distinction between the three different types.[38]

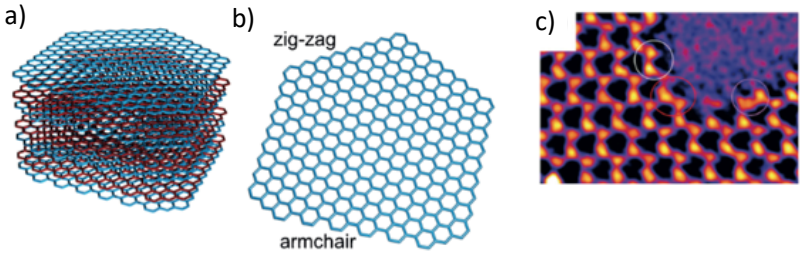

Figure 1.1. Schematic representation of a) the ideal structure of AB-stacked graphite and b) the structure of a sheet of graphene with zig-zag and armchair edges. c) HRTEM image of graphene with one edge.

Besides this classification, other form to categorize graphene relates with the modification of its structure. Pristine graphene refers to graphene produced without any defect or functional group on its surface. Whereas chemically modified graphene indicates the presence of sp^3 defects in the basal plane or in the rims. In this last group, it can be distinguished between two types: graphene oxide and reduced graphene oxide.

Graphene oxide (GO) is a chemically modified graphene composed by a single layer of graphite oxide. The modification consists in the presence of different

[36] J. C. Meyer, A. K. Geim, M. I. Katsnelson, K. S. Novoselov, T. J. Booth, S. Roth, *Nature* **2007**, *446*, 60.
[37] S. Eigler, A. Hirsch, *Angew. Chem. Int. Ed*. **2014**, *53*, 7720.
[38] A. K. Geim, K. S. Novoselov, *Nat. Mater*. **2007**, *6*, 183.

oxidized groups attached to the surface that make GO hydrophilic and allow the stabilization of layers in water (Figure 1.2). This material is obtained by the oxidative treatment of graphite, where the graphene layers in graphite become intercalated by the acid to form, in a first instance, an intercalation compound. Subsequent oxygenation of such intercalation material occurs on both sides of the basal plane and, in this way, graphite oxide is formed. Delamination of single layers of graphite oxide provides GO.

The exact nature of the functional groups in GO strongly depends on the reaction conditions, such as preparation time and temperature as well as on the work-up procedure. Nevertheless, due to the polydispersity of this material is really difficult to define the exact structure. One of the most suitable structural model for GO is based on the investigations of Lerf, Klinowski, and co-workers,[39] which were further confirmed by the research groups of Ishii[40] and Gao[41], mostly through solid state NMR, the proposed structures incorporate a high number of hydroxy an epoxy groups in the basal plane which coexist with sp^2 carbons preserved during the oxidation process.

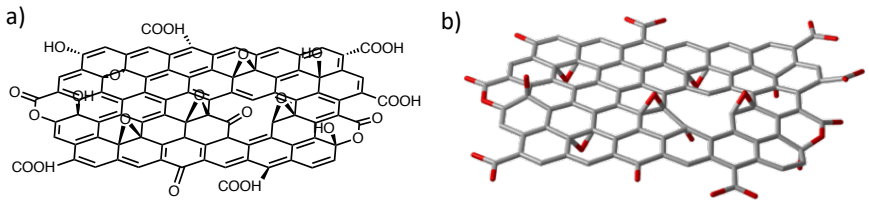

Figure 1.2. a) Proposed structural model of GO with different oxygenated groups in the surface. b) 3D representation of the model proposed in a).

Other oxygen functionalities identified in GO structure are carboxylic acids, carbonyl groups and lactones, which usually are located on the edges of the layer. The formation of these last species requires the rupture of C-C bonds, which may be accompanied by the loss of carbon induced by overoxidation and CO_2 formation during the synthesis. It was reported that about one molecule of

[39] H. He, J. Klinowski, M. Forster, A. Lerf, *Chem. Phys. Lett.* **1998**, *287*, 53.
[40] W. Cai, R. D. Piner, F. J. Stadermann, S. Park, M. A. Shaibat, Y. Ishii, D. Yang, A. Velamakanni, S. J. An, M. Stoller, J. An, D. Chen, R. S. Ruoff, *Science* **2008**, *321*, 1815.
[41] W. Gao, L. B. Alemany, L. Ci, P. M. Ajayan, *Nat. Chem.* **2009**, *1*, 403.

CO_2 is formed per 35–55 lattice carbon atoms during the oxidation process, and the final material presents about one carbonyl group per 10–12 lattice carbon atoms.[42] Moreover, the loss of carbon from the carbon skeleton results in the generation of permanent defects, including holes, in the lattice.

The major drawback of this method is that both, graphite oxide and therefore GO, are insulators after the disruption of the π-conjugated graphene layer by the sp^3 defects. These defects, originated with the oxidation process, severely modify the structure and, hence, the properties. Although these functional groups can be removed by reduction (chemical,[43] thermal and electrochemical[44]) obtaining what is named reduced graphene oxide (rGO), the structural defects introduced by the oxidative treatment continue modifying the unique properties of graphene, in particular its high electrical and thermal conductivity.[45] Nevertheless, in some applications related with catalysis or the biomedical area, GO and rGO have been extensively used, since these large surfaces feature great chemical complexity.

In the following, we will discuss the production of pristine graphene and GO as well as their chemical functionalization.

1.1.2. Pristine graphene production methods

The methods employed in pristine graphene production, or simply graphene from now on, can be classified in: bottom-up and top-down approaches. Bottom-up methods consider the preparation of graphene from the covalent assembly of polycyclic aromatic hydrocarbons (PAHs),[46] by growth on different supports by silicon evaporation from SiC,[47] or by chemical vapor

[42] A. Dimiev, D. V. Kosynkin, L. B. Alemany, P. Chaguine J. M. Tour, *J. Am. Chem. Soc*. **2012**, *134*, 2815.
[43] S. Stankovich, D. A. Dikin, R. D. Piner, K. A. Kohlhaas, A. Kleinhammes, Y. Jia, Y. Wu, S. T. Nguyen, R. S. Ruoff, *Carbon* **2007**, *45*, 1558.
[44] D. R. Dreyer, S. Park, C. W. Bielawski, R. S. Ruoff, *Chem. Soc. Rev*. **2009**, *39*, 228.
[45] C. Gómez-Navarro, R. T. Weitz, A. M. Bittner, M. Scolari, A. Mews, M. Burghard, K. Kern, *Nano Lett*. **2007**, *7*, 3499.
[46] X. Yang, X. Dou, A. Rouhanipour, L. Zhi, H. J. Räder, K. Müllen, *J. Am. Chem. Soc*. **2008**, *130*, 4216.
[47] C. Berger, Z. Song, X. Li, X. Wu, N. Brown, C. Naud, D. Mayou, T. Li, J. Hass, A. N. Marchenkov, E. H. Conrad, P. N. First, W. A. de Heer, *Science* **2006**, *312*, 1191.

deposition (CVD) of small molecular precursors.[48] These methods give rise to high quality graphene sheets with large areas and a low level of defects. Nevertheless, these methods are not suitable for the production of large quantities, which is a drawback for industrial applications.

Top-down methods, however, are based in the exfoliation of graphite to give graphene layers. The first example reported implied a graphite exfoliation by mechanical cleavage (the scotch-tape technique)[15] providing high quality sheets. The main problem is to scale-up the production due to the long times involved in the production. A faster method to exfoliate graphene is ball-milling,[49] where large amounts of graphene can be produced in a planetary mill using as starting material graphite and melamine or glucose (Figure 1.3). Nevertheless, during the mechanical treatment graphene layers can break apart resulting in additional defects in the structure. In addition, a further step of purification is required to remove the exfoliating agent by dialysis.

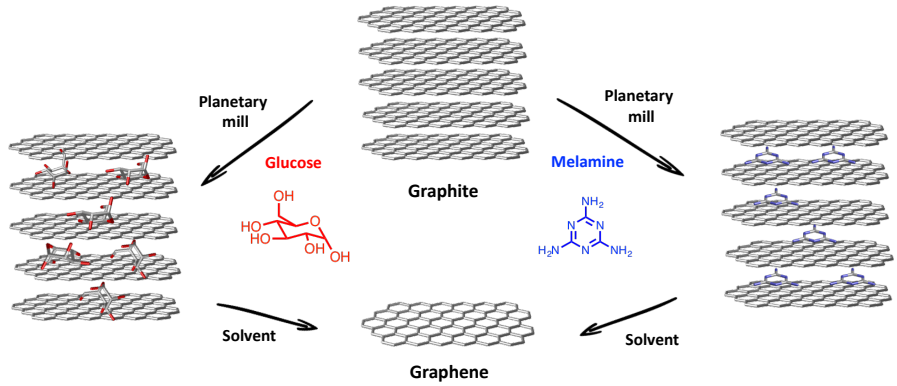

Figure 1.3. Schematic illustration for the exfoliation of graphite through the ball-milling approach.

[48] K. S. Kim, Y. Zhao, H. Jang, S. Y. Lee, J. M. Kim, K. S. Kim, J. Ahn, P. Kim, J. Choi, B. H. Hong, *Nature* **2009**, *457*, 706.

[49] a) V. León, A. M. Rodriguez, P. Prieto, M. Prato, E. Vázquez, *ACS Nano* **2014**, *8*, 563. b) V. J. González, A. M. Rodríguez, V. León, J. Frontiñán-Rubio, J. L. G. Fierro, M. Durán-Prado, A. B. Muñoz-García, M. Pavone, E. Vázquez, *Green Chem*, **2018**, *20*, 3581.

The above-mentioned methods do not use solvents during the exfoliation process, however, there is a prominent third method that considers the dispersion and exfoliation of graphite in liquid phase. In particular, the ultra-sound-induced liquid-phase exfoliation[50] presents some advantages such us its potential scalability, the high-quality layers obtained (free of structural defects) and the straightforward transfer to different substrates for many applications.[51]

This procedure is usually performed in three steps: i) dispersion of graphite in a solvent, ii) exfoliation and iii) removal of the bulk starting material (usually by centrifugation). Graphene can be produced by ultrasonication in organic solvents or with the assistance of surfactants and dispersion stabilizing agents in a wider selection of solvents (Figure 1.4).

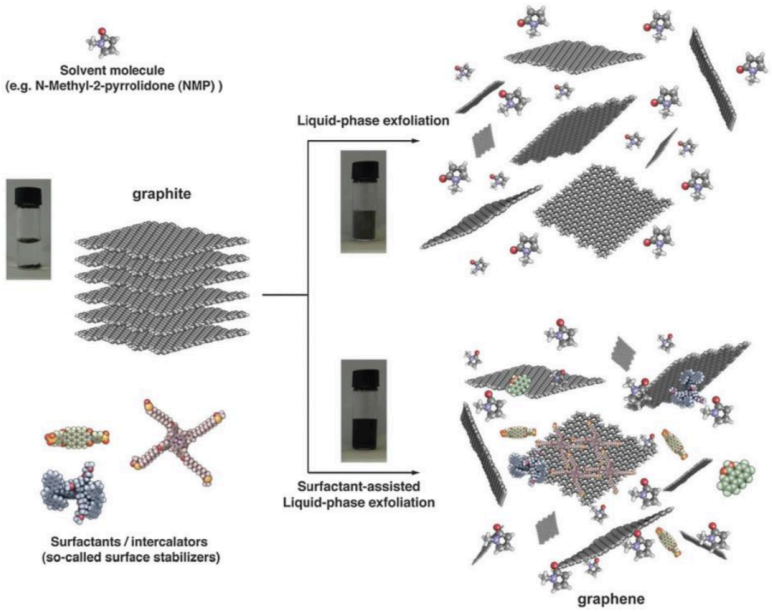

Figure 1.4. Schematic representation of the liquid-phase exfoliation of graphite in the absence (top) and presence (bottom) of stabilizing agents.

[50] Y. Hernandez, V. Nicolosi, M. Lotya, F. M. Blighe, Z. Sun, S. De, I. T. McGovern, B. Holland, M. Byrne, Y. K. Gun'Ko, J. J. Boland, P. Niraj, G. Duesberg, S. Krishnamurthy, R. Goodhue, J. Hutchison, V. Scardaci, A. C. Ferrari, J. N. Coleman, *Nat. Nanotechnol.* **2008**, *3*, 563.
[51] A. Ciesielski P. Samorì, *Adv Mater*. **2016**, *28*, 6030.

The first requirement in order to exfoliate graphite is overcome the van der Waals interaction between layers, which can be achieved by external forces such us sonication in liquid phase. Once the exfoliation takes place, due to the cavitation and the shear forces that act on the bulk material, it is required to stabilize the graphene layers and avoid its reaggregation.

When exfoliation is accomplished just in the presence of solvents, the stabilization of the graphene layers comes from the strong interactions between the solvent and the graphene sheets, which minimizes the enthalpy of mixing. The value of this thermodynamic parameter depends on the balance of the solvent and the graphene surface energies. Coleman[52] found out that solvents with surface energies close to the surface energy of graphene are able to stabilize graphene sheets in dispersion. These solvents possess surface energies of ~ 70 mJ/m^2, which are equivalent to surface tensions of ~ 40 mJ/m^2, *N*-methyl-2-pyrrolidone (NMP = 40 mJ/m^2) or *N,N*-dimethylformamide (DMF = 37 mJ/m^2) are some of the solvents in this range. Other investigations demonstrated that the surface energy can be divided in dispersive, polar and H-bonding components, namely, Hansen solubility parameters.[53] Bearing in mind all these considerations, several organic solvents can be used in the formation and stabilization of graphene dispersions (Figure 1.5).

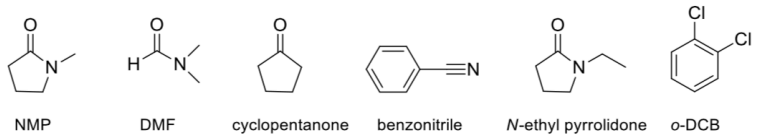

Figure 1.5. Common solvents used in the exfoliation of graphite.

Remarkable results in graphene exfoliation were obtained using NMP as a solvent, being the one with the best number fraction of few-layer graphene and the highest number fraction of monolayer graphene. Other solvent that allows an efficient exfoliation was *ortho*-dichlorobenzene (*o*-DCB),[54] which is a nonpolar solvent with an appropriate surface tension (*o*-DCB ~ 37 mJ/m^2). The

[52] J. N. Coleman, *Acc. Chem. Res*. **2013**, *46*, 14.
[53] Y. Hernandez, M. Lotya, D. Rickard, S. D. Bergin, J. N. Coleman, *Langmuir* **2010**, *26*, 3208.
[54] C. E. Hamilton, J. R. Lomeda, Z. Sun, J. M. Tour, A. R. Barron, *Nano Lett*. **2009**, *9*, 3460.

dispersions obtained in *o*-DCB are homogeneous and the layers do not present defects. The major drawback of these solvents is that most of them have high boiling points, which is an inconvenient for many applications. Other alternatives have been tested, such as the exfoliation with aromatic electron-accepting[55] or electron-donor[56] solvents or performing a solvent exchange in previously exfoliated graphene dispersions.[57]

In a recent example, Pénicaud, Drummond *et al.*,[58] showed that homogeneous stable dispersions of single-layer graphene in water can be obtained by mixing graphenide (negatively charged graphene) solutions in tetrahydrofuran with degassed water and evaporating the organic solvent. The resulting additive-free stable water dispersions contain 400 $m^2 \cdot l^{-1}$ of developed graphene surface.

According to Coleman and co-workers,[59] besides of the solvent choice, there are other parameters that can affect the production of graphene by liquid phase exfoliation. They explored different sonication times and observed that this parameter is a direct function of the concentration, but indirect to the produced sheets dimensions. Thus, longer sonication times result in smaller flakes which can be dispersed at higher concentration. Another key parameter evaluated was the centrifugation rate, in this case the concentration decreased for a fixed sonication time with the rotation rate, since only the smaller flakes remained dispersed due to their low weight.

The small number of solvents in which graphene can be exfoliated, prompted searching for new alternatives. An interesting option is the use of common solvents (water, alcohol, THF) and a dispersion-stabilizing agent that hampers the re-aggregation of the graphene layers. A summary of some common stabilizing agents used in graphene exfoliation is presented in the following paragraphs (Figure 1.6).

---

[55] A. B. Bourlinos, G. Vasilios, Z. Radek, T. A. Steriotis, A. K. Stubos, *Small* **2009**, *5*, 1841.

[56] Z. Sun, X. Huang, F. Liu, X. Yang, C. Rosler, R. A. Fischer, M. Muhler, W. Schuhmann, *Chem. Commun*. **2014**, *50*, 10382.

[57] X. Zhang, A. C. Coleman, N. Katsonis, W. R. Browne, B. J. van Wees, B. L. Feringa, *Chem. Commun*. **2010**, *46*, 7539.

[58] G. Bepete, E. Anglaret, L. Ortolani, V. Morandi, K. Huang, A. Pénicaud, C. Drummond, *Nat. Chem*. **2016**, *9*, 347.

[59] K. Umar, O'Neill Arlene, L. Mustafa, D. Sukanta, J. N. Coleman, *Small* **2010**, *6*, 864.

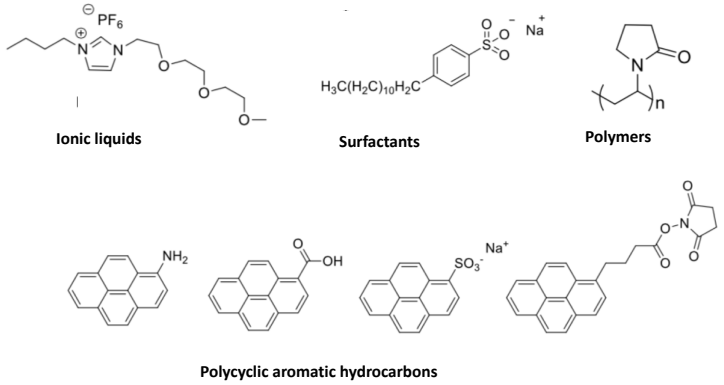

Figure 1.6. Different exfoliating agents used in the stabilization of graphene.

Ionic Liquids (IL) are semiorganic salts (organic and inorganic ions) whose melting point is below 100 °C and present hydrophobic and hydrophilic components. These ionic species allow the stabilization of graphene layers by Coulombic interactions and have the advantage of presenting surface tensions near that of graphite. In this case, ionic liquids act at the same time as solvent and as dispersion-stabilizing agent. One of the most striking investigations based in these fundaments, is the work reported by Aida and co-workers.[60] They presented a microwave assisted graphene exfoliation with oligomeric ionic liquids, which resulted in almost quantitative yields (93 %) with a high selectivity towards single layer graphene (95 %).

Surfactants have been shown to be good stabilizing agents of graphene sheets mainly in aqueous media. The first example using this approach was described by Coleman and co-workers,[61] performing the exfoliation of graphene in water using sodium dodecylbenzene sulfonate (SDBS) as surfactant. Since then, other procedures have been reported in this line with the use of other surfactants such as sodium cholate[62] or cetyltrimethylammonium bromide (CTAB).[63] In all cases, the dispersions are stabilized against re-aggregation by the Coulomb repulsion due to the adsorption of the surfactant.

[60] M. Matsumoto, Y. Saito, C. Park, T. Fukushima, T. Aida, *Nat. Chem*. **2015**, *7*, 730.
[61] M. Lotya, Y. Hernandez, P. J. King, R. J. Smith, V. Nicolosi, L. S. Karlsson, F. M. Blighe, S. De, Z. Wang, I. T. McGovern, G. S. Duesberg, J. N. Coleman, *J. Am. Chem. Soc*. **2009**, *131*, 3611.
[62] M. Lotya, P. J. King, U. Khan, S. De, J. N. Coleman, *ACS Nano* **2010**, *4*, 3155.
[63] S. Vadukumpully, J. Paul, S. Valiyaveettil, *Carbon* **2009**, *47*, 3288.

Polymers are found to be stabilizing agents in both, aqueous and organic dispersions of graphene. Hence, polyvinylpyrrolidone (PVP) forms stable colloidal aqueous dispersions of graphene as demonstrated by Bourlinos and co-workers.[64] In terms of stabilization efficiency when comparing different non-ionic and ionic polymers, it was pointed out that non-ionic polymers significantly outperform their ionic counterparts. However, more recent investigations have considered polysaccharides with different electrostatic nature showing that the different surface free energy and thermodynamic affinity also play a major role in the stabilization of the graphene sheets.[65] As in the case of stabilization with ionic liquids, the adsorbed polymers are difficult to remove even after several washings, due to the strong interactions with graphene's surface.

Polycyclic aromatic hydrocarbons (PAHs) can be used as stabilizers in graphene dispersions, being the major driving force the π-π interactions. In these non-covalent interactions, both PAHs and graphene aromatic planar surfaces share electrons of the π-orbitals, resulting in the reduction of the surface free energy of the dispersions. In this sense, pyrene derivatives have been extensively investigated for the exfoliation and stabilization of graphene. An interesting example is the one described by Green and co-workers, where a whole family of pyrene derivatives were used to investigate the mechanism of stabilization of aqueous dispersions by these molecules.[66] They found that the stabilization effectiveness strongly depends on the electron density of the organic molecule. Apart from pyrene derivatives, other PAHs have been used in the stabilization of graphene in water such as triphenylene,[67] diazaperopyrenium dications,[68] and naphthalenediimide derivatives.[69]

[64] A. B. Bourlinos, V. Georgakilas, R. Zboril, T. A. Steriotis, A. K. Stubos, C. Trapalis, *Solid State Commun*. **2009**, *149*, 2172.
[65] I. Uysal Unalan, C. Wan, S. Trabattoni, L. Piergiovanni, S. Farris, *RSC Adv*. **2015**, *5*, 26482.
[66] D. Parviz, S. Das, H. S. T. Ahmed, F. Irin, S. Bhattacharia, M. J. Green, *ACS Nano* **2012**, *6*, 8857.
[67] S. Das, F. Irin, H. S. Tanvir Ahmed, A. B. Cortinas, A. S. Wajid, D. Parviz, A. F. Jankowski, M. Kato, M. J. Green, *Polymer* **2012**, *53*, 2485.
[68] S. Srinivasan, A. N. Basuray, K. J. Hartlieb, A. Taner, S. I. Stupp, S. J. Fraser, *Adv. Mater*. **2013**, *25*, 2740.
[69] L. Zhang, Z. Zhang, C. He, L. Dai, J. Liu, L. Wang, *ACS Nano* **2014**, *8*, 6663.

1.1.3. Graphene oxide and reduced graphene oxide production methods

Up to now there are plenty of different methodologies reported for the production of graphite and graphene oxide. The first graphite oxidation was reported in 1840, by Schafhaeutl, [70] who referred to graphite oxide as "graphitic acid". It was in 1859 when Brodie discovered the formation of graphite oxide by the oxidation of graphite in nitric acid with potassium chlorate.[71] The addition of potassium chlorate results in the formation of chlorine dioxide (ClO_2), which is explosive in high concentrations. About 40 years later, Staundemaier optimized Brodi's method to minimize the explosion risk.[72] The improved procedure used sulfuric acid, nitric acid and potassium chlorate as reagents, the latter was added slowly and carefully in the reaction flask. In the following decades similar methodologies were reported, where it is important to highlight the method described by Charpy in 1909.[73] Herein, the temperature was kept below 45 ºC for reducing the CO_2 formation, sulfuric acid, sodium nitrate and potassium permanganate were used as oxidant agents. Afterwards, this method resulted to be scaled-up resulting in what is known as "Hummers' method".[74,75] Many modifications have been proposed since then, but the general method involves several oxidation and hydration steps carried out at different temperatures. More recently, Kovtyukhova reported an improved Hummers' method,[76] where graphite was subjected to a preoxidation step using as oxidizing agent potassium peroxodisulfate. Furthermore, in Kovtyukhova's method it was avoided the use of sodium nitrate as an oxidizing agent, keeping away the release of NO_x species and increasing the hydrophilic character of the as-prepared graphite oxide. This has been a brief summary of the most outstanding methods since the origins of oxidized graphite, about 150 years ago. Currently there are new methods that are based on small modifications of the aforementioned processes.

---

[70] C. Schafhaeutl, *J. Prakt. Chem*. **1840**, *21*, 129.
[71] B. C. Brodie, *Ann. Chim. Phys*. **1855**, *45*, 351.
[72] a) L. Staudenmaier, *Ber. Dtsch. Chem. Ges*. **1898**, *31*, 1481. b) L. Staudenmaier, *Ber. Dtsch. Chem. Ges.* **1899**, *32*, 1394. c) L. Staudenmaier, *Ber. Dtsch. Chem. Ges*. **1899**, *32*, 2824.
[73] G. Charpy, C. R. Hebd. *Seances Acad. Sci*. **1909**, *148*, 920.
[74] J. William, S. Hummers, R. E. Offeman, *J. Am. Chem. Soc*. **1958**, *80*, 1339.
[75] W. S. Hummers, *Preparation of graphitic acid*, US2798878, **1957**.
[76] N. I. Kovtyukhova, P. J. Ollivier, B. R. Martin, T. E. Mallouk, S. A. Chizhik, E. V. Buzaneva, A. D. Gorchinskiy, *Chem. Mater*. **1999**, *11*, 771.

Importantly, it has been demonstrated that the products of these reactions show a strong variance, depending not only on the particular oxidants used, but also on the graphite source and reaction conditions. Moreover, it is necessary to mention that this kind of procedures, at first instance, give rise to graphite oxide and it is necessary an additional step of delamination for obtaining GO. In the following paragraphs are explained the different steps to obtain GO. All these methods, despite of using different reaction conditions and reagents, present a similar synthetic pathway (Figure 1.7).

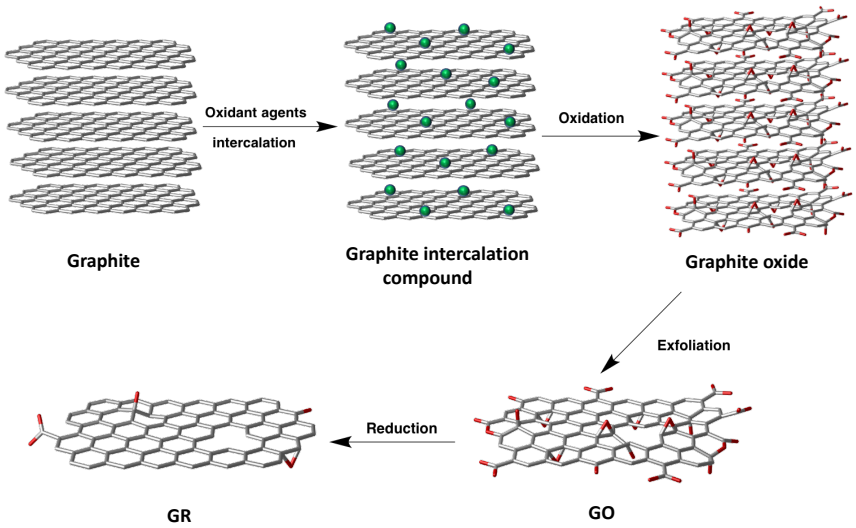

Figure 1.7. Schematic representation of the synthesis pathway followed to produce GO and GR.

In general, natural graphite is used as the starting material to enable the large-scale synthesis of GO. During the first step graphite is usually dispersed in sulfuric acid in the presence of different oxidant agents. These molecules are intercalated between the graphite layers resulting in the formation of graphite sulfate intercalated compound.[77] As consequence of this, it is produced an increase of the d-spacing layers which results in the activation of graphite. At this point the oxidant species diffuse through the interlayer space of graphite sulfate and produce the oxidation of the graphite layers with a consequent change of hybridization of the oxidized carbon atoms from planar sp^2 to tetrahedral sp^3. The oxidation step is accompanied by a hydrolysis step for the

[77] A. M. Dimiev, S. M. Bachilo, R. Saito, J. M. Tour, *ACS Nano* **2012**, *6*, 7842.

solubilization of the oxidant species as well as to hydrolyze the cyclic organosulfate derivatives formed in the reaction.[78] The as-produced graphite oxide is further purified by washing, centrifugation or by dialysis steps.[79] Finally, delamination of graphite to GO implies the dispersion of graphite oxide in water or other polar solvents, followed by a sonication step.

Another interesting approach is the reduction of GO to graphene. One of the simplest strategies is through the thermal annealing of graphite oxide. This approach results in the formation of graphene and CO_2. However, the recovery of pristine graphene is not completed because the presence of σ-holes in the sp^2 network as a well as some oxygenated groups such as carbonyl and ether (Figure 1.8).[80] Temperatures higher than 1500 ºC are required for the full deoxygenation of GO[81] through the reorganization of the carbon network. Nevertheless, this method implies a high energy cost.

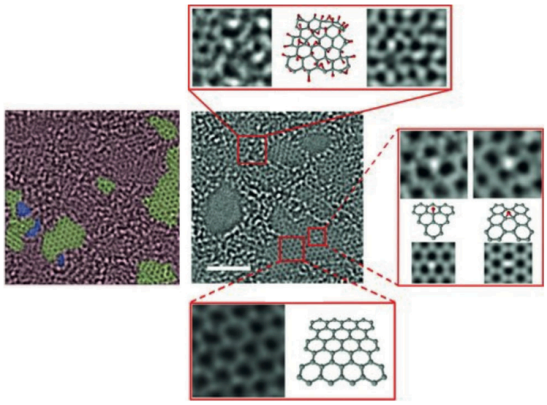

Figure 1.8. HRTEM image of GO displaying the preserved regions (green) of graphene (1–2 nm), holes (blue), and heavily oxidized regions (red). Insets: comparison of the measured and simulated images with structural models.

[78] S. Eigler, S. Grimm, F. Hof, A. Hirsch, *J. Mater. Chem. A*. **2013**, *1*, 11559.
[79] O. C. Compton, S. W. Cranford, K. W. Putz, Z. An, L. C. Brinson, M. J. Buehler, S. T. Nguyen, *ACS Nano* **2012**, *6*, 2008.
[80] a) A. Ganguly, S. Sharma, P. Papakonstantinou, J. Hamilton, *J. Phys. Chem. C*. **2011**, *115*, 17009; b) C. Botas, P. Álvarez, P. Blanco, M. Granda, C. Blanco, R. Santamaría, L. J. Romasanta, R. Verdejo, M. A. López-Manchado, R. Menéndez, *Carbon* **2013**, *65*, 156.
[81] R. Rozada, J. I. Paredes, S. Villar-Rodil, A. Martínez-Alonso, J. M. D. Tascón, *Nano Res*. **2013**, *6*, 216.

An alternative, which requires softer conditions, is the use of reducing agents. The most common reducing agents are hydrazine and hydriodic acid.[82] Despite the fact that this method is a good alternative to the annealing, with this methodology the total recovery of the sp^2 surface is neither achieved. There are additional procedures where annealing processes are combined with reducing agents with similar results to those achieved in the independent methodologies.

1.1.4. Techniques involved in the characterization of graphene-based materials

Regarding the characterization of graphene derivatives, it is necessary to highlight that some techniques are essential to evaluate the quality of these materials. UV-Vis spectroscopy allows estimating the concentration of dispersed material using the Lambert-Beer Law. The number of layers can be determined by different complementary techniques like transmission electron microscopy (TEM), atomic force microscopy (AFM) and Raman spectroscopy. TEM is useful for the morphological study of the material, besides the number of graphene layers can be estimated by the analysis at the edges[83] and by the study of the electron diffraction patterns. AFM makes possible the estimation of layers by measuring the height of the graphene flakes. This height depends on the substrate and on the environmental conditions.[84,85]

Raman spectroscopy is one of the most powerful methods for characterizing graphene, GO, and their covalent derivatives. It allows obtaining information about the thickness of the material and the structural defects. Raman spectra of graphene are characterized by three bands: D band (~1350 cm^{-1}, associated to carbon atoms with sp^3 hybridization, meaning defects), G band (~1580 cm^{-1}, associated to carbon atoms with sp^2 hybridization) and 2D band (~2700 cm^{-1}, indicating the number of layers). Raman spectra of graphene when increasing the number of layers, from single layer to bilayer and to few-layer graphene, present very different features, which permit their differentiation.[83]

[82] C. K. Chua, M. Pumera, *Chem. Soc. Rev*. **2014**, *43*, 291.
[83] A. C. Ferrari, J. C. Meyer, V. Scardaci, C. Casiraghi, M. Lazzeri, F. Mauri, S. Piscanec, D. Jiang, K. S. Novoselov, S. Roth, A. K. Geim, *Phys. Rev. Lett*. **2006**, *97*, 187401.
[84] C. Vallés, C. Drummond, H. Saadaoui, C. A. Furtado, M. He, O. Roubeau, L. Ortolani, M. Monthioux, A. Pénicaud, *J. Am. Chem. Soc*. **2008**, *130*, 15802.
[85] K. S. Novoselov, D. Jiang, F. Schedin, T. J. Booth, V. V. Khotkevich, S. V. Morozov; A. K. Geim, *Proc. Natl. Acad. Sci. U.S.A*. **2005**, *102*, 10451.

Furthermore, the introduction of sp^3 defects in the basal plane results in an increase of the I_D/I_G ratio as well as in the widening of all the bands.

Furthemore, there are other additional techniques for determining the surface area (BET analysis)[86], the colloidal stability of the dispersions (zeta-potential),[87] the thermal stability or the presence of different components (thermogravimetric analysis, TGA)[88] and the elements present in a graphene layer (X-ray photoelectron spectroscopy, XPS).[89]

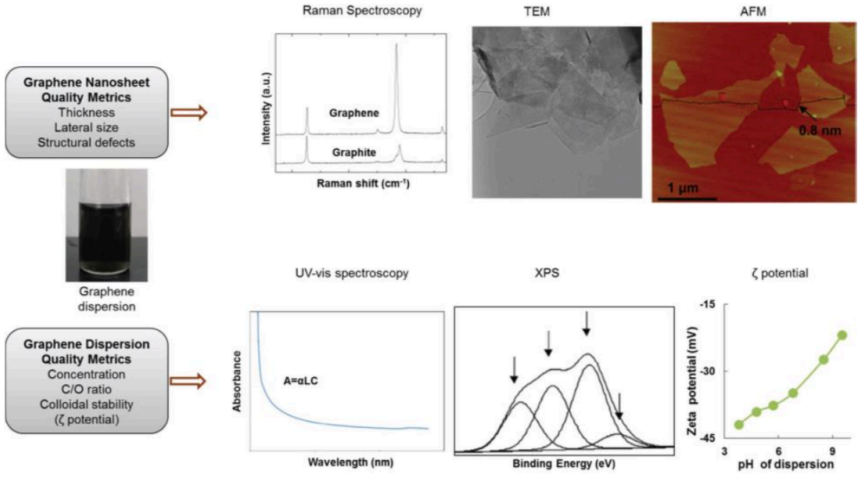

Figure 1.9. Experimental techniques used to determine the quality of graphene flakes and their dispersions.

1.1.5. Graphene functionalization

As it was discussed above, one of the greatest challenges in graphene production is its individualization and stabilization in solution. Even though, the hydrophobic character of graphene makes really difficult its solubilization in polar solvents. Therefore, the obtained dispersions present low concentrations and are instable resulting in the re-aggregation and

[86] K. S. Subrahmanyam, S. R. C. Vivekchand, A. Govindaraj, C. N. R. Rao, *J. Mater. Chem*. **2008**, *18*, 1517.
[87] P. Dorsa, I. Fahmida, S. A. Shah, D. Sriya, C. B. Sweeney, M. J. Green, *Adv. Mater.* **2016**, *28*, 8796.
[88] M. Shtein, I. Pri-Bar, M. Varenik, O. Regev, *Anal. Chem*. **2015**, *87*, 4076.
[89] D. R. Dreyer, S. Park, C. W. Bielawski, R. S. Ruoff, *Chem. Soc. Rev*. **2009**, *39*, 228.

sedimentation of the material. In order to overcome these drawbacks, ne interesting approach is the chemical functionalization of graphene. The doping of the sp^2 network by different molecules could result not only in a solubility enhancement, but also in new and better properties of the material. Graphene bandgap can be modulated by the addition of photo- and/or electroactive molecules, improving its applicability in photovoltaic and optoelectronic devices.

In general, graphene functionalization is divided into two different types, covalent and non-covalent approaches. The former implies the creation of new bonds and is accompanied by the rehybridization of carbon atoms from sp^2 to sp^3. This type of binding is stable and robust but involves the introduction of sp^3 defects in the basal plane of graphene. In this sense, any disruption of the π lattice implies the modification of the properties that make graphene an outstanding material. Otherwise, non-covalent functionalization is based in the adsorption of molecules onto graphene surface through weak forces. This method is attractive from the point of view of the sp^2 network preservation. Several recent review articles and books deal with this topic,[90] in the next pages only a selection of examples are commented. It is important to mention that only examples considering chemical functionalization in solution are mentioned.

1.1.5.1. Pristine graphene covalent functionalization

Although an excess of sp^3 defects on the graphene lattice could dramatically change the properties, the wet covalent modification is used in the controlled modification of graphene, which might be mandatory for certain applications, such as obtaining semiconductors by inducing holes in graphene electronic structure.[91] In contrast to fullerenes and carbon nanotubes that exhibit a curved surface, graphene is planar and, therefore, it is considerably less reactive.[92] Due to the one-atom-thick flat sheet nature of graphene, the chemical reactivity of this carbon nanoform may occur on the basal plane and/or on the edges. The

[90] For a recent overview see *Chem. Soc. Rev.* themed issue on *Graphene Chemistry*: T. Torres (Ed.), *Chem. Soc. Rev.* **2017**, *46*, 15, 4377-4810.

[91] G. Luo, L. Liu, J. Zhang, G. Li, B. Wang, J. Zhao, *ACS Appl. Mater. Interfaces*. **2013**, *5*, 11184.

[92] a) L. Rodriguez-Perez, M. A. Herranz, N. Martín, *Chem. Commun.* **2013***, 49*, 3721. b) K. Dirian, M. A. Herranz, G. Katsukis, J. Malig, L. Rodríguez-Pérez, C. Romero-Nieto, V. Strauss, N. Martín, D. M. Guldi. *Chem. Sci.* **2013***, 4*, 4335.

introduction of tetrahedral sp^3 carbon atoms resulting from the covalent attachment induces a strong strain, which is lowered when these defects are formed in the sheets edges. For this reason, carbon atoms at the edges are supposed to be more reactive. Furthermore, graphene presents sp^3 defects along the carbon network which usually came from the production method. The carbon atoms surrounding the defects present a different electronic structure and, therefore, they are chemically activated for further chemical reactions, thus enhancing the chemical reactivity of graphene.[93] Unlike graphite, graphene chemistry can occur in both sides of the layer which affords species that would be unthinkable on graphite.[94]

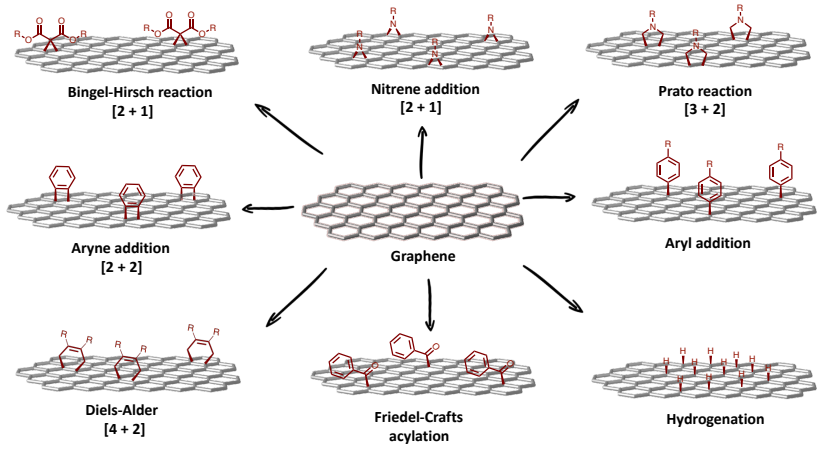

Figure 1.10. Schematic representation of different strategies for the covalent functionalization of graphene.

The most common strategies followed for the covalent modification of graphene are summarized in Figure 1.10. One of the first modifications explored was the reduction of graphene upon hydrogenation by plasma treatment, generating an insulator called graphane. Herein, hydrogen atoms were covalently attached onto the π-conjugated system of graphene. This process was reversible since the sp^2 surface was totally recovered under

[93] a) X. Gao, Y. Wang, X. Liu, T. L. Chan, S. Irle, Y. Zhao, S. B. Zhang, *Phys. Chem. Chem. Phys*. **2011**, *13*, 19449. b) G. Bottari, M. Á Herranz, L. Wibmer, M. Volland, L. Rodríguez-Pérez, D. M. Guldi, A. Hirsch, N. Martín, F. D'Souza, T. Torres, *Chem. Soc. Rev*. **2017**, *46*, 4464.

[94] K. C. Knirsch, R. A. Schäfer, F. Hauke, A. Hirsch, *Angew. Chem. Int. Ed*. **2016**, *55*, 5861.

annealing treatment.[95] Regardless the complete hydrogenation of graphene has not yet been realized, it was synthesized graphene totally fluorinated. The reaction of graphene with xenon difluoride affords an insulator whose mechanical properties are quite similar to graphene but with an improved solubility and stability.[96]

The low reactivity of graphene requires the use of highly reactive species such as radicals. The reaction with peroxides was described observing a remarkable increase in the D mode of the Raman spectrum due to the introduction of sp^3 atoms.[97] One of the most striking covalent strategies is that established by Tour and co-workers. Originally, this methodology was investigated for the covalent functionalization of carbon nanotubes but later was also extended to pristine graphene chemistry.[98] This reaction consists in an aryl radical addition onto graphene surface via the *in situ* generation of diazonium salts. In general, in this approach the diazonium salt is formed through the reaction of an aniline molecule and isopentyl nitrite. The injection of an electron from graphene to the aryldiazonium salt, resulted in N_2 release and the formation of a reactive aryl radical (Figure 1.11).[99] The introduction of sp^3 atoms results in a band gap opening affording a semiconductor material with different conductor and insulator domains into the structure.

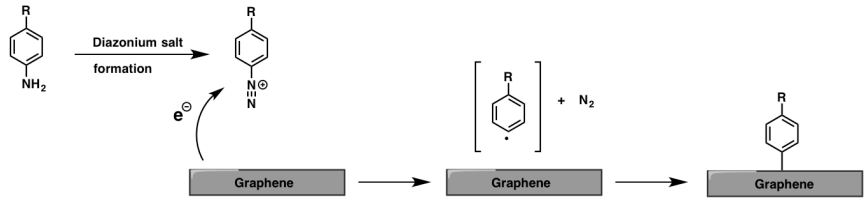

Figure 1.11. Tour addition reaction mechanism on graphene surface.

[95] A. Savchenko, *Science* **2009**, *323*, 589.
[96] R. R. Nair, R. Wencai, J. Rashid, R. Ibtsam, V. G. Kravets, B. Liam, B. Peter, S. Fredrik, A. S. Mayorov, Y. Shengjun, M. I. Katsnelson, Cheng Hui-Ming, S. Wlodek, L. G. Bulusheva, A. V. Okotrub, I. V. Grigorieva, A. N. Grigorenko, K. S. Novoselov, A. K. Geim, *Small* **2010**, *6*, 2877.
[97] H. Liu, S. Ryu, Z. Chen, M. L. Steigerwald, C. Nuckolls, L. E. Brus, *J. Am. Chem. Soc*. **2009**, *131*, 17099.
[98] E. Bekyarova, M. E. Itkis, P. Ramesh, C. Berger, M. Sprinkle, W. A. de Heer, R. C. Haddon, *J. Am. Chem. Soc*. **2009**, *131*, 1336.
[99] A. Criado, M. Melchionna, S. Marchesan, M. Prato, *Angew. Chem. Int. Ed.* **2015**, *54*, 10734.

An interesting modification of this methodology was reported by Hirsch et. al., where before the radical addition to graphene, layers were negatively charged providing an activated intermediate.[100] In this process graphite forms an intercalated material with alkaline metals such as sodium or potassium which at the same time act as electron-donors (Figure 1.12). Moreover, the ionic intermediate can be utilized not only to the reaction with aryl diazonium salts, but also with other electrophiles or halogenated compounds such as *n*-hexyl iodide.[101] In addition, if the attached phenyl rings bear other functional groups, such as azides of iodines, the material can be further functionalized. For instance, electron-donor π-extended tetrathiafulvalene (exTTF) units have been incorporated to the graphene layer through [3+2] cycloaddition after the initial aryl addition.[102]

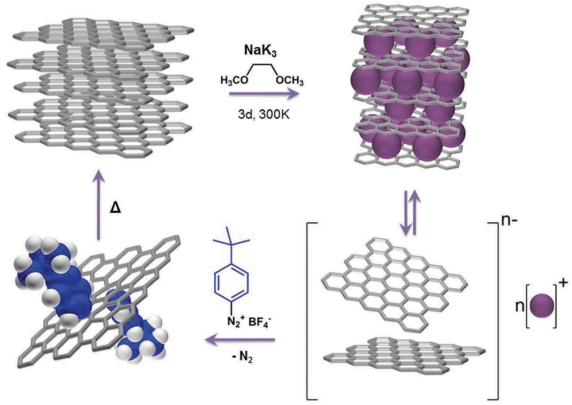

Figure 1.12. Reductive covalent functionalization of graphene with phenyl diazonium tetrafluoroborate.

Friedel–Crafts acylation reactions were reported as a previous step for an improved chemical exfoliation of graphite, reacting at the edges of graphite and facilitating through this way the wettability with the exfoliating solvent.[103]

---

[100] J. M. Englert, C. Dotzer, G. Yang, M. Schmid, C. Papp, J. M. Gottfried, H. Steinrück, E. Spiecker, F. Hauke, A. Hirsch, *Nat. Chem.* **2011**, *3*, 279.

[101] J. M. Englert, K. C. Knirsch, C. Dotzer, B. Butz, F. Hauke, E. Spiecker, A. Hirsch, *Chem. Commun*. **2012**, *48*, 5025.

[102] J. Mateos-Gil, L. Rodriguez-Perez, M. Moreno Oliva, G. Katsukis, C. Romero-Nieto, M. A. Herranz, D. M. Guldi, N. Martín, *Nanoscale* **2015**, *7*, 1193.

[103] E. Choi, I. Jeon, S. Bae, H. Lee, H. S. Shin, L. Dai, J. Baek, *Chem. Commun*. **2010**, *46*, 6320.

Besides the different methodologies mentioned above, pristine graphene has been modified considering other general reactions, such as cycloaddition processes. The 1,3-dipolar cycloaddition reaction of azomethyne ylides, the so-called Prato reaction, which has been deeply investigated for fullerenes and carbon nanotubes, was also extended to pristine graphene. Prato and co-workers reported the chemical functionalization of exfoliated graphene with a protected α-amino acid and paraformaldehyde followed by a deprotection step in acid media. Moreover, the resulting free amino group, in a second step, was the anchoring point for the further incorporation of gold nanorods.[104] [2+2] cycloadditions have been also tested over graphene by the addition of aryne moieties. Taking advantage from this cycloaddition, a C_{60} molecule was introduced onto the graphene lattice giving rise to a nanomaterial composed by two different carbon nanoforms.[105]

Additionally, the zero band gap presented in graphene inspired Haddon and co-workers in the use of this material in [4+2] Diels-Alder reactions, acting either as diene or dienophile.[106] Nitrene additions have also been performed onto the graphene lattice in order to modulate the material solubility.[107] The reaction mechanism involves a [2+1] cycloaddition to the C–C double bonds of graphene forming an aziridino-ring linkage by thermal decomposition at high temperatures. Finally, it is necessary to mention graphene's modification through another [2+1] process, the Bingel-Hirsch cyclopropanation reaction. This reaction has been tested on graphene by using bromomalonate derivatives assisted by microwave irradiation.[108]

[104] M. Quintana, K. Spyrou, M. Grzelczak, W. R. Browne, P. Rudolf, M. Prato, *ACS Nano* **2010**, *4*, 3527.

[105] D. García, L. Rodríguez-Pérez, M. A. Herranz, D. Peña, E. Guitián, S. Bailey, Q. Al-Galiby, M. Noori, C. J. Lambert, D. Pérez, N. Martín, *Chem. Commun*. **2016**, *52*, 6677.

[106] a) S. Sarkar, E. Bekyarova, S. Niyogi, R. C. Haddon, *J. Am. Chem. Soc*. **2011,** *133*, 3324. b) S. Sarkar, E. Bekyarova, R. C. Haddon, *Acc. Chem. Res*. **2012**, *45*, 673.

[107] T. A. Strom, E. P. Dillon, C. E. Hamilton, A. R. Barron, *Chem.Commun*. **2010**, *46*, 4097.

[108] S. P. Economopoulos, G. Rotas, Y. Miyata, H. Shinohara, N. Tagmatarchis, *ACS Nano* **2010**, *4*, 7499.

1.1.5.2. Pristine graphene non-covalent functionalization

It is a well-known fact that the formation of stable supramolecular complexes based on graphene requires the presence of species able to establish strong interactions with the graphene layers. Thereby, the introduction of these agents disrupts the huge tendency of graphene sheets to stack by π-π interactions. This approach also allows modulating the solubility of graphene layers in different solvents. Figure 1.13 shows the main strategies employed for the non-covalent functionalization of graphene, which will be summarized in the following paragraphs.

As it was discussed above, the stabilization of graphene layers in solution requires molecules whose surface energy matches that of graphene. Some of the solvents most employed in graphene exfoliation are DMF, NMP, *o*-DCB or 1-chloronaphtalene.[109] The high boiling points that present some of them as well as the chemical incompatibility with the functionalities present in the surface could be a limitation for further applications. In order to overcome this problem, water soluble graphene has been obtained with surfactants such as SDBS or sodium cholate.[61, 62] Ionic liquids have been tested in a similar approach, allowing the dispersion of graphene in a variety of organic solvents.[60]

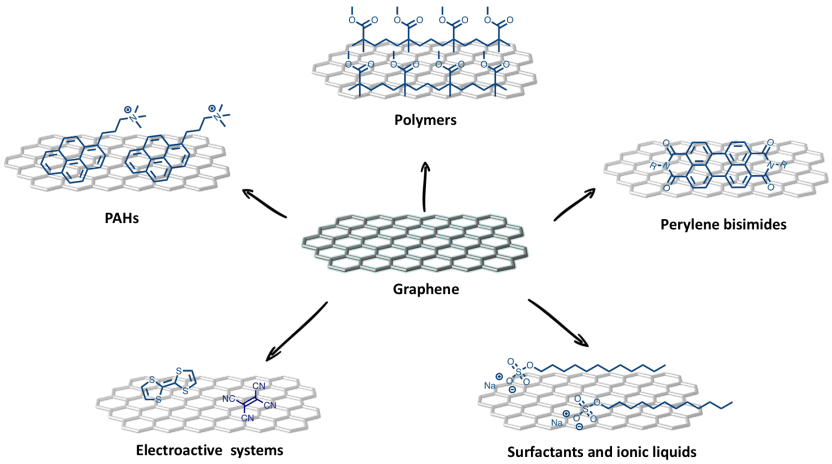

Figure 1.13. Schematic representation of different strategies for the non-covalent functionalization of graphene.

[109] A. Ciesielski, P. Samori, *Chem. Soc. Rev*. **2014**, *43*, 381

In section 1.1.2 it was discussed the adsorption of polymers onto graphene and the formation of stable dispersions in both, organic solvents and aqueous media. However, the use of polymers not only facilitates the obtention of exfoliated graphene, it also results in an amazing improvement of the composite mechanical properties. For example, a nanocomposite containing poly(methyl methacrylate) (PMMA)/graphene (1% graphene) increases in a 80% the elastic modulus and about a 20% the tensile strength reported for PMMA.[110]

The supramolecular interactions between graphene layers and other molecules could be enhanced by additional electronic interactions. This type of interactions are an interesting tool for modulating the band gap of graphene and, as a consequence, its electronic properties for further applications. One of the first examples reported involved the supramolecular interaction of graphene with tetrathiafulvalene (TTF) units (donor) or tetracyanoethylene (TCNE) units (acceptor).[111] In both cases, due to the electronic interactions, significant changes in the Raman G band as well as charge transfer bands in the visible region were observed.

Most of the supramolecular complexes based on graphene interact via π-π stacking.[112] For that reason, the vast majory of examples related with the non-covalent modification of graphene employ non-planar aromatic molecules and derivatives. In this direction, pyrene derivatives have shown strong affinities towards the graphene basal plane via π-π stacking. One out of many examples is the reported by Wood and co-workers, where a photo-switchable Zn^{2+} sensitive material was prepared by non-covalent functionalization of graphene with a pyrene-spiropyran derivative (Figure 1.14).[113] Spiropyran moieties are photochromic molecules that switches to their structural isomer (merocyanine) upon UV irradiation. In this particular case, the merocyanine is able to interact with the metal forming the chelate complex. This process was perfectly monitored by UV-Vis absorption spectroscopy.

[110] D. Barun, K. E. Prasad, U. Ramamurty, C. N. R. Rao, *Nanotechnology* **2009**, *20*, 125705.
[111] V. Rakesh, D. Barun, R. Chandra Sekhar, C. N. R. Rao, *J. Phys. Condens. Matter.* **2008**, *20*, 472204.
[112] E. M. Pérez, N. Martín, *Chem. Soc. Rev*. **2015**, *44*, 6425.
[113] A. Perry, S. J. Green, D. W. Horsell, S. M. Hornett, M. E. Wood, *Tetrahedron* **2015**, *71*, 6776.

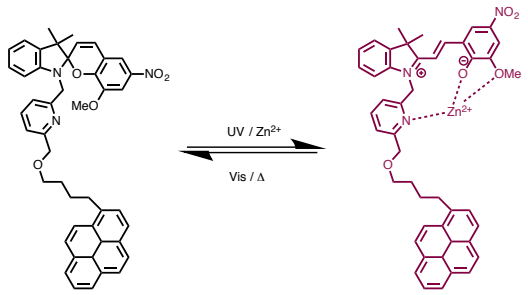

Figure 1.14. Spiropyran-merocyanine equilibrium.

Another polyaromatic systems with remarkable properties are perylene bisimides (PBI). This kind of systems has proved to carry out the exfoliation of graphene at the time that set electronic communication between both units even in water.[114]

In section 1.1.6. will be mentioned some more examples related with the supramolecular functionalization of graphene involving electron donor-acceptor interactions.

1.1.5.3. Graphene oxide functionalization

Graphene oxide has been modified using various chemical reactions through either covalent and non-covalent approaches. In most of the cases, the incorporation of different molecules with the functionalization renders new graphene oxide materials which could be interesting for a wide range of applications. According to the generally accepted Lerf–Klinowski model,[39] GO presents different reactive oxygen functionalities such as carboxylic acids at their edges and epoxy and hydroxyl groups on the basal planes. These groups are the anchoring point for the attachment of other molecules by diverse synthetic approaches (Figure 1.15). The problem of the covalent functionalization in GO is the difficulty in performing selective reactions because of the competition between the different functional groups. The chemical reactivity of GO has been widely investigated,[90] and here we will comment only some relevant examples.

[114] N. V. Kozhemyakina, J. M. Englert, Y. Guang, S. Erdmann, C. D. Schmidt, H. Frank, A. Hirsch, *Adv. Mater*. **2010**, *22*, 5483.

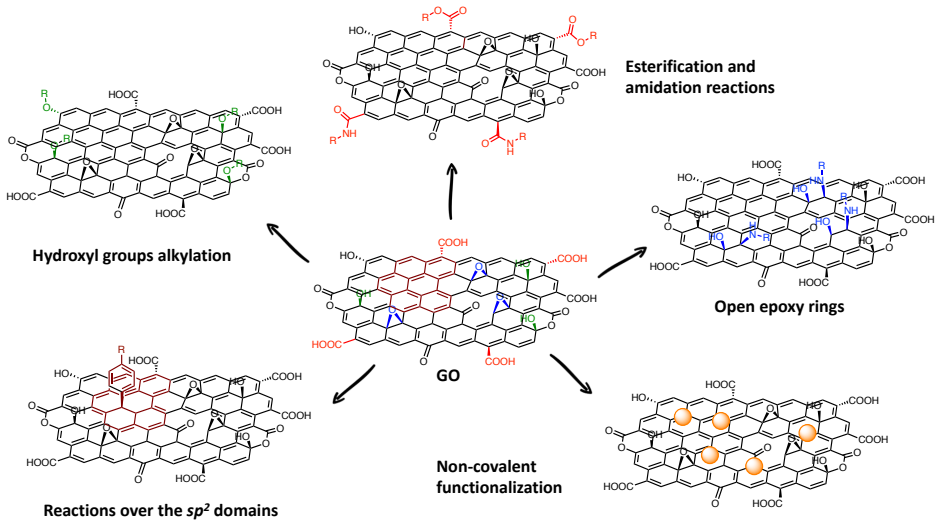

Figure 1.15. Schematic representation of different strategies for the functionalization of GO.

Functionalization at the carboxylic acid groups. In GO structure, carboxylic acids are mainly located at the edges of the sheets or at the edges of the σ-holes. There are a huge range of organic reactions which involve the employ of carboxylic acids in small molecules, and many of them can be also applied to GO. The first step in these coupling reactions is the activation of the carboxylic acids using agents as thionyl chloride ($SOCl_2$), 1-ethyl-3-(3-dimethylaminopropyl)- carbodiimide (EDC), *N,N'*-dicyclohexylcarbodiimide (DCC), or 2-(7-aza-1H-benzotriazole-1-yl)-1,1,3,3-tetramethyluronium hexafluorophosphate (HATU). Once activated, the next step includes the addition of nucleophiles, such as amines or hydroxy groups, yielding the formation of amides or esters, respectively.

One example of this methodology is the work described by J. G. Tian and co-workers,[115] where porphyrin and fullerene molecules were introduced in GO surface via amidation. The newly formed hybrids shown to be useful in nonlinear optics. Other functionalities have also been grafted to GO in order to improve its solubility in organic solvents.[116] In this case the introduction of regioregular poly(3-hexylthiophene) (P3HT) via esterification made GO

[115] Z. Liu, Y. Xu, X. Zhang, X. Zhang, Y. Chen, J. Tian, *J. Phys. Chem. B*. **2009**, *113*, 9681.
[116] D. Yu, Y. Yang, M. Durstock, J. Baek, L. Dai, *ACS Nano*. **2010**, *4*, 5633.

soluble in common organic solvents, facilitating the structure/property characterization and the device fabrication for photovoltaics applications. Sometimes in the course of this reactions (amidation and esterification) could occur simultaneously the opening of epoxy rings,[117] which is commented below.

Functionalization at the epoxy and hydroxyl groups. Both epoxy and hydroxyl groups are the main oxygenated species present in GO basal plane. The epoxy groups can be easily modified through ring-opening reactions under various conditions. The most common method consists in the nucleophilic attack to the α-carbon by an amine.

This methodology was applied in order to obtain highly stacked graphene papers.[118] For that task, GO was reacted with ethylenediamine resulting in the interconnection of the different GO sheets via epoxy ring opening reaction. It was also observed the formation of amides at the edges, which reflects the difficulty in controlling selectivity in the reaction. The obtained stacked graphene showed a smaller interlayer distance and an higher electric conductivity than that of unmodified graphene oxide papers.

On the other hand, the functionalization of hydroxyl groups is less used. These species could be modified by the reaction with previously activated carboxylic acids through esterification reaction, or by the reaction with halogenated derivatives resulting in o-alkylation reactions. This latter methodology was used for the incorporation of an atom transfer radical polymerization (ATRP) initiator in the GO lattice.[119] Afterwards, this fragment started the *in situ* polymerization of poly-(2-(dimethylamino)ethyl methacrylate) (PDMAEMA) chains on the surface of GO sheets.

Non-covalent functionalization of GO. Non-covalent interactions for the adsorption of different molecules on GO surface have also been investigated. The involved forces consider oxygenated groups able to interact by hydrogen bonding or carbon sp^2 networks that are not oxidized and are available for π-π stacking, cation-π or van der Waals interactions. According to this

[117] I. A. Vacchi, C. Spinato, J. Raya, A. Bianco, C. Menard-Moyon, *Nanoscale* **2016**, *8*, 13714.
[118] J. U. Lee, W. Lee, J. W. Yi, S. S. Yoon, S. B. Lee, B. M. Jung, B. S. Kim, J. H. Byun, *J. Mater. Chem. A*. **2013**, *1*, 12893.
[119] Y. Yang, J. Wang, J. Zhang, J. Liu, X. Yang, H. Zhao, *Langmuir* **2009**, *25*, 11808.

methodology, a hybrid material based on GO and doxorubicin hydrochloride (DXR) was prepared via non-covalent interactions. Herein, the main interactions that linked both species were π–π stacking and the hydrophobic interactions between the quinone functionality of DXR and sp^2 domains of GO.[120] Besides, the authors suggested that strong hydrogen bonding may be present between hydroxyl and carboxylic acids groups of GO and the hydroxyl and amine groups in DXR.

Functionalization of reduced GO. In section 1.1.3 it was mentioned that GO can recover the graphitic network in the basal plane by chemical or thermal reduction. The chemical reactivity of reduced GO (rGO) is similar to that of graphene and the restored sp^2 lattice facilitates the formation of supramolecular complexes by π–π stacking interactions. For instance, Müllen *et al*. performed the formation of stable aqueous dispersions of rGO by the intercalation of perylene and pyrene derivatives by π–π stacking.[121] Concerning covalent modification, over rGO can be carried out the reactions already discussed for pristine graphene, still being the attachment of phenyldiazonium derivatives one of the most employed methods. This approach was used for the *in situ* development of composite polymers based on GO and styrene.[122] Carbene additions were also reported for the incorporation of other functional groups over rGO. Indeed, this strategy was useful for the covalent functionalization of the graphene layers with gold nanoparticles.[123] Moreover, other alternative for the covalent functionalization of rGO takes advantage of the remaining oxygenated defects located in the surface. Based on this consideration, rGO was reported to be covalently functionalized by an amine linker with a polymer that reacts with residual epoxy groups at the defect sites, to form stable dispersions in tetrahydrofuran.[124]

[120] X. Yang, X. Zhang, Z. Liu, Y. Ma, Y. Huang, Y. Chen, *J. Phys. Chem. C.* **2008**, *112*, 17554.
[121] S. Qi, P. Shuping, A. Vajiheh, L. Chen, F. Xinliang, Müllen Klaus, *Adv. Mater*. **2009**, *21*, 3191.
[122] M. Fang, K. Wang, H. Lu, Y. Yang, S. Nutt, *J. Mater. Chem*. **2010**, *20*, 1982.
[123] H. Ismaili, D. Geng, A. X. Sun, T. T. Kantzas, M. S. Workentin, *Langmuir* **2011**, *27*, 13261.
[124] M. Hsiao, S. Liao, M. Yen, P. Liu, N. Pu, C. Wang, C. M. Ma, *ACS Appl. Mater. Interfaces*. **2010**, *2*, 3092.

1.1.6. Donor-acceptor interactions in graphene-based hybrids

In the last few decades, an enormous effort has been directed towards the preparation of model compounds of natural photosynthetic systems with the ultimate goal of studying and understanding energy conversion processes.[5,125] Therefore, a wide range of covalent and non-covalent D-A systems have been designed, frequently using carbon nanostructures like fullerenes, carbon nanotubes and, more recently, graphene.[126] This section reviews several examples where the photophysical properties of donor–acceptor (D-A) systems based on graphene have been reported. In particularly, few-layer graphene, GO and rGO have been employed as electron acceptor species and, sometimes, as electron donor, although to a much lesser extent. Firstly are described remarkable examples of D–A systems based on mono-layer and few-layer graphene, to then move towards a few examples of hybrids integrating chemically modified graphene such as GO and rGO. In each subtopic, both covalent and non-covalent methodologies are considered.

Pyrene derivatives are known to feature strong affinities towards the graphene basal plane via π-π stacking. As such, graphene electron donor-acceptor hybrids have been created using this anchoring motif. Guldi, Torres and co-workers described the formation of a supramolecular complex composed by phthalocyanine-pyrene conjugates and exfoliated graphene through π–π stacking interactions (Figure 1.16).[127] The presence of the pyrene units in the conjugates is decisive in terms of non-covalently immobilizing the phthalocyanines onto the basal plane of graphene. In this particular case, graphene acts as electron donor and the phthalocyanine is the acceptor counterpart. By means of transient absorption spectroscopy, it was corroborated that upon irradiation at 387 nm, an ultrafast charge transfer process takes place from the graphene to the phthalocyanine units. The process is followed by a slow charge recombination.

---

[125] N. Armalori, V. Bolzoni, *Chem. Eur. J.* **2016**, *22*, 32.

[126] a) N. Martín, *Adv. Energy Mater*. **2017**, *7*, 1601102. b) J. L. Delgado, S. Filippone, F. Giacalone, M. A. Herranz, B. Illescas, E. M. Pérez, N. Martín, *Top. Curr. Chem*. **2014**, *350*, 1. c) D. M. Guldi, N. Martín, *Carbon Nanotubes and Related Structures*, Wiley-VCH, Weinheim, **2010**.

[127] A. Roth, M. Ragoussi, L. Wibmer, G. Katsukis, G. d. l. Torre, T. Torres, D. M. Guldi, *Chem. Sci*. **2014**, *5*, 3432.

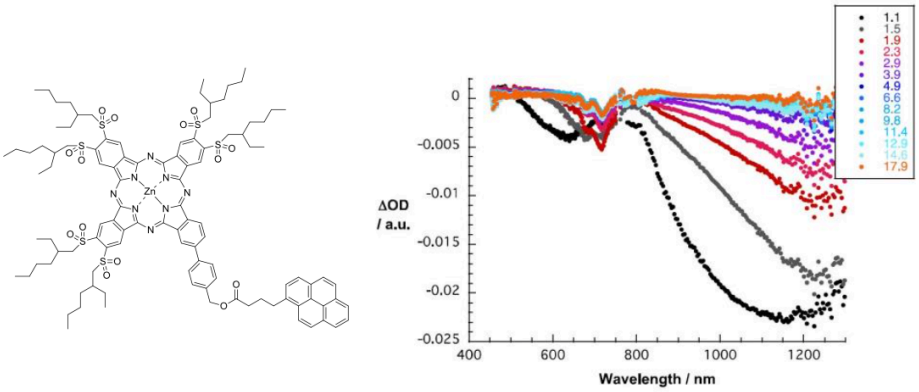

Figure 1.16. Phthalocyanine-pyrene dyad used in the non-covalent functionalization of graphene (left). Differential absorption spectra of phthalocyanine-pyrene/graphene nanohybrids (right). Time delays between 1.1 and 17.9 ps at room temperature.

In a recent report from the same groups, phthalocyanines equipped with Newkome-type dendritic branches and terminal carboxylate functional groups, were used to successfully exfoliate graphite in water.[128] The signature of the one-electron oxidation of ZnP (730 nm) in differencial absorption experiments, corroborates the electron transfer in the excited state. Exfoliated graphene has also been covalently decorated with phthalocyanines. The functionalization was achieved in two synthetic steps (Figure 1.17).[129] The first step was a 1,3-dipolar cycloaddition onto exfoliated graphite, which afforded a carboxyphenyl modified graphene. This reaction was followed by an esterification reaction between the carboxyphenyl modified graphene and an hydroxyl-terminated phthalocyanine yielding graphene-phthalocyanine nanoconjugates. Herein, interactions in the ground state were evidenced by Raman and absorption spectroscopy. Furthermore, the decrease of the quantum yield as well as lifetime of phthalocyanine species were indicative of excited state interactions in the hybrid. The photophysical characterization confirmed an ultrafast charge separation from the photoexcited phthalocyanine to graphene followed by a slower charge recombination.

[128] A. Hirsch, C. Methfessel, M. Volland, K. Brunner, L. Wibmer, U. Hahn, T. Torres, D. Guldi, l. T. de, *Chem. Eur. J.* **2018**, *2*4, 18696.
[129] M. Ragoussi, J. Malig, G. Katsukis, B. Butz, E. Spiecker, G. de la Torre, T. Torres, D. M. Guldi, *Angew. Chem. Int. Ed*. **2012**, *51*, 6421.

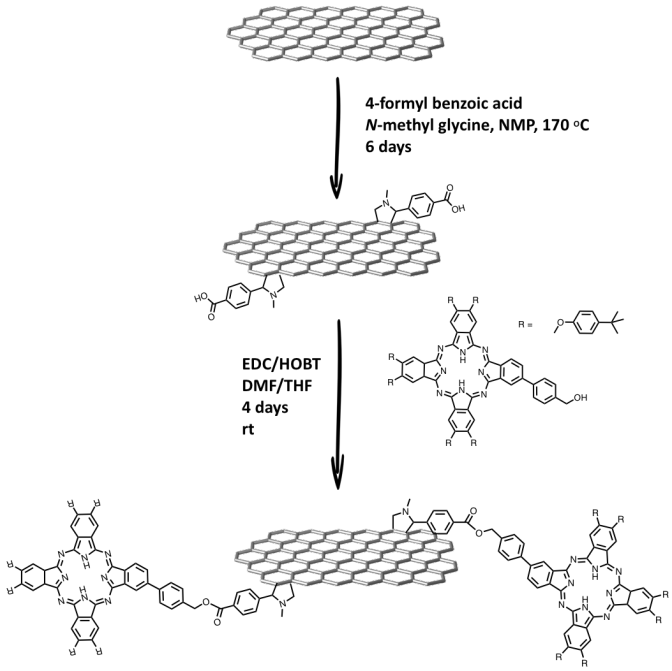

Figure 1.17. Synthetic route towards graphene– phthalocyanine nanoconjugates.

Regarding GO D-A hybrids, the photoinduced charge separation in ordered self-assemblies of perylenediimide-GO hybrid (PDI-GO) layers in water was investigated by Supur *et al.*[130] PDI is an interesting building block for the formation of GO hybrids because its strong absorption in the visible region and low reduction potential. These features make it a powerful light harvester and a good electron acceptor.

The interaction of PDI with GO surface was driven by π–π stacking interactions with the basal plane of GO and electrostatic interactions with the functional groups of GO. The existence of a photoinduced electron transfer in the PDI-GO supramolecular assemblies was investigated by transient absorption spectroscopy. The obtained results pointed to an electron migration mechanism among the π-stacks of PDI during a possible photoinduced electron transfer process with the GO sheets (Figure 1.18).

[130] M. Supur, K. Ohkubo, S. Fukuzumi, *Chem.Commun*. **2014**, *50*, 13359.

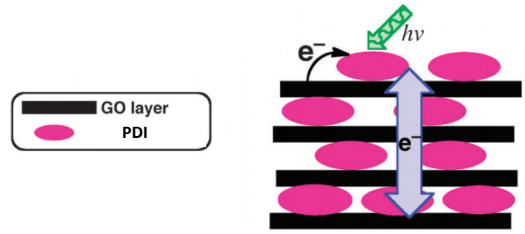

Figure 1.18. Proposed photoinduced charge separation and interlayer charge migration in ordered self-assemblies of PDI–GO hybrid layers.

GO was also employed as a platform to anchor donor and acceptor entities. In this context, GO was covalently modified with C_{60} electron-acceptor units and units of the photo-sensitizer ZnP as electron-donors, resulting in the new material ZnP-GO-C_{60} (Figure 1.19).[131] First insights into excited states revealed a photoinduced charge separation leading to a $ZnP^{\cdot+}$-GO- $C_{60}^{\cdot-}$ charge separated state with a lifetime in the range of 0.04 μs. In a subsequent study, these D-A decorated hybrids were subjected to a photocatalytic electron pooling experiment. Electron accumulation in the form of a one-electron reduced product of methyl viologen (MV) was obtained in high yields in a system involving the ZnP-GO-C_{60} hybrid and a sacrificial electron-donor. The results were compared with control hybrids involving either ZnP-GO or C_{60}-GO hybrids were no charge accumulation was observed. Therefore, this result revealed that ZnP-GO-C_{60} is a suitable catalyst for solar fuel production.

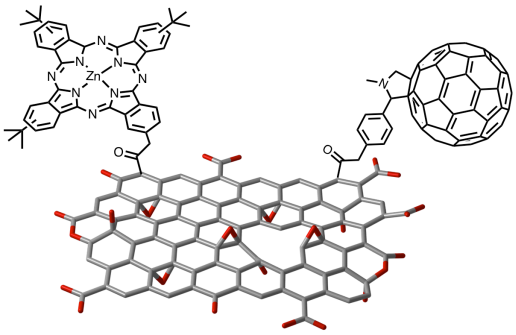

Figure 1.19. Structure of Zn(II)Pc-GO-C_{60} hybrid material.

[131] S. K. Das, C. B. KC, K. Ohkubo, Y. Yamada, S. Fukuzumi, F. D'Souza, *Chem.Commun.* **2013**, *49*, 2013.

Reduced GO (rGO) has also been widely explored as a scaffold for D-A systems. Kalita *et al.*[132] reported a rGO covalently decorated with ferrocene (Fc) instead of porphyrin-based sensitizers (Figure 1.20). Photoresponsivity of the prepared rGO –Fc composite was investigated by fabricating a metal/ rGO –Fc/metal device. The fabricated device showed enhanced current density under light illumination, suggesting a photo-induced charge transfer process in the developed rGO –Fc composite.

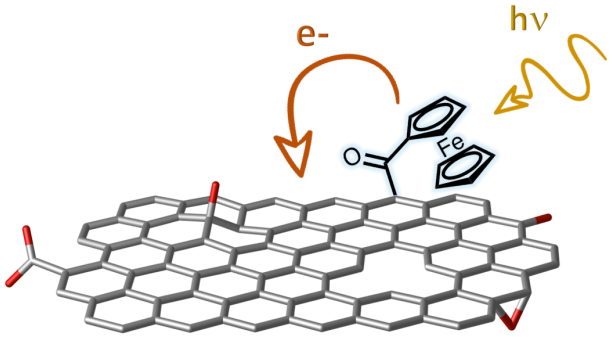

Figure 1.20. Schematic representation of the rGO–Fc hybrid and photo-induced charge transfer process.

Zhang and co-workers[133] used a layer-by-layer self-assembly method for producing rGO films with high photoelectronic activity. For this purpose 10,15,20-tetrakis(p-*N,N,N*-trimethyl anilinium)porphyrin tetraiodide (TAPPI) and tetrasulfonated CuPc were assembled. The main driving force for the assembly of the rGO /TAPPI/CuPc were the π–π and electrostatic interactions. The linear dependence of the absorption on the layer numbers of the films demonstrated the formation of the ordered films. In the composite film, an efficient photoinduced electron transfer was evidenced by fluorescence spectroscopy. The comparison with the references (rGO /TAPPI, GR/CuPc or TAPPI/CuPc films) showed that rGO /TAPPI/CuPc films present a better photoelectronic response.

[132] G. Kalita, S. Sharma, K. Wakita, M. Umeno, Y. Hayashi, M. Tanemura, *Phys. Chem. Chem. Phys*. **2013**, *15*, 1271.
[133] M. Zhang, B. Yuan, S. Kang, L. Qin, G. Li, X. Li, *RSC Adv*. **2015**, *5*, 42063.

1.1.7. Cyanine dyes

Cyanines (Cy) represent an interesting class of light harvesters to be combined with carbon nanostructures in electron-donor/-acceptor systems for artificial photosynthesis or photovoltaics.

Within this family, cationic dyes bear a positive charge completely delocalized between two electron-donor groups. These groups are linked by a hydrocarbon skeleton formed by an odd number of carbon atoms (Figure 1.21).[134] These compounds exhibit a strong light absorption capacity that can be modulated by the addition of double bonds to the hydrocarbon skeleton. When its skeleton length increases, a striking bathochromic shift in the absorption and emission spectra is observed. Moreover, this change is also accompanied by a decrease in photochemical and thermal stability, a factor that limits the range of application.

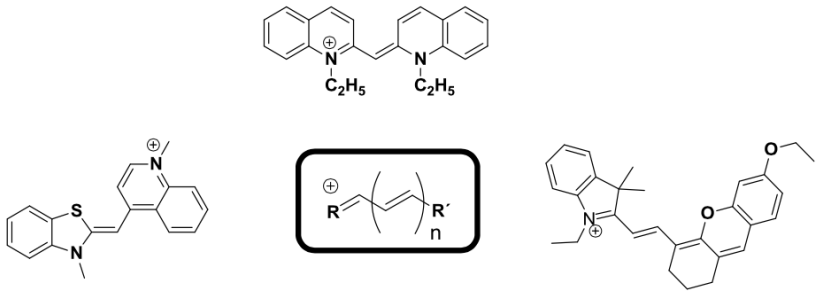

Figure 1.21. Representative examples of cyanine cationic dyes.

Otherwise from the strong capacity for light absorption, this type of compounds can be prepared on a large scale in a few synthetic steps. These compounds exhibit, in general, high solubility in most organic solvents, thermal stability and excellent non-linear optical properties. In particulat their optical properties make Cy really interesting for different applications such as

[134] A. Mishra, R. K. Behera, P. K. Behera, B. K. Mishra, G. B. Behera, *Chem. Rev.* **2000**, *100*, 1973.

materials science (storage and transport of energy)[135] or in biomedical applications (drug delivery or photodynamic therapy).[136]

The electron donating behavior of Cy has been useful for applications such as photothermal therapy. For instance, Chen and co-workers[137] reported the preparation of graphene-based material with a cationic Cy attached to its surface, which showed to be helpful in the field of cancer therapy (Figure 1.22). In this proof-of-concept GO was selected as a typical model receptor of fluorescence resonance energy transfer (FRET) and the Cy was the donor of near-infrared fluorescence (NIRF). The photothermal nanoconjugate with broad NIR absorbance and the effective receptor of FRET can smartly convert emitted NIRF energy from the donor Cy into an additional photothermal effect for improving photothermal therapy.

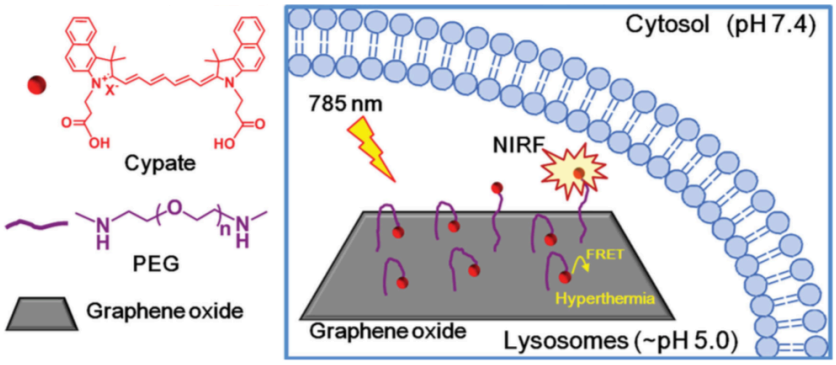

Figure 1.22. Schematic illustration of smart GO nanoconjugate exhibiting enhanced transfer (FRET) from Cypate to GO, a highly photothermal performance mediated by FRET.

Anionic cyanine dyes can be also easily synthesized. Figure 1.23 shows an anionic heptamethine cyanine[138] formed by two units of tricyanofurane (TCF) linked by a π-conjugated skeleton where a negative charge is delocalized.

[135] C. Wang, E. A. Weiss, *J. Am. Chem. Soc*. **2016**, *138*, 9557.
[136] W. Sun, S. Guo, C. Hu, J. Fan, X. Peng, *Chem. Rev*. **2016**, *116*, 7768.
[137] M. Guo, J. Huang, Y. Deng, H. Shen, Y. Ma, M. Zhang, A. Zhu, Y. Li, H. Hui, Y. Wang, X. Yang, Z. Zhang, H. Chen, *Adv. Funct. Mater*. **2015**, *25*, 59.
[138] P. Bouit, E. Di Piazza, S. Rigaut, B. Le Guennic, C. Aronica, L. Toupet, C. Andraud, O. Maury, *Org. Lett*. **2008**, *10*, 4159.

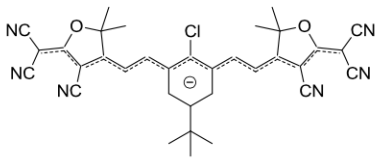

Figure 1.23. Anionic heptamethine cyanine.

The incorporation of TCF units results in anionic dyes with high solubility in organic solvents keeping their thermal stability. The TCF electron-withdrawing groups are responsible of the strong red-shift of this Cy in the visible spectrum in comparison with the cationic analogous.[139] Regarding the redox properties of anionic Cy, they behave as electron oxidants and can accept one electron in redox processes forming stable radical species.

One interesting example related with the electron-donating behavior of anionic Cy is that these molecules were involved in the formation of molecular electron donor-acceptor conjugates with fullerene molecules.[140] In this work, time resolved transient absorption measurements revealed that upon photoexcitation of the anionic heptamethine cyanine, a charge transfer process occurred, where the cyanine act as the electron-donor and the fullerene (C_{60} or C_{70}) as the electron-acceptor moiety (Figure 1.24).

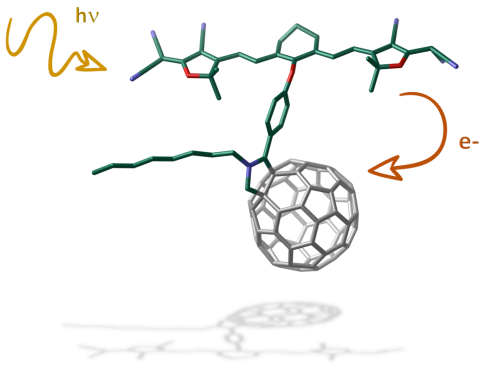

Figure 1.24. Schematic representation of photoinduced electron transfer in a CyC_{60} dyad.

[139] P. Bouit, D. Rauh, S. Neugebauer, J. L. Delgado, E. D. Piazza, S. Rigaut, O. Maury, C. Andraud, V. Dyakonov, N. Martín, *Org. Lett*. **2009**, *11*, 4806.
[140] C. Villegas, E. Krokos, P. Bouit, J. L. Delgado, D. M. Guldi, N. Martín, *Energy Environ. Sci*. **2011**, *4*, 679.

In a recent report, anionic heptamethine cyanine dyes and single-walled carbon nanotubes (SWCNT) or few-layer graphene, have been covalently linked by using 1,3-dipolar cycloaddition reactions. The nanoconjugates obtained synchronize the properties of both materials, although no photophysical investigations were carried out.[141]

Due to the strong absorption in the NIR region of Cy, in a region where many of the polymers used in photovoltaic devices do not absorb,[142] the use of these molecules as donor compounds presents an alternative strategy to improve the efficiencies in light conversion. With the aim to broader the absorption range of Cy, a salt formed by two Cy (anionic and cationic) was synthesized and, actually showed an absorption in the NIR which was the sum of the different cyanine absorptions (Figure 1.25).

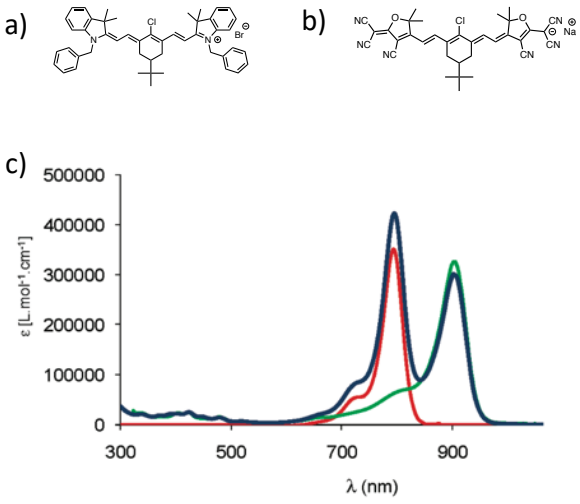

Figure 1.25. a) Cationic heptamethine cyanine structure. b) Anionic heptamethine cyanine structure. c) Uv-vis-NIR spectra of the compounds shown in figure a (red), figure b (green) and the salt composed for both cyanines (blue) in dichoromethane (DCM).

[141] L. Rodríguez-Pérez, C. Villegas, M. Á Herranz, J. L. Delgado, N. Martín, *ACS Omega* **2017,** *2*, 9164.

[142] J. L. Delgado, P. Bouit, S. Filippone, M. Á Herranz, N. Martín, *Chem. Commun.* **2010**, *46*, 4853.

In a related work, Jen and co-workers[143] demonstrated that anionic and cationic Cy can be organized into complementary cyanine salts, offering potential building blocks to modulate their intra/ intermolecular interactions in the solid state. Herein, they explain how the structures of the salts can be tuned to achieve highly ordered J-type supramolecular aggregate structures of heptamethine dyes in crystalline solids. Such rational design can be interesting for further applications in biomedicine, optics, and further technologies.

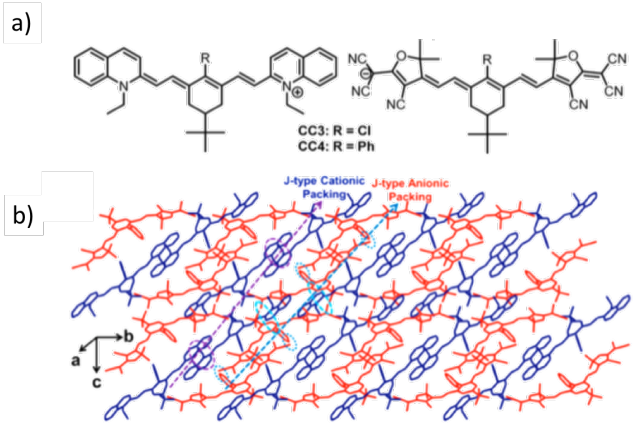

Figure 1.26. a) Molecular structure of cyanines and complementary cyanine salts. b) Crystal structure of the cyanine salt shown in a).

[143] Z. Li, S. Mukhopadhyay, S. Jang, J. Brédas, A. K. Jen, J. *Am. Chem. Soc*. **2015**, *137*, 11920.

1.2. OBJECTIVES

1.2. OBJECTIVES

Considering the aforementioned precedents, the general aim of this chapter is the synthesis and characterization of graphene-based functional materials as model systems for optoelectronics and energy conversion. Different moieties were introduced on these materials using both, covalent and supramolecular approaches, with the purpose of modulating graphene's electronic properties and to establish structure-property relationships in the obtained hybrids. The following specific goals are considered in Chapter 1:

i) Pristine graphene and graphene oxide production

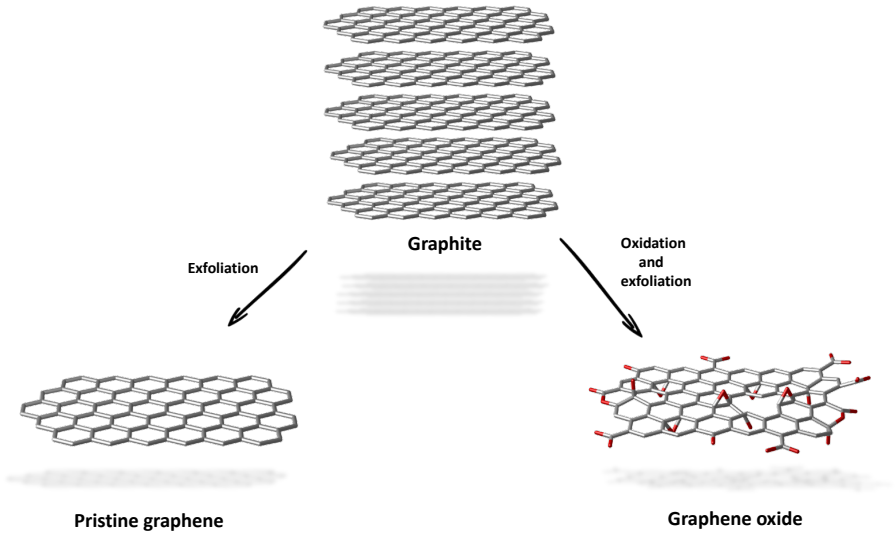

- Production of graphene by mechanical exfoliation of graphite in liquid phase. This production involves the use of different solvents such as NMP and *o*-DCB.
- Characterization and quality evaluation of the exfoliated sheets by different techniques (TGA, TEM, FTIR and Raman).
- Production of graphene oxide considering the oxidation and subsequently exfoliation of graphite.

- Fully characterization of graphene oxide and comparison with the exfoliated pristine graphene produced by mechanical exfoliation in liquid phase.

ii) Chemical functionalization of graphene-based materials

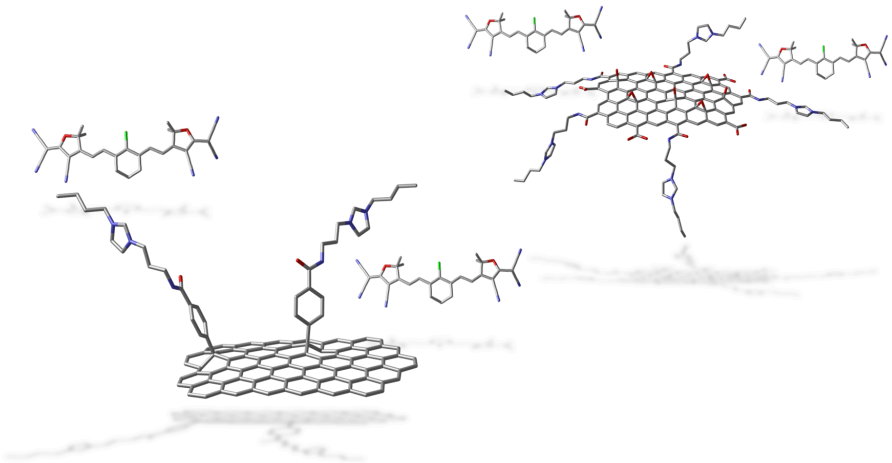

- Chemical modification of both graphene and graphene oxide surfaces by covalent and non-covalent approaches. The final goal of these modifications is the incorporation of electroactive cyanine dyes in order to form donor-acceptor materials based on graphene.
- The oxygenated groups of graphene oxide will be the anchoring points for the introduction of new species through covalent chemistry. In this manner, imidazolium salts will be connected to graphene by amidation reactions. A last step implies the introduction of anionic heptamethine cyanines as the counter ion of the imidazolium salts through ionic exchange.
- In the case of pristine graphene, the covalent introduction of imidazolium salts will be performed by an aryl addition over the sp^2 lattice of graphene (Tour reaction). Finally, the introduction of cyanine dyes will be done also by an anion exchange.
- The synthesis and characterization of these hybrids (based on graphene and graphene oxide) will be compared and discussed in terms of chemical reactivity.
- Additionally, new supramolecular complexes will be formed using both SWCNT and graphene as scaffolds. Herein, an heptamethine

anionic cyanine with a pyrene fragment in their structure will be incorporated to the surfaces of graphene or SWCNT by π-π interactions.

- The formation of these hybrids will be monitored and investigated by complementary spectroscopic, electrochemical and microscopic techniques.

iii) Photophysical study of the synthesized nanoconjugates

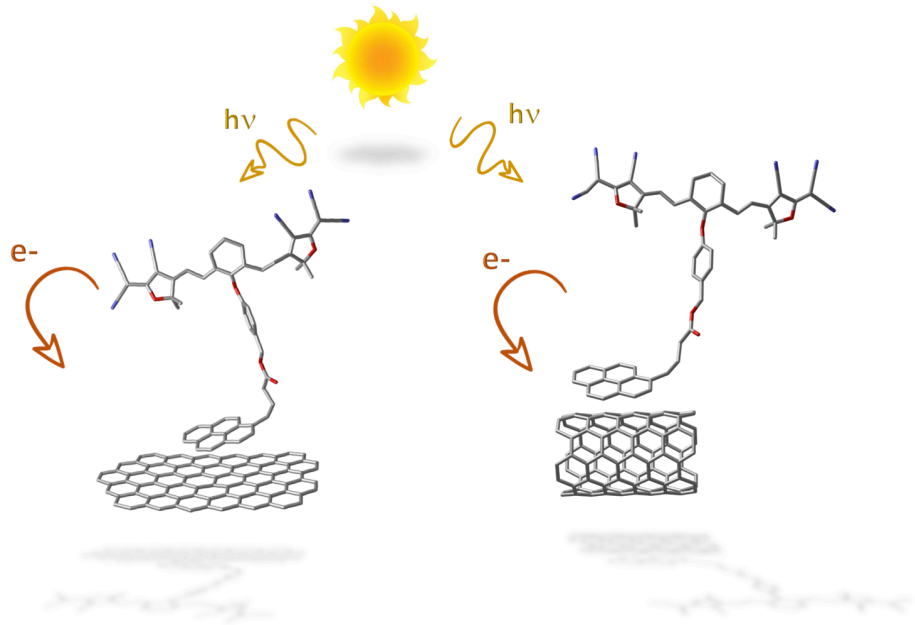

- Study of the electronic interactions between the pyrene-cyanine units and the carbon nanoforms by a series of steady-state and time resolved experiments.

1.3. RESULTS AND DISCUSSION

1.3. RESULTS AND DISCUSSION

1.3.1. Production of few-layer graphene and graphene oxide

The synthesis of pristine graphene (GR) and graphene oxide (GO) was carried out using the different methodologies previously reported in the bibliography. The first stage of this work was the production of pristine graphene. In particular, the solution synthesis of few-layer graphene which refers to aggregates with less than ten layers.[144] In order to produce a good-quality GR, we took advantage from the methodology developed by Coleman and co-workers, which consists in a mechanical exfoliation of graphite in liquid phase.[50, 52]

A key issue in the dispersion and exfoliation of graphite in organic solvents is to select solvents with the nearest surface energy to that of graphite, making possible the exfoliation process due to the solvent-flake interactions, which balance the energy required in the exfoliation mechanism. In the present work, we selected NMP and *o*-DCB as organic solvents due to the good results shown in the exfoliation process in comparison with other solvents such as DMF or chlorobenzene.

The first step of this method was the graphite sonication in the selected organic solvent followed by centrifugation, where large aggregates are removed giving rise to a stable dispersion of GR. Specifically, the optimal conditions included a sonication step of 2 h. and subsequently centrifugation at 500 r.p.m. for 45 min. (Scheme 1.1). Eventually, the supernatant was isolated, resulting in a grey colour dispersion that was stored for further analysis.[145]

[144] S. Eigler, A. Hirsch, *Angew. Chem. Int. Ed*. **2014**, *53*, 7720.
[145] M. Garrido, J. Calbo, L. Rodríguez-Pérez, J. Aragó, E. Ortí, M. Á Herranz, N. Martín, *Chem. Commun*. **2017**, *53*, 12402.

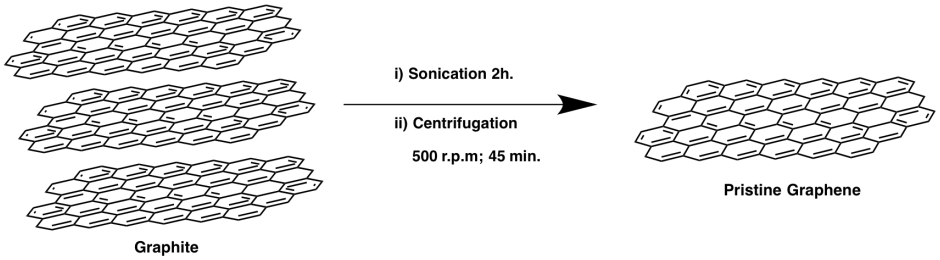

Scheme 1.1. Schematic representation of the exfoliation of graphite in liquid phase.

First insights into the exfoliation process came from TEM analysis. Figure 1.27 reveals the presence of homogeneous aggregates of GR composed by few layers after the exfoliation, whereas graphite exhibits the characteristic morphology for a great number of stacked sheets.

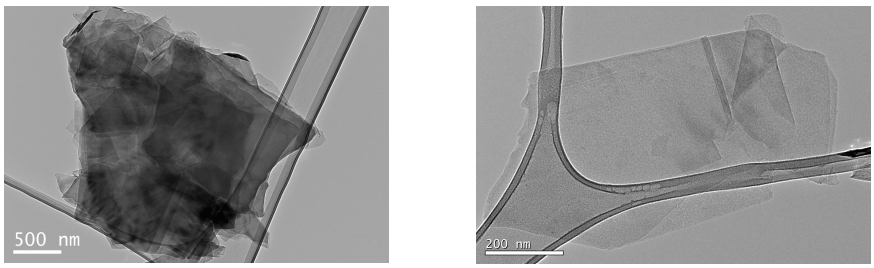

Figure 1.27. Representative TEM images of graphite (left) and GR (right) exfoliated in NMP.

Above all, it is worthy to point out that GR dispersions in NMP were stable for around one week, meanwhile those in *o*-DCB tended to re-aggregate after two days. Comparative TEM images (Figure 1.28) show the presence of GR nanosheets with lateral sizes of a few micrometers (100-500 nm) and, in some cases, with scrolled and slightly folded edges. Moreover, it is important to highlight that most of the aggregates were composed by only a few layers of graphene and larger objects were rarely observed. Besides this first observation, the dispersions of GR in NMP were highly homogeneous and stable with the presence of aggregates composed of 5 to 15 layers. On the contrary, in the samples of GR dispersed in *o*-DCB a more heterogeneous picture was obtained, where larger aggregates formed by more than twenty layers coexist with smaller aggregates of around 10 layers.

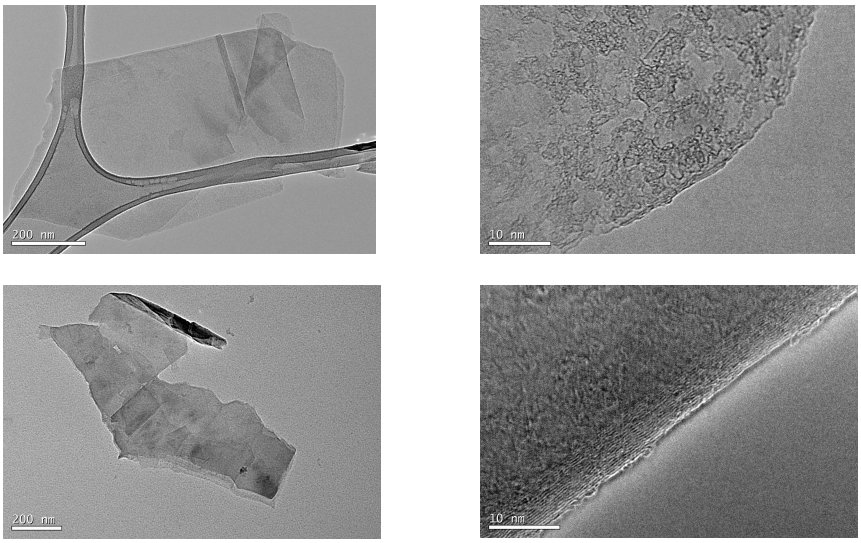

Figure 1.28. Representative TEM images of GR exfoliated in NMP (top) and *o*-DCB (bottom).

Additional information about the structural features of the exfoliated GR was obtained by Raman spectroscopy. As already mentioned, this technique is a powerful non-destructive tool to characterize graphene samples and to obtain straightforward information about the number of layers,[83] the edges,[146] the doping effects, or the functionalization efficiency of a given reaction[147] carried out in the graphene structure.

GR's Raman spectrum, is characterized by three main bands (Figure 1.29): the D band (~ 1350 cm^{-1}), related with defects which, in fact, requires a defect for its activation; the G band (~ 1580 cm^{-1}), due to the in-plane vibration of carbon atoms with sp^2 hybridization and; the 2D band (~ 2700 cm^{-1}), whose evolution with the number of layers allows to obtain information about the number of flakes in the material. In addition, G and 2D bands are very sensitive to doping in the case of non-covalent immobilization of molecules onto the basal plane of graphene. An overall broadening of the two modes is observed and p-doping or

[146] C. Casiraghi, A. Hartschuh, H. Qian, S. Piscanec, C. Georgi, A. Fasoli, K. S. Novoselov, D. M. Basko, A. C. Ferrari, *Nano Lett*. **2009**, *9*, 1433.

[147] J. M. Englert, P. Vecera, K. C. Knirsch, R. A. Schäfer, F. Hauke, A. Hirsch, *ACS Nano* **2013**, *7*, 5472.

n-doping result in an upshift or a downshift of the G band, respectively.[148,149]

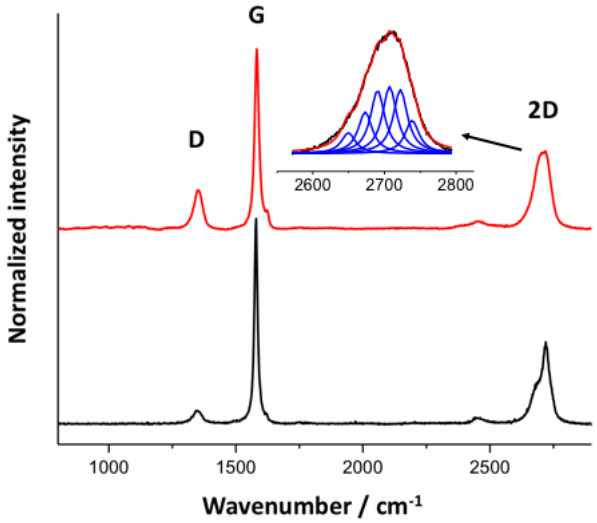

Figure 1.29. Raman spectra of graphite (black) and exfoliated graphene in NMP (red) recorded at 532 nm. The inset image shows the deconvolution of the 2D band.

From the deconvolution of the 2D band, it is possible to assess the number of layers present in the sample. Thus, for a single layer of graphene, the 2D band displays a single Lorentzian fit with a full-width half-maximum (FWHM) value of ~ 24 cm^{-1} and very high intensity, originated from a triple resonance process only presents in the perfect monolayer. In a bilayer, due to π- π^* interactions, more electron-phonon scattering processes are possible which leads to a broadening of the 2D band. In our case, the 2D band was fitted to six components and can be established that our GR is a three layer material.[150] For more than five layers, the Raman spectra of graphite and GR are indistinguishable, because of this reason, the fitting was not performed for samples exfoliated in *o*-DCB.

[148] X. Dong, D. Fu, W. Fang, Y. Shi, P. Chen, L. Li, *Small* **2009**, *5*, 1422.
[149] Q. Su, S. Pang, V. Alijani, C. Li, X. Feng, K. Müllen, *Adv. Mater.* **2009**, *21*, 3191.
[150] a) Z. Ni, Y. Wang, T. Yu, Z. Shen, *Nano Res.* **2008**, 1, 273. b) L. M. Malard, M. A. Pimenta, G. Dresselhaus, M. S. Dresselhaus, *Phys. Rep.* **2009**, *473*, 51.

Finally, it is important to highlight that in the TGA analyses of GR samples, is observed the weight loss corresponding to the intercalated solvent molecules between the layers. As a matter of fact, this feature was observed in both, GR samples exfoliated in NMP and in *o*-DCB (Figure 1.30).

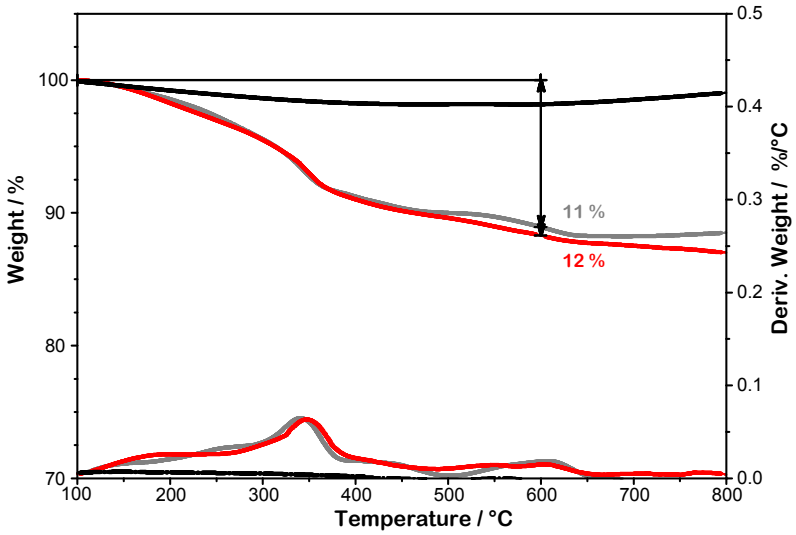

Figure 1.30. TGA and first derivative under inert conditions of: GR exfoliated in NMP (red) and in *o*-DCB (grey).

After the production of GR, the next step was the generation of the oxygenated form of graphene, namely, graphene oxide (GO). Normally, the production of GO uses graphite as starting material which is subjected to an oxidation process. The exact nature of the functional groups in GO strongly depends on the reaction conditions, such as preparation time and temperature as well as on the work-up procedure. Nevertheless, due to its polydisperse nature, it is rather difficult to define an exact structure for GO.

Here, two different strategies have been explored for the production of GO. One approach was based on the Kovtyukhova-Hummers method[151] and will be discussed in the second chapter of this Thesis. In this chapter, we focused on

[151] K. Mei, N. Rubio, P. M. Costa, H. Kafa, V. Abbate, F. Festy, S. S. Bansal, R. C. Hider, K. Al-Jamal, *Chem.Commun*. **2015**, *51*, 14981.

the Staundemaier method,[152] which provided exfoliated graphene sheets with a large amount of oxygenated species on the surface. The Staundemaier GO (GO_S) was produced through the treatment of graphite with $KClO_4$ in a mixture of H_2SO_4 and HNO_3 (Scheme 1.2).

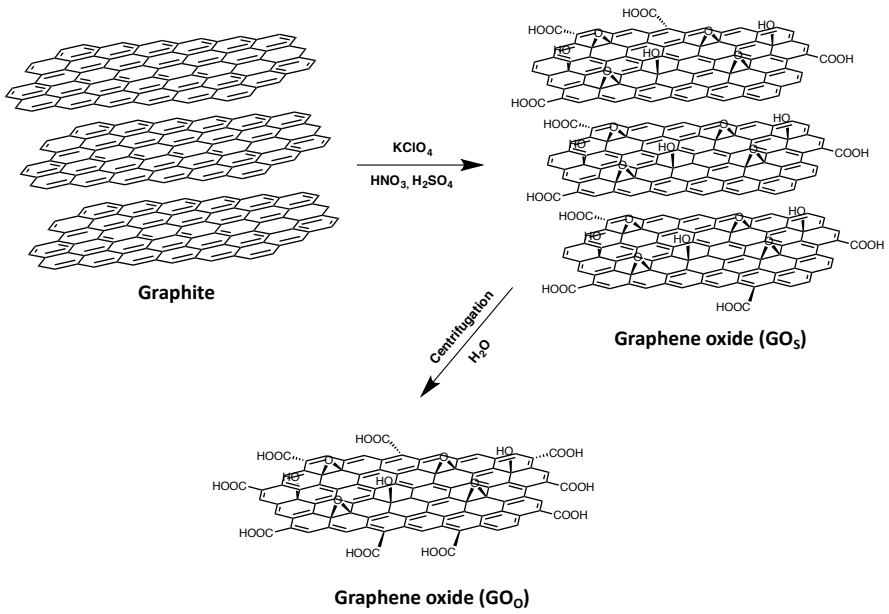

Scheme 1.2. Schematic representation of the preparation of GO_S and GO_O.

The intercalation of these molecules between graphite sheets resulted in the formation of different oxidized functional groups. Epoxide rings and hydroxy groups are incorporated to the basal plane of graphene, while the edges ended up functionalized with hydroxy and carboxylic acid groups, which are the driving force of the exfoliation process. After neutralization of the solution and filtration to obtain GO_S, the obtained solid was subjected to a centrifugation process in water in order to remove the layers with a lower percentage of oxygen. Therefore, highly functionalized sheets (GO_O) were presented in the supernatant, which is the material that will be used as scaffold for further functionalization.

[152] M. J. McAllister, J. Li, D. H. Adamson, H. C. Schniepp, A. A. Abdala, J. Liu, M. Herrera-Alonso, D. L. Milius, R. Car, R. K. Prud'homme, I. A. Aksay, *Chem. Mater*. **2007**, *19*, 4396.

From the presence of oxygenated functional groups, a hydrophilic character emerged in the material, which can be perfectly dispersed in aqueous media in contrast with the former hydrophobic graphite (Figure 1.31).

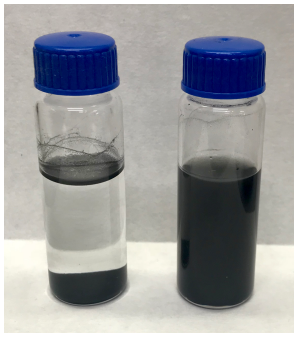

Figure 1.31. Dispersions of graphite (left) and GO_O (right) in water.

The success in GO_S synthesis and the isolation of the highly functionalized GO_O was confirmed by TEM and TGA. Figure 1.32 shows the presence of aggregates with few layers after the graphite oxidation (GOs) and, the obtained aggregates of GO_O that exhibit a more homogeneous surface and a decreasing number of sheets.

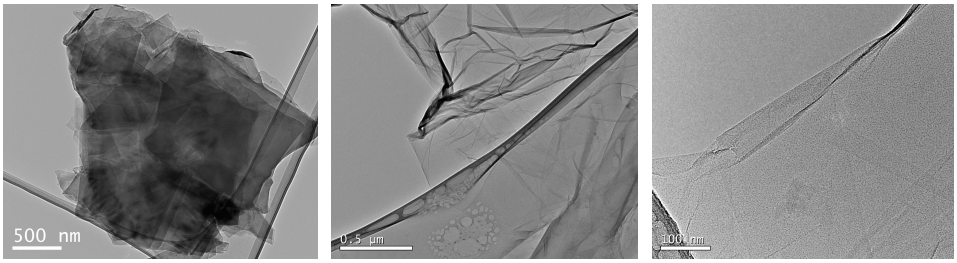

Figure 1.32. Representative TEM images of graphite (left), GOs (middle) and GO_O (right).

These results are in good agreement with those revealed by TGA (Figure 1.33). Herein, the thermogram of graphite, as expected, did not show any significant weight loss presenting the characteristic thermal stability observed for carbon-based materials with a small degree of defects. However, in the case of GOs a marked weight loss, of 13 % at around 600 ºC, was observed as a result of the decomposition of the oxygen-containing groups attached to the GOs surface. According to the literature,[121] the byproducts of this decomposition are CO_2 and

H_2O. In the GO_O thermogram, the above-mentioned loss of mass increased to a 16 % as a consequence of the sedimentation of less-functionalized sheets.

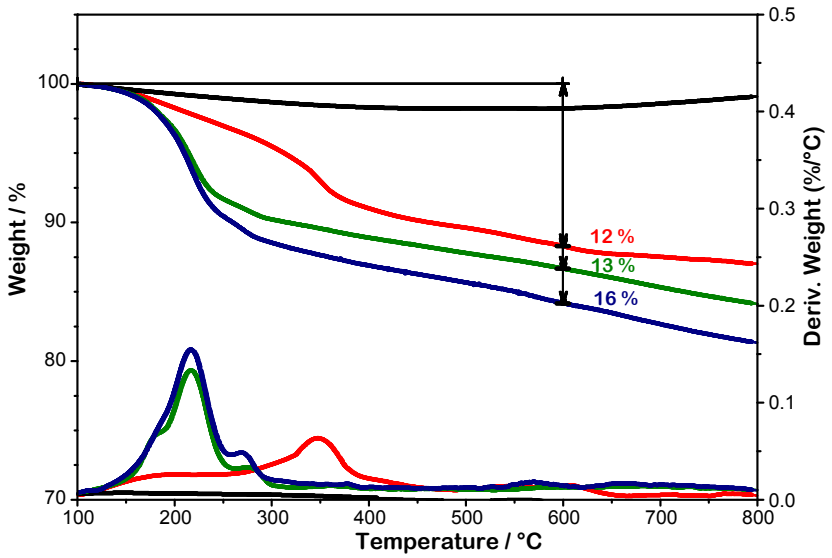

Figure 1.33. TGA and first derivative under inert conditions of: graphite (black), GR exfoliated in NMP (red), GOs (green) and GO_O (blue).

Additional structural information about the synthesized GO was obtained by FTIR and Magic Angle Spinning (MAS) ^{13}C-NMR spectroscopies. In Figure 1.34, the FTIR spectra of pristine graphite and GO_O are compared. Both spectra exhibit overlapping bands in the 3600-3200 cm^{-1} range belonging to the stretching vibrations of -OH groups. In the graphite spectrum, these bands are due to physisorbed water molecules, whereas in GO_O result from the covalently bonded hydroxy groups stretching vibrations and water molecules. Another characteristic fingerprint is the C=C skeletal in-plane vibration, which is located in both samples at 1581 cm^{-1}. Additionally, the aliphatic C–H stretching mode located between 2854 and 2925 cm^{-1} and the C–H bending mode at around 1250–1500 cm^{-1} are discernable. Therefore, these results demonstrate that GO_O retains part of the sp^2 domains from the starting graphite.

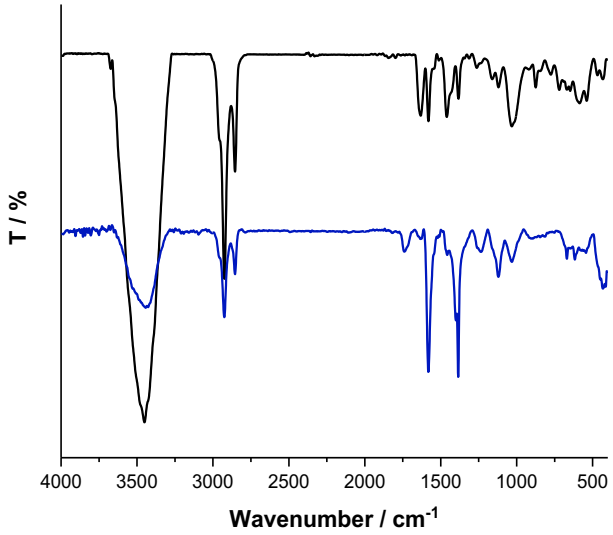

Figure 1.34. FTIR spectra of graphite (black) and GO_O (blue).

As a result of the formation of oxygen-containing groups, new features were found in the GO_O spectrum in comparison with the starting material. The peaks at 1029 and 1234 cm^{-1} are related to C-O and C-OH vibrations, and the broad peak at 1739 cm^{-1} is attributed to the C=O stretching band. This band is mainly associated to carboxylic acid groups, but due to the broadness of the band, other species could be involved such as anhydrides or lactones.

MAS ^{13}C-NMR is depicted in Figure 1.35. In the spectrum, three different resonances located at 60, 70 and 130 ppm are observed. It is well-known that the first two peaks are related with C-OH and C-O-C groups whereas the last, at 130 ppm, is attributed to C=C bonds of the carbon backbone.[153]

[153] W. Cai, R. D. Piner, F. J. Stadermann, S. Park, M. A. Shaibat, Y. Ishii, D. Yang, A. Velamakanni, S. J. An, M. Stoller, J. An, D. Chen, R. S. Ruoff, *Science* **2008**, *321*, 1815.

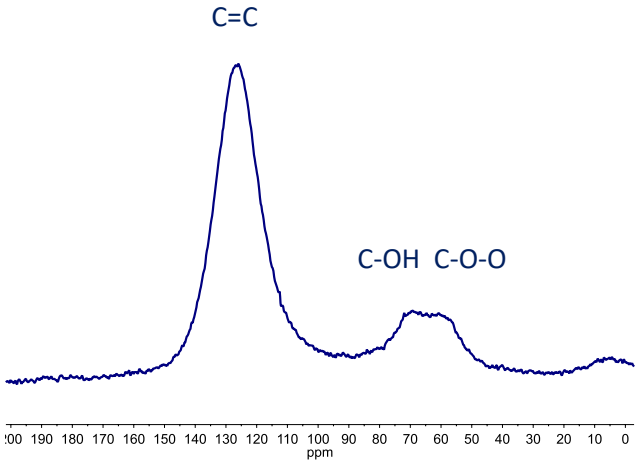

Figure 1.35. MAS ^{13}C-NMR spectrum of GO_O.

One of the most striking observations about this study is the lack of signals belonging to the C=O groups of carboxylic acids and their derivatives, which usually appear in the range of 160-190 ppm. FTIR analysis evidenced the presence of this kind of groups in the structure, but the number of them attached to the carbon sheets might not be enough to be detected by MAS ^{13}C-NMR. One explanation to this fact is that carboxylic acids and their derivatives are only located in the edges of the layer, whereas epoxy and hydroxy groups or sp^2 carbons are in the basal plane of the graphene oxide.[154]

In order to estimate the number of carboxylic acids presented in the surface of GO_O an indirect acid-base titration was performed.[155] This titration method allowed to quantify specifically the carboxylic acid functions presented on the surface, in contrast to the Boehm method where all the acidic functions are analyzed.[156] This method consists in mixing sodium oxalate and GO_O in deionized water in order to form oxalic acid, which is neutralized with NaOH in the titration experiment (Figure 1.36) (more details are given in the experimental section).

[154] W. Gao, L. B. Alemany, L. Ci, P. M. Ajayan, *Nat. Chem.* **2009**, *1*, 403.
[155] M. L. Toebes, van Heeswijk, Jürgen M. P, J. H. Bitter, v. D. Jos, K. de Jong, *Carbon* **2004**, *42*, 307.
[156] H. P. Boehm, *Carbon* **1994**, *32*, 759.

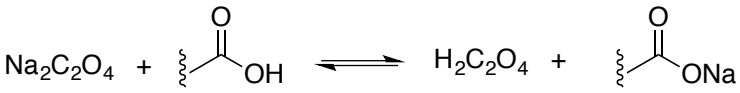

Figure 1.36. Schematic representation of the equilibrium generated with GO_O and $Na_2C_2O_4$.

The number of μmol of NaOH was calculated based on the change in the pH value, the volume of the sample and the original NaOH concentration. A value of 22 μmol of COOH/ g of C was estimated for our GO_O which is in the same order of magnitude of other previously published works.[157]

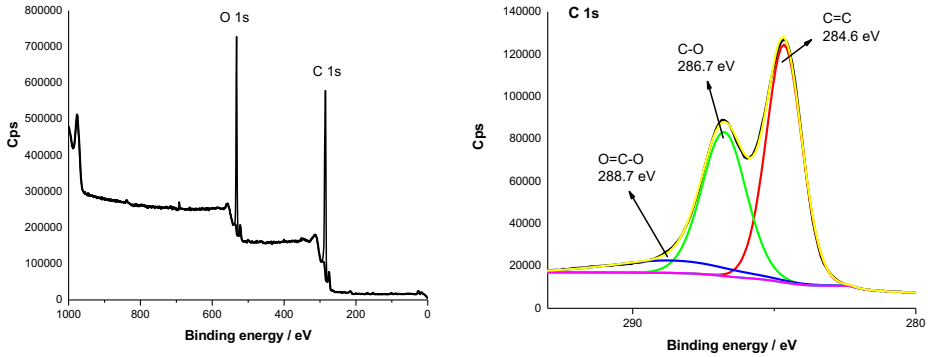

Figure 1.37. XPS survey spectrum of GO_O (left) and high-resolution C 1s core spectrum (right).

Finally, X-ray photoelectron spectroscopy (XPS) was found to be an interesting tool to identify the surface groups, the chemical state of the atoms, and their relative abundance in the material. Figure 1.37 (left) shows the survey spectrum of GO_O, with peaks corresponding to C 1s and O 1s core levels at 284.8 and 532.3 eV, respectively. The absence of other elements confirmed that during the purification, all byproducts from the oxidation process were removed. With the aim of investigating the composition of GO_O, semiquantitative XPS was also employed. This technique informs about the elements abundance. The XPS spectrum was normalized to the C 1s peak, and

[157] S. Peng, C. Liu, X. Fan, *Integrated Ferroelectr.* **2015**, *163*, 42.

ratios of 78.3 % for C and 21.7 % for O atoms were obtained. Furthermore, the high-resolution C 1s core-level spectrum was comprised of the expected components: sp^2 carbons (C=C) at 284.6 eV, epoxy and hydroxy groups (C-O) at 286.7 eV and the minor component due to carboxylic acids and derivatives (O=C-O) at 288.7 eV. The high content in oxygen made the C 1s peak to split into two due to the high contribution of the C-O bonds.[158]

1.3.2. Anionic heptamethine cyanine dyes

Anionic heptamethyine cyanines (Cy) belong to a class of ionic light harvesters with a skeleton of an odd number of π-conjugated carbon atoms, which guarantees an intense NIR absorption that spans from 750 to 900 nm.[138, 139] The excellent electron-donating features of Cy have already been considered when used as a complement to electron-accepting species widely used in molecular photovoltaics, such as fullerenes (C_{60} and C_{70})[140] to drastically improve their NIR absorption, or perfluorinated subphthalocyanines to afford panchromatic light harvesting systems.[159]

The synthesis of NIR absorbing nanomaterials considering Cy and SWCNT or GR was recently achieved by using using 1,3-dipolar cycloaddition reactions.[141] However, the low degree of functionalization obtained precluded the observation of photoinduced charge separated species in photophysical investigations.

With this information in mind, we decided to synthesize new Cy molecules to perform the n-doping of carbon nanomaterials such as SWCNT and GR by using not only covalent methodologies, but also exploring π- π stacking interactions and complementary ionic forces in the aggregates formation. To start, the synthesis and characterization of the different Cy employed in this Thesis project are discussed in the following subsections.

[158] J. Chen, Y. Zhang, M. Zhang, B. Yao, Y. Li, L. Huang, C. Li, G. Shi, *Chem. Sci*. **2016**, *7*, 1874.

[159] C. Romero, J. Guilleme, C. Villegas, J. L. Delgado, D. Gonzalez-Rodriguez, N. Martín, T. Torres, D. M. Guldi, *J. Mater. Chem*. **2011**, *21*, 15914.

1.3.2.1. Synthesis of the cyanine-pyrene (CyPyr) dye

It is well-known that pyrene entities feature a strong affinity to form stable supramolecular complexes with carbon-based materials via π-π stacking. [24,62,82] To ensure the supramolecular interaction between cyanine dyes and carbon nanomaterials (in this case GR or SWCNT), we designed and developed the synthesis of an anionic heptamethine cyanine with a pyrene moiety covalently connected to its backbone.

The synthesis of the cyanine started from the precursors chlorobisaldehyde (**1**)[160] and tricyanofuran (**2**, TCF).[161] The former was synthesized from cyclohexanone, $POCl_3$ and DMF, and the latter was synthesized in a single step through the condensation of 3-hydroxy-3-methyl-2-butanone and malononitrile under basic conditions using microwave irradiation (Scheme 1.3).

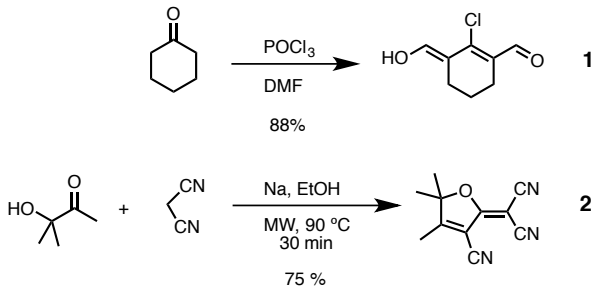

Scheme 1.3. Synthesis of chlorobisaldehyde (**1**) and TCF (**2**) precursors.

The formation of the characteristic skeleton of the desired anionic heptamethine cyanine occurred through a double Knoevenagel reaction between **1** and **2**.[159] Two equivalents of **2** vs. one of **1** gave rise to the desired cyanine dye **3** with sodium as a counter anion in a 65% yield (Scheme 1.4). The next step in this synthetic route was the quantitative cation exchange of sodium for tetrabutylammonium (**4**) to enhance solubility in different organic solvents.

A substitution reaction of the chlorine atom by 4-hydroxybenzyl alcohol provided the intermediate **5**.[159]In this reaction only one equivalent of NaH was used in order to deprotonate just the phenol group against the benzylic alcohol.

[160] G. A. Reynolds, K. H. Drexhage, *J. Org. Chem*. **1977**, *42*, 885.
[161] G. Melikian, F. P. Rouessac, C. Alexandre, *Synth Commun*. **1995**, *25*, 3045.

Finally, through the esterification reaction of derivative **5** and 1-pyrene butyric acid in the presence of *N*-ethylcarbodiimide hydrochloride (EDC·HCl) and 4-dimethylaminopyridice (DMAP), compound **6** (CyPyr) was obtained in a 66% yield.

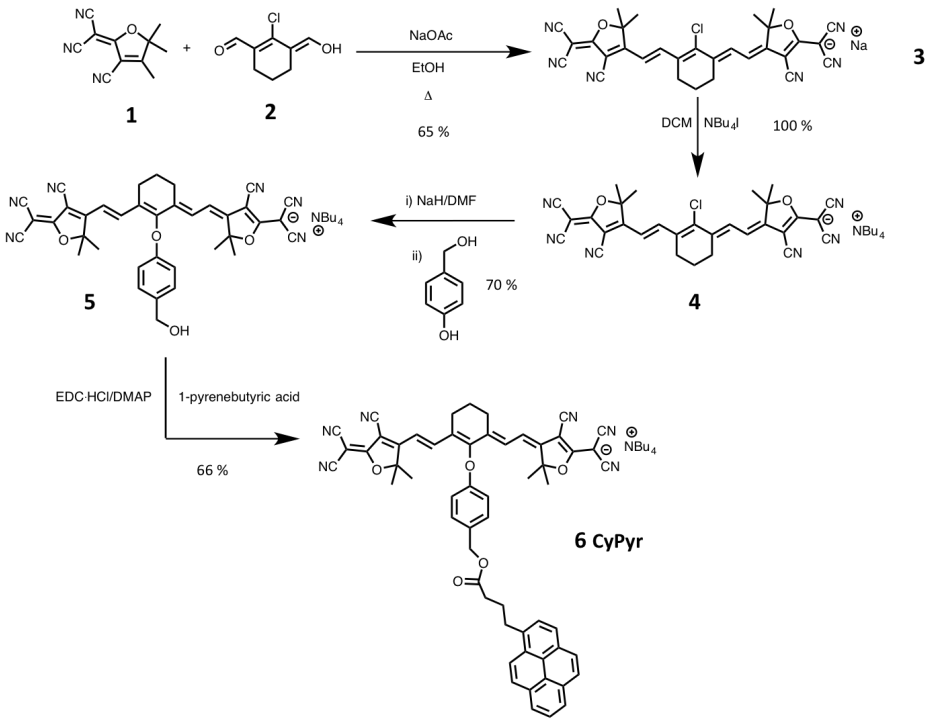

Scheme 1.4. Synthetic route to obtain **CyPyr** (**6**).

The structure of compounds **3-6** was confirmed by common characterization techniques (^{1}H-NMR, ^{13}C-NMR, HR-MS, FTIR and UV-vis) and details are given in the Experimental Section. ^{1}H-NMR was particularly useful to follow the different steps in the synthetic pathway, since the methylenic, methyne and aromatic protons change notably from one compound to the other (Figure 1.38).

In the ^{1}H-NMR spectrum of compound **3** is observed the presence of two doublets at 8.20 (J = 14.0 Hz) and 6.08 (J = 14.0 Hz) ppm, which correspond to the olefinic protons of the cyanine skeleton. These protons conserved the same chemical shifts and coupling constants after cation exchange in compound **4**.

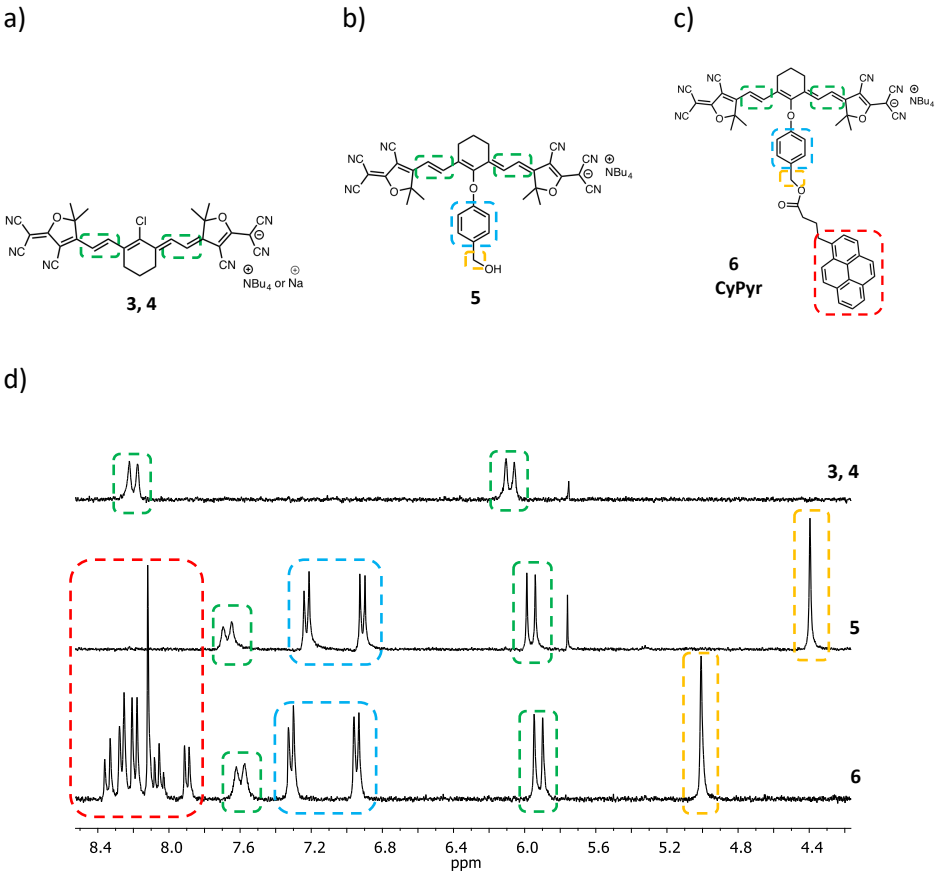

Figure 1.38. a-c) Structure of compounds **3**-**6** with their characteristic protons labeled with colors. d) ^{1}H-NMR spectra of compounds **3** and **4** (top), **5** (middle) and **6** (bottom).

On the other hand, the structure of compound **5** was verified by the signal corresponding to the two benzylic protons of the molecule, which appear as a singlet at 4.39 ppm. In addition, the appearance of two doublets at 7.22 and 6.91 ppm with a J = 8.0 Hz confirms the presence of the four protons of the para-substituted benzene ring. When comparing the ^{1}H-RMN of **6** with that of **5**, it is possible to see a new aromatic multiplet (8.40–7.91 ppm) belonging to the nine protons of the incorporated pyrene fragment. Furthermore, it is also observed that after the incorporation of the pyrene, the benzylic protons were remarkably upshifted (from 4.39 ppm in compound 5 to 5.02 ppm in **6**)

The structure of **CyPyr** (**6**) was further confirmed by high resolution mass spectrometry, which provided the peak of the molecular ion $C_{57}H_{43}N_6O_5^-$ at 891.3296 m/z (calculated for $C_{57}H_{43}N_6O_5^-$ = 891.3300 m/z). FTIR spectroscopy revealed one of the most characteristic fingerprints of **CyPyr**, which is the peak at 2208 cm^{-1} related with the conjugated -CN groups presented in the structure. This feature was also discerned in the FTIR of compounds **3**-**5**, since the conjugated carbon skeleton of the cyanine is present in all of them.

Regarding the optical properties, all the cyanine dyes synthesized (**3**-**6**) exhibit a strong absorption in the UV-Vis-NIR region (Figure 1.39).This strong absorption can be seen with the naked eye due to the deep green color that these dyes show in solution (Figure 1.39).

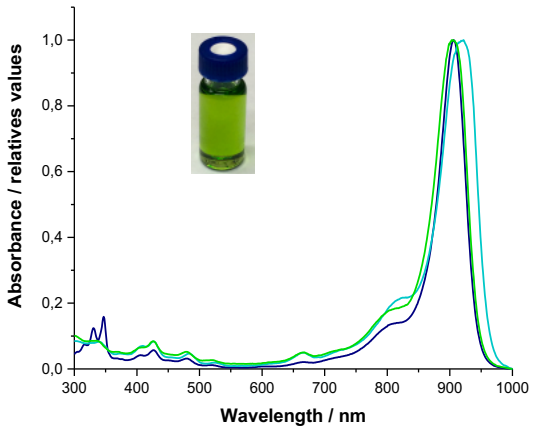

Figure 1.39. UV-Vis-NIR spectra of compounds **4** (cyan), **5** (green) and **CyPyr** (**6**) (deep blue) in *o*-DCB. Inset: Photography of **CyPyr** (**6**) solution in *o*-DCB.

Indeed, **CyPyr** showed a maximum centered at 906 nm when the sample was dissolved in *o*-DCB. The characteristic absorption features of the pyrene fragment were found at 346 and 331 nm. The optical and photophysical properties of **CyPyr** will be discussed in more detail in Section 1.3.3.

1.3.2.2. Synthesis of the cyanine-C_{60} (CyC_{60}) dye

Following a similar procedure to that previously reported in our group, we have carried out the synthesis of a cyanine derivative bonded to a [60]fullerene (**CyC_{60}**).[140] This molecule was employed for the functionalization of a modified graphene and graphene oxide with imidazolium salts (GO^{IL} and GR^{IL}) as we

will see later in this chapter. In this case, **CyC$_{60}$** was synthesized as a sodium salt in order to enhance its solubility in water and improve further functionalization of GR^{IL} and GO^{IL}.

For the synthesis of **CyC$_{60}$** (Scheme 1.5), the first step was the substitution of the chlorine atom of compound **3** for 4-(5,5-dimethyl-1,3-dioxan-2-yl)phenol. Subsequently, the acetal group was hydrolyzed in acid media to give rise to the formyl-functionalized cyanine **7** with a 76% yield. Finally, reaction with *n*-octylglicine led to the formation of the corresponding azomethine ylide which, through a 1,3-dipolar cycloaddition with pristine C_{60}, afforded compound **8** (**CyC$_{60}$**).

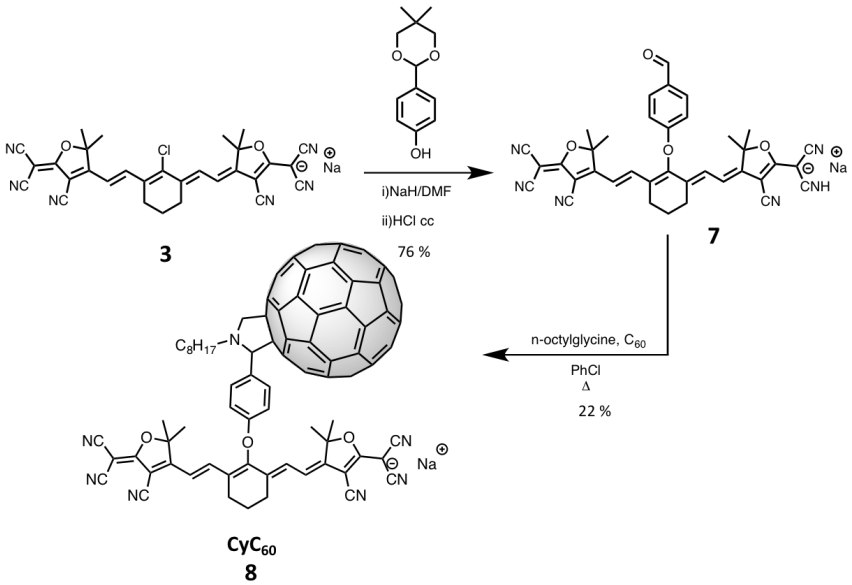

Scheme 1.5. Synthetic pathway used for the preparation of **CyC$_{60}$** (**8**).

^{1}H-NMR spectroscopy was also essential to track the different steps of the synthesis (Figure 1.40). After the addition of the phenol fragment to the skeleton of **3** it was observed the presence of two doublets at 7.88 (J = 8.1 Hz) and 7.15 (J = 8.1 Hz) ppm, corresponding to the four protons of the p-substituted benzene ring. The spectrum of **8** showed, in addition to the aromatic protons, the expected protons coming from the pyrrolidine ring at 5.12-5.07 and 4.12 ppm. Furthermore, the disappearance of the aldehyde singlet at 9.87

ppm of compound **7** was observed and further confirmed the formation of compound **8**.

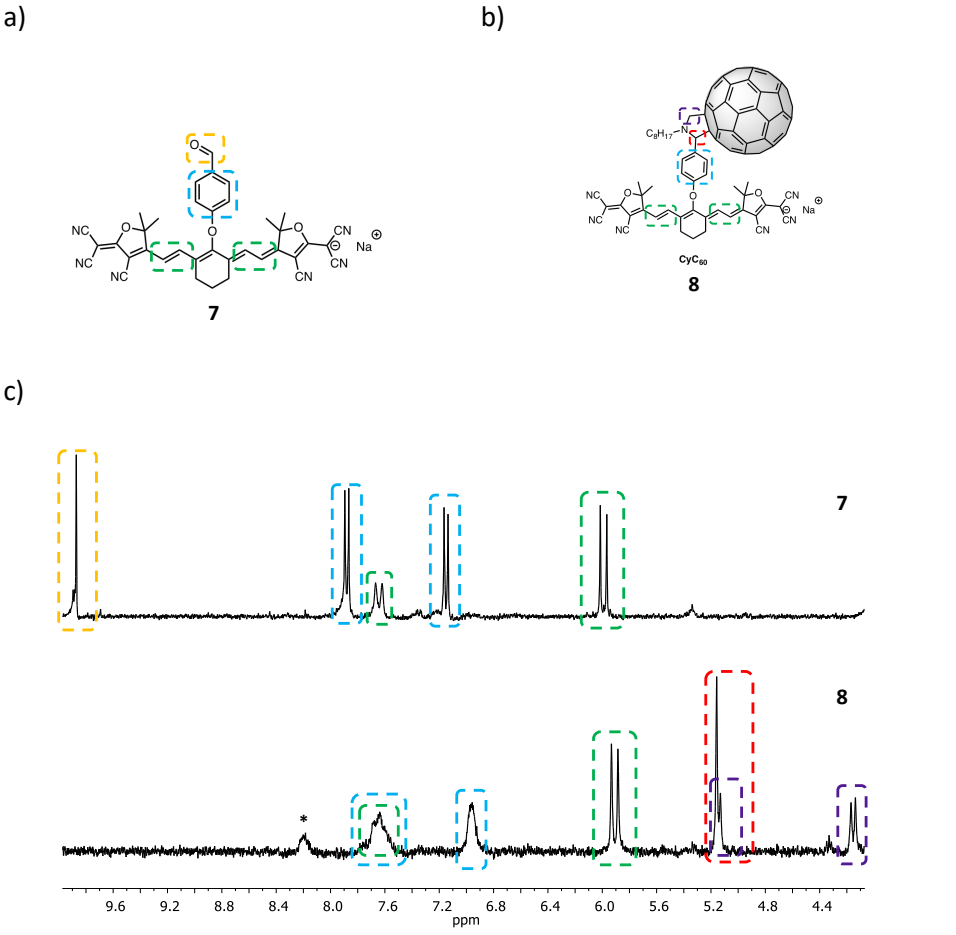

Figure 1.40. a), b) Structure of compounds **7** and **8** with their characteristic protons labeled with colors. c) ^{1}H-NMR spectra of compounds **7** (top) and **8** (bottom).

In addition to NMR spectroscopy, the structure of **CyC$_{60}$ (8)** was confirmed by high resolution mass spectrometry, which provided the molecular ion peak of $C_{106}H_{46}N_7O_3^-$ at 1465.3575 m/z (calculated for $C_{106}H_{46}N_7O_3^-$ = 1465.3699 m/z). The presence of the conjugated cyano groups was additionally corroborated by the intense band at 2213 cm^{-1} in the FTIR spectrum (Figure 1.41). By FTIR it was also possible to detect at 526 cm^{-1} the distinctive vibration mode of [60]fullerene species.

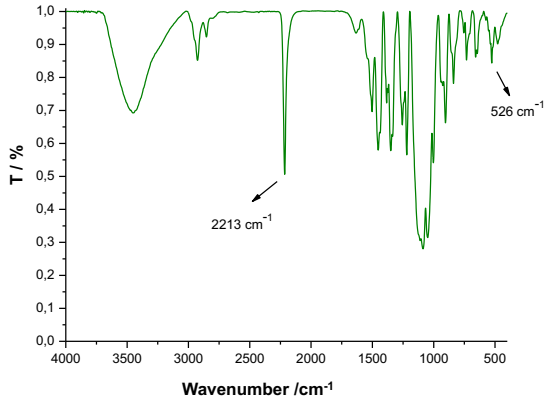

Figure 1.41. FTIR spectrum of compound **8**.

The absorption properties of **8** are depicted in Figure 1.42. In the UV-Vis-NIR spectrum recorded using dichloromethane as solvent, similar features to those discussed above for **CyPyr** and its derivatives are observed. Thus, compound **8** displayed an intense absorption band in the NIR centered at 896 cm^{-1} due to the heptamethine conjugated backbone. Besides this absorption band, in the UV-Vis region are discerned low absorption features associated to the C_{60} molecule.

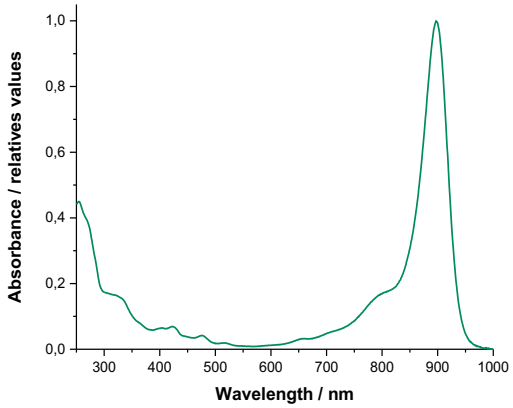

Figure 1.42. UV-Vis-NIR spectrum of **8** in dichloromethane.

1.3.3. Supramolecular complexes of GR and SWCNT with CyPyr

The use of non-covalent interactions, such as π–π stacking, and/or charge transfer, has been actively explored as a tool for the functionalization of GR and SWCNT. This strategy offers some important advantages with respect to the covalent approach, the main one, that preserves the π-conjugated electronic structure and, thus, the electrical transport properties of the carbon nanomaterial. Furthermore, it also allows, in principle, the preparation of hybrid materials with a high degree of functionalization.

In this sense, we have investigated the formation of supramolecular complexes between **CyPyr** and GR or SWCNT, in collaboration with the group of Prof. D. M. Guldi at Erlangen-Nuremberg University. In a first instance, it is described the distinct near-infrared absorption and the electronic properties of the **CyPyr** molecule, which assists in visualizing the electronic interactions with GR and SWCNT, what is detailed in the second part of this section.

1.3.3.1. Optical and electronic properties of CyPyr

Steady-state absorption spectroscopy of **CyPyr** in MeOH showed two maxima at 230 and 350 nm and a very broad and intense band with the maximum at 874 nm (Figure 1.43a). The UV-Vis bands are related with the absorption of the pyrene fragment, whereas the NIR absorption is associated with the heptamethine cyanine. Supplementary to absorption measurements, fluorescence experiments were carried out. Figure 1.43b shows that, regardless the pyrene or the cyanine units were excited, the emission is governed by the strong NIR fluorescence of the cyanine moiety. Pyrene photoexcitation led to an energy transfer from this unit to the cyanine, which activates the heptamethine-cyanine-centered fluorescence. In line with these results, fluorescence quantum yields of 0.05% and 4.5% were obtained for the pyrene and heptamethine cyanine fluorescence, respectively.

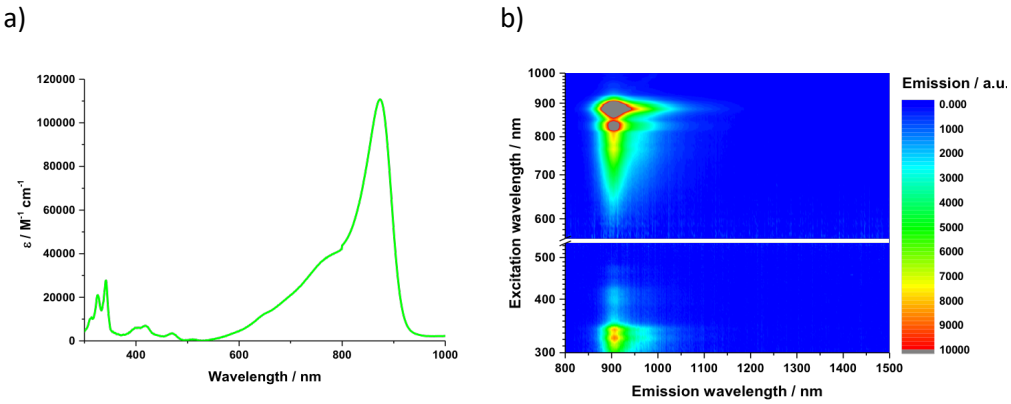

Figure 1.43. a) UV-vis-NIR absorption spectrum of **CyPyr** in MeOH. b) 2D NIR fluorescence spectrum of **CyPyr** in MeOH.

The electrochemical behavior of **CyPyr** was also evaluated in MeOH. A single reduction wave was observed at -1.06 eV, whereas three oxidation processes took place at +0.03, +0.55, and +0.83 V (*vs*. Fc/Fc^{+}). The oxidized state of **CyPyr** was further characterized by spectroelectrochemistry using tetrabutylammonium perchlorate ($TBAClO_4$) as supporting electrolyte (Figure 1.44). Herein, we obtained the differential absorption spectra by applying a potential of 0.45 V *vs*. a silver wire. It is remarkable the observed bleaching of the ground-state absorption at 874 nm and new absorption maxima which emerged at 513, 540, 585, 641, and 1068 nm.

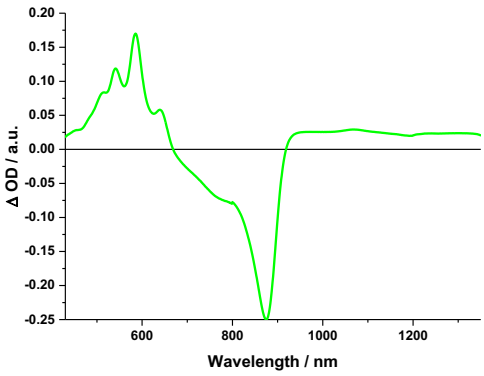

Figure 1.44. Differential absorption changes of **CyPyr** in MeOH obtained upon electrochemical oxidation at 0.45 V *vs.* an Ag-wire.

Finally, femtosecond transient absorption spectroscopy measurements were performed. Figure 1.45 shows the differential absorption spectra of **CyPyr**, where it is displayed the absorption characteristics of the singlet excited state given that it is developed immediately after excitation at 387 nm. Moreover, new maxima at 554, 614, and 1246 nm, new shoulders at 494, 561, and 625 nm, and a new minimum at 893 nm were discernable. The 893 nm minimum was accompanied by a 972 nm shoulder as a superimposition of ground-state bleaching and stimulated fluorescence.

a) b)

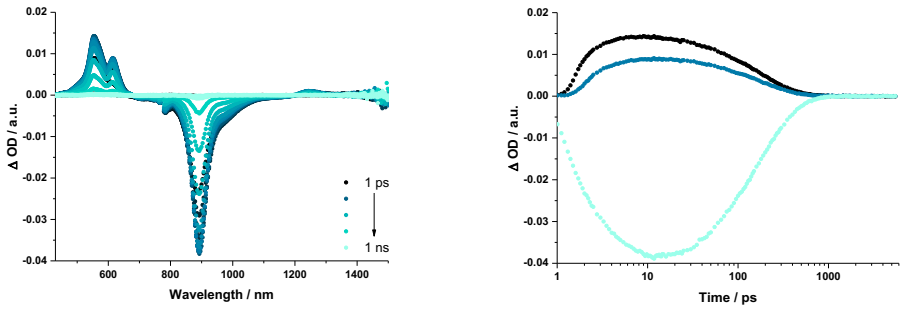

Figure 1.45. a) Differential absorption spectra of **CyPy**r in MeOH obtained upon 387 nm laser excitation with time delays between 1 ps and 1 ns. b) Corresponding time absorption profiles at 554 nm (black), 614 nm (dark cyan), and 892 nm (cyan).

Additional information about the deactivation was inferred from global fitting. Short-lived and long-lived components of 3.4 and 171 ps, respectively, were obtained (Figure 1.46). The short-lived component came from the population of the first singlet excited state, which was most likely formed by vibrational relaxation. After its formation, the first singlet excited state decayed as the long-lived component occurred via recovery of the ground state.

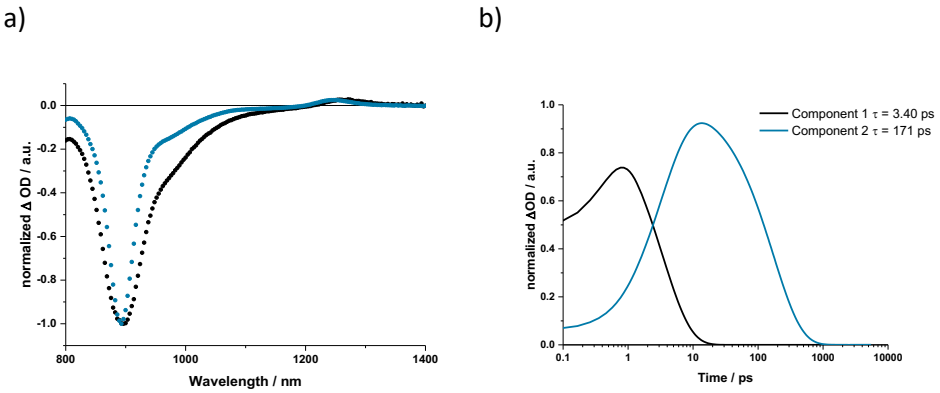

Figure 1.46. a) Deconvoluted transient absorption spectra of **CyPyr** obtained by global analysis. b) Corresponding concentration-time profiles.

1.3.3.2. Synthesis and characterization of GR-CyPyr and SWCNT-CyPyr hybrids

Once **CyPyr** was fully characterized, the next step was the formation of the desired supramolecular complexes (Figure 1.47). Supramolecular aggregates with graphene (**GR-CyPyr**) as well as with single-wall carbon nanotubes (**SWCNT-CyPyr**) were obtained. As it was mentioned above, the driving force to afford these complexes, comes from π-π stacking interactions between the pyrene and the sp^2 lattice of GR or SWCNT. The details of the protocols employed for the formation of **GR-CyPyr** and **SWCNT-CyPyr** are given in the experimental section. Below is discussed the tracking of the complexes' formation as well as their characterization.

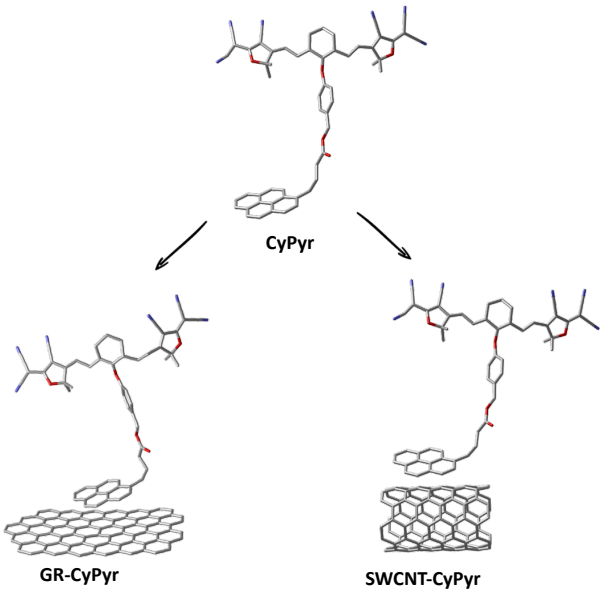

Figure 1.47. Schematic representation of π-π interaction between CyPyr and GR and SWCNT to afford **GR-CyPyr** and **SWCNT-CyPyr**, respectively.

The formation process was monitored step-by-step by steady-state absorption and by fluorescence spectroscopy. Titration experiments (Figure 1.48) revealed that upon the addition of SWCNT or GR, the original absorption of **CyPyr** at 874 nm decreased whereas a new absorption feature arised at 944 nm.

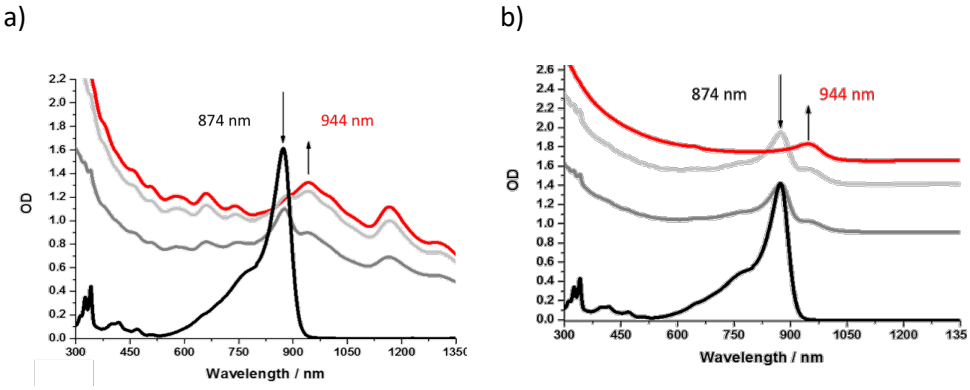

Figure 1.48. a) Absorption spectra of **CyPyr** (black) and **SWCNT-CyPyr** (grey, light grey and red) for three enrichment cycles in MeOH. b) Absorption spectra of **CyPyr** (black) and **GR-CyPyr** (grey, light grey and red) for three enrichment cycles in MeOH.

Furthermore, the fluorescence of **CyPyr** was completely quenched upon the last enrichment step (Figure 1.49a). When looking at the SWCNT-centered transitions, in particular when using (7,6) enriched SWCNT, during the titrations steps, it was observed a red-shift from 1169 to 1175 nm (Figure 1.49b).

a) b)

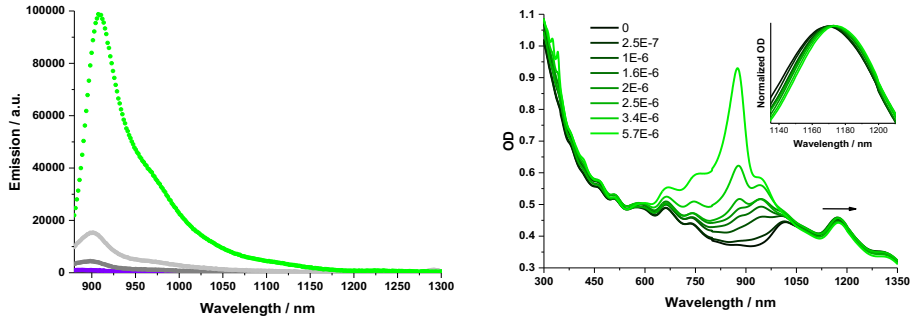

Figure 1.49. a) Fluorescence spectra of **CyPyr** (green) and **GR-CyPyr** (light grey, grey and purple) for three enrichment cycles in MeOH following 860 nm excitation. b) Titration assay, showing absorption spectra of SWCNT in MeOH upon the stepwise addition of **CyPyr**. The inset shows a zoom into the NIR region of normalized spectra of the SWCNT centered absorption.

To rule out possible decomposition of **CyPyr** during **SWCNT-CyPyr** or **GR-CyPyr** formation, the supramolecular complexes were disaggregated into the individual components. Tween 60, a non-ionic surfactant, was added in order to break down the aggregates and give rise to the former GR, SWCNT and **CyPyr**. This process was monitored by absorption spectroscopy, where it was observed the recovery of the initial absorption spectrum of **CyPyr** upon the addition of Tween 60 (Figure 1.50). This fact confirmed that **SWCNT-CyPyr** and **GR-CyPyr** are based on non-covalent forces between **CyPyr** and SWCNT and GR, respectively.

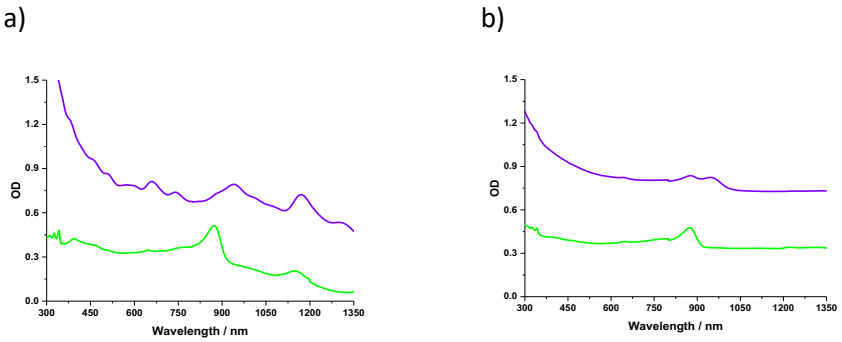

Figure 1.50. a) Absorption spectra of **SWCNT-CyPyr** before (purple) and after (green) addition of Tween 60 showing the recovery of the 874 nm absorption maximum of **CyPyr**. b) Absorption spectra of **GR-CyPyr** before (purple) and after (green) addition of Tween 60 showing the recovery of the 874 nm absorption maximum of **CyPyr**.

Additional information came from the comparison of **CyPyr** and **GR-CyPyr** by electrochemical assays. The addition of GR over a **CyPyr** solution resulted in a shift in the first reduction of **CyPyr** from -1.07 to -0.88 V in the hybrid. However, in the oxidation potentials only negligible changes were found. The electrochemical gap between the first reduction and the first oxidation was reduced by 0.21 V when going from **CyPyr** to **GR-CyPyr**. This decrease in the band gap is in good agreement with the 70 nm bathochromic shift seen in the absorption spectra and signifies that ground-state interactions mostly affected the lowest unoccupied molecular orbital of **CyPyr**.

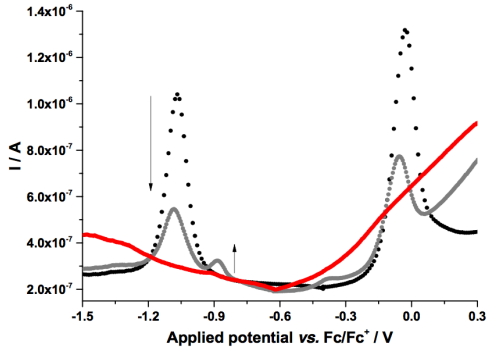

Figure 1.51. Differential pulse voltammograms of **CyPyr** (black) and **GR-CyPyr** (grey and red) resulting from a stepwise enrichment of GR in a methanol solution of **CyPyr** with $TBAClO_4$ as supporting electrolyte.

The incorporation of **CyPyr** on the GR or SWCNT surface was also corroborated by thermogravimetric analysis under inert conditions (Figure 1.52). First of all, the decomposition of **CyPyr** gave rise to two different transitions, at 195.5 ºC and at 289.4 ºC, leading to an overall weight loss of 85 %. On the contrary, both GR and SWCNT, showed to be stable up to 800 ºC with minor weight losses, of a 7 % and a 12 %, respectively. In the case of **SWCNT-CyPyr** and **GR-CyPyr** hybrids, we could discern an additional weight loss as consequence of the release of **CyPyr** from the basal plane of SWCNT or GR. For **SWCNT-CyPyr**, the desorption of **CyPyr** caused an additional weight loss of a 11 %, whereas for **GR-CyPyr**, a 13 % extra weight loss relative to that of GR was observed.

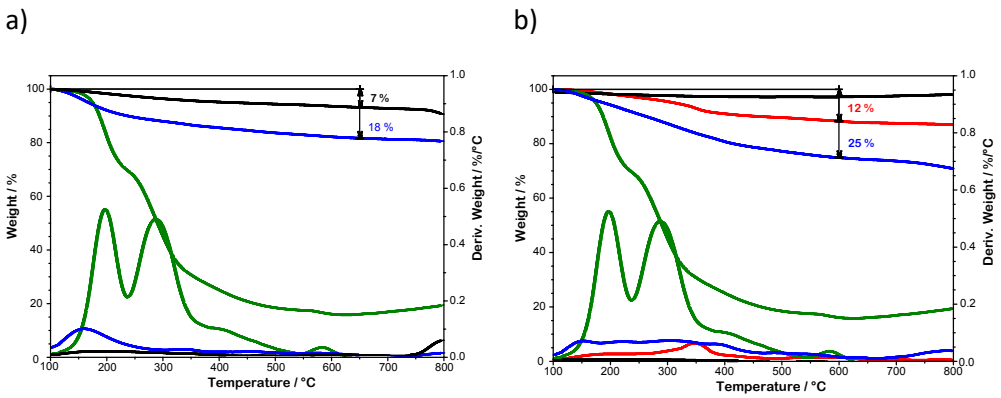

Figure 1.52. a) TGA analysis under inert conditions of **SWCNT-CyPyr** (blue) compared to **CyPyr** (green) and the pristine SWCNT material (black). b) TGA analysis of **GR-CyPyr** (blue) compared to that of **CyPyr** (green), GR (red), and the starting graphitic material (black).

FTIR spectroscopy and X-ray photoelectron spectroscopy (XPS) gave further information about the structure and composition of **SWCNT-CyPyr** and **GR-CyPyr**. FTIR spectra of both samples (Figure 1.53) revealed the stretching vibration of carbonyl and cyano functional groups at 1736 and 2214 cm^{-1}, respectively. Furthermore, the characteristic fingerprints of the carbon nanomaterial were also found. On one hand, the in-plane vibration band of C=C was recognized at 1575 cm^{-1} for **SWCNT-CyPyr** and at 1584 cm^{-1} for GR-CyPyr. On the other hand, the aliphatic C-H stretching vibrations between 2850-2950 cm^{-1} and the bending vibrations between 1250-1500 cm^{-1}, were also discernible.

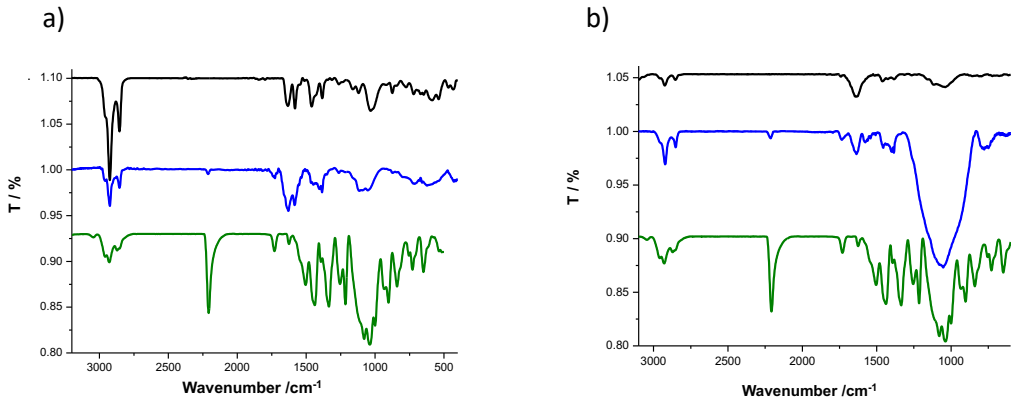

Figure 1.53. a) FTIR spectra of **GR-CyPyr** (blue) compared to the exfoliated GR (black) and **CyPyr** (green). b) FTIR spectra of **SWCNT-CyPyr** (blue) compared with pristine SWCNT (black) and **CyPyr** (green).

The elemental compositions of **CyPyr**, **SWCNT-CyPyr** and **GR-CyPyr** were gathered by XPS analysis. The survey spectra of the three samples are composed by the element signals of C 1s, N 1s, and O 1s at 284.6, 398.6, and 532.6 eV, respectively (Figure 1.54). Information regarding the chemical state of the atoms was revealed from the deconvolution of the high-resolution spectra of each core-level signal. The deconvolution of the C 1s energy levels was accomplished with five components, which are attributed to photoelectrons originated from sp^3 carbon atoms, sp^2 carbon atoms and C-O, C-N, and C=O bonds. In the O 1s spectra, signals at 531.4 and 532.1 eV are assigned to C=O surface groups and C-O groups, respectively. Finally, the high-resolution N 1s core-level spectra of **SWCNT-CyPyr** and **GR-CyPyr** showed three different contributions at 403.1, 399.7, and 398.8 eV. The first with a higher binding energy is attributed to quaternary ammonium salts. The second is associated to cyano groups as a part of the cyanine skeleton. The last one is assigned to cyano groups, which are shifted toward lower binding energies because they are predominantly involved in the stabilization of the negative charge density of the cyanine.[162,163]

[162] L. Rodríguez-Pérez, R. García, M. Á Herranz, N. Martín, *Chem. Eur. J.* **2014**, *20*, 7278.

[163] T. Tseng, C. Urban, Y. Wang, R. Otero, S. L. Tait, M. Alcamí, D. Ecija, M. Trelka, J. M. Gallego, N. Lin, M. Konuma, U. Starke, A. Nefedov, A. Langner, C. Wöll, M. A. Herranz, F. Martín, N. Martín, K. Kern, R. Miranda, *Nat. Chem*. **2010**, *2*, 374.

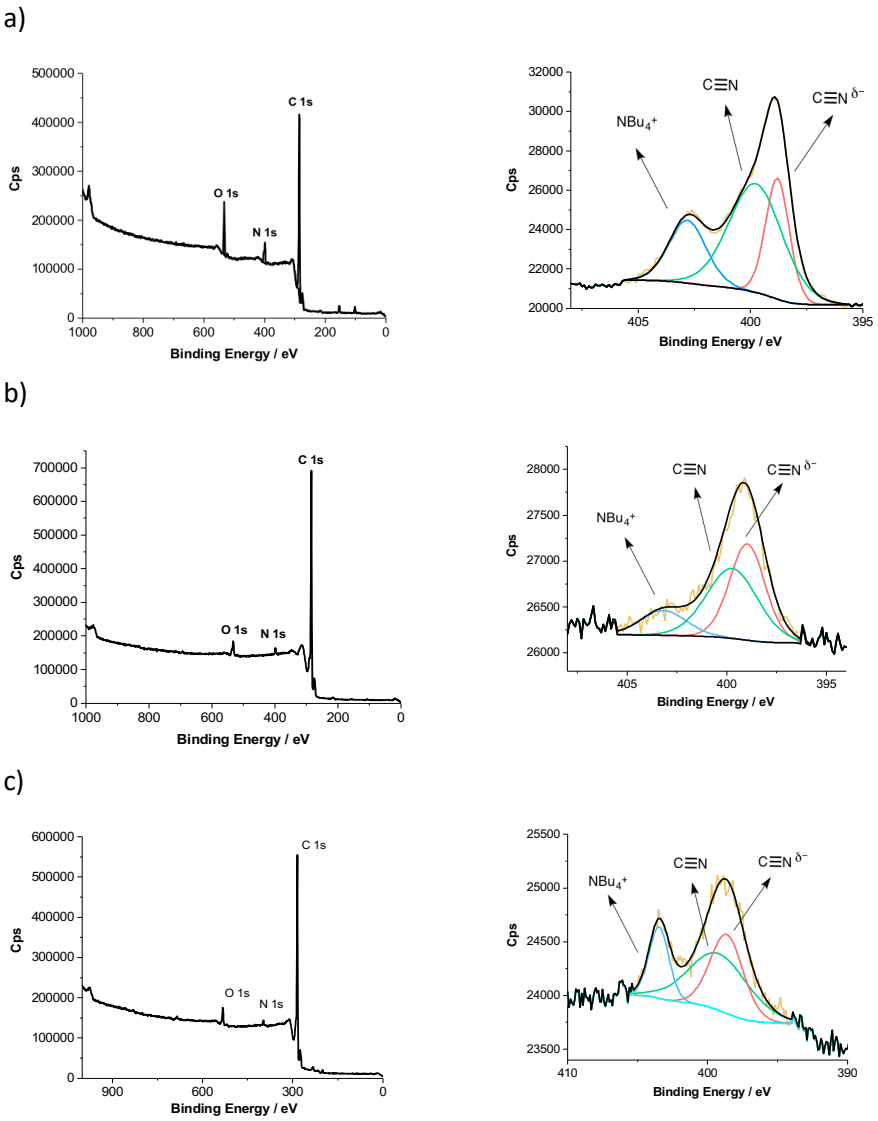

Figure 1.54. XPS survey spectra and XPS N 1s component deconvolution of a) **CyPyr**, b) **SWCNT-CyPyr** and c) **GR-CyPyr**.

The morphology of **SWCNT-CyPyr** and **GR-CyPyr** was analyzed by TEM (Figure 1.46). The solutions were prepared in MeOH and subsequently drop casted onto lacey carbon-coated copper grids. Before discussing the TEM analysis, it is worthy to mention the enhanced stability observed in **SWCNT-CyPyr** and **GR-CyPyr** dispersions in comparison with pristine SWCNT and GR dispersions, which revealed aggregation on a timescale of a few minutes

(Figure 1.55). TEM images of **SWCNT-CyPyr** pointed to debundling of the SWCNT and showed the coexistence of individual and smaller bundles of **SWCNT-CyPyr**. Regarding **GR-CyPyr**, exfoliation of graphite was evident by the existence of barely restacked GR as a result of interactions with **CyPyr**.

a) b)

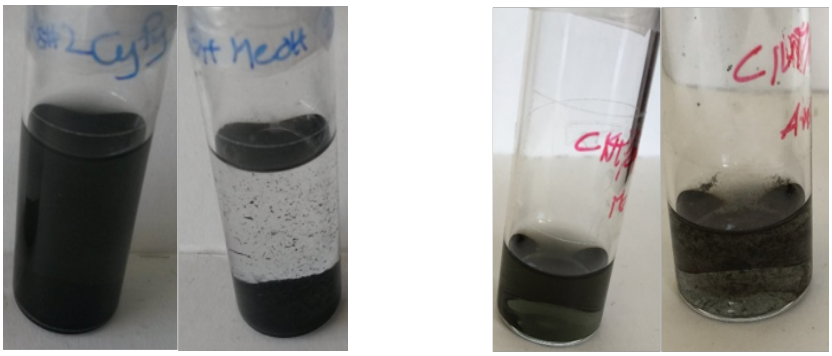

Figure 1.55. a) Images of **GR-CyPyr** and GR in MeOH prepared in equal conditions. b) Images of **SWCNT-CyPyr** and SWCNT in MeOH prepared in equal conditions.

a) b)

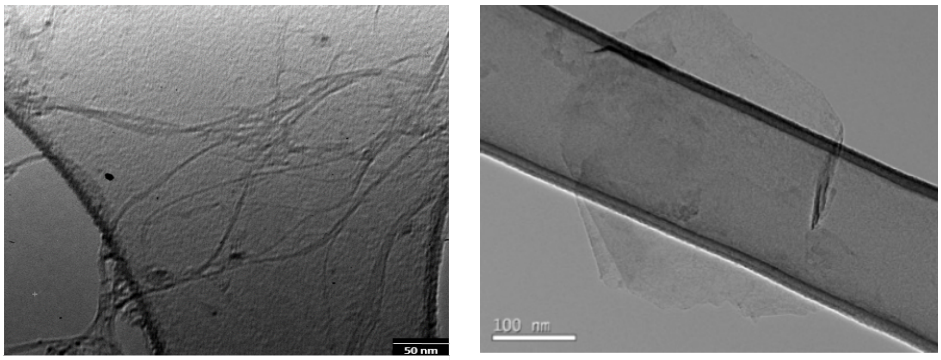

Figure 1.56. TEM images of: a) **SWCNT-CyPyr** and b) **GR-CyPyr**.

Insights into doping effects were gathered from statistical Raman analysis. In the course of these experiments about 1000 spectra of each sample with 532 and 633 nm laser excitations wavelengths were measured. The reference systems SWCNT and GR were analyzed and compared with the hybrids of **SWCNT-CyPyr** and **GR-CyPyr**.

Figure 1.57 shows the mean spectra of these samples, where is compared SWCNT *vs*. **SWCNT-CyPyr** and GR *vs*. **GR-CyPyr**. In terms of SWCNT and **SWCNT-CyPyr**, the radial breathing modes (RBM) for (8,7) and (7,6) SWCNT were detected at 222 and 258.5 cm^{-1} for SWCNT and at 220 and 258 cm^{-1} for **SWCNT-CyPyr**.

Regarding the G and 2D modes of SWCNT, they were detected at 1591 and 2607 cm^{-1}, respectively. In the case of **SWCNT-CyPyr** these modes are downshifted, with the G band shifted to 1588 cm^{-1} and the 2D band shifted to 2604 cm^{-1}. The obtained results are in good agreement with recent reports, which ascribe this behavior to an n-type doping.[164,165]

Moving to GR and **GR-CyPyr**, in both samples the D mode was found at 1343 cm^{-1}, whereas significant changes were observed for G and 2D modes. The G modes were observed at 1576 and 1572 cm^{-1} and the 2D modes were observed at 2680 and 2695 cm^{-1} for GR and **GR-CyPyr**, respectively. The upshifting in 2D band in combination with the downshifting in the G band pointed to an n-type doping of the graphene layers.[166]

[164] H. Terrones, A. M. Rao, M. Terrones, H. Qian, N. Anderson, A. Hartschuh, M. A. Pimenta, L. Novotny, A. Jorio, I. O. Maciel, J. Campos-Delgado, *Nat. Mater*. **2008**, *7*, 878.

[165] R. Voggu, C. S. Rout, A. D. Franklin, T. S. Fisher, C. N. R. Rao, *J. Phys. Chem. C.* **2008**, *112*, 13053.

[166] X. Dong, D. Fu, W. Fang, Y. Shi, P. Chen, L. Li, *Small* **2009**, *5*, 1422.

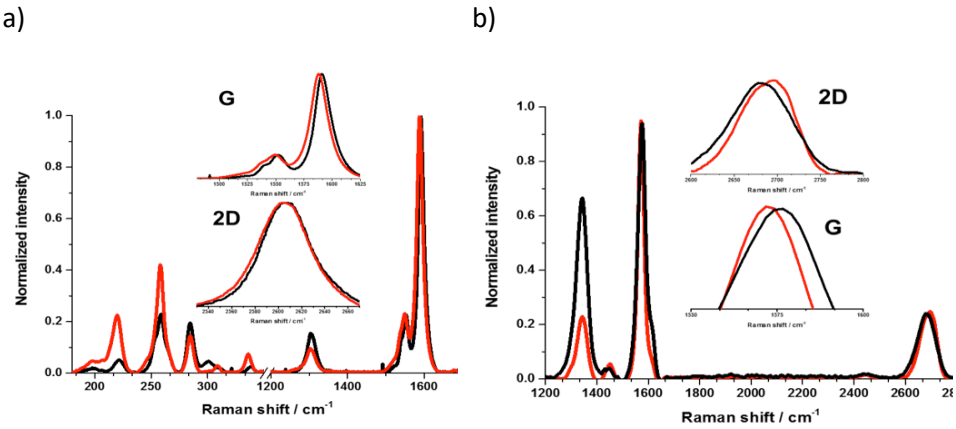

Figure 1.57. a) Raman spectra of SWCNT (black) and **SWCNT-CyPyr** (red) after 633 nm excitation. b) Raman spectra of GR (black) and **GR-CyPyr** (red) after 532 nm excitation.

The electron-donating behavior of the cyanine observed by Raman spectroscopy motivated us to look into the excited-state dynamics of **SWCNT-CyPyr** and **GR-CyPyr**.[167] Therefore, transient absorption measurements were performed and analyzed by global and target analyses. Figure 1.58 shows the deconvoluted transient absorption spectra of **SWCNT-CyPyr** and **GR-CyPyr** obtained by target and global analysis and their corresponding concentration-time profiles. First insights in the excited state revealed that none of them present the characteristic fingerprints of photoexcited **CyPyr** (see previous subsection).

On account of the lack of ground-state bleaching of **CyPyr** at 874 nm, it was confirmed the absence of any free, non-immobilized **CyPyr**. Instead, the bleaching is in line with the ground-state absorptions of **SWCNT-CyPyr** and **GR-CyPyr** red shifted to 944 and 947 nm, respectively.

[167] This photophysical study was carried out in the group of Prof. D. M. Guldi (Erlangen-Nuremberg University). Part of these results were also presented in the Thesis work of Alexandra Roth (2017).

a)

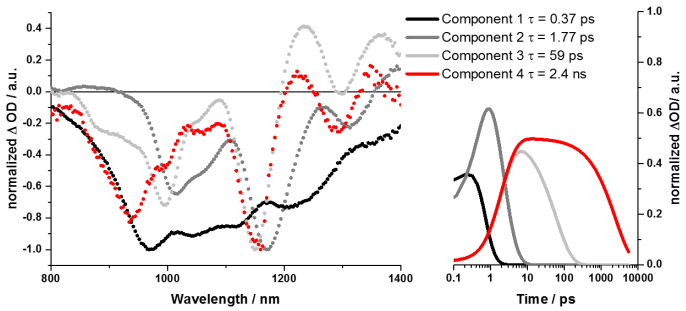

b)

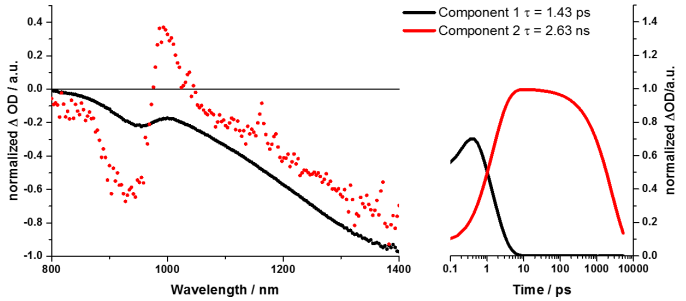

Figure 1.58. a) Deconvoluted transient absorption spectra obtained by target and global analysis and corresponding concentration-time profiles of **SWCNT-CyPyr**. b) Deconvoluted transient absorption spectra obtained by target and global analysis and corresponding concentration-time profiles of **GR-CyPyr**.

Regarding the reference SWCNT and GR, Figure 1.60 and Figure 1.62 show the corresponding evolution-associated spectra after 387 nm excitation. In the case of the SWCNT reference, instantaneous formation of minima at 665, 743, 1017, 1170, and 1312 nm corresponding to the ground-state bleaching of the S22 and S11 transitions are discernible (Figure 1.59). In terms of **SWCNT-CyPyr**, due to the debundling observed in TEM, these absoption features are hypsochromically shifted to 661, 738, 1006, 1156, and 1302 nm (Figure 1.61). Global and target analysis gave lifetimes of 0.4, 1.89, and 115 ps for SWCNT and 0.37, 1.77, and 59 ps as well as 2.40 ns for **SWCNT-CyPyr** and 3.4 and 175 ps for **CyPyr**.

a) b)

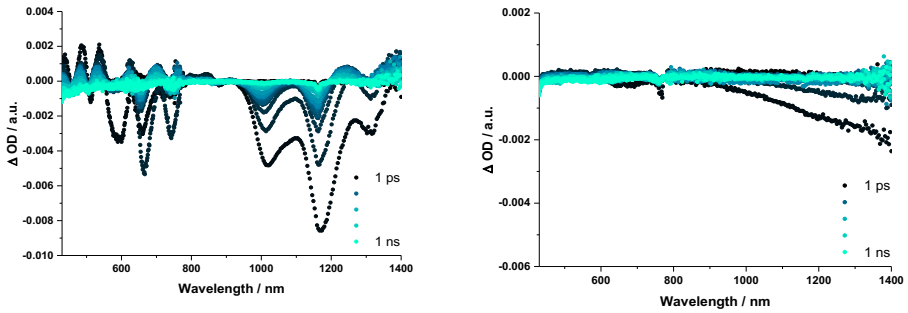

Figure 1.59. a) Differential absorption spectra of SWCNT in methanol obtained upon 387 nm laser excitation with time delays between 1 ps and 1 ns. b) Differential absorption spectra of GR in MeOH obtained upon 387 nm laser excitation with time delays between 1 ps and 1 ns.

Turning to GR and **GR-CyPyr** samples, it were discerned broad and featureless negative transients in the NIR, which were caused by phonon-related bleaching of GR (Figure 1.59). For this bleaching, a lifetime of 1.7 and 1.4 ps was determined for GR and **GR-CyPyr**, respectively. Next to the rather broad bleaching, new distinct features in the form of a minimum at 944 nm and a maximum at 996 nm were seen for **GR-CyPyr** (Figure 1.63). Nevertheless, these transients were not found for **CyPyr** or GR. From global analysis, we derived a lifetime of 2.63 ns for the latter transient.

a) b)

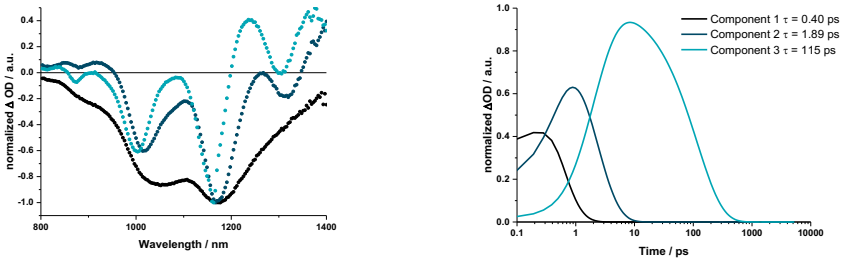

Figure 1.60. a) Deconvoluted transient absorption spectra of SWCNT obtained by global analysis. b) Corresponding concentration-time profiles.

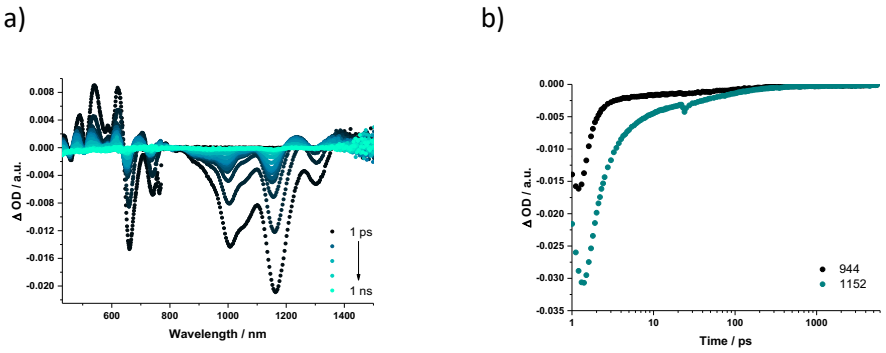

Figure 1.61. a) Differential absorption spectra of **SWCNT-CyPyr** upon 387 nm laser excitation with time delays between 1 ps and 1 ns. b) Corresponding time absorption profiles of **SWCNT-CyPyr** at 944 (black) and 1152 nm (dark cyan).

The decay and evolution-associated spectra of **SWCNT-CyPyr** and **GR-CyPyr** related to the longest lifetimes both have a minimum at 944 nm and a maximum at around 996 nm, which resemble the pattern of oxidized **CyPyr**. It is slightly superimposed by SWCNT-centered transients in **SWCNT-CyPyr**. Taking the aforementioned into account, we reached the conclusion that photoexciting both **SWCNT-CyPyr** and **GR-CyPyr** is the start of an ultrafast charge separation. As such, radical-ion-pair states in which **CyPyr** is oxidized and either SWCNT or NG is reduced are formed. Charge recombination at 2.40 and 2.63 ns is much slower and affords the ground state.

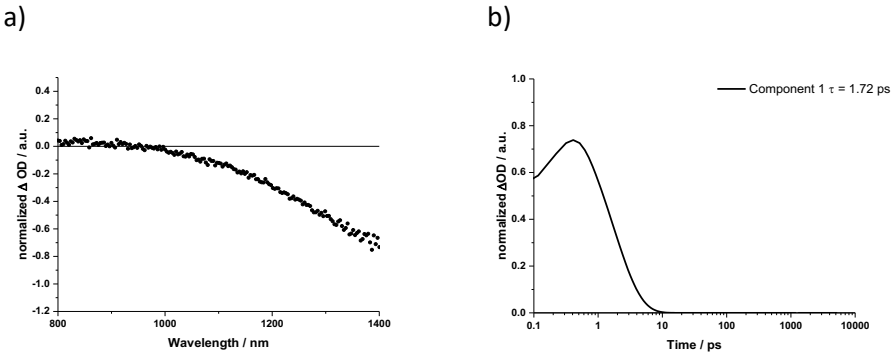

Figure 1.62. a) Deconvoluted transient absorption spectra of GR obtained by global analysis. b) Corresponding concentration-time profile.

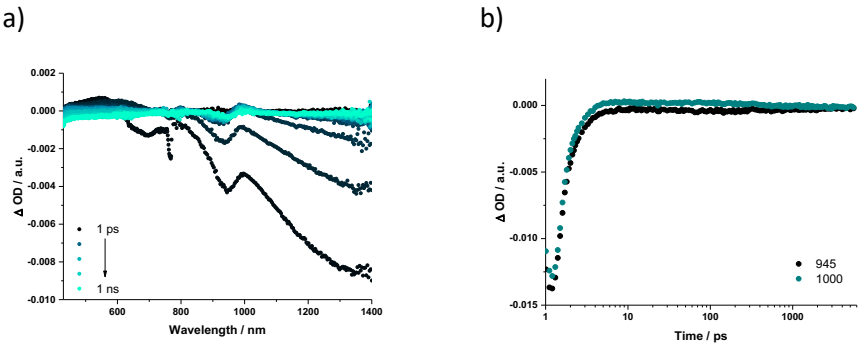

Figure 1.63. a) Differential absorption spectra of **GR-CyPyr** in MeOH obtained upon 387 nm laser excitation with time delays between 1 ps and 1 ns. b) Corresponding time absorption profiles of **GR-CyPyr** at 945 (black) and 1000 nm (dark cyan).

1.3.4. Synthesis of GR and GO imidazolium salts and Cy hybrids

Ionic liquids (IL), in particular, imidazolium salts composed of imidazolium-based cations, are gaining popularity in their combination with carbon nanostructures since they can provide the formed hybrid structures with different hydrophobicity/hydrophilicity, which typically improves the dispersion and solubilization of the nanocarbons. At the same time, IL allow the properties of carbon nanostructures to be combined with those of them, thus facilitating the development of functional nanomaterials.[50, 162]

This section describes the results obtained in the connection of graphene-based materials with IL. In the first part of this section we will discussed the incorporation of imidazolium salts in GO and, in the second part, we will focus in the functionalization of GR. In both cases, we employed a covalent approach for the attachment of the imidazolium moiety and a non-covalent approach for the further incorporation of the cyanine dyes **3** (**Cy**) and **8** (**CyC$_{60}$**) through anion exchange.

1.3.4.1. Synthesis of GO imidazolium salts and Cy hybrids

The employed GO was synthesized by the Staundemaier method as described in section 1.3.1. The highly functionalized fraction (GOo) was the one used in further work, even when for the sake of clarity we will refer to this materials as GO. The synthesis carried out for the preparation of the Cy hybrid materials is depicted in Scheme 1.6. Firstly, we took advantage of the carboxylic acids

presented in the GO surface, which were previously activated forming the corresponding acid chlorides. Once activated, the material was reacted with an excess of 1-(3-aminopropyl)imidazole at 120 ºC for 24 hours under inert atmosphere. In competition with this reaction, ring opening of the epoxides groups present in the basal plane of GO can occur.[168] In the next step, the imidazole fragment was alkylated with an excess of *n*-butyl bromide giving rise to GO^{IL}. Finally, we carried out the exchange of the bromide anions[169] by heptamethine cyanines (**Cy** or **CyC$_{60}$**) for generating two different materials, **GO^{IL}-Cy** and **GO^{IL}-CyC$_{60}$**.

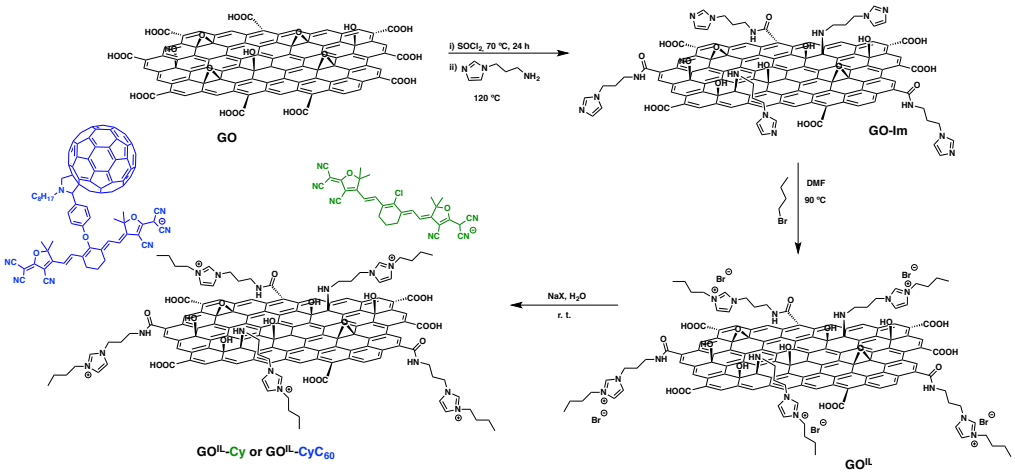

Scheme 1.6. Synthetic route employed to obtain **GO^{IL}-Cy** and **GO^{IL}-CyC$_{60}$**.

The course of the different synthetic steps was followed by using different techniques such as absorption spectroscopy (UV-Vis-NIR), FTIR, TGA and XPS. First evidences about the success in the synthesis of **GO^{IL}-Cy** and **GO^{IL}-CyC$_{60}$** were obtained from UV-Vis-NIR spectroscopy. Figure 1.64 shows the absorption spectra of **GO^{IL}-Cy** and **GO^{IL}-CyC$_{60}$** together with the corresponding reference systems, the **GO^{IL}-Cy** spectrum reveals the characteristic absorption fingerprints of the **Cy** molecule as well as the absorption along the visible range due to the graphene oxide layers. The maximum absorption peak of **GO^{IL}-Cy** is located at 890 cm^{-1} and for **GO^{IL}-**

[168] I. A. Vacchi, C. Spinato, J. Raya, A. Bianco, C. Menard-Moyon, *Nanoscale* **2016**, *8*, 13714.

[169] N. Karousis, S. P. Economopoulos, E. Sarantopoulou, N. Tagmatarchis, *Carbon* **2010**, *48*, 854.

CyC$_{60}$ at 888 cm^{-1}. These bands are slightly upshifted in comparison with the references **Cy** and **CyC$_{60}$**, which are located at 887 and 886 nm, respectively. Similarly to the results obtained in the supramolecular hybrids of SWCNT and GR with **CyPyr**, these bathochromic shifts might be an indication of a ground-state interaction between the GO^{IL} and the **Cy** and **CyC$_{60}$** units.

a) b)

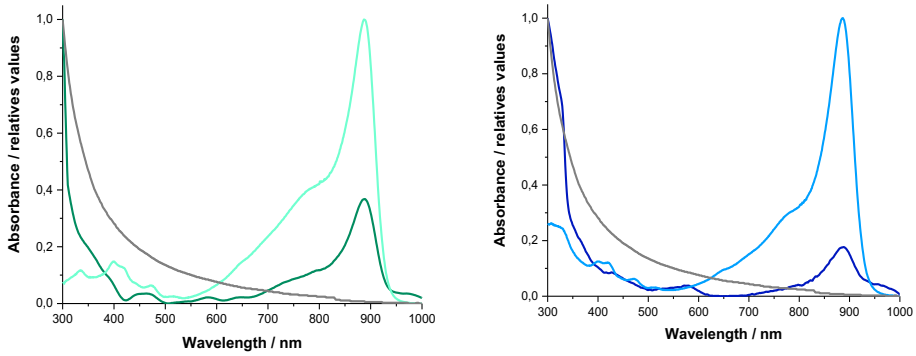

Figure 1.64. a) Absorption spectra of GO (grey), **Cy** (light green) and **GO^{IL}-Cy** (dark green) in MeOH. b) Absorption spectra of GO (grey), **CyC$_{60}$** (light blue) and **GO^{IL}-CyC$_{60}$** (dark blue) in MeOH.

Structural changes after each reaction step were detected by FTIR (Figure 1.65). Firstly, after the oxidation process of graphite it was possible to see the vibration at 1739 cm^{-1} due to the presence of the C=O stretching mode of the newly formed carboxylic acids. After the introduction of the imidazole moiety (**GO-Im**) a new band related to the C=O stretching mode of the formed amide bond is observed at 1662 cm^{-1}. It is important to mention that after the amidation reaction some carboxylic acids still remain, as can be noticed due to the presence of the band at 1739 cm^{-1}. Moreover, once performed the anion exchange, the stretching mode of -CN at 2222 cm^{-1} for **GO^{IL}-Cy** and at 2213 cm^{-1} for **GO^{IL}-CyC$_{60}$** appeared. In the case of **GO^{IL}-CyC$_{60}$**, it was also discerned at 526 cm^{-1} the characteristic vibration mode of the fullerene skeleton. These results confirmed the successful anion exchange in both cases.

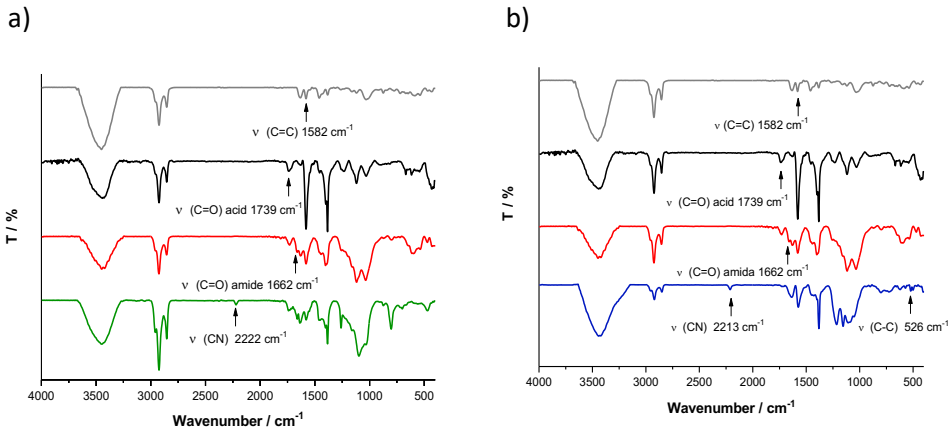

Figure 1.65. a) FTIR spectra of graphite (grey), GO (black), **GO-Im** (red) and **GO^{IL}-Cy** (green). b) FTIR spectra of graphite (grey), GO (black), **GO-Im** (red) and **GO^{IL}-CyC$_{60}$** (blue).

TGA analyses were carried out with the aim of obtaining information about the grafting density and the thermal stability of each material. Figure 1.66 shows the thermograms of the materials obtained after each reaction step in the synthesis of **GO^{IL}-Cy** and **GO^{IL}-CyC$_{60}$**. Herein, as it was expected, in the course of the reaction pathway it is observed an increase of the weight loss after each reaction step.

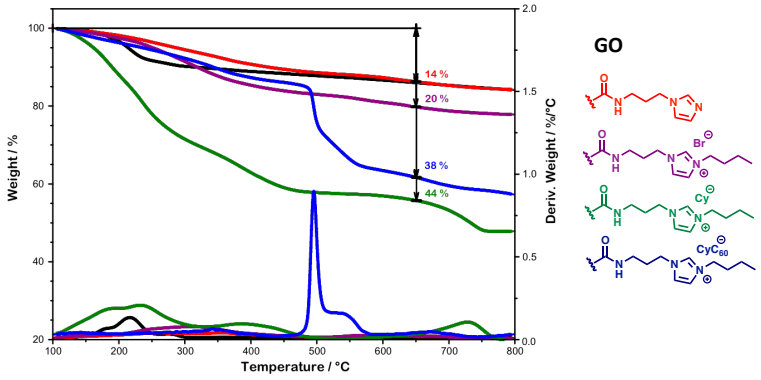

Figure 1.66. TGA and first derivative curves under inert atmosphere of GO (black), **GO-Im** (red), **GO^{IL}** (purple) and **GO^{IL}-Cy** (green) and **GO^{IL}-CyC$_{60}$** (blue).

The thermogram of the final material, **GO^{IL}-CyC$_{60}$**, revealed a weight loss of a 38 % whereas for the **GO^{IL}-Cy** it was obtained a weight loss of a 44 %. The

aforementioned differences are probably due to the different sizes of **Cy** and **CyC$_{60}$**, thus the anion exchange is less efficient for the C_{60} derivative which has a larger molecular weight.

Another interesting tool for confirming the functionalization of the carbon materials was XPS (Figure 1.67 and Figure 1.68). The survey spectrum of GO showed the characteristics peaks belonging to the C 1s and O 1s core-level signals as expected. Upon the incorporation of the 1-(3-aminopropyl) imidazole it was observed the presence of the N 1s core-level signal due to the incorporation of the imidazole moieties, and when these imidazole fragments were alkylated in the next reaction step, a significant amount of Br was detected in the GO^{IL} species. Finally, after the anion exchange of bromide by cyanines the peak of the Br 3p core-level completely vanished confirming the synthesis of our desired products.

Furthermore, the high-resolution spectrum of the N 1s core-level signal of **GO^{IL}-Cy** can be deconvoluted into two components (Figure 1.67b). The former at lowest binding energies could be assigned to the nitrile groups (C≡N) belonging to the cyanine skeleton, and the latter, at higher binding energies might be related with the quaternary ammonium of the imidazolium ions. Similar results were found for **GO^{IL}-CyC$_{60}$**, with the presence of the above-mentioned components and an extra one related with the pyrrolidinic N atoms presented in **CyC$_{60}$**. (Figure 1.68b)

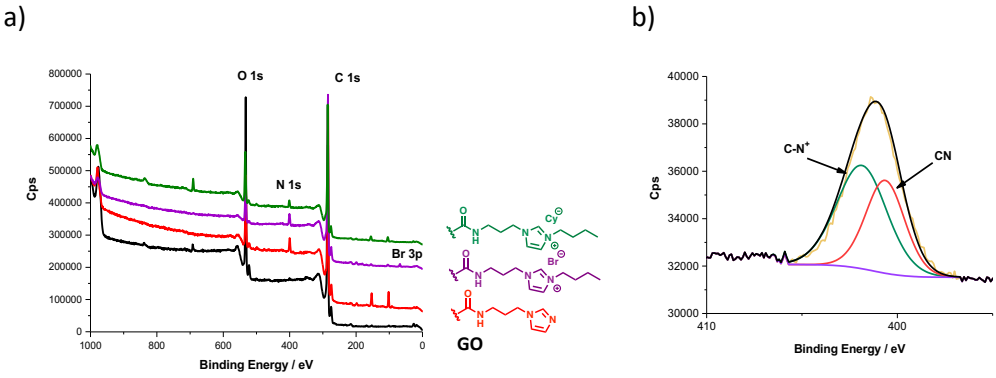

Figure 1.67. a) XPS survey spectra of GO (black), **GO-Im** (red), **GO^{IL}** (purple) and **GO^{IL}-Cy** (green). b) XPS N 1s component deconvolution of **GO^{IL}-Cy**.

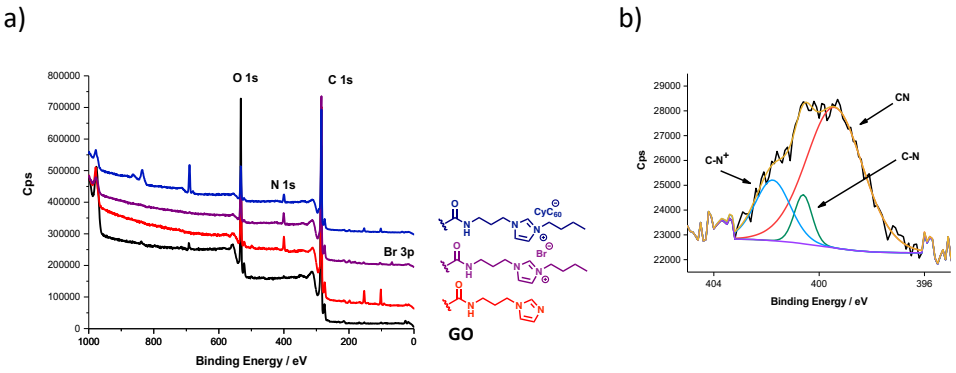

Figure 1.68. a) XPS survey spectra of GO (black), **GO-Im** (red), **GO^{IL}** (purple) and **GO^{IL}-CyC$_{60}$** (blue). b) XPS N (1s) component deconvolution of **GO^{IL}-CyC$_{60}$**.

To complete the structural characterization of the obtained materials, the morphology of the as-prepared hybrids was studied by TEM. For the two Cy-based resulting materials, the TEM images revealed the presence of graphene sheets which appeared intertwined in most of the cases (Figure 1.69a and Figure 1.69b). Most important is the fact that after the functionalization there is no evidence of aggregation processes between layers. Another interesting point, is that in the case of **GO^{IL}-CyC$_{60}$** it was possible to see spherical particles at the edges with a diameter around 1 nm (Figure 1.69c and Figure 1.69d). Some reports in the bibliography ascribe this observation to the presence of the [60]fullerene structures attached to the graphene surface, which perfectly match with our results. [170]

[170] a) J. Guan, X. Chen, T. Wei, F. Liu, S. Wang, Q.Yang, Y. Lu, S. Yang, J. *Mater. Chem. A.* **2015,** *3*, 4139. b) M. Barrejón, M. Vizuete, M. J. Gómez-Escalonilla, J. L. G. Fierro, I. Berlanga, F. Zamora, G. Abellán, P. Atienzar, J.-F. Nierengarten, H. García, F. Langa, *Chem. Commun.* **2014**, *50*, 9053.

a) b)

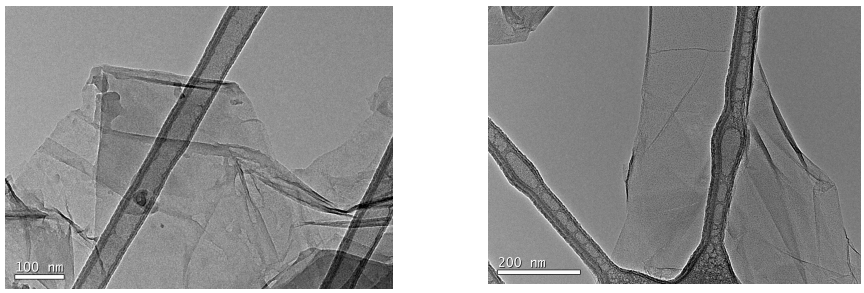

c)

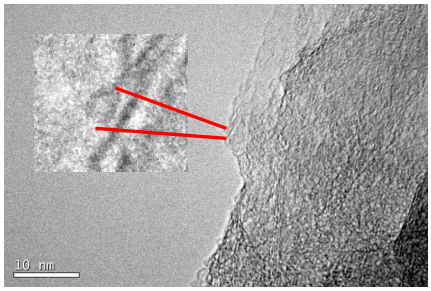

Figure 1.69. a) TEM image of **GO^{IL}-Cy**. b) and c) TEM images of **GO^{IL}-CyC$_{60}$**.

1.3.4.2. Synthesis of GR imidazolium salts and Cy hybrids

The last subsection of this chapter focuses in the introduction of imidazolium salts onto the basal plane of GR. Similarly, to the case of GO, the final goal is the anion exchange between the bromide present in the imidazolium salts by heptamethine anionic cyanines. The starting material in this case is exfoliated GR produced from graphite and using NMP as solvent (see section 1.3.1. for more details). The lack of oxygenated functional groups on the GR surface made us to change the strategy in order to incorporate the desired fragments. Instead of an amidation reaction we carried out an aryl addition, the so-called Tour reaction.[171] As stated in the background, Tour reactions involve the use of aniline derivatives in the presence of isopentyl nitrite to yield a material with phenyl units directly attached to the GR surface.

[171] J. L. Bahr, J. M. Tour, *Chem.Mater*. **2001**, *13*, 3823.

In order to apply this methodology to our materials, it was necessary to synthesize an imidazolium salt with a hanging up aniline group to be anchored to GR. Scheme 1.7 shows the synthetic route employed to obtain it and its subsequent reaction with the GR surface through Tour reaction. Finally, the bromide anions were exchanged by **Cy** or **CyC$_{60}$** resulting in the final materials **GR^{IL}-Cy** and **GR^{IL}-CyC$_{60}$**.

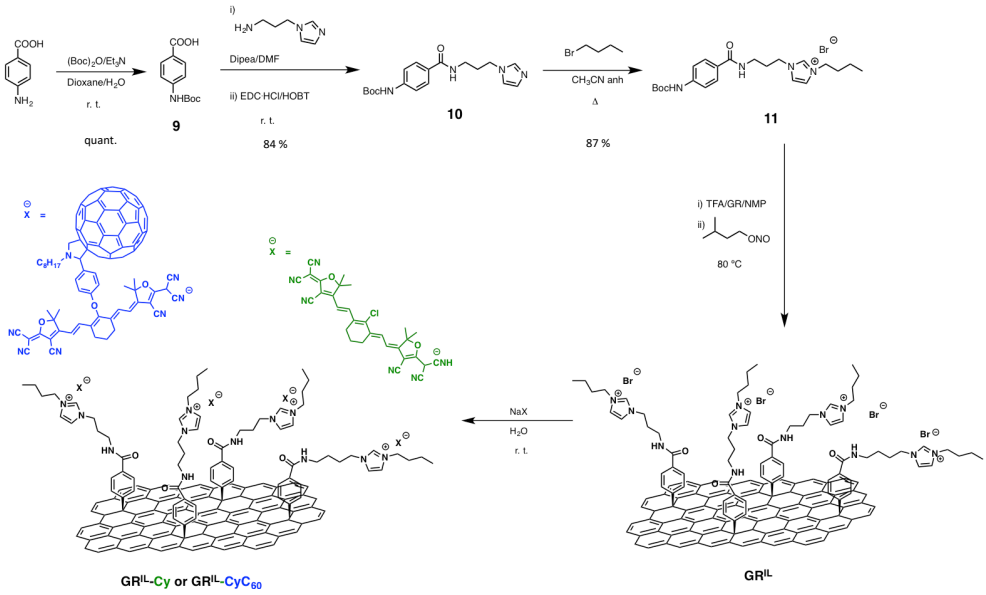

Scheme 1.7. Synthetic route employed to obtain **GR^{IL}-Cy** and **GR^{IL}-CyC$_{60}$**.

The synthetic pathway started with the treatment of 4-amino benzoic acid with di-*tert*-butyl dicarbonate and triethylamine in aqueous dioxane, resulting in the *tert*-butyloxycarbonyl (BOC)-protected intermediate **9**. The ^{1}H-NMR spectrum of **9** showed a singlet located at 1.5 ppm due to the *tert*-butyl group (Figure 1.70). Afterwards, reaction of **9** with 1-(3-aminopropyl)imidazole using typical conditions of amidation (EDC·HCl / HOBT) afforded product **10**. Therefore, new ^{1}H-NMR features were discerned at 6.88, 7.21 and 7.65 due to the imidazole and amide protons, as well as aliphatic signals at 4.0, 3.2 and 2.0-1.86 ppm due to the propyl chain. Finally, the imidazole moiety was subsequently alkylated resulting in the ionic liquid-type molecule **11**. After this reaction, new aliphatic signals were observed in the ^{1}H-NMR spectrum due to the butyl fragment incorporated in this last step of the molecular precursor

preparation. Moreover, the protons located in the imidazole ring were notably upshifted due to the formation of the imidazolium cation.

The next step was the incorporation of compound **11** onto the GR surface. For that task, a mixture formed by compound **11** and GR in NMP was stirred in acid media to allow the deprotection of the aniline group. In a second step, the *in situ* formed aniline group reacted with isopentyl nitrite generating the corresponding aryldiazonium salt. At this point, the injection of electrons from GR to the aryldiazonium salt, resulted in N_2 release and the formation of a reactive aryl radical that was attached to GR to form the GR^{IL} material. Finally, the anion exchange was carried out under the same conditions that for GO^{IL}.[169] This process resulted in two different materials, **GR^{IL}-Cy** and **GR^{IL}-CyC_{60}** which were afterwards characterized.

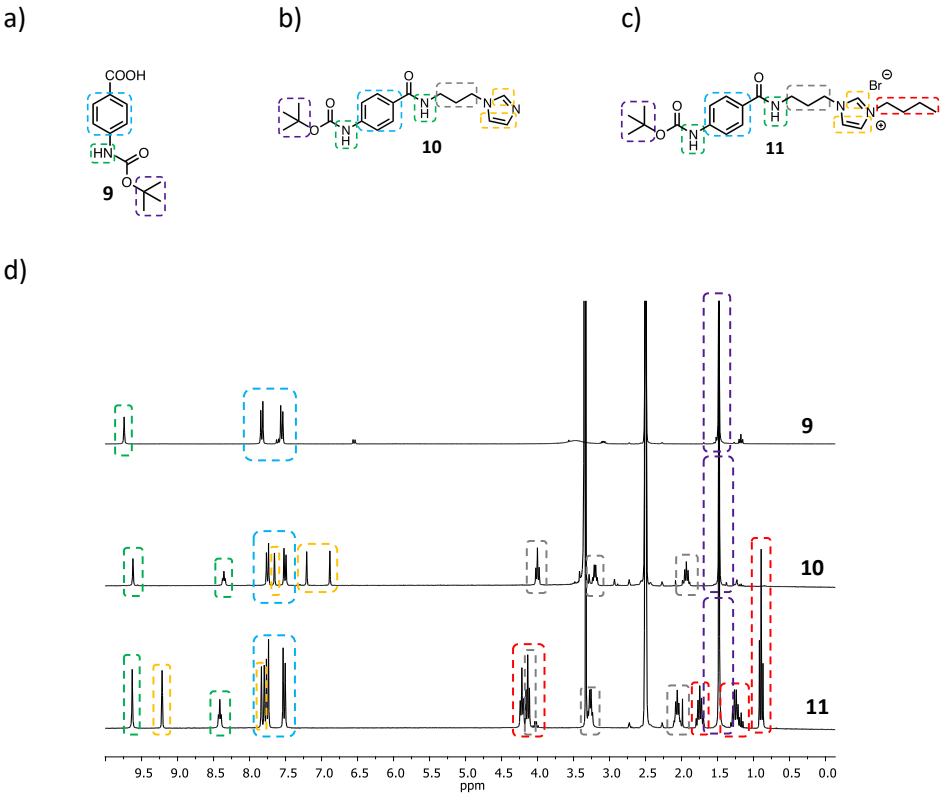

Figure 1.70. a-c) Structures of compounds **9**, **10**, and **11** with their characteristic protons labeled with colors. d) ^{1}H-NMR spectra of compounds **9** (top), **10** (middle) and **11** (bottom).

First evidences about the functionalization of GR came from TGA. In Figure 1.71 the thermogram of GR^{IL} showed a slightly more accused weight loss after the grafting of the imidazolium salt in comparison with exfoliated pristine graphene. Moreover, the anion exchange of bromide by **Cy** or **CyC_{60}** resulted in an increase of the weight loss from 16 % to 21% for both **GR^{IL}-Cy** and **GR^{IL}-CyC_{60}**.

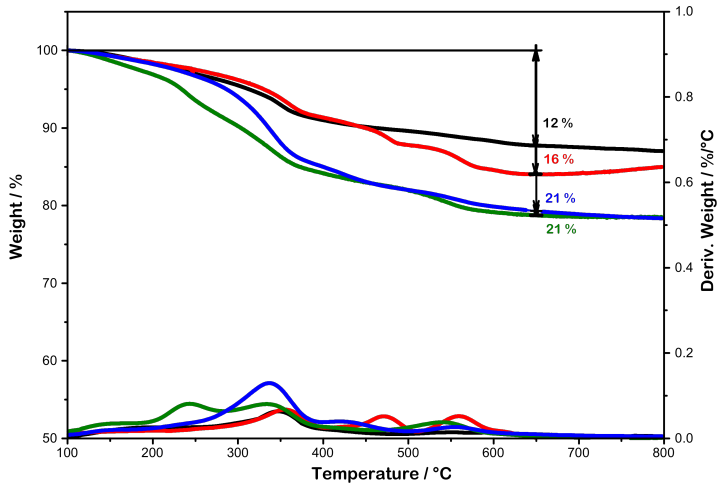

Figure 1.71. TGA and first derivative curves under inert atmosphere of GR (black), GR^{IL} (red), **GR^{IL}-Cy** (green) and **GR^{IL}-CyC_{60}** (blue).

The presence of the heptamethine cyanines was also discerned by UV-Vis-NIR and FTIR spectroscopies. Figure 1.72 shows the absorption spectra of **GR^{IL}-Cy** and **GR^{IL}-CyC_{60}** and their respective references in methanol. Both hybrids present the characteristic broad absorption in the visible region due to GR layers as well as the the distinctive absorption of the cyanines in the NIR region. The absorption maximum of **GR^{IL}-Cy** is located at 890 nm whereas the one belonging to **GR^{IL}-CyC_{60}** at 888 nm. As it happened with the supramolecular **SWCNT-CyPyr** and **GR-CyPyr** hybrids, and with those based on GO, it is also observed a slight bathochromic shift in comparison with the free molecules **Cy** and **CyC_{60}**, which have maximum absorptions centred at 887 and 886 nm, respectively.

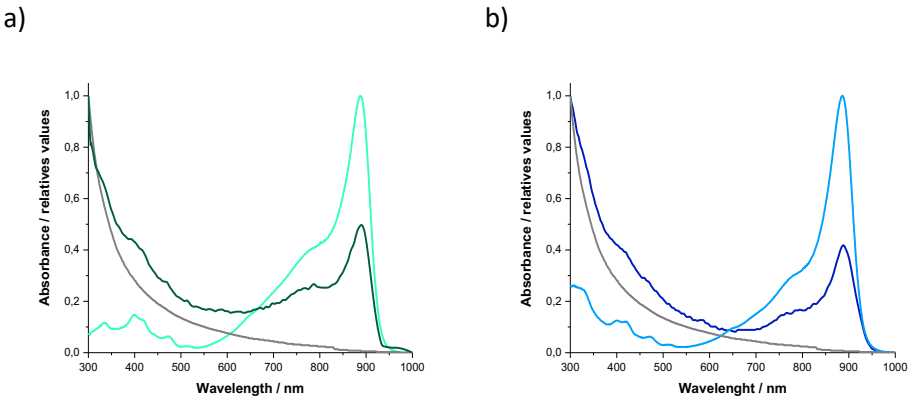

Figure 1.72. a) Absorption spectra of GR (grey), **Cy** (light green) and **GR^{IL}-Cy** (dark green) in MeOH. b) Absorption spectra of GR (grey), **CyC$_{60}$** (light blue) and **GR^{IL}-CyC$_{60}$** (dark blue) in MeOH.

As expected from FTIR, both materials (**GR^{IL}-Cy** and **GR^{IL}-CyC$_{60}$**) showed the typical graphene skeleton in-plane vibrations at 1582 cm^{-1}, the vibration corresponding to the amide bond at 1632 cm^{-1} and the vibration of the cyano groups around 2200 cm^{-1}. Moreover, for **GR^{IL}-CyC$_{60}$** was also discerned the characteristic vibrational peak of C_{60} at 527 cm^{-1}.

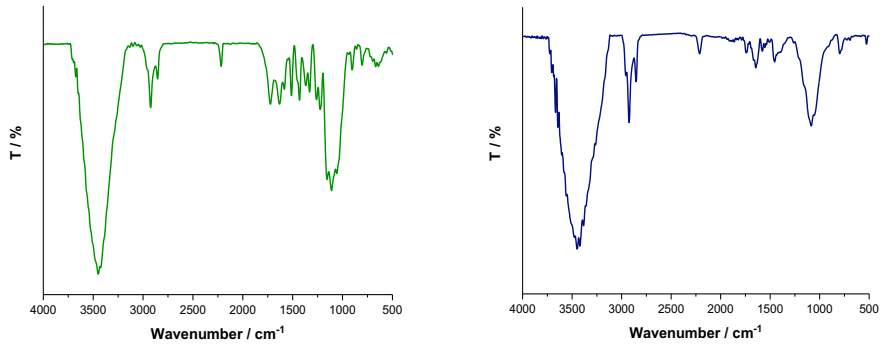

Figure 1.73. FTIR spectra of **GR^{IL}-Cy** (green) and **GR^{IL}-CyC$_{60}$** (blue).

GR^{IL}-Cy and **GR^{IL}-CyC$_{60}$** were also analysed by XPS. Survey spectra of both materials are represented in Figure 1.74 and Figure 1.75. All the spectra contain three different components, C 1s, N 1s, and O 1s, which appear at 284.6, 398.6, and 532.6 eV, respectively. The presence of the N 1s core-level

band is related with the incorporated functionalities in the GR surface. The high-resolution spectra of the N 1s peak of **GR^{IL}-Cy** and **GR^{IL}-CyC$_{60}$** was deconvoluted in three components. The component at lower binding energies was associated to the cyano groups of the heptamethine cyanines **Cy** and **CyC$_{60}$**. The component at higher binding energies is attributed to the imidazolium rings which are holding a positive charge. Finally, the central component is due to the amide bond presented in the organic moiety attached through Tour reaction.

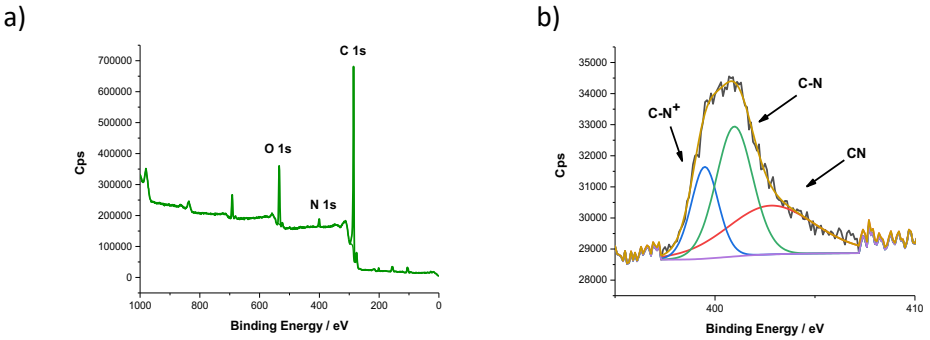

Figure 1.74. a) XPS survey spectra of **GR^{IL}-Cy** (green). b) XPS N 1s component deconvolution of **GR^{IL}-Cy.**

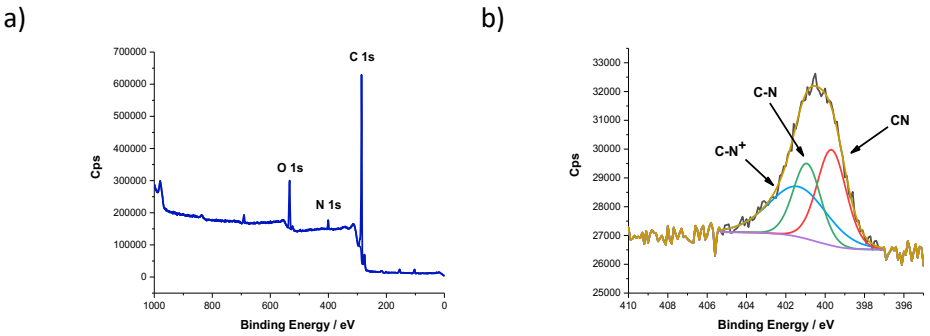

Figure 1.75. a) XPS survey spectra of **GR^{IL}-CyC$_{60}$** (blue). b) XPS N 1s component deconvolution of **GR^{IL}-CyC$_{60}$**.

The hybrids morphology was investigated by TEM and quite similar images are obtained for both **GR^{IL}-Cy** and **GR^{IL}-CyC$_{60}$**. The re-aggregation of graphene flakes after the functionalization and washing processes is prevented by the incorporation of the organic molecules, since TEM analysis revealed homogeneous nanomaterials with regular flakes that randomly stacked onto each other. The dimensions of these flakes do not seem to have decreased

during the functionalization process. In addition, TEM micrographs of **GR^{IL}-CyC$_{60}$** disclosed the presence of spheres located in the edges of the sheets whith a diameter of around 1 nm. As it was hypothesized in the case of **GO^{IL}-CyC$_{60}$**, these spherical forms could be fullerene molecules present in the GR sheets.[29]

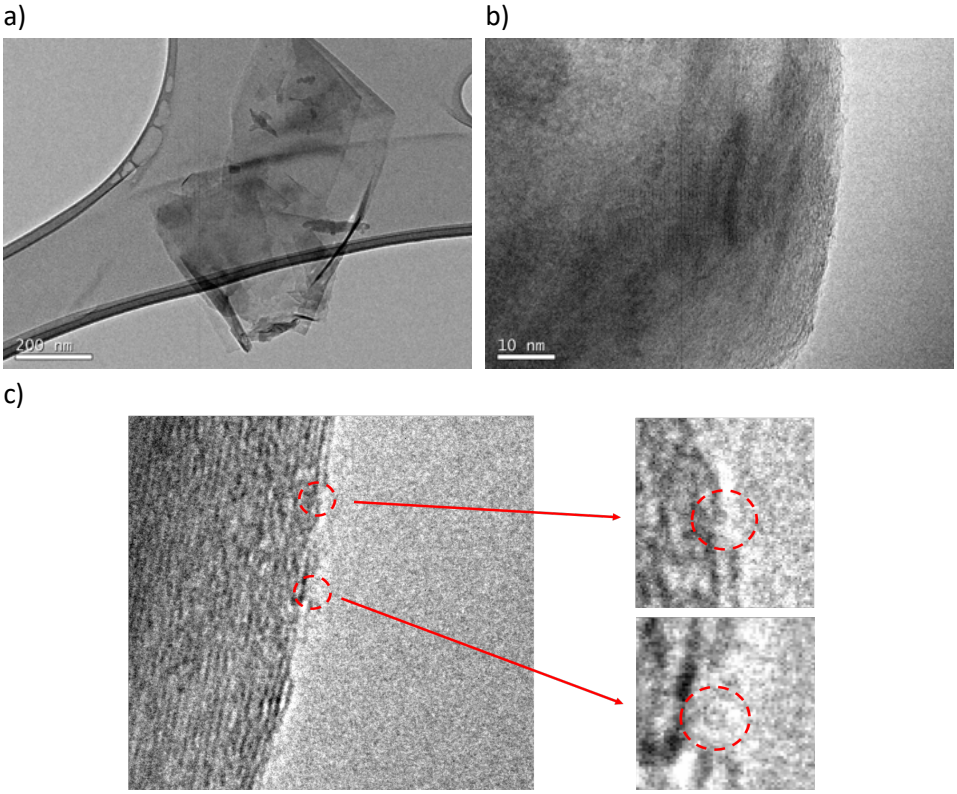

Figure 1.76. a) TEM image of **GR^{IL}-Cy**. b) TEM image of **GR^{IL}-CyC$_{60}$**. c) Amplifications of the image showed in b).

GR^{IL}-Cy and **GR^{IL}-CyC$_{60}$** nanomaterials were also studied by Raman spectroscopy. Irradiation of the samples at 532 nm allowed observing the characteristic D, G and 2D modes of graphene-based materials. The comparison of GR with **GR^{IL}** resulted in the increase of the I_D/I_G ratio after the Tour reaction as a consequence of the saturation of carbon atoms upon functionalization and their conversion from sp^2 to sp^3. The I_D/I_G ratio for GR was 0.10 and for **GR^{IL}** was 0.20. This relationship remained constant after the anion exchange (I_D/I_G = 0.19 for **GR^{IL}-Cy** and **GR^{IL}-CyC$_{60}$**) which ruled out the introduction of extra defects during this step. The electronic characteristics

of **GR^{IL}-Cy** and **GR^{IL}-CyC$_{60}$** were investigated by comparison of their G band mode with the G band of GR. The G band of GR exfoliated in NMP was observed at 1587 cm^{-1} whereas the G bands of **GR^{IL}-Cy** and **GR^{IL}-CyC$_{60}$** were discerned at 1584 and 1585 cm^{-1}, respectively. Due to the electron-donating behavior of these anionic cyanines, the observed downshift could be due to donor-acceptor interactions where the cyanines are transferring electronic density to the sp^2 skeleton of graphene. These observations go along with the UV-Vis-NIR results where small bathochromic shifts are detected for the hybrid materials.

a) b)

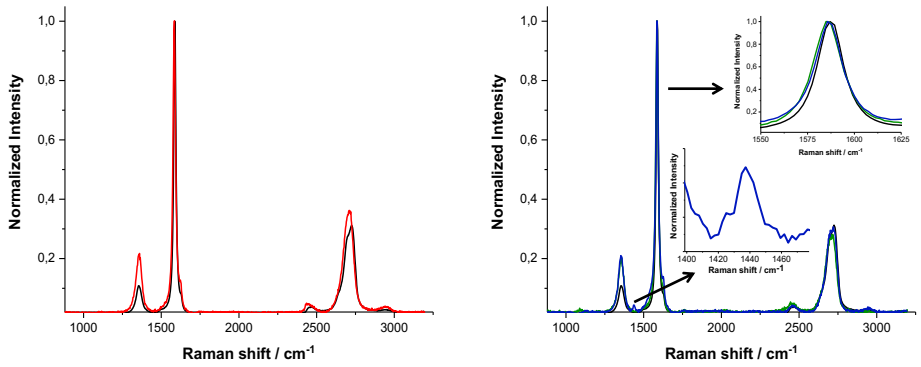

Figure 1.77. a) Raman spectra of GR (black) and GR^{IL} (red). b) Raman spectra of GR (black) and **GR^{IL}-Cy** (green) and **GR^{IL}-CyC$_{60}$** (blue). Inset: Amplification of b) figure in the G band region and amplification of the characteristic fingerprint of the C_{60} molecule at 1440 cm^{-1}.

It is noticeable that the downshift is somewhat less accused for **GR^{IL}-CyC$_{60}$**, probably due to the acceptor character of the fullerene which can withdraw electron density from the cyanine through donor-acceptor intramolecular interactions. However, additional experiments are in course to corroborate the possible charge transfer processes that could occur in these hybrids upon photoexcitation. Finally, it is important to stand out the presence of a small band in the **GR^{IL}-CyC$_{60}$** at 1440 cm^{-1} which is the characteristic fingerprint of the C_{60} molecule.[170]

1.4. EXPERIMENTAL SECTION

1.4. EXPERIMENTAL SECTION

Materials

All reagents were purchased from commercial sources and used without further purification. Solvents were dried and distilled using standard techniques.[172] Those reactions requiring an inert atmosphere were carried out using Argon as source.

The graphite used for graphene exfoliation was purchased from TIMCAL (TIMREX SFG15, ρ = 2.26 g/cc, particle size = 8.80 μm, surface area = 9.50 m^2/g, ash ≤ 0.100%, interlaminar distance = 0.3354-0.3358 nm).

Vacuum filtrations of graphene materials were carried out with polycarbonate track etched (PCTE) (pore size = 0.2 μm, Φ = 47 cm) and polytetrafluoroethylene (PTFE) (pore size = 0.2 μm, Φ = 47 cm) membranes.

General Methods

Analytical thin-layer chromatography (TLC): was performed using aluminum coated Merck Kieselgel 60 F254 plates to check the evolution of reactions. Visualization was made by UV light (λ = 254 or 365 nm).

Purification of crude reaction mixtures: was achieved by flash column chromatography or gravity-fed column chromatography using silica gel.

NMR spectra: were recorded on a Bruker DPX-300, Bruker AV-500 or Bruker AVIII-700 at 298 K, using partially deuterated solvents as internal standards. Chemical shifts (δ) are expressed in ppm and are referred to the residual peak of the solvent. Spin multiplicities are reported as singlet (s), doublet (d), triplet (t), quartet (q), multiplet (m) and broad (br), with proton-proton coupling constants (*J*) given in Hz.

FTIR spectra: were recorded on a Bruker TENSOR 27 (ATR device, 7500-370 cm^{-1}), with a resolution of 1 cm^{-1}.

---

[172] W. L. F. Armarego, C L L Chai, *Purification of Laboratory Chemicals*, Elsevier **2003**.

Mass spectra: were realized by the mass spectra services at the Universidad Complutense de Madrid and at the Universidad Autónoma de Madrid. *Electronic Impact measurements (EI)* were recorded using a HP 5989A apparatus (70 eV, 200 ºC). MALDI-TOF measurements were recorded utilizing a BRUKER-REFLEX III apparatus (matrix: dithranol, N_2 laser at 337 nm) or Brucker Ultraflex III apparatus (matrix: trans-2-[3-(4-*tert*-butylphenyl)-2-methyl-2-propenylidene]malononitrile (DCTB)).

UV-Vis-NIR spectra: were recorded with a Shimadzu Spectrophotometer UV-3600 at 298 K, with a resolution of 1 nm or with a Cary 5000 double beam spectrometer from Varian.

Fluorescence spectra: were recorded with a Fluoromax-4 spectrofluorometer (HORIBA) at 298 K or with a FluoroLog 3 spectrometer from HORIBA Yobin Yvon using a 450 W Xenon lamp and a Symphony InGaAs array in combination with an iHR320 imaging spectrometer.

Raman spectra: were recorded on a NT-MDT in Via Microscope at room temperature or with a WiTec alpha300r confocal Raman microscope using an exciting laser source of 532 or 633 nm.

Thermogravimetric analyses (TGA): were carried out with a thermobalance TA-TGA-Q-500 under N_2. The sample (≈ 0.5 mg) was introduced inside a platinum crucible and equilibrated at 90 ºC followed by a 10 ºC/min ramp between 90 and 1000 ºC.

XPS analysis: were performed on a SPECS GmbH (PHOIBOS 150 9MCD) spectrometer operating in the constant analyzer energy mode. A non monochromatic aluminium X-ray source (1486.61 eV) was used with a power of 200 W and voltage of 12 kV. Pass energies of 75 and 25 eV were used for acquiring both survey and high resolution spectra, respectively. Survey data were acquired from kinetic energies of 1487-400 eV with an energy step of 1 eV and 100 ms dwell time per point. SpecsLab Version 2.48 software was used for spectrometer control and data handling. The semi-quantitative analysis were performed from the C 1s (284.3 eV) signal. The samples were introduced as pellets of 8 mm diameter.

Transmission electron microscopy (TEM): was performed on a JEOL JEM 2100, with an acceleration voltage of 200 kV equipped with a camera CCD ORIUS SC1000 (model 832) and the microanalysis were performed by XEDS

(OXFORD INCA). The samples were dispersed in NMP, water or methanol and dropped onto a holey carbon copper grid (200 mesh), the solvent was removed in a vacuum oven for 48 hours.

Electrochemistry: A glassy carbon working electrode, a Pt-wire as counter electrode, and an Ag-wire as quasi-reference electrode were used. The redox potentials were determined in methanol *vs*. the Fc/Fc^+ redox couple, which served as an internal standard. As supporting electrolyte 0.1 M $TBAClO_4$ was added. Spectroelectrochemistry measurements were done in a home-made three neck glass cell with a three-electrode setup comprised of a platinum mesh as working electrode, an Ag-wire as pseudo reference electrode, and a platinum wire as counter electrode. To control the applied potentials a Metrohm PGStat 101 was used.

Femtosecond transient absorption spectroscopy: A transient absorption pump probe system HELIOS from Ultrafast Systems was employed. To generate laser pulses with a pulse width of 150 fs and a wavelength of 775 nm a CPA-2110 titanium:sapphire laser system from Clark-MXR Inc. was utilized. Global and target analysis was performed with the open-source software package Glotaran, a free graphical user interface to the R package TIMP. The wavelength dependent character (dispersion) of the instrument response fuction (IRF) was modeled and taken into account.[173,174]

1.4.1. Synthesis of cyanine dyes and molecular precursors

(E)-2-chloro-3-(hydroxymethylene)cyclohex-1-ene-1-carbaldehyde (1)[160]

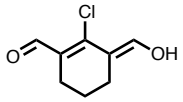

To a solution of dimethylformamide (6.4 mL, 0.08 mol) at 0 ºC under argon atmosphere, $POCl_3$ (7.5 mL, 0.08 mol) was added dropwise. Afterwards, cyclohexanone (2.13 mL, 0.02 mol) was added slowly and the resulting mixture was allowed to stir for 30 min. at 0 ºC. After 30 min. the reaction

[173] J. J. Snellenburg, S. Laptenok, R. Seger, K. M. Mullen; van Stokkum, I H M, *J. Stat. Soft*. **2012**, 49, 1.
[174] K. M. Mullen, I. H. M. van Stokkum, *J. Stat. Soft*. **2007**, *18*, 1.

mixture was heated at 80 ºC for 3 h. Finally, the mixture was cooled to r.t. and poured over an ice/water bath. This step yields a precipitate that was filtered and washed with cold water (88 % yield).

^{1}H-NMR (DMSO-d_6, 300 MHz), δ: 10.88 (s, 1H), 8.88 (s, 1H), 3.34 (s, 1H), 2.35 (t, J = 6 Hz, 4H), 1.61-1.53 (m, 2H).

2-(3-Cyano-4,5,5-trimethylfuran-2(5H)-ylidene)malononitrile (2)[161]

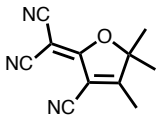

A solution of 3-hydroxy-3-methyl-2-butanone (1.06 mL, 9.38 mmol), malononitrile (1.3 g, 19.70 mmol) and sodium (cat.) in absolute ethanol was irradiated in a microwave reactor at 90 ºC for 20 min. The resulting mixture was precipitated in absolute ethanol at 0 ºC, filtered and washed with cold ethanol several times. A pale yellow solid was obtained (75 % yield).

^{1}H-NMR ($CDCl_3$, 300 MHz), δ: 2.37 (s, 6H), 1.63 (s, 3H).

Cyanine Dye 3[159]

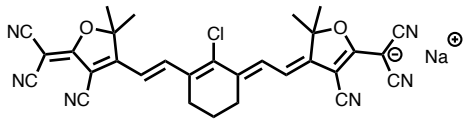

Chlorobisaldehyde **1** (130 mg, 0.75 mmol) and tricyanofurane **2** (300 mg, 1.5 mmol) were dissolved in 20 mL of absolute ethanol under argon atmosphere. Once they were dissolved, sodium acetate (0.162, 1.57 mmol) was added and the solution was heated to 80 ºC for 5 h. Afterwards, the mixture was cooled to r.t. and the solvent was removed under reduced pressure. The solid was purified by silica gel column chromatography, using DCM/MeOH (9/1) as eluent (65 % yield).

^{1}H-NMR (DMSO-d_6, 300 MHz), δ: 8.20 (d, J = 14 Hz, 2H), 6.08 (d, J = 14 Hz, 2H), 2.60-2.56 (m, 4H), 1.78-1.73 (m, 2H), 1.59 (s, 12H).

Cyanine Dye 4[159]

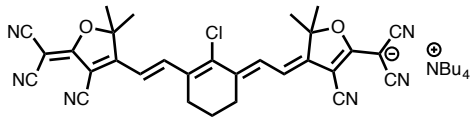

Cyanine **3** was dissolved in DCM and tetrabutylammonium iodide added (255 mg, 0.69 mmol). The solution was stirred at room temperature for 1 h. Subsequently, it was washed with water (3 x 30 ml) and dried over $MgSO_4$. The solvent was evaporated to afford a dark green solid (quantitative yield).

^{1}H-NMR (DMSO-d_6, 300 MHz), δ: 8.20 (d, J = 14 Hz, 2H), 6.08 (d, J = 14 Hz, 2H), 3.19-3.13 (m, 8H), 2.60-2.56 (m, 4H), 1.78-1.73 (m, 2H), 1.58 (s, 12H), 1.58-1.51 (m, 8H), 1.33-1.24 (m, 8H), 0.93 (t, J = 7 Hz, 12H).

Cyanine Dye 5[159]

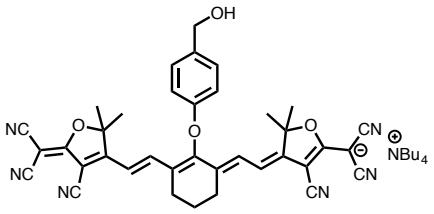

4-Hydroxybenzyl alcohol (48 mg, 0.32 mmol) was dissolved in 9 mL of dry DMF under argon atmosphere, then sodium hydride 60 % (15 mg, 0.39 mmol) was added and the solution was stirred at r.t. for 30 min. After 30 min., **4** (250 mg, 0.32 mmol) was added dropwise, dissolved in 3 mL of dry DMF. This solution was allowed to stir at r.t. for 12 h. under argon atmosphere and then was poured into a water/ice bath with hydrochloric acid (0.2 mL). The resulting green solid was filtered, redissolved in DCM, and washed with water and Na_2CO_3. The organic layer was dried with $MgSO_4$, and precipitated in pentane, to afford **5** as a green solid (70 % yield).

^{1}H-NMR (DMSO-d_6, 300 MHz), δ: 7.67 (d, J = 14 Hz, 2H), 7.22 (d, J = 8 Hz, 2H), 6.91 (d, J = 8 Hz, 2H), 5.96 (d, J = 14 Hz, 2H), 4.39 (s, 2H), 3.18-3.13 (m, 8H), 2.59-2.56 (m, 4H), 1.88-1.83 (m, 2H), 1.59-1.54 (m, 8H), 1.38 (s, 12H), 1.34-1.24 (m, 8H), 0.93 (t, J = 7 Hz, 12H).

Cyanine-Pyrene Dye 6 (CyPyr)

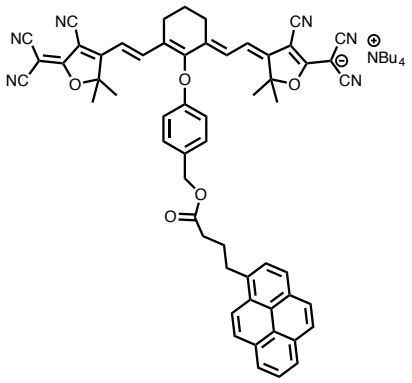

1-Pyrenebutyric acid (35 mg, 0.12 mmol), EDC·HCl (23 mg, 0.12 mmol) and DMAP (15 mg, 0.12 mmol) were added to 10 mL of DCM. The mixture was stirred for 20 min. in an ice-water bath and under Ar atmosphere. Then, cyanine **5** (69 mg, 0.08 mmol) was added dropwise, and the mixture was stirred for another 30 min. The cooling bath was removed, and the mixture was stirred at room temperature for 24 h. The reaction mixture was washed with deionized water (3 x 30 mL). The organic layer was dried over $MgSO_4$, filtered, and evaporated. The residue was subjected to column chromatography in DCM/MeOH (9/1) for further purification (66 % yield).

^{1}H-NMR (DMSO-d_6, 300 MHz), δ: 8.40–7.91 (m, 9H), 7.61 (d, J = 14.0 Hz, 2H), 7.32 (d, J = 8.1 Hz, 2H), 6.95 (d, J = 8.1 Hz, 2H), 5.93 (d, J = 14.0 Hz, 2H), 5.02 (s, 2H), 3.21–3.09 (m, 8H), 2.63–2.42 (m, 2H), 2.04–1.97 (m, 6H), 1.88–1.80 (m, 2H), 1.61–1.51 (m, 8H), 1.31 (s, 12H), 1.26–1.23 (m, 8H), 1.17 (t, J = 7.0 Hz, 2H), 0.94 (t, J = 7.0 Hz, 12H).

^{13}C-NMR (THF-d_8, 75 MHz), δ: 173.41, 137.21, 132.63, 132.17, 131.46, 131.25, 131.18, 129.86, 128.50, 128.42, 128.28, 127.58, 126.78, 126.15, 126.07, 125.90, 125.80, 125.71, 124.44, 116.03, 95.22, 66.23, 59.45, 34.41, 33.59, 28.09, 27.19, 20.74, 14.14.

UV-Vis-NIR (*o*-DCB), λ_{max} (nm): 906 (ε = 254000 L·mol^{-1}·cm^{-1}), 346, 331.

FTIR (KBr), ν (cm^{-1}): 2928, 2208, 1730, 1625, 1504, 1438, 1335, 1254, 1214, 1080, 1038, 1000, 903, 840, 729, 648.

MS (ESI) (*m/z*): calculated for $C_{57}H_{43}N_6O_5^-$ = 891.3300; found = $C_{57}H_{43}N_6O_5^-$ = 891.3297.

Cyanine Dye 7

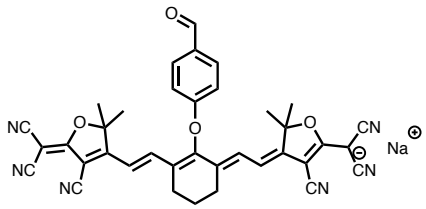

4-(5,5-Dimethyl-1,3-dioxan-2-yl)phenol (73 mg, 0.4 mmol) was dissolved in 5 mL of dry DMF under argon atmosphere, then sodium hydride 95 % (12 mg, 0.48 mmol) was added and the solution was stirred at r.t. for 30 min. After 30 min., it was added dropwise cyanine **3** (150 mg, 0.27 mmol) dissolved in 3 mL of dry DMF. This solution was allowed to stir at r.t. for 12 h. under argon atmosphere and then was poured into a water/ice bath with hydrochloric acid (4 mL). The resulting green solid was filtered, redissolved in ethyl acetate, and washed with water and Na_2CO_3. The organic layer was dried with $MgSO_4$, and precipitated in pentane, to afford **7** as a green solid (76 % yield).

^{1}H-NMR (DMSO-d_6, 300 MHz), δ: 9.87 (s, 1H), 7.88 (d, J = 8.1 Hz, 2H), 7.64 (d, J = 14.0 Hz, 2H), 7.15 (d, J = 8.1 Hz, 2H), 5.99 (d, J = 14.0 Hz, 1H), 2.65-2.55 (m, 4H), 1.94-1.82 (m, 2H), 1.39 (s, 12H).

^{13}C-NMR (DMSO-d_6, 75 MHz), δ: = 191.4 176.3, 166.5, 163.3, 159.3, 136.4, 132.0, 130.7, 122.7, 115.5, 115.3, 114.4, 114.0, 106.3, 95.2, 82.6, 57.6, 57.4, 44.8, 26.1, 23.8, 20.6.

UV-Vis-NIR (MeOH), λ_{max} (nm): 887 nm (ε= 300000 L·mol^{-1}·cm^{-1}).

FTIR (KBr), ν (cm^{-1}): 2209, 1688, 1086, 1045.

MS (ESI) (*m/z*): calculated for $C_{37}H_{27}N_6O_4^-$ = 619.2; found = $C_{37}H_{27}N_6O_4^-$ = 619.0.

Cyanine-C_{60} Dye 8 (CyC_{60})

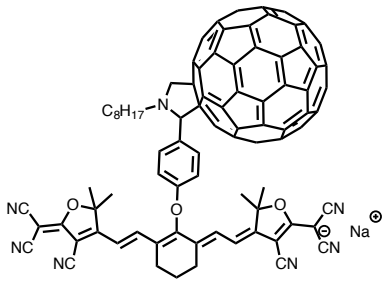

To a solution of C_{60} (419 mg, 0.58 mmol) in 50 mL of chlorobenzene, *N*-octylglycine (72 mg, 0.39 mmol) and cyanine **7** (120 mg, 0.19 mmol) was added. The solution was refluxed for 5 h. Then the solvent was evaporated, and the solid was purificated by column chromatography on silica gel, initially with toluene to remove the unreacted C_{60} and afterwards with DCM/MeOH (9/1). (22 % yield).

^{1}H-NMR (DMSO-d_6, 300 MHz), δ: 7.76-7.60 (m, 4H), 7.00-6.93 (m, 2H), 5.91 (d, J = 15 Hz, 2H), 5.12-5.07 (m, 2H), 4.12 (d, J = 9 Hz, 1H), 2.65-2.55 (m, 4H), 1.94-1.82 (m, 2H), 1.39 (s, 12H).

^{13}C-NMR (DMSO-d_6, 75 MHz), δ: 175.9, 166.4, 160.7, 158.9, 156.8, 154.2, 153.6, 147.6, 147.5, 147.3, 147.3, 147.2, 146.9, 146.9, 146.8, 146.8, 146.7, 146.6, 146.5, 146.4, 146.3, 146.1, 146.0, 145.9, 145.7, 145.6, 145.5, 145.5, 145.4, 145.3, 145.2, 145.0, 144.8, 144.6, 144.4, 143.9, 143.8, 143.3, 143.3, 143.3, 142.9, 142.8, 142.7, 142.4, 142.3, 142.1, 142.0, 141.9, 141.8, 141.5, 141.4, 141.2, 140.8, 140.3, 140.3, 140.3, 140.2, 140.2, 139.4, 137.1, 135.9, 135.5, 135.4, 130.2, 122.8, 116.1, 116.1, 116.0, 115.2, 115.1, 115.1, 114.4, 114.4, 114.3, 113.5, 105.9, 94.8, 80.5, 76.6, 68.5, 65.8, 52.0, 45.1, 31.3, 28.9, 28.7, 27.5, 27.0, 26.3, 26.1, 23.7, 22.1, 20.6, 14.0.

UV-Vis-NIR (MeOH), λ_{max} (nm): 886 nm (ε= 270.000·L·mol^{-1}·cm^{-1}), 421, 330.

FTIR (KBr), ν (cm^{-1}): 2213, 1086, 1045, 526.

HRMS (ESI) (*m/z*): calculated for $C_{106}H_{46}N_7O_3^-$ = 891.3300; found = $C_{106}H_{46}N_7O_3^-$ = 891.3297.

4-(*tert*-Butoxycarbonyl)amino)benzoic acid (9)[175]

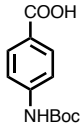

To a round bottom flask was added 4-aminobenzoic acid (0.75 g, 5.47 mmol) with dioxane (37.5 mL) and water (12.5 mL). It was stirred at room temperature for 15 min. Afterwards, triethylamine (1.5 mL, 8.15 mmol) was added and the solution stirred for another 15 min. Finally di-*tert*-butyl dicarbonate (1.78 g, 8.15 mmol) was added and the final solution stirred at room temperature for 24 h. The day after, dioxane was removed under reduced pressure and the product was precipitated by adding a few drops of HCl solution (1 N). The solid was filtered and washed several times with water resulting in a white solid (quantitative yield).

^{1}H-NMR (DMSO-d_6, 300 MHz), δ (ppm): 9.74 (s, 1H), 7.83 (d, J = 8.7 Hz), 7.55 (d, J = 8.7 Hz), 1.48 (s, 9H).

***tert*-Butyl(4-((3-(1H-imidazol-1-yl)propyl)carbamoyl)phenyl)carbamate (10)**

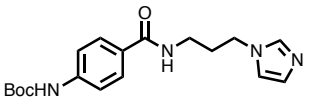

A mixture of compound **9** (0.3 g, 1.26 mmol), 1-(3-aminopropyl) imidazole (0.24 mL, 1.9 mmol) and *N*, *N*-diisopropylethylamine (0.34 ml, 1.9 mmol) was dissolved in dry DMF (10 ml) and under Ar atmosphere. The solution was stirred at room temperature for 30 min. and afterwards were added *N*-(3-dimethylaminopropyl)-*N*′-ethylcarbodiimide hydrochloride (0.362 g, 1.9 mmol) and 1-hydroxybenzotriazole hydrate (0.256 g, 1.9 mmol) and the stirring was maintained at room temperature for 48 h. Ethyl acetate (20 mL) was added to the crude of reaction and it was washed with water several times. Finally, the organic solution was dried over $MgSO_4$ and the solvent removed under reduced pressure giving rise to a white solid (84% yield).

[175] F. Mu, S. L. Coffing, D. J. Riese, R. L. Geahlen, P. Verdier-Pinard, T. E. Hamel, J. Johnson, M. Cushman, *J. Med. Chem.* **2001**, *44*, 441.

^{1}H-NMR (DMSO-d_6, 300 MHz), δ: 9.62 (s, 1H), 8.36 (t, J = 5.5 Hz, 1H), 7.75 (d, J = 8.7 Hz, 2H), 7.6 (s, 1H), 7.51 (d, J = 8.7 Hz, 2H), 7.21 (s, 1H), 6.88 (s, 1H), 4.00 (t, J = 6.9 Hz, 2H), 3.20 (dd, J = 12.3, 6.4 Hz, 2H), 2.00-1.86 (m, 2H), 1.48 (s, 9H).

^{13}C-NMR (DMSO-d_6, 75 MHz), δ: 165.91, 152.59, 142.18, 137.31, 128.33, 128.00, 127.82, 119.33, 117.06, 79.43, 43.81, 36.42, 30.84, 28.06.

FTIR (KBr), ν (cm^{-1}): 2976, 2933, 1521, 1635, 1605, 1515, 1315,1238, 1158.

HRMS (ESI) (m/z): calculated for $C_{18}H_{24}N_4O_3$ = 344.1813; found = $C_{18}H_{24}N_4O_3$ = 344.1836.

1-(3-(4-((*tert*-Butoxycarbonyl)amino)benzamido)propyl)-3-butyl-1H-imidazol-3-ium bromide (11)

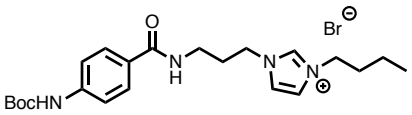

Compound **10** (0.150 g, 0,44 mmol) was suspended in dry acetonitrile (60 mL) and 1-bromobutane (0.47 mL, 4.36 mmol) was added. The reaction mixture was stirred at reflux for 48 h. and the solvent was removed in vacuum to afford a pale-yellow oil. The resulting oil was redissolved in acetonitrile and was added over a solution of ethyl acetate at -30 ºC, then was cooled at this temperature for 6 h. Finally, the resulting white solid was filtered and was dried under vacuum (87% yield).

^{1}H-NMR (DMSO-d_6, 300 MHz), δ: 9.62 (s, 1H), 9.23 (s, 1H), 8.43 (t, *J* = 5.6 Hz, 1H), 7.84 (t, *J* = 1.7 Hz, 1H), 7.80 (t, *J* = 1.7 Hz, 1H), 7.75 (d, *J* = 8.7 Hz, 2H), 7.52 (d, *J* = 8.7 Hz, 2H), 4.22 (t, *J* = 7.2, 2H), 4.14 (t, *J* = 7.2, 2H), 3.27 (dd, *J* = 12.1, 6.1 Hz, 3H), 2.06 (m, 2H), 1.85-1.65 (m, 2H), 1.34-1.16 (m, 2H), 0.89 (t, *J* = 7.3 Hz, 3H).

^{13}C-NMR (DMSO-d_6, 75 MHz), δ: = 165.96, 152.58, 142.28, 136.20, 128.05, 127.52, 122.47, 122.37, 117.02, 79.45, 48.55, 46.96, 35.90, 31.22, 29.57, 28.05, 18.77, 13.26.

FTIR (KBr), ν (cm^{-1}): 2963, 2935, 1721, 1636, 1517, 1314, 1237, 1159.

HRMS (ESI) (*m/z*): calculated for $C_{22}H_{33}N_4O_3^+$ = 401.2556; found = $C_{22}H_{33}N_4O_3^+$ = 401.2566.

1.4.2. Synthesis and preparation of nanocarbon hybrids

1.4.2.1. Reference SWCNT and GR materials

For the preparation of SWCNT and GR dispersions, pristine graphite or SWCNT were added to either methanol, anhydrous *o*-DCB or NMP and dispersed in a sonication bath for 10 min. (sweep mode, 37 kHz, 330 W). After sonication, the resulting dispersions were centrifuged, SWCNT at 5kG for 10 min. and GR at 2krpm for 5 min., the supernatant was separated from the precipitate and kept in solution for further use.

1.4.2.2. Supramolecular complexes of GR and SWCNT with CyPyr

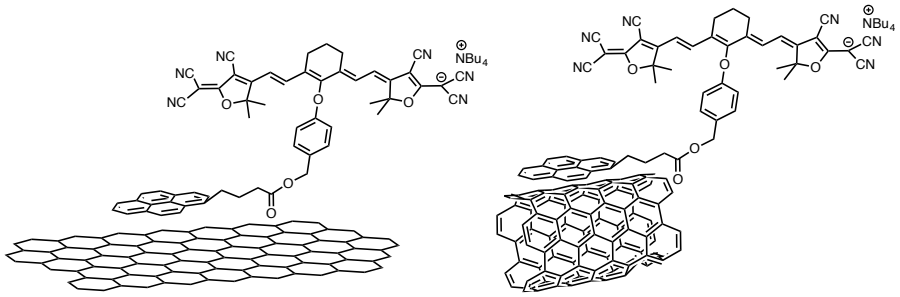

SWCNT-CyPyr and **GR-CyPyr** were produced via similar procedures. A solution of **CyPyr** (**6**) was prepared, and pristine SWCNT or graphite was added. The resulting mixtures were dispersed in an ultrasonication bath. Hybrid formation could be done either stepwise, where SWCNT or graphite flakes were added in small portions to the solution of **CyPyr** with intermediate ultrasonication steps until no free **CyPyr** was in solution, or by the addition of an excess of **CyPyr** to SWCNT or GR dispersions and then only one sonication step. In the latter case, a filtration step was added, whereas for the first option, the samples were centrifuged in the last step for the removal of non-exfoliated graphite flakes or bundled of SWCNT.

SWCNT-CyPyr

FTIR (KBr), ν (cm^{-1}): 2924, 2214, 1736, 1635, 1575, 1456, 1401, 1055.

TGA (N_2 atmosphere): weight loss and temperature desorption (organic anchoring groups): 11.52 %, 650 ºC.

XPS: % atomic: C (284.6 eV) = 93.14, N (398.6 eV) = 1.15, O (532.6 eV) = 5.11

GR-CyPyr

FTIR (KBr), ν (cm^{-1}): 2934, 2214, 1736, 1628, 1584, 1404, 1384, 1117, 1050, 712, 623.

TGA (N_2 atmosphere): weight loss and temperature desorption (organic anchoring groups): 14.05 %, 650 ºC.

XPS: % atomic: C (284.6 eV) = 94.76, N (398.6 eV) = 1.09, O (532.6 eV) = 4.14.

1.4.2.3. Synthesis of GO imidazolium salts and cyanine dyes hybrids

GO obtained by the Staundenmaier method[152]

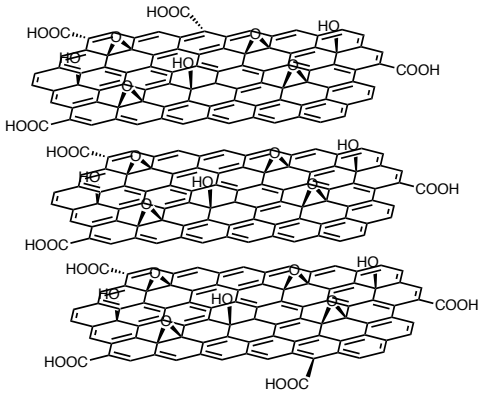

5 g of graphite were mixed with concentrated nitric (45 mL) and sulfuric (87.5 mL) acids in a three-neck reaction flask. The flask was placed in an ice bath, and then potassium chlorate (55 g) was added slowly over 1 h. to avoid any

sudden increase of the temperature. Upon completion of the reaction, the mixture was added to excess water, washed with a 5 % solution of HCl, and then repeatedly washed with water until the pH of the filtrate was neutral. Afterwards the product was dried in a vacuum oven at 70 ºC for 72 h (5.84 g).

FTIR (KBr), ν (cm^{-1}): 1739 (C=O stretching mode) and 1234 (C-O stretching mode) cm^{-1}.

TGA (N_2 atmosphere): weight loss and temperature desorption (organic anchoring groups): 14.68 %, 700 °C.

Highly functionalized GO (GO_O)

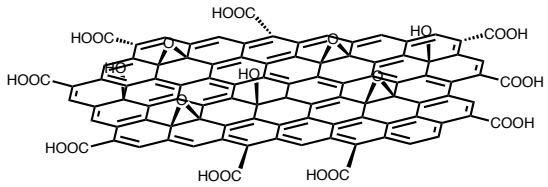

The GO obtained by the Staundenmaier method (1.5 g) was suspended in H_2O (300 mL) and was sonicated for 1 h. The dispersion was centrifuged at 500 rpm for 45 min. and the supernatant was filtered over a 0.2-µm pore size polycarbonate membrane. Finally, the collected solid was dried under vacuum at 70 ºC for 72 h. Afterwards it was stored until the next use.

FTIR (KBr), ν (cm^{-1}): 1739 (C=O stretching mode) and 1234 (C-O stretching mode) cm^{-1}.

TGA (N_2 atmosphere): weight loss and temperature desorption (organic anchoring groups): 17.35 %, 700 °C.

XPS: % atomic: C (284.4 eV) = 78.31, O (532.3 eV) = 21.1.

Quantification of carboxylic acids in GO[155]

In a polyethylene bottle with 200 mg of GO_O it were added 25 ml of a solution containing NaCl 0.1 M (supporting electrolyte) and 0.1mM oxalic acid in deonized water, acidified to pH = 3 with HCl (conc). The bottle was sealed, sonicated for 5 min. and stirred at r.t. for 48 h. The suspension was filtered in PCTE membrane and the resulting solution was employed for titration

experiments. The carboxylic acid groups were determined by neutralization with aqueous sodium hydroxide (0.08 M). The number of μmoles of NaOH was calculated based on the change in the pH value and the volume of the sample. A value of 2.2 μmol of COOH/ g was obtained after repeating the titration three times.

The $Na_2C_2O_4$/NaCl and NaOH solutions were prepared using deionized water which was previously boiled for 20 min. in order to remove CO_2 from the water.

GO-Imidazole (GO-Im)[169]

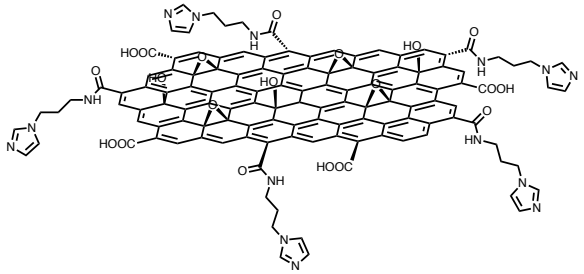

The highly functionalized GO (GO_O) (60 mg) was stirred in 40 mL of thionyl chloride at 70 °C under argon atmosphere for 24 h. in order to form the corresponding acyl chlorides. Once evaporated the thionyl chloride, 1-(3-aminopropyl) imidazole (40 mL) was added and the temperature was increased to 120 ºC and the reaction kept under argon atmosphere for 24 h. in order to complete the amidation reaction. After this period of time, the dispersion was cooled down to room temperature and filtered over a 0.2-μm poly(tetrafluoroethylene) (PTFE) membrane. Further washing was carried out with THF, HCl 5% (v/v), $NaHCO_3$ and finally with deionized water until the pH was neutral (45 mg).

FTIR (KBr), ν (cm^{-1}): 1739 (C=O), 1662 (C=O) and 1234 (C-O).

TGA (N_2 atmosphere): weight loss and temperature desorption (organic anchoring groups): 14.72%, 700 °C.

XPS: % atomic: C (281.5 eV) = 84.7, O (532.0 eV) = 11.6, N (400 eV) = 4.7.

GO bromide imidazolium salt (GO^{IL})

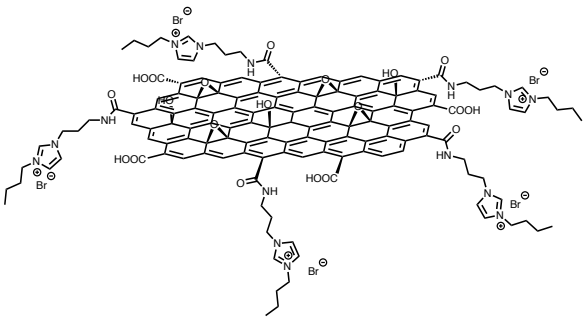

GO-Im (45 mg) was dispersed in DMF (20 mL) and reacted with 1-bromobutane (20 mL) at 90 ºC under argon atmosphere for 24 h. Afterwards, the dispersion was cooled down to room temperature and filtered over a 0.2-μm poly(tetrafluoroethylene) (PTFE) membrane and further washed with THF (1 L) until the collected solution was colorless (27 mg).

TGA (N_2 atmosphere): weight loss and temperature desorption (organic anchoring groups): 21.27 %, 700 °C.

XPS: % atomic: C (284.6 eV) = 88.6, O (532.6 eV) = 7.4, N (400.6 eV) = 3.5, Br (67.6 eV) = 1.1.

GO cyanine imidazolium salts

GO^{IL} (5 mg) was dispersed in deionized water (5 mL) and sonicated for 1 h. On the other hand, cianine **3** or **8** (5 mg) was dispersed also in deionized water (5 mL) and sonicated for 1 h. Afterwards, both dispersions were mixed in a round bottom flask and the resulting dispersion was stirred at room temperature for 72 h. Finally, the mixture was filtered over a 0.2 μm pore size polycarbonate membrane and intensively washed with water and methanol until the collected solution was colorless, obtained mass: **GO^{IL}-Cy** 4.6 mg, **GO^{IL}-CyC_{60}** 4.8 mg.

GO^{IL}-Cy

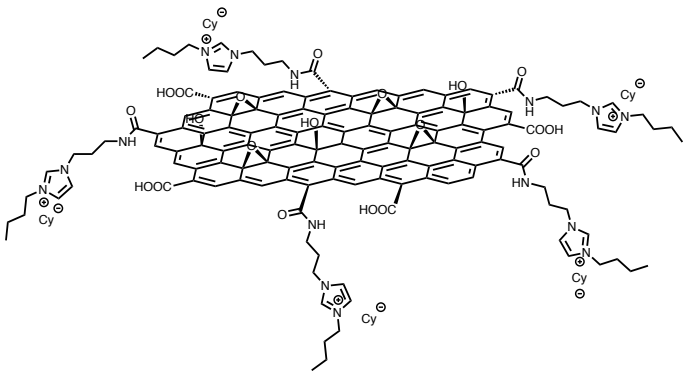

FTIR (KBr), ν (cm^{-1}): 2222 (C≡N), 1739 (C=O,), 1662 (C=O,) and 1234 (C–O).

TGA (N_2 atmosphere): weight loss and temperature desorption (organic anchoring groups): 46.80 %, 700 °C.

XPS: % atomic: C (285.6 eV) = 82.5, O (533.6 eV) = 14.1, N (400.6 eV) = 3.0, Cl (197.6 eV) = 0.4.

UV-Vis-NIR (MeOH), λ_{max} (nm): 890.

GO^{IL}-CyC_{60}

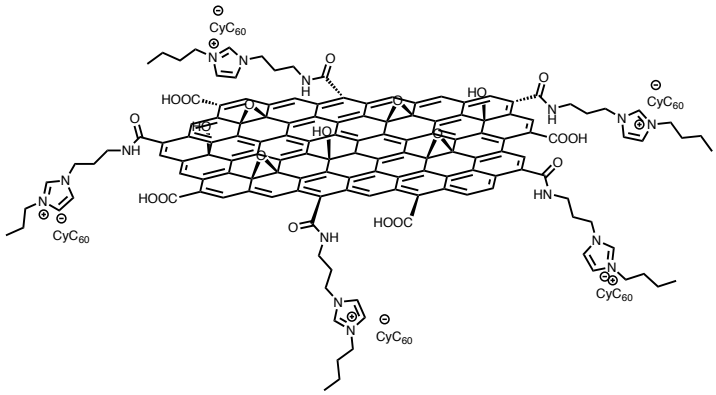

FTIR (KBr), ν (cm^{-1}): 2213 (C≡N), 1739 (C=O), 1662 (C=O), 1234 (C–O) and 526 (C-C).

TGA (N_2 atmosphere): weight loss and temperature desorption (organic anchoring groups): 40.50 %, 700 °C.

XPS: % atomic: C (284.6 eV) = 85.5, O (532.6 eV) = 10.4, N (400.6 eV) = 4.1.

UV-Vis-NIR (MeOH), λ_{max} (nm): 888, 430, 328.

1.4.2.4. Synthesis of GR imidazolium salts and cyanine dye hybrids

GR bromide imidazolium salt (GR^{IL})

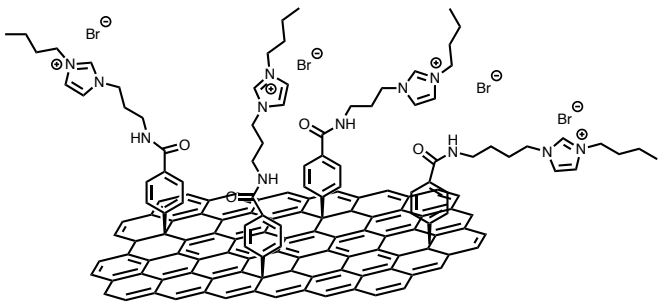

The imidazolium salt **11** (0.050 g) was added over a GR suspension in NMP and sonicated for 15 min. Afterwards, TFA was added (7.5 mL) and the reaction stirred for 5 h. After this period of time, the reaction was gently bubbled with Ar in order to remove the oxygen present in the dispersion. Finally, it was added isopentyl nitrite (0.01 mL) and the dispersion was heated at 80 ºC for 48 h. The functionalized material was isolated by filtration over a PTFE membrane and purified by washing with NMP, DCM, methanol and water.

FTIR (KBr), ν (cm^{-1}): 1632 (C=O) and 1582 (C=C).

TGA (N_2 atmosphere): weight loss and temperature desorption (organic anchoring groups): 12.44 %, 700 °C.

XPS: % atomic: C (284.6 eV) = 88.2, O (532.6 eV) = 7.3, N (400.6 eV) = 3.5, Br (181.0 eV) = 0.9.

GR cyanine imidazolium salts

GR^{IL} (7 mg) was dispersed in deionized water (5 mL) and sonicated for 1 h. On the other hand, cyanine **3** or **8** (7 mg) was dispersed also in deionized water (5 mL) and sonicated for 1 h. Afterwards, both dispersions were mixed in a round bottom flask and the resulting dispersion was stirred at room temperature for 72 h. Finally, the mixture was filtered over a 0.2-µm pore size polycarbonate membrane and intensively washed with water and methanol until the collected solution was colorless, obtained mass: **GR^{IL}-Cy** 5.9 mg, **GR^{IL}-CyC_{60}** 6.3 mg.

GR^{IL}-Cy

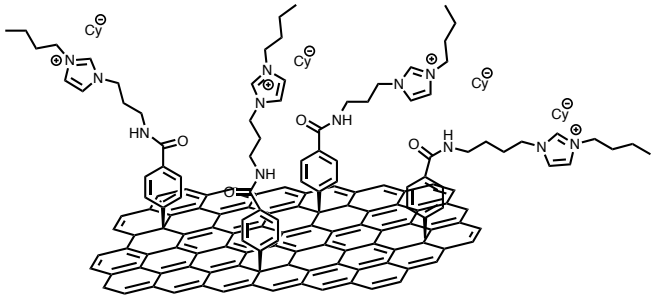

FTIR (KBr), ν (cm^{-1}): 2217 (C≡N), 1632 (C=O,) and 1582 (C=C).

TGA (N_2 atmosphere): weight loss and temperature desorption (organic anchoring groups): 21.41 %, 700 °C.

XPS: % atomic: C (285.6 eV) = 84.1, O (534.6eV) = 12.6, N (400.6 eV) = 2.6, Cl (201.6 eV) = 0.7.

UV-Vis-NIR (MeOH), λmax (nm): 890.

GR^{IL}-CyC_{60}

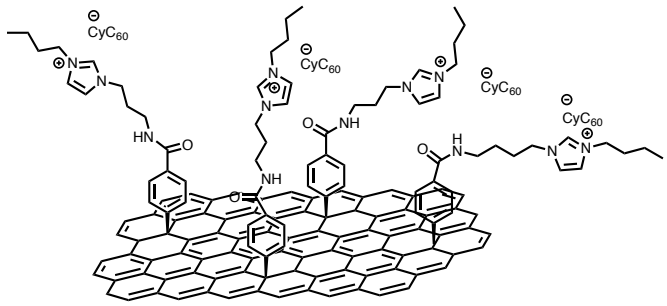

FTIR (KBr), ν (cm^{-1}): 2213 (C≡N), 1667 (C=O),1582 (C=C) and 527 (C-C).

TGA (N_2 atmosphere): weight loss and temperature desorption (organic anchoring groups): 21.11 %, 700 °C.

XPS: % atomic: C (285.6 eV) = 86.6, O (533.6 eV) = 10.7, N (400.6 eV) = 2.7.

UV-Vis-NIR (MeOH), λ_{max} (nm): 888, 421, 337.

Chapter 2

2.1. BACKGROUND

2.1. BACKGROUND

2.1.1. Types of carbon-based fluorescents nanodots

In the last two decades fluorescent nanodots have emerged as an alternative to metal-based semiconductor quantum dots (SQD), which were reported for a first time in 1981.[176] The presence of fluorescent nanoparticles based on carbon was observed in 2004 by Scrivens and co-workers,[177] as a mayor impurity in the synthesis of single-walled carbon nanotubes by an arc-discharge method. Nevertheless, it was not until two years later when Sun's group referred to these particles as prominent new carbon nanomaterials and coined them "carbon dots".[178]

The above-mentioned photoluminescent carbon nanoparticles exhibit a diameter in the range from 1 to 20 nm, and have different functional groups attached to their surface such as amines, alcohols and carboxylic acids. These functionalities make carbon dots to present a hydrophilic character, compatible with reactions in aqueous media. Moreover, they present a low toxicity and are considered environmentally benign, resulting really interesting for bioimaging applications.[179] Regarding to their optical properties, all types of carbon-based nanoparticles present a remarkable fluorescence and a strong absorption in the UV-Vis range. Even so, it is important to mention that factors such as the structure and the production method have a great impact in the optical properties, as we will see along this section.

Carbon-based nanodots present some advantages in comparison with SQD, such as convenient syntheses, prominent biocompatibility, colorful

[176] A. I. Ekimov, A. A. Omushchenko, *J. Exp. Theor. Phys*. **1981**, *34*, 345.

[177] X. Xu, R. Ray, Y. Gu, H. J. Ploehn, L. Gearheart, K. Raker, W. A. Scrivens, *J. Am. Chem. Soc*. **2004**, *126*, 12736.

[178] Y. Sun, B. Zhou, Y. Lin, W. Wang, K. A. S. Fernando, P. Pathak, M. J. Meziani, B. A. Harruff, X. Wang, H. Wang, P. G. Luo, H. Yang, M. E. Kose, B. Chen, L. M. Veca, S. Xie, *J. Am. Chem. Soc*. **2006**, *128*, 7756.

[179] a) S. E, Q. Mao, X. Yuan, X. Kong, X. Chen, J. Wang, *Nanoscale* **2018**, *10*, 12788. b) W. Li, Z. Wang, S. Hao, L. Sun, M. Nisic, G. Cheng, C. Zhu, Y. Wan, L. Ha, S. Zheng, *Nanoscale* **2018**, *10*, 3744.

photoluminescence, and low cost.[180] Since 2006 the number of scientific publications on carbon dots increased exponentially (Figure 2.1), and such explosion of interest is primarily due to the advantages above-mentioned in regard to SQD.[181] Along this time, a variety of additional terms have emerged in the bibliography describing different categories of carbon nanoparticles, such as graphene quantum dots, carbon nanodots, carbon nanoclusters, C-dots and carbon dots. The main problem in most of the cases has been the lack of rigor in the established terminology, without taking into account factors such as the structure of the particle or the quantum effects. Apart from the starting distinction between SQD and "carbon dots," the latter can be also classified in different types. According to Válcarcel *et al*.[182] the term "carbon dots" can be categorized in three groups (Figure 2.2) considering aspects such as their nature, quantum confinement and crystalline structure. The three distinct categories are graphene quantum dots (GQD), carbon quantum dots (CQD) and carbon nanodots (CND).

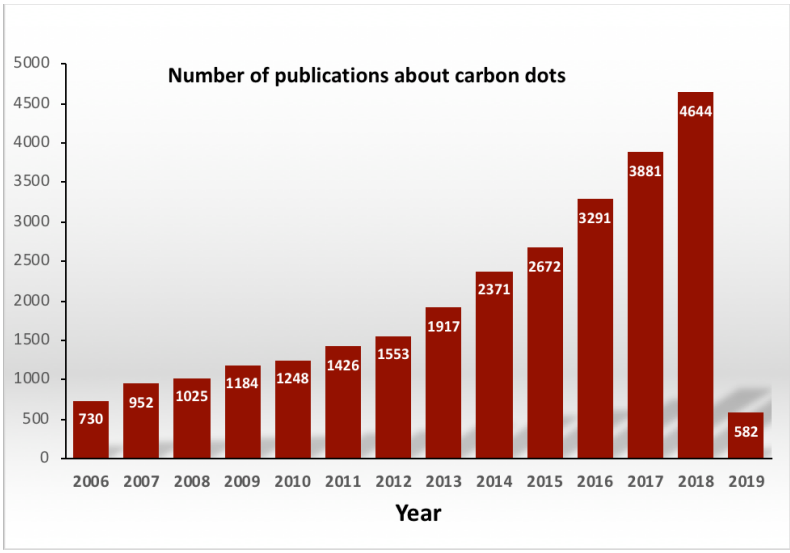

Figure 2.1. Number of publications about carbon dots since 2006. Data generated from the Web of Science Core Collection until February 11, 2019. Search criteria: topic "carbon dots" or "C-dots" or "carbon nanodots" or "graphene quantum dots".[181]

[180] S. Y. Lim, W. Shen, Z. Gao, *Chem. Soc. Rev*. **2015**, *44*, 362.
[181] L. Xiao, H. Sun, *Nanoscale Horiz.* **2018**, *3*, 565.
[182] A. Cayuela, M. L. Soriano, C. Carrillo-Carrión, M. Valcárcel, *Chem. Commun.* **2016**, *52*, 1311.

GQD are two-dimensional disc-shaped nanoparticles which usually are produced by fragmentation and exfoliation of graphene-based materials. The reduction of graphene layers results in new features in regard to the initial graphene material, such as the appearance of photoluminescence and the presence of a bandgap in the electronic structure. These small graphene sheets are formed by a sp^2 lattice with different oxygenated groups in their surface which stem from the production method.

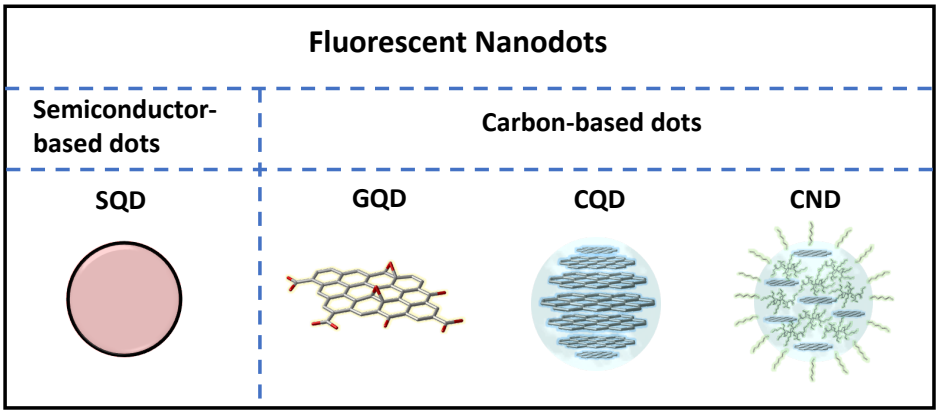

Figure 2.2. Different types of fluorescent nanodots.

On the other hand, CQD are quasi-spherical nanoparticles which present a crystalline multilayered graphitic core in their structure. CQD can be produced from other precursors with crystalline structure, such as carbon nanotubes, or by pyrolysis of organic molecules subjected to very high temperatures. In both cases (GQD and CQD), the term "quantum" refers to particles that present a predominately delocalized band structure, which can additionally have some contribution from molecular surface states.

Finally, CND can be described as amorphous quasi-spherical particles with polymeric nature composed mainly by sp^3 and some sp^2 domains. The CND excites states are mainly dominated by molecular surface states and, therefore, do not present any quantum confinement effects. In most of the cases the differentiation between quasi-spherical CND and CQD is really difficult because the structure could present a partial or a highly graphitic core, and therefore the nanomaterials may exhibit neither a fully delocalized nor a molecular electronic structure.

As a consequence of this fact, sometimes it is difficult to experimentally confirm the presence or absence of quantum confinement effects in these systems, which would require an exhaustive control of the particle sizes and production methods. Indeed, up to now, true CQD have not been reported unequivocally.[183] For that reason, in the following discussion the term of CQD will be changed for gCND which refers to quasi-spherical particles which exhibit a crystalline structure formed by a graphitic core.

2.1.2. Synthesis of fluorescent carbon-based dots

Since the discovery of these nanoparticles, there has been a lot of effort in the development of easy, economic, fast and reproducible new synthetic methodologies for the production of high quality carbon dots. In general, carbon dots syntheses can be classified in two different groups: top-down and bottom-up approaches.

Top-down methods are realized by the fragmentation of bulk carbon sources such as graphite, graphene, carbon nanotubes or carbon fibers in small fragments (carbon dots) which usually are subjected to a further surface treatment. On the contrary, bottom-up methods synthesize carbon dots using as starting materials small precursors (glucose, citric acid,..) which usually are decomposed by thermal treatment and lead to the formation of carbon nanoparticles.

Apart from these methods, here we would like to briefly mention the molecular approach, which consists in the formation of atomically precise and uniform nanographene structures by taking advantage from controlled organic reactions.[184] Through this method can be synthesized well-defined monodispersed structures, but it is difficult to prevent aggregation caused by π−π stacking, unless bulky substituents are introduced, and the yields are low due to the multistep synthetic methods typically required. For instance, Yan and co-workers[185] performed an oxidative condensation of aryl groups of polyphenylene dendritic precursors through stepwise solution chemistry leading to GQDs containing 168, 132 and 170 conjugated carbon atoms (Figure 2.3).

[183] G. A. M. Hutton, B. C. M. Martindale, E. Reisner, *Chem. Soc. Rev*. **2017**, *46*, 6111.
[184] A. Narita, X.-Y. Wang, X. Feng, K. Müllen, *Chem. Soc. Rev.* **2015**, *44*, 6616.
[185] X. Yan, X. Cui, L. Li, *J. Am. Chem. Soc*. **2010**, *132*, 5944.

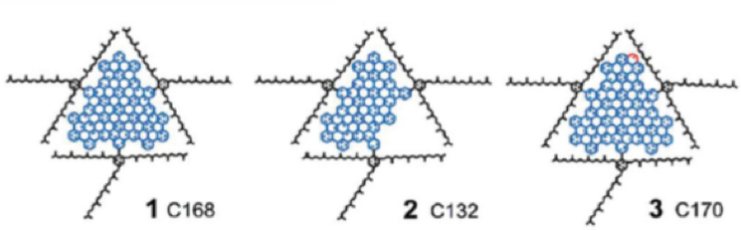

Figure 2.3. GQD structures synthesized by a bottom-up method using stepwise solution chemistry.

More recently, Martín *et al.*[186] described the synthesis of a chiral bilayer nanographene in a three steps synthesis from previously obtained helicenes (Figure 2.4). Herein, the folded nanographene is composed of two hexa-peri-hexabenzocoronene layers fused to a [10]helicene, resulting in a system of 30 fused benzene rings that is also chiral, rigid, and remains soluble in common organic solvents.

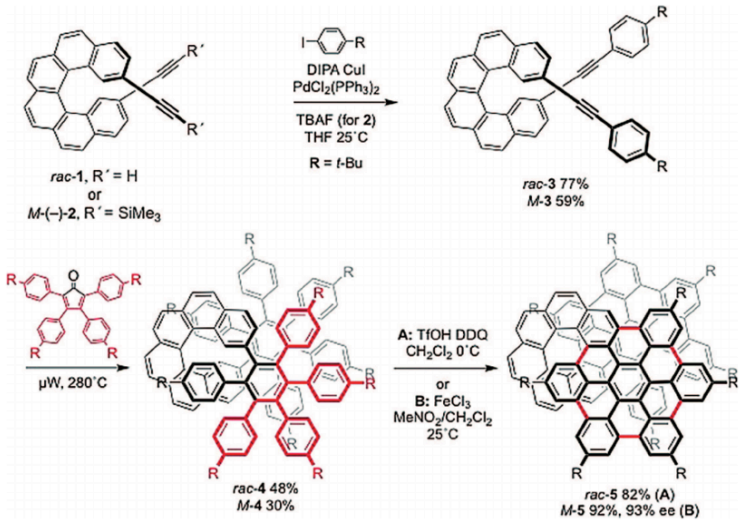

Figure 2.4. Synthesis of racemic and enantiopure chiral bilayer nanographenes. Structures drawn as a single enantiomer for clarity. Red highlights are used to illustrate important transformations.

[186] P. J. Evans, J. Ouyang, L. Favereau, J. Crassous, I. Fernández, J. Perles, N. Martín, *Angew. Chem. Int. Ed.* **2018**, *57*, 6774.

However, in this section we will focus in the two main methods reported in the bibliography for producing carbon dots, based on the two approaches above mentioned to nanomaterials.

2.1.2.1. Top-down synthesis

Top-down methodologies involve cleaving or breaking down a carbon material source via chemical, electrochemical, or physical approaches (Figure 2.5). These methods provide the formation of nanoparticles with a significant graphitic structure retained from the initial material, which can be small fragments of single or few-layer graphene sheets (GQD) or quasi-spherical nanoparticles with a graphitic core (gCND).

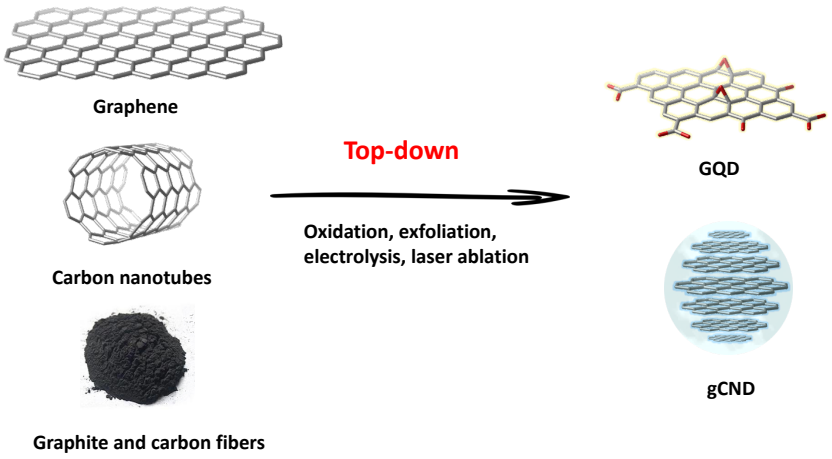

Figure 2.5. Schematic representation of top-down methodologies involved in the synthesis of carbon dots.

Acidic oxidation. One of the most employed techniques is the acid treatment for the synthesis of GQD and gCND from carbon fibers, carbon nanotubes, graphene oxide, and other carbon sources. This method affords the introduction of negatively charged oxygenated groups onto the obtained GQD or gCND, making them hydrophilic and with a graphitic structure that bears some defects on its surface. The mechanism of oxidative top-down routes can be explained as a defect-mediated fragmentation process (Figure 2.6).[187]

[187] X. T. Zheng, A. Ananthanarayanan, K. Q. Luo, P. Chen, *Small* **2015**, *11*, 1620.

The oxygenated groups (mainly hydroxy and epoxy groups) present in the starting carbon material surface can generate additional defects that serve as reactive sites, thus allowing the starting carbon material to be cleaved into smaller fragments. In general, during the oxidation process epoxy groups tend to appear linearly onto the carbon surface, which makes the graphitic domains fragile, causing a rupture of the C–C bonds. Therefore, the rupture of these sp^2 domains by the epoxy lines results in the formation of GQD or gCND. In addition, the fragmentation process mediated by oxidation, can be accompanied by other treatments (heat, sonication, pressure, nucleophiles attack…) for improving the rupture of the initial carbon source into sub-nanosized particles as we will see in the next paragraphs.

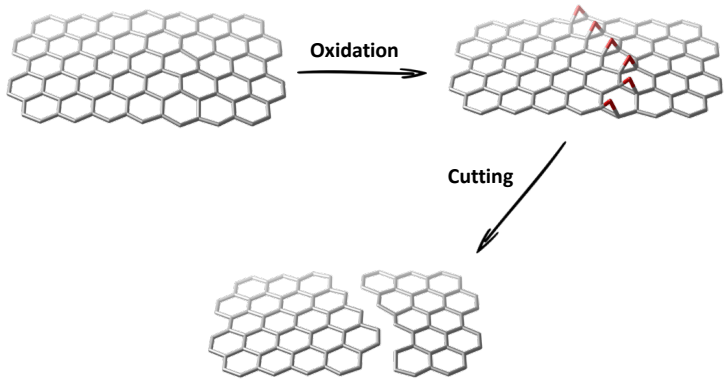

Figure 2.6. Schematic representation of the proposed mechanism for the oxidative cutting of carbon materials into carbon dots (GQD and gCND).

Haino and co-workers[26,188] reported the formation of controlled-size GQD through this oxidative cutting. In this case, commercial graphite was exfoliated and oxidatively fragmented using a mixture of concentrated H_2SO_4 and HNO_3 at 120 ºC for 24 h., giving rise to water-soluble GQD obtained in a gram scale and suitable for a further functionalization. A similar procedure was used by Peng *et al*., but using as carbon source carbon fibers instead of graphite.[189] Herein, they also performed the oxidation with a mixture of concentrated H_2SO_4 and HNO_3, which was heated for 24 h. at three different temperatures

[188] R. Sekiya, Y. Uemura, H. Naito, K. Naka, T. Haino, *Chem. Eur. J.* **2016**, *22*, 8198.

[189] J. Peng, W. Gao, B. K. Gupta, Z. Liu, R. Romero-Aburto, L. Ge, L. Song, L. B. Alemany, X. Zhan, G. Gao, S. A. Vithayathil, B. A. Kaipparettu, A. A. Marti, T. Hayashi, J. Zhu, P. M. Ajayan, *Nano Lett*. **2012**, *12*, 844.

(80°C, 100°C and 120°C). This experiment revealed that the reaction temperature could tune the size of the GQD and affect their optoelectronic properties. The results of this work showed that lower temperatures lead to GQD absorptions at longer wavelengths. Therefore, the GQD synthesized at temperatures of 120, 100, and 80 °C showed blue, green, and yellow emission colors, respectively, under 365 nm light illumination.

Hydrothermal or solvothermal synthesis. The hydrothermal method typically uses graphene oxide as starting material which is firstly subjected to an acidic oxidation step in order to generate epoxy groups as cleavage sites. Afterwards, under hydrothermal conditions, it is produced the cutting of the layers usually in alkaline media (NaOH, ammonia) in order to enhance the fragmentation in small carbon dots. For instance, Lin and co-workers[190] reported an efficient methodology for the synthesis of fluorescents GQD through a one-pot hydrothermal reaction between graphene oxide and ammonia. This method presented a high conversion ratio, where the 60 wt % of the initial graphite was transformed into GQD with quantum yields up to 18.2 %.

Microwave- and sonication-assisted methods. The previous methods present a major drawback which is the long reaction times. For that reason, new high-energy technologies have been included in the procedures in order to seek facile synthetic methods for the production of carbon dots. On one hand, microwave-assisted technique offers rapid and uniform heating of the reaction medium, therefore reducing reaction times and improving the products yields and quality. Li and co-workers[191] reported a microwave-assisted synthesis of GQD from graphene oxide under acidic conditions. Herein, in a one-pot reaction of 3 h., the authors obtained yellow luminescent GQD with an average diameter of 4.5 nm. Moreover, the reduction of these GQD with $NaBH_4$ resulted in the formation of blue luminescent GQD with the same dimensions.

On the other hand, ultrasound can generate alternating low-pressure and high-pressure waves in a liquid phase, leading to the formation and violent collapse of small vacuum bubbles which, in turn, produce high-speed liquid jets and strong hydrodynamic shear forces to break the layered carbon structures into

[190] X. Wu, L. Ma, S. Sun, K. Jiang, L. Zhang, Y. Wang, H. Zeng, H. Lin, *Nanoscale* **2018**, *10*, 1532.

[191] L. Ling-Ling, J. Jing, F. Rong, W. Chong-Zhi, L. Qian, Z. Jian-Rong, J. Li-Ping, Z. Jun-Jie, *Adv. Funct. Mater*. **2012**, *22*, 2971.

carbon dots. Prasad *et al*.[192] reported a new methodology where gCND were obtained by a sonication step of polythiophene in DMF. Furthermore, they demonstrated the use of these nanoparticles for cellular imaging, and the sensitive and specific optical detection of mercury ions.

Electrochemical exfoliation. An interesting alternative for the production of GQD and CND is through the electrochemical cleavage of carbon precursors. The application of high redox potentials (1.5−3.0 eV) could oxidize the C-C bonds as well as water to generate OH· and O· radicals that can act as electrochemical scissors releasing carbon dots. Loh and co-workers,[193] performed the synthesis of fluorescent carbon nanoparticles following the above-mentioned strategy, and demonstrated that the fluorescence of the nanoparticles can be tuned by controlling the water content in the synthesis. Furthermore, they confirmed the key role of PF_6^- which has the ability of intercalate between the layers and therefore improving the cutting of graphite layers. Other species have been employed for the generation of carbon dots by electrochemical methods, for example, using $K_2S_2O_8$ as supporting electrolyte, Yang *et al*.,[194] exfoliated and fragmented graphite. In this case, the electrochemical reaction of $S_2O_8^{2-}$ generated the strong oxidant SO_4^{2-}, which cutted graphene layers into small red-fluorescent sp^2 fragments.

Other physical routes. The first example based in these alternative methodologies was that reported for Xu *et al*. in 2004, where gCND were isolated for the first time from the production of single-walled carbon nanotubes by the arc-discharge method.[177] The obtained crude was purified by electrophoresis resulting in long nanotubes, short tubular materials and fluorescent gCND. In addition, carbon dots have been ablated from carbon materials by high power laser irradiation. According to this method, Yang and co-workers[195] synthesized GQD by a one-step pulsed laser ablation of carbon nano-onions in water. In the same work, the synthesis of GQD was also carried out through the chemical oxidation of carbon nano-onions. The characteristics of both nanomaterials were compared, and the authors concluded that GQD

[192] K. P. Prasad, Y. Chen, M. A. Sk, A. Than, Y. Wang, H. Sun, K. Lim, X. Dong, P. Chen, *Mater. Horiz*. **2014**, *1*, 529.
[193] J. Lu, J. Yang, J. Wang, A. Lim, S. Wang, K. P. Loh, *ACS Nano* **2009**, *3*, 2367.
[194] X. Tan, Y. Li, X. Li, S. Zhou, L. Fan, S. Yang, *Chem. Commun*. **2015**, *51*, 2544.
[195] R. L. Calabro, D. Yang, D. Y. Kim, *J. Colloid Interface Sci*. **2018**, *527*, 132.

produced by laser ablation presented a smaller size, a lower degree of sp^2 domains and a blue-shifted luminescence.

2.1.2.2. Bottom-up synthesis

This methodology mostly involves the thermal decomposition of small organic molecules or polymers to generate fluorescent carbon dots. The pyrolysis or hydrothermal treatment of these molecules heated above their melting points leads to the condensation and nucleation of carbon dots, which is accompanied by the release of H_2O and CO_2. The precursors are usually organic molecules which present different functional groups (e.g. carboxylic acids, hydroxy groups, amines..) to facilitate the built-up of the carbon core. Some examples are citric acid,[196] sugars[197] and aminoacids[198] or other exotic precursors such as coffee grounds[199] and orange peel waste.[200] The carbon dots synthesized according to this method have diameters between 2-10 nm and present different carbon core compositions. Depending on the employed temperatures for the syntheses, are obtained amorphous nanodots (CND) composed by sp^3 carbons or graphitic nanodots (gCND) composed of sp^2 and sp^3 domains. In general, temperatures above 300 ºC lead to significant graphitization, whilst those below 300 ºC result in amorphous particles.[182,201] In accordance with Reisner *et al.*,[183] the bottom-up methodologies could be classified in two different categories, depending on the number of precursors used are distinguished "single source precursor" or "multicomponent" approaches (Figure 2.7).

[196] C. X. Guo, D. Zhao, Q. Zhao, P. Wang, X. Lu, *Chem. Commun*. **2014**, *50*, 7318.
[197] G. Huang, X. Chen, C. Wang, H. Zheng, Z. Huang, D. Chen, H. Xie, *RSC Adv*. **2017**, *7*, 47840.
[198] F. Li, Y. Li, X. Yang, X. Han, Y. Jiao, T. Wei, D. Yang, H. Xu, G. Nie, *Angew. Chem. Int. Ed*. **2018**, *57*, 2377.
[199] P. Hsu, Z. Shih, C. Lee, H. Chang, *Green Chem*. **2012**, *14*, 917.
[200] A. Prasannan, T. Imae, *Ind. Eng. Chem. Res*. **2013**, *52*, 15673.
[201] M. J. Krysmann, A. Kelarakis, P. Dallas, E. P. Giannelis, *J. Am. Chem. Soc*. **2012**, *134*, 747.

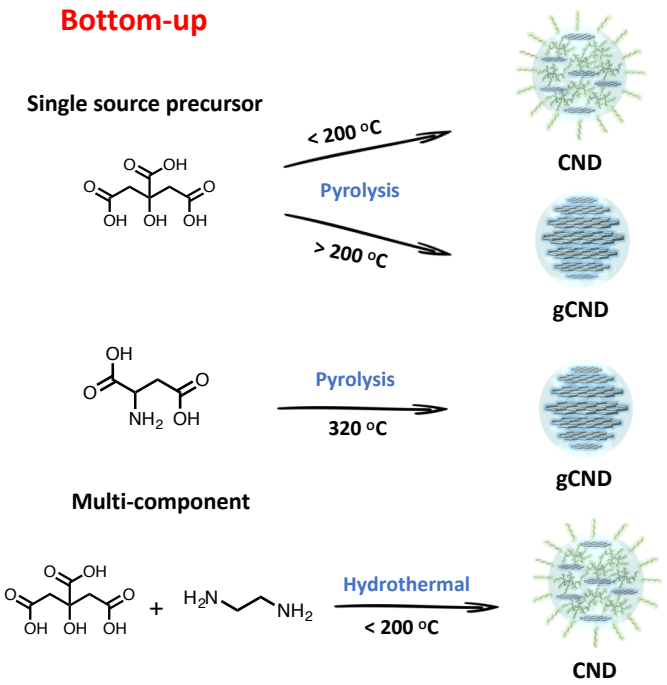

Figure 2.7. Schematic representation of bottom-up methodologies involved in the synthesis of carbon dots: single source precursor and multi-component synthetic procedures.

Single source precursor. In this method, it is necessary to choose a suitable precursor for its pyrolysis which usually present a carbon skeleton with amines/alcohols and carboxylic acid functionalities. These functional groups initiate the condensation and growth of the carbon dots core through dehydration and decarboxylation reactions.[202,203] For instance, one of the most common precursors used in both, single source and multi-component approaches, is citric acid, which is able to form carbon nanoparticles through its pyrolysis due to the alcohol and the carboxylic acids present in its structure.[196]

[202] S. Tao, S. Zhu, T. Feng, C. Xia, Y. Song, B. Yang, *Mater. Today Chem.* **2017**, *6*, 13.

[203] S. Zhu, Q. Meng, L. Wang, J. Zhang, Y. Song, H. Jin, K. Zhang, H. Sun, H. Wang, B. Yang, *Angew. Chem. Int. Ed.* **2013**, *52*, 3953.

A key issue in the synthesis of carbon dots is the selection of the reaction temperature, which should be chosen above the decomposition temperature of the precursor. The use of higher temperatures results in faster decomposition times, but it is important not to exceed the boiling/sublimation temperature of the organic precursor. Therefore, the optimal temperature is those where the precursor can decompose as a melt in order to obtain good yields and reproducibility. In general, temperatures above 300 ºC lead to the synthesis of carbon dots with high graphitization (gCND), whereas the temperatures below 300 ºC produce amorphous carbon dots (CND), unless the precursors present sp^2 or *sp* carbon atoms in their structures.[182,201] Furthermore, CND are more soluble in water and other polar solvents such as methanol or acetone than gCND, which are more soluble in other organic solvents such as DMSO or DMF. gCND present fewer hydrophilic functional groups in the surface and more sp^2 domains due to the higher reaction temperatures, which leads to the loss of certain groups as carboxylic acids by decarboxylation.

All the carbon dots (CND or gCND) synthesized by the bottom-up methodology are significantly more disordered than GQD or nanoparticles prepared by top-down methods. The reaction time is another key factor in the synthesis, since it is necessary to ensure the complete decomposition of the precursor in order to facilitate the additional purification process.

The introduction of heteroatoms in the carbon nanodots could provide significant changes in properties such as the solubility or the absorption and emission wavelengths. This heteroatom doping can be achieved by selecting a precursor in which the dopant atom is present in the structure. In this manner, during the carbon dot formation the heteroatom will be incorporated as part of the new carbon dot core. For example, Reisner and co-workers reported the synthesis of nitrogen doped gCND using aspartic acid as single precursor.[204]

Multi-component. In this method, a typical carbonaceous precursor like citric acid is decomposed in the presence of a second precursor which contains heteroatoms such as urea, ethylenediamine (nitrogen doping),[205,206] H_3PO_4

[204] B. C. M. Martindale, G. A. M. Hutton, C. A. Caputo, S. Prantl, R. Godin, J. R. Durrant, E. Reisner, *Angew. Chem. Int. Ed.* **2017**, *56*, 6459.

[205] V. Strauss, J. T. Margraf, C. Dolle, B. Butz, T. J. Nacken, J. Walter, W. Bauer, W. Peukert, E. Spiecker, T. Clark, D. M. Guldi, *J. Am. Chem. Soc*. **2014**, *136*, 17308.

[206] F. Arcudi, L. Đorđević, M. Prato, *Angew. Chem. Int. Ed*. **2016**, *55*, 2107.

(phosphorus doping)[207] or H_3BO_3 (boron doping)[208] among others. These heteroatoms modify the surface groups of the CND, which is a key factor to achieve further functionalization processes and to modulate the optical properties of the as-formed carbon dots.

The multi-component synthesis is usually performed in hydrothermal conditions, in an autoclave, and sometimes using a co-solvent like ethylenediamine, which could act at the same time as a reactant. This methodology makes the reaction temperature do not exceed 200 ºC, and therefore leads to the formation of amorphous CND. The purification is an important step after the synthesis, since the low reaction temperature and the close system of the autoclave lead to an incomplete reaction of the precursors.[203]

When the multi-component synthesis is carried out in an open atmosphere, the obtained CND show different optical properties than those synthesized under pressure.[205,209] Furthermore, multi-component syntheses lead to carbon dots with different optical properties than those synthesized by single source precursors, as discussed in the section devoted to "optical properties".

Two recent reports from Prato and co-workers document the crucial importance of the precursors selection in multi-component synthesis, in order to achieve specific properties. In the first one, they demonstrated that the redox potentials of CND can be modulated by employing different quinones as electroactive precursors during a microwave-assisted synthesis (Figure 2.8a and Figure 2.8b). Furthermore, they probed that this new library of CND could have applications in photocatalysis.[210]

---

[207] M. K. Barman, B. Jana, S. Bhattacharyya, A. Patra, *J. Phys. Chem. C*, **2014**, *118*, 20034.

[208] A. B. Bourlinos, G. Trivizas, M. A. Karakassides, M. Baikousi, A. Kouloumpis, D. Gournis, A. Bakandritsos, K. Hola, O. Kozak, R. Zboril, I. Papagiannouli, P. Aloukos, S. Couris, *Carbon* **2015**, *83*, 173.

[209] V. Strauss, A. Kahnt, E. M. Zolnhofer, K. Meyer, H. Maid, C. Placht, W. Bauer, T. J. Nacken, W. Peukert, S. H. Etschel, M. Halik, D. M. Guldi, *Adv. Funct. Mater*. **2016**, *26*, 7975.

[210] F. Rigodanza, L. Đorđević, F. Arcudi, M. Prato, *Angew. Chem. Int. Ed*. **2018**, *57*, 5062.

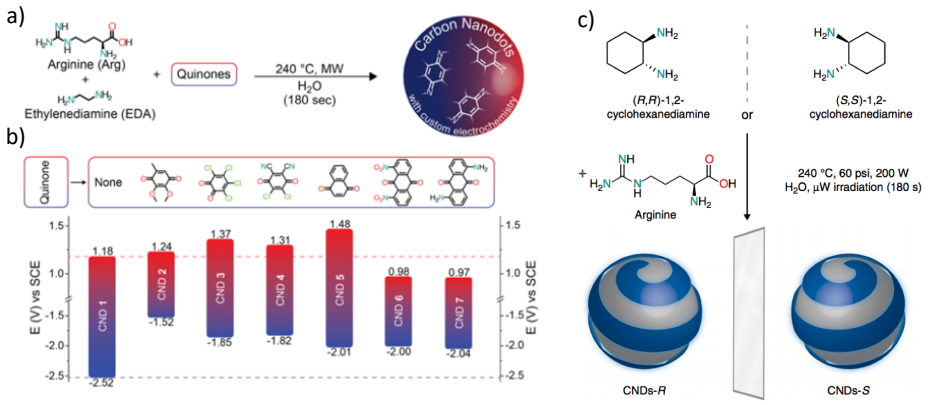

Figure 2.8. a) Reaction scheme for the bottom-up synthesis of CND. b) Redox potentials of the different CND obtained (with the structures of the corresponding starting quinones employed as precursors). c) Design and synthesis of chiral CND. Chiral CND were synthesized starting from (*R,R*)- or (*S,S*)-1,2-cyclohexanediamine and arginine, under hydrothermal microwave-assisted conditions.

In the second, they described the synthesis of chiral CND produced by a single step in a hydrothermal microwave-assisted synthesis by using arginine and (*R,R*)-1,2-cyclohexanediamine or (*S,S*)-1,2-cyclohexanediamine (Figure 2.8c).[211] This resulted in the formation of two different chiral carbon dot nanomaterials that display a bisignated response in their circular dichroism spectra.

In conclusion, both single source precursor and multi-component approaches are simple, cost-effective, and scalable methods, which allow to tune the final properties of the as-formed carbon dots by selecting the precursors and conditions for the synthesis.

Formation mechanism of CND. When still under debate, the carbon dots mechanism formation is believed to consist in two steps, where the former implies a polymerization step of the precursors and the latter a carbonization step to form a carbogenic core by graphitization. According to Yang and co-workers,[202] polymer-like clusters are always formed as intermediate products at early stages in the bottom-up synthesis by pyrolysis or hydrothermal methods.

[211] L. Đorđević, F. Arcudi, A. D'Urso, M. Cacioppo, N. Micali, T. Bürgi, R. Purrello, M. Prato, *Nat. Commun*. **2018**, *9*, 3442.

At the initial stage, with the increase of the temperature, the dehydration and condensation of the organic precursors occurs through reaction of their functional groups. This leads to the formation of long molecular chains, which can be cross-linked to each other (Figure 2.9).

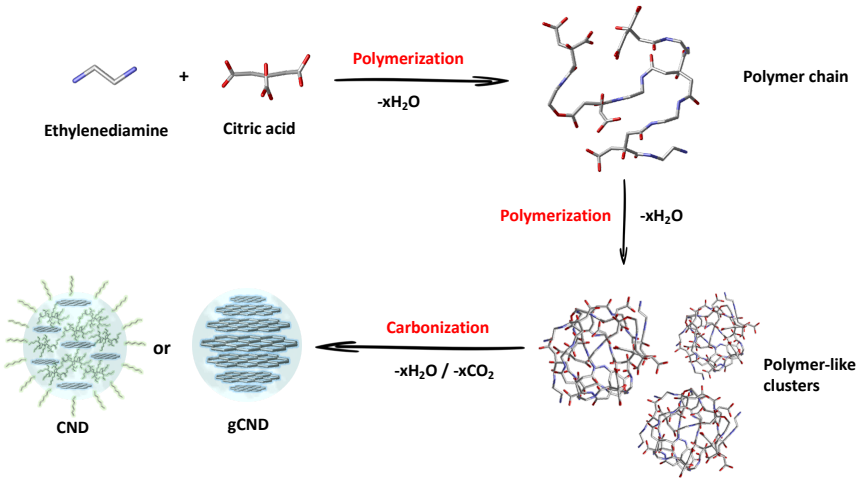

Figure 2.9. Schematic representation of the formation mechanism of carbon dots by bottom-up methodologies (pyrolysis and hydrothermal treatment).

As the reaction proceeds, the activation energy of some potential processes can be decreased under such high temperature and pressure. Therefore, more pathways could appear, which potentiates the growth and partial carbonization of polymer clusters and, finally, generates the CND. Thus, depending on reaction conditions (temperature, pressure and time) the synthesis could lead to different products, such as polymeric structures, polymer/carbon hybrid structures (CND) or graphite-like structures (gCND). In general, most of the produced nanomaterials are formed by an internal hydrophobic core (highly dehydrated and crosslinked carbon skeletons or graphitic structures) enfolded by the external hydrophilic polymer chains. In conclusion, carbon dots are supposed to be nanoparticles formed by polymer structures with certain degree of graphitization, leading to CND or gCND depending on the carbonization step.

2.1.3. Purification and isolation of carbon-based dots

The isolation and purification of carbon dots is one of the greatest challenges in this topic due to the difficulty in distinguishing carbon dots and molecular species after the synthesis.[212] Typical procedures imply the isolation of carbon dots by filtration[213] and purification by several washing steps with different solvents. The purification could be also done by centrifugation.[214] These methodologies could be appropriated when the reaction is completed. However, when a significant number of small byproducts and starting materials are presented, the isolation is challenging as the small size and low density of carbon dots render them difficult to isolate by centrifugation or filtration.

An interesting alternative is the purification by dialysis,[215] where small molecules and salts can be removed in a few days avoiding significant loss of material. Sephadex gel chromatography[216] can be employed to separate the carbon dots in different fractions according to their size. Other techniques such as column chromatography[217] and electrophoresis[218] have been reported for the identification of fluorescent molecular species in the carbon dots samples. Besides, other common strategy is the freeze-drying of aqueous solutions of carbon dots for obtaining isolated carbon dots as a powder. To sum up, the isolation and differentiation of carbon dots and molecular species remains still a challenge, and depending on the particular case (reaction conditions, reactants, etc) it would be more convenient to use one specific purification method or a combination of different methods.

[212] J. B. Essner, J. A. Kist, L. Polo-Parada, G. A. Baker, *Chem. Mater.* **2018**, *30*, 1878.
[213] X. T. Zheng, A. Than, A. Ananthanaraya, D. Kim, P. Chen, *ACS Nano* **2013**, *7*, 6278.
[214] X. Wu, F. Tian, W. Wang, J. Chen, M. Wu, J. X. Zhao, *J. Mater. Chem. C* **2013**, *1*, 4676.
[215] J. Liu, S. Lu, Q. Tang, K. Zhang, W. Yu, H. Sun, B. Yang, *Nanoscale* **2017**, *9*, 7135.
[216] X. Wang, L. Cao, S.-T. Yang, F. Lu, M. J. Meziani, L. Tian, K. W. Sun, M. A. Bloodgood and Y.-P. Sun, *Angew. Chem. Int. Ed.* **2010**, *49*, 5310.
[217] H. Ding, S. Yu, J. Wei, H. Xiong, *ACS Nano* **2016**, 10, 484.
[218] H. Liu, T. Ye, C. Mao, *Angew. Chem. Int. Ed.* **2007**, *46*, 6473.

2.1.4. Optical properties

Absorption. Carbon dots (CND and GQD) are effective in photon-harvesting in the short-wavelength region of the UV-Vis spectra due to their structural features. The origin of this absorption stems from a variety of π-π^* (C=C) and n-π^* (C=O) transitions in the core and on the surface of the particles.[219] In general, the spectra of these species show strong absorptions in the UV-Vis region (260-320 nm) due to the C=C transitions, with a tail extending into the visible range.[219,220] In some cases, it is also observed a shoulder peak in the range of 270-390 nm which can be ascribed to n-π^* transitions of C=O bonds.[221] Carbon dots with higher levels of graphitization display much higher absorptions than amorphous carbon dots, due to the greater number of π-π^* (C=C) transitions present. Moreover, CND are relatively more efficient in the absorption of long wavelengths than GQD. The introduction of different groups and the surface passivation can alter the absorption features of carbon dots.

Photoluminescence. One of the most striking features of carbon dots is their photolumiscence, which has attracted research attention for further applications in different fields such as biological imaging and sensing.[203] Nevertheless, the origin of this photoluminescence is still under debate and different mechanisms have been proposed to explain this phenomenon. Valcárcel and co-workers postulated three different mechanism to explain the origin of photoluminescence in carbon dots (Figure 2.10).[182]

[219] N. Dhenadhayalan, K. Lin, R. Suresh, P. Ramamurthy, *J. Phys. Chem. C* **2016**, *120*, 1252.

[220] L. Li, G. Wu, G. Yang, J. Peng, J. Zhao, J. Zhu, *Nanoscale* **2013**, *5*, 4015.

[221] G. Eda, Y. Lin, C. Mattevi, H. Yamaguchi, H. Chen, I. Chen, C. Chen, M. Chhowalla, *Adv. Mater.* **2010**, *22*, 505.

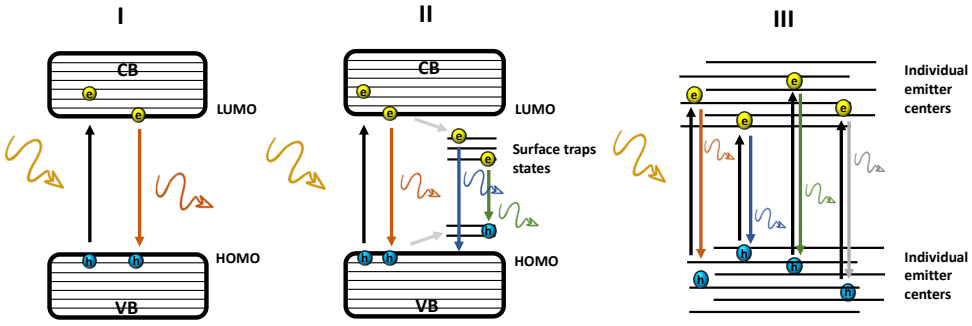

Figure 2.10. Mechanisms proposed for the different photoluminescence pathways in carbon dots.

The first mechanism (I) is proposed for classic quantum dots where the photoluminescence arise from the radiative band-edge recombination. Herein, upon the absorption of one photon, an electron located in the valence band (VB) is promoted to the conduction band (CB) leaving a hole behind, the subsequent recombination affords the emission of a photon. Therefore, this mechanism is only valid for defect-free and impurity-free quantum dots in which no intermediate states exist within the bandgap. In this case, the exciton confinement effects confer size-dependence and the emission properties could change as a function of the particle size. Moreover, these systems exhibit a narrow photoluminescence band. This mechanism is widely accepted for explaining the photoluminescence in semiconductor quantum dots, regardless of their composition and synthetic method.

The second proposed mechanism (II) occurs when trap states are introduced in the bandgap by the presence of impurities, functional groups, surface defects or adsorbed molecules. In this particular case, the photoexcited electron and/or hole can be trapped and the further recombination leads to a radiative emission of lower energy. Accordingly, the photoluminescence is a combination of at least two different mechanism with different sources. On the one hand, one mechanism is due to the core with its intrinsic quantization effects and, on the other hand, the surface functional groups and/or surface defects (trap states) govern the emissive response. This mechanism is employed to explain the photoluminescence of GQD and gCND in many articles, where an excitation-dependent emission is observed. Furthermore, a decreased fluorescence

intensity signal, which is also displaced toward longer wavelengths, is registered as the excitation wavelength increases.[201]

The third type of photoluminescence (III) is due to the emission from molecular-like fluorophores or emitter functional groups generally located on the nanoparticle surface.[182,201,219,222] In this particular case, neither quantum confinement or collective excitonic effects exist and, therefore the emission is similar to that observed in metal nanoclusters.[223] The amorphous CND obtained by bottom-up strategies at low temperatures emit via this mechanism with the superposition of several emissions. The contributions from the sp^2 domains are only observed when the reaction temperature is set above 200 ºC, and a carbogenic core starts forming and the resulting photoluminescence is due to both, the molecular-like fluorophores and the carbogenic core emissions. Only at high temperatures, between 300 and 400 ºC, it is possible to get mostly gCND where the photoluminescence is governed by the carbogenic core and the trap states (mechanism II).[224] If the formation of a carbogenic core is not achieved, the photoluminescence is due to surface trap states which act as individual emitter centers. Due to the absence of collective effects in the emission of CND, there is not a strong correlation between the position of the spectral bands and the particles size. Therefore, the differences in the optical properties of CND are due to their different compositions and functional groups on the surfaces.

In the different approaches for the bottom-up synthesis of CND, multi-component synthesis generally results in amorphous CND where the photoluminescence arise from highly emissive amide-containing molecular-like fluorophores. Therefore, CND synthesized through multi-component methods give rise to excitation wavelength independent emissions and to higher quantum yields (until 50 %) than those CND synthesized according to a single source methodologies (< 10 %).[201,203,222,225] There are some exceptions of multi-component synthesis using tertiary amines or high temperatures (300 ºC)

[222] J. Schneider, C. J. Reckmeier, Y. Xiong, M. von Seckendorff, A. S. Susha, P. Kasák, A. L. Rogach, *J. Phys. Chem. C.* **2017**, *121*, 2014.

[223] M. O. Dekaliuk, O. Viagin, Y. V. Malyukin, A. P. Demchenko, *Phys. Chem. Chem. Phys*. **2014**, *16*, 16075.

[224] S. Baker, G. Baker, *Angew. Chem. Int. Ed*. **2010**, *49*, 6726.

[225] Y. Song, S. Zhu, S. Zhang, Y. Fu, L. Wang, X. Zhao, B. Yang, *J. Mater. Chem. C.* **2015**, *3*, 5976.

where the molecular-like fluorophores do not form or are carbonized, providing carbon dots with no resolved absorption peaks, excitation-wavelength dependent emissions and low quantum yields (< 10 %). In addition, multi-component syntheses performed in open atmosphere rather than in autoclave reactors have shown non-uniform photoluminescence properties.[205,226]

In conclusion, unlike classic semiconductor quantum dots, in which the emission is originated by intrinsic band edge transitions, in carbon-based dots (GQD, gCND and CND) the photoluminescence properties depend on the synthetic methods employed, the reaction conditions and the functionalization carried out on the surface. Depending on these factors, the competition between intrinsic state emissions and surface trap states will be different, and therefore the photoluminescent behaviour could be explained by mechanisms II or III (Figure 2.10).

2.1.5. Characterization techniques

Different techniques have been handled for the characterization of carbon dots. By means of TEM and AFM, it is possible to obtain information about the morphology of the nanoparticles. TEM experiments provide information about the size of the dots,[227] and when the sample presents high order it is also possible to obtain information about the crystalline structure.[228] This information has been only obtained in GQDs and gCND where it was possible to measure the lattice spacing between the graphitic layers. Nevertheless, TEM samples could be difficult to prepare, due to the high tendency of carbon dots to aggregate on the grill and sometimes present a low contrast in the images.[205] Complementary to TEM, AFM is a useful technique which provides information about the heights as well as the shape of the carbon dots. It is common to perform statistical analysis of the heights in order to obtain an average size of each sample.[206] The ideal situation is to combine both techniques in order to have a complete idea of the carbon dots morphology and dimensions.

[226] M. Righetto, A. Privitera, I. Fortunati, D. Mosconi, M. Zerbetto, M. L. Curri, M. Corricelli, A. Moretto, S. Agnoli, L. Franco, R. Bozio, C. Ferrante, *J. Phys. Chem. Lett*. **2017**, *8*, 2236.

[227] S. H. Jin, D. H. Kim, G. H. Jun, S. H. Hong, S. Jeon, *ACS Nano* **2013**, *7*, 1239.

[228] H. Ding, S. Yu, J. Wei, H. Xiong, *ACS Nano* **2016**, *10*, 484.

In addition, dynamic light scattering (DLS) experiments could be used to determine the hydrodynamic radio, but might be challenging due to the polydispersity, small size and fluorescence of the samples.[229] MALDI-TOF experiments have been carried out to estimate the molecular weight of CND revealing, in all cases, a polymeric nature with a polydisperse weight distribution.[230] Regarding to the charge of the carbon dots, zeta potential is an interesting tool that has been employed to determine it.[231]

Raman and X-ray Powder Diffraction (XRD) are techniques which can provide information about the nature of the carbon surface.[202] Characteristic Raman spectra of GQD and CND are composed by the D and G bands, which are a distinctive of samples with a high content in sp^2 domains. In the case of polymeric CND, mostly composed by sp^3 carbon, no signal is observed by Raman spectroscopy. The XRD pattern reveals information about the crystallinity of the samples, even though in most of the cases present an amorphous profile. GQD usually exhibit a diffractogram similar to graphite or graphene-based materials.

FTIR and NMR spectroscopies are techniques widely used for revealing the surface functionalities in carbon dots. FTIR, in particular, has shown to be really useful for tracking surface reactions when the as-incorporated functionalities present characteristic fingerprints which are easy to monitor (C=O, C≡N….).[231] These tracking of the functionalities can be complementary done by ^{1}H-NMR and ^{13}C-NMR, which are useful in determining the different sp^2 and sp^3 signals. Additional structural information is obtained by 2D correlation experiments.[206] Moreover, NMR can also be used to ensure the complete decomposition of the precursors after the carbon dots syntheses. In addition to ^{1}H and ^{13}C-NMR, the samples doped with heteroatoms which are NMR-active nuclei (^{15}N, ^{31}P, ^{11}B) could offer additional structural information. It is important to mention that NMR experiments require high concentration of sample as well as a large number of scans in comparison with those employed

[229] R. C. So, J. E. Sanggo, L. Jin, J. M. A. Diaz, R. A. Guerrero, J. He, *ACS Omega* **2017**, *2*, 5196.

[230] D. Mazzier, M. Favaro, S. Agnoli, S. Silvestrini, G. Granozzi, M. Maggini, A. Moretto, *Chem. Commun*. **2014**, *50*, 6592.

[231] G. A. M. Hutton, B. Reuillard, B. C. M. Martindale, C. A. Caputo, C. W. J. Lockwood, J. N. Butt, E. Reisner, *J. Am. Chem. Soc*. **2016**, *138*, 16722.

in simple organic samples. Therefore, there are examples where the samples have been enriched with ^{13}C in order to have a better signal quality in the experiments.[206]

The characterization by XPS provides information about the elemental composition and identify the different hybridization states of each element present in the sample.[228] Finally, the optical properties of GQD and CND discussed in the previous section are usually determined by UV-Vis absorption and fluorescence spectroscopies. Furthermore, the interaction of carbon dots with other electroactive molecules, by covalent or supramolecular approaches, might be also monitored through these spectroscopic techniques.[232,233] Some examples in this regard are found in the next section.

2.1.6. Surface functionalization

Carbon-based dots (GQD and CND) are species really appealing to be modified by chemical functionalization due to their solubility as well as the diversity of functional groups attached to their surface. On one hand, due to the high content of amine and carboxylic acid groups in the carbon dots surface, the covalent functionalization is usually performed through these functional groups. On the other hand, carbon dots can present charged species, heteroatoms and sp^2 domains in their surfaces, which allow the possibility of incorporating other entities by supramolecular strategies.

Covalent functionalization. According to the bibliography, two main strategies are widely used for the covalent attachment of molecules onto the carbon dots surface.[183] One approach is the use of coupling agents (EDC, DCC, or *N*-hydroxysuccinimide (NHS)..) for the incorporation of molecules which contain carboxylic acids by condensation with the amine functionalities of the carbon dots. For instance, De Cola and co-workers reported the synthesis of a new covalent hybrid of CND with $Ru(bpy)_3^{2+}$ according to this methodology.[233] Herein, the used $Ru(bpy)_3^{2+}$ complex presents carboxylic acids which were activated with NHS and subsequently reacted with amine-terminated CND through an amidation reaction (Figure 2.11). In this work, the CND have been employed as co-reactants in electrochemiluminescence (ECL) processes. It is

[232] V. Strauss, J. T. Margraf, K. Dirian, Z. Syrgiannis, M. Prato, C. Wessendorf, A. Hirsch, T. Clark, D. M. Guldi, *Angew. Chem. Int. Ed.* **2015**, *54*, 8292.
[233] S. Carrara, F. Arcudi, M. Prato, L. De Cola, *Angew. Chem. Int. Ed.* **2017**, *56*, 4757.

quite common to use tripropyl amine (TPrA) as co-reactant in ECL processes, but TPrA is toxic, corrosive and volatile. The major advantage of using CND as a co-reactant instead of TPrA is that the ECL signal obtained for Ru-CND is almost the same than that of Ru-TPrA, although using lower concentrations and, therefore, avoiding the TPrA drawbacks mentioned above.

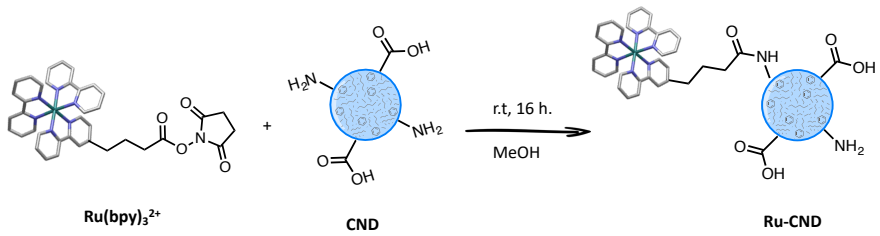

Figure 2.11. Schematic representation of the synthesis of Ru-CND covalent hybrids.

An alternative methodology for the covalent modification, is treating the carboxylic acids onto the carbon dots surface with thionyl chloride or oxalyl chloride for producing the corresponding acyl chlorides. Once formed, the acyl chlorides will react with alcohols or amines in the formation of covalent hybrids. This approach presents some advantages in regard to strategies which use coupling agents. Firstly, the purification in this type of synthesis is easier since the byproducts of the reaction are volatile. Secondly, thionyl chloride or oxalyl chloride can be used as a solvent, in large excess and without reaction stoichiometry considerations.

Martín *et al.*[234] carried out the synthesis of chiral GQD according to this synthetic strategy. In this work, the first step was the activation of the carboxylic acids present in the GQD with $SOCl_2$, generating the corresponding acyl chlorides. In a second step, (*R*)-2-phenyl-1-propanol or (*S*)-2-phenyl-1-propanol were introduced by esterification, giving rise to GQD-(*R*) and GQD-(*S*), respectively (Figure 2.12).

[234] M. Vázquez-Nakagawa, L. Rodríguez-Pérez, M. A. Herranz, N. Martín, *Chem. Commun*. **2016**, *52*, 665.

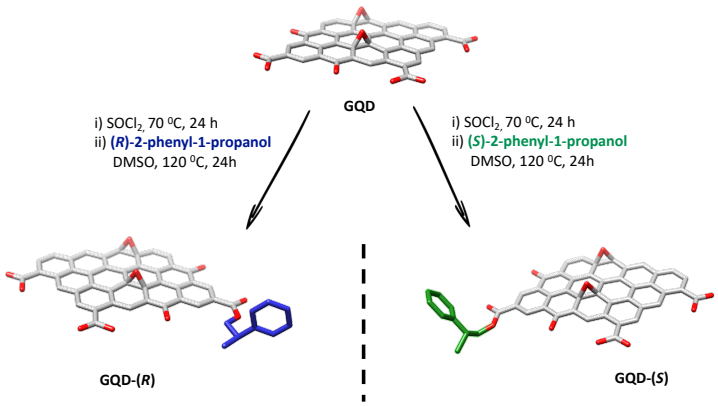

Figure 2.12. Schematic representation of the synthesis of GQD-(*R*) and GQD-(*S*).

Moreover, it was proof the concept that the chirality induced by the covalent functionalization in GQD could be transferred to other molecules by supramolecular interactions. Indeed, they formed supramolecular complexes of GQD-(*R*) and GQD-(*S*) with pyrene molecules where the GQD/pyrene ensembles showed a characteristic chiroptical signal depending on the configuration of the organic molecule introduced by esterification (Figure 2.13).

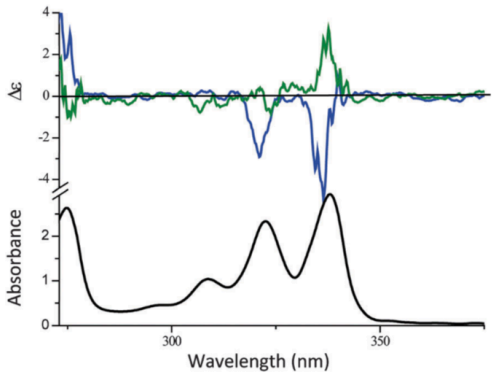

Figure 2.13. Top: Circular dichroism spectra in NMP for aggregates GQD-(*R*)/pyrene (blue) and GQD-(*S*)/pyrene (green). Bottom: UV-Vis spectrum of pyrene in NMP (bottom).

Supramolecular functionalization. As aforementioned, the presence of a rich functional structure in CND and GQD, with charged species, heteroatoms and

sp^2 domains, opened the opportunity to modify carbon dots by supramolecular approaches. One interesting example is that reported by Kim *et al*. where it was synthesized a supramolecular hybrid of CND and a cobalt polyoxometalate (Co-POM) with a direct application in water splitting.[235] Through a microwave-assisted pyrolysis synthesis, using alginate and ethylenediamine as precursors, amine-terminated CND were synthesized. These amine groups were further protonated in acidic media to be assembled with the negative charges present in Co-POM, the electrostatic and hydrogen-bonding interactions facilitate the formation of the supramolecular hybrids (Figure 2.14a). The as-formed hybrids were able to act as photocatalyst in visible-light-driven water oxidations, resulting in an interesting alternative to conventional $[Ru(bpy)_3]^{2+}$-based composites.

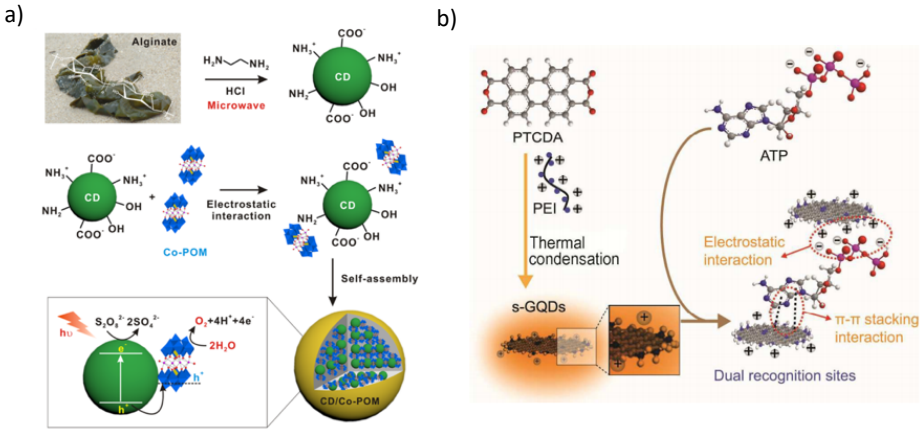

Figure 2.14. a) Synthesis of the supramolecular hybrid CND/Co-POM used in photocatalytic water oxidation processes. b) Schematic synthesis of GQD from 3,4,9,10-perylenetetracarboxylic acid anhydride (PTCDA) and polyethylenimine (PEI) and interaction mechanism with ATP.

GQD can also establish supramolecular interactions with other molecules. This is the case of the work reported by Huang and co-workers, which synthesized GQD able to recognize adenosine triphosphate (ATP) molecules by

[235] Y. Choi, D. Jeon, Y. Choi, J. Ryu, B. Kim, *ACS Appl. Mater. Interfaces*. **2018**, *10*, 13434.

supramolecular interactions.[236] The large π-conjugated, plane and positively charged sites of these GQD result in different domains to establish interactions with ATP molecules, since the latter present an aromatic fragment as well as negative charges in their structure (Figure 2.14b). Indeed, the GQD recognize purine nucleosides through π-π stacking interactions and also are able to differentiate tri-, di- and monophosphate nucleotides through electrostatic interactions. This work resulted to be useful for the study of cell metabolism and mitochondria malfunction related diseases.

Donor-acceptor hybrids. It is well-known that carbon dots are new nanoforms of carbon which, in contrast to other carbon nanomaterials, present interesting features such as photoluminescence, water solubility or low cytotoxicity. These facts have made carbon dots widely investigated for further biological applications. Nevertheless, carbon dots are also able to participate in charge transfer reactions opening new pathways for the development of photocatalysis[231] and energy conversion applications.[5] In this sense, carbon dots have recently been explored in charge transfer assays with electroactive molecules in order to get a better understanding of the photophysical features of these novel nanoparticles. The formation of CND-based donor-acceptor systems has been carried out using both, covalent and supramolecular approaches, as discussed in the next paragraphs.

One of the first examples of supramolecular donor-acceptor hybrids based on carbon dots was reported by Guldi and co-workers. The authors employed pressure-synthesized carbon nanodots (pCND) using citric acid and urea as precursors for their synthesis.[205,209] The next step was the formation of a charge transfer complex formed by the as-prepared pCND, acting as electron-donating materials when combined with electron-accepting perylenediimides (PDI).[232] The driving force in the formation of this complex was the electrostatic and π-stacking interactions established between pCND and PDI. Indeed, the functionalities of PDI were designed to improve these forces, bearing extended π-systems and positive charges to interact with the negative charges of the carboxylic acids present in the pCND surface (Figure 2.15). By means of absorption and fluorescence titration assays, the electronic interactions in the ground and excited states of pCND and PDI were corroborated. Furthermore, a

[236] J. H. Liu, R. S. Li, B. Yuan, J. Wang, Y. F. Li, C. Z. Huang, *Nanoscale* **2018**, *10*, 17402.

binding constant of 8 x 10^4 M^{-1} was calculated, and pump probe experiments revealed a lifetime of 210 ps for the generated charge-separated state.

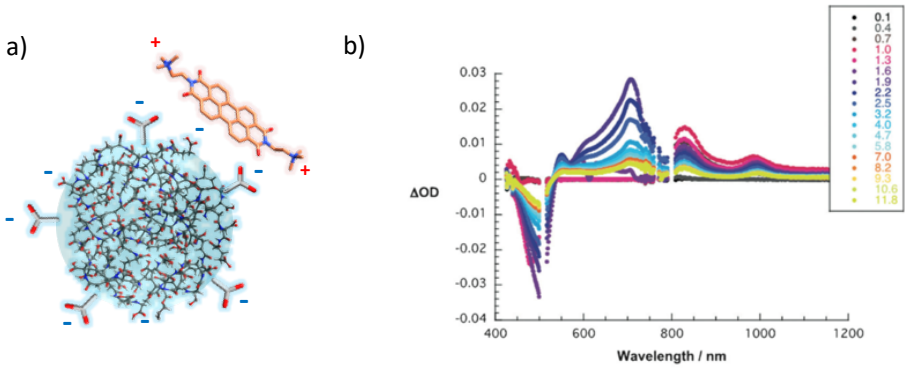

Figure 2.15. a) Donor-acceptor complex formed by pCND and PDI. b) Differential absorption spectra obtained upon femtosecond pump probe experiments of pCND/PDI in phosphate-buffered D_2O (pH 7.2) with several time delays in ps.

More recently, the same authors carried out photophysical investigations which revealed the electron accepting nature of pCND when combined with electron-donating porphyrins through supramolecular interactions.[237] For that task, a diverse series of porphyrins (free base, with a metallic central core, and bearing positively or negatively charged substituents) have been investigated in electron donor-acceptor assemblies with pCND (Figure 2.16). In this case, the formation of the assemblies is mainly governed by electrostatic attractions involving the negative charges present on the pCND surface, which are essential to observe charge separation and charge recombination processes in the excited state.

The supramolecular assembly of pCND and porphyrins has also been explored by using amidinium-carboxylate interactions.[238] In the obtained nanostructures, an ultrafast charge separation is observed upon photoexcitation and a subsequent charge recombination in 27 ps, a lifetime in the range found for

[237] A. Cadranel, V. Strauss, J. T. Margraf, K. A. Winterfeld, C. Vogl, L. Đorđević, F. Arcudi, H. Hoelzel, N. Jux, M. Prato, D. M. Guldi, *J. Am. Chem. Soc.* **2018**, *140*, 904.
[238] T. Scharl, A. Cadranel, P. Haines, V. Strauss, S. Bernhardt, S. Vela, C. Atienza, F. Gröhn, N. Martín, D. M. Guldi, *Chem. Commun.* **2018**, *54*, 11642.

charge-separated states in the related electrostatically assembled carbon nanodots / porphyrins mentioned above.

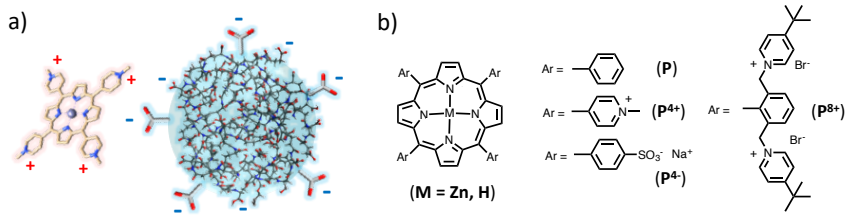

Figure 2.16. a) Donor-acceptor complex formed by pCND and ZnP^{4+}. b) Different porphyrins used for the formation of supramolecular complexes with pCND.

In fact, charge recombination is *ca.* 6 times faster than that of the covalent conjugates obtained with the nitrogen-doped CND described by Prato and co-workers.[239] These CND were prepared in a microwave assisted-synthesis using ethylenediamine and arginine, which result in CND with a high content of amine groups attached to the surface. The amine groups were further coupled with the carboxylic acids present in the porphyrin (P) structure, using EDC·HCl and NHS as coupling agents (Figure 2.17).

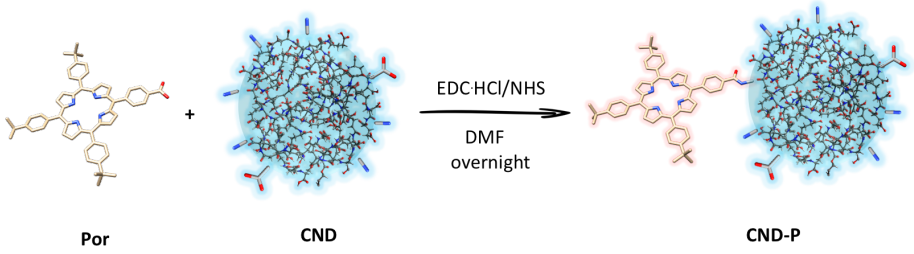

Figure 2.17. Schematic representation of the synthesis of CND-P hybrids.

First insights on the electronic interactions in the ground state between CND and P came from UV-Vis and emission spectroscopies. On one hand, through UV-Vis it was discerned that the Soret and Q-band absorptions are significantly red-shifted in the CND-P hybrids in comparison with free P. On

[239] a) F. Arcudi, L. Đorđević, M. Prato, *Angew. Chem. Int. Ed*. **2016**, *55*, 2107. b) F. Arcudi, V. Strauss, L. Đorđević, A. Cadranel, D. M. Guldi, M. Prato *Angew. Chem. Int. Ed*. **2017**, *56*, 12097.

the other hand, fluorescence emission spectroscopy revealed a CND fluorescence quenching from 17 % in CND to 9 % in the CND-P hybrid. Further experiments in the excited state revealed an ultrafast process ($> 10^{12}$ s^{-1}), where the strongly quenched porphyrin singlet excited states are transformed into short-lived (225 ps) charge-separated states.

Recently, CND have been explored in donor-acceptor hybrids in combination with 2D materials such as molybdenum disulfide (MoS_2) and tungsten disulfide (WS_2).[240] In this work, reported by Tagmatarchis and co-workers, the exfoliated MoS_2 and WS_2 were covalently functionalized with 1,2-dithiolane-modified CND (Figure 2.18). The characterization of these two hybrids by absorption and fluorescence spectroscopies showed a modulation of the optical properties upon the incorporation of the CND in the transition metal dichalcogenides.

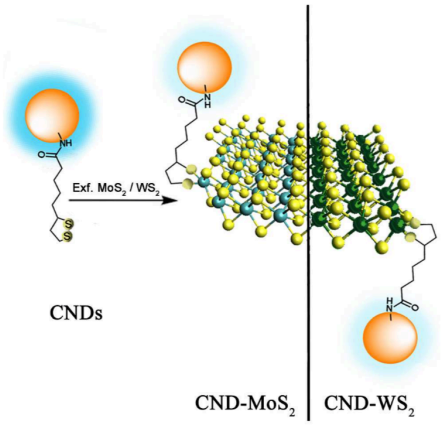

Figure 2.18. Schematic representation of the synthesis of CND-MoS_2 and CND-WS_2.

Furthermore, additional experiments in the excited state by femtosecond transient absorption spectroscopy, revealed an ultrafast energy transfer from CND to both MoS_2 and WS_2 upon photoexcitation. These results opened new pathways for the development of novel materials based in transition metal dichalcogenides for light energy harvesting and optoelectronic applications.

[240] L. Vallan, R. Canton-Vitoria, H. B. Gobeze, Y. Jang, R. Arenal, A. M. Benito, W. K. Maser, F. D'Souza, N. Tagmatarchis, *J. Am. Chem. Soc*. **2018**, *140*, 13488.

Regarding GQD, they have been less explored than CND in the formation of donor-acceptor hybrids, even though some examples can be found in the bibliography. One of those examples is that reported by Gong *et al*. where is described the formation of a nanoconjugate with nitrogen-doped GQD covalently functionalized with a typical photosensitive drug, Rose Bengal (RB).[241]

In this hybrid, the nitrogen-doped GQD act as donor and the traditional photosensitizer RB acts as the acceptor counterpart. Upon light irradiation this hybrid undergoes a fluorescence resonance energy transfer (FRET) process from the GQD to the RB, which resulted to be interesting for applications in photodynamic therapy, since GQD–RB exhibits high cytotoxicity after irradiation (Figure 2.19).

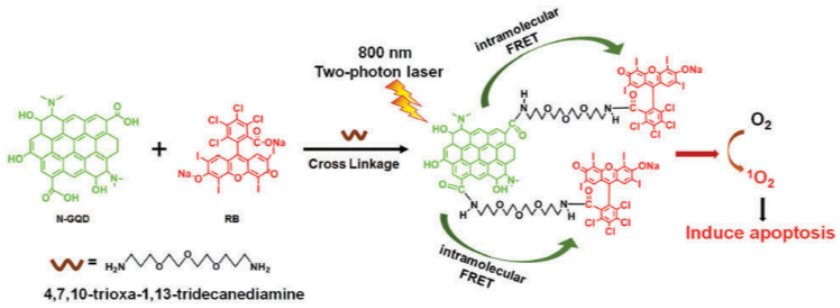

Figure 2.19. Schematic representation of the synthesis of the GQD–RB hybrid and its application in photodynamic therapy via a FRET process.

[241] J. Sun, Q. Xin, Y. Yang, H. Shah, H. Cao, Y. Qi, J. R. Gong, J. Li, *Chem.Commun*. **2018**, *54*, 715.

2.2. OBJECTIVES

2.2. OBJECTIVES

The main objective of this chapter is the synthesis and characterization of different types of carbon dots and their implementation in covalent donor-acceptor functional ensembles. Herein, we tested both, top-down and bottom-up approaches, for the synthesis of carbon dots which were further functionalized with different electroactive molecules. The obtained nanoconjugates were characterized by different structural and spectroscopic techniques in order to investigate their main differences and how that might influence the optoelectronic properties and, in some of the cases, the charge-transfer dynamics in excited state events.

The following specific goals are considered in Chapter 2:

i) Graphene quantum dots (GQD) and carbon nanodots (CND) production

- Production of GQD using a top-down approach where GO, produced from graphite, was cut off in small fragments under acidic treatment.
- Production of CND by a single source approach considering the pyrolysis of *L*-glutamic acid in a microwave-assisted synthesis (CND_{aGlu}).
- Annealing experiments of these CND at different temperatures for graphitization studies.
- Production of CND by a multi-component approach in a pressure-controlled microwave-assisted synthesis using citric acid and urea as precursors (pCND).
- Structural and optical characterization of GQD and CND and evaluation of their different characteristics and properties.

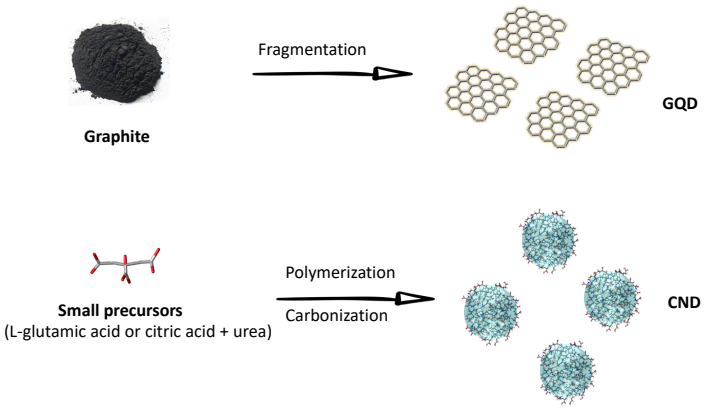

ii) pCND and GQD covalent functionalization with exTTF units

- Covalent functionalization of GQD and pCND with electron-donor exTTF units. The carboxylic acids in GQD and pCND are the anchoring points for the incorporation of exTTF through esterification reactions.

- Characterization of the GQD-exTTF and pCND-exTTF hybrids by different structural and spectroscopic techniques.

- Study of the electronic interactions between the exTTF units and the carbon dots by a series of steady-state and time resolved experiments. Comparison of the charge-transfer dynamics of GQD-exTTF and pCND-exTTF nanoconjugates in excited state events.

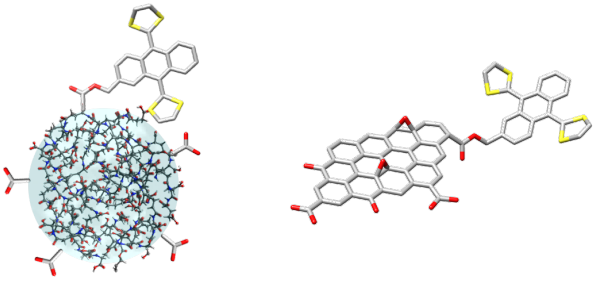

iii) pCND covalent functionalization with different electron-acceptor molecules

- Covalent functionalization of pCND with the electron-acceptor 11,11,12,12-tetracyano-9,10-anthra-*p*-quinodimethane (TCAQ) and phenylbutyric acid methyl esters of C_{60} and C_{70} ($PC_{60}BM$ and $PC_{70}BM$) by esterification reactions.

- Characterization of the structural features of the obtained nanoconjugates by different analytical and spectroscopic methods.

- Investigation of the ground-state and, in the case of TCAQ, excited state interactions between the electron-acceptor units and the pCND core.

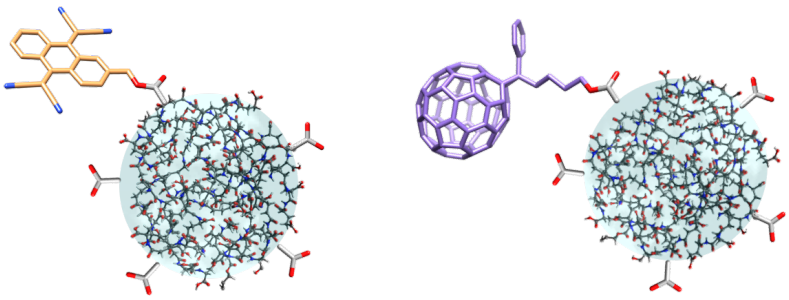

2.3. RESULTS AND DISCUSSION

2.3. RESULTS AND DISCUSSION

2.3.1. Synthesis and characterization of GQD

The production of GQD has been carried out by a top-down approach using GO as starting material. GO is a convenient material for the production of GQD because it presents a high number of oxygenated defects that facilitate the fragmentation under acidic treatment and heat. The fragmentation products of GO are photoluminescent GQD.

In this task, the first step was the synthesis of GO which was performed by the Kovtyukhova-Hummer's method.[76] By this procedure, pristine graphite was exposed to different oxidizing steps in order to obtain exfoliated graphene sheets with a large amount of oxygenated functional groups on their surfaces (Scheme 2.1).

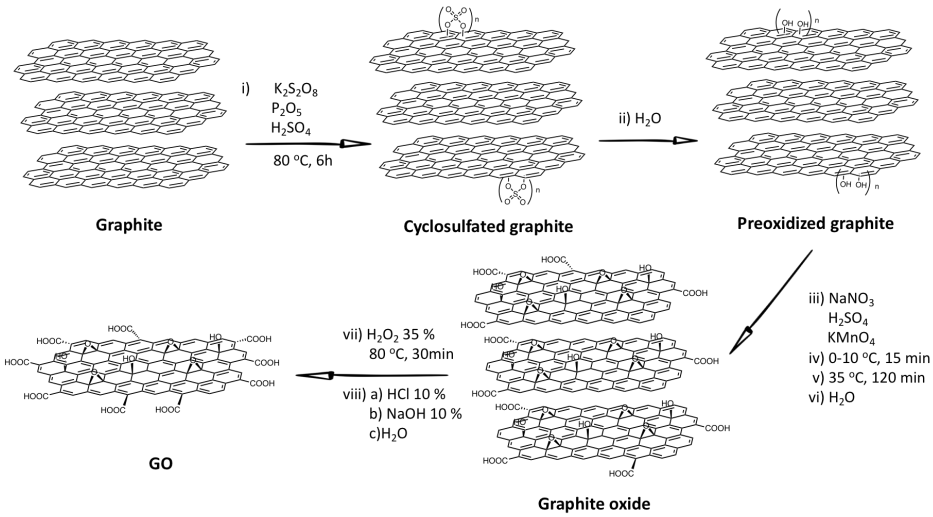

Scheme 2.1. Synthesis of GO by the Kovtyukhova-Hummer's method.

The starting graphite was subjected to a treatment with $K_2S_2O_8$, P_2O_5 and H_2SO_4 at 80 ºC in order to form an intermediate intercalated graphite material, which contains cyclosulfate groups attached. These groups were subsequently hydrolyzed with water giving rise to pre-oxidized graphite. The treatment of this pre-oxidized graphite with oxidizing agents, in acidic media and moderate heating, resulted in graphite oxide which was finally exfoliated when reacted with H_2O_2 (35 %) and heated under reflux.

The obtained GO was studied by TEM analysis (Figure 2.20a), where it was possible to discern large aggregates composed by a few layers, which confirmed the exfoliation of the pristine graphite after the oxidative processes. Moreover, FTIR analysis (Figure 2.20b) revealed the presence of new functional groups after the graphite oxidation such as the overlapping bands around 3600-3200 cm^{-1} due to the stretching vibrations of -OH groups, the peaks between 1000-1300 cm^{-1} related with C-O and C-OH vibrations, and the peak at 1719 cm^{-1} is due to the C=O stretching band. Furthermore, at 1561 cm^{-1} is present the broad and intense C=C skeletal in-plane vibration related with the sp^2 domains remaining in the structure.

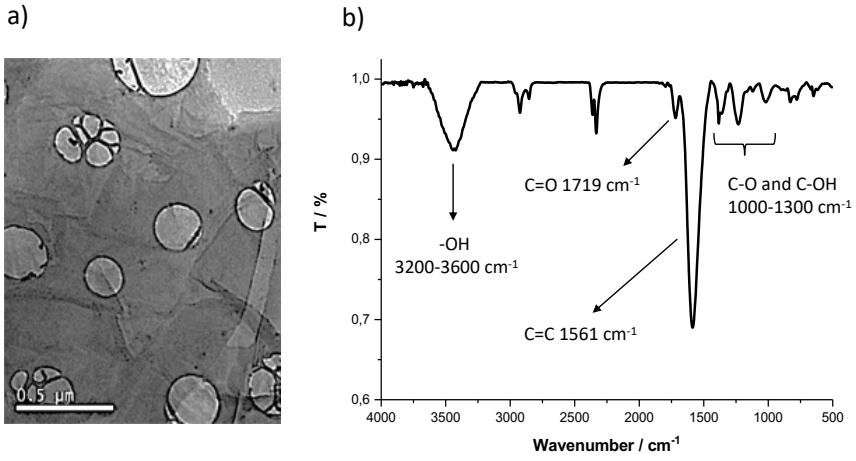

Figure 2.20. a) Representative TEM image of GO. b) FTIR spectrum of GO.

Additional information about the composition and the functional groups of GO was obtained from XPS.[157] The survey spectrum showed two different components as it was expected, corresponding to the C 1s and O 1s cores. The XPS spectrum was normalized to the C 1s signal, and ratios of 70.1 % for C and 29.9 % for O atoms were obtained. These results point to a more oxygenated material in comparison with the GO synthesized in Chapter 1 by the Staudenmaier method (C: 78.3 % and O: 21.1 %), which could be due to the pre-oxidation step during the synthesis following the Kovtyukhova-Hummer's method. Furthermore, the high-resolution C 1s core-level spectrum was deconvoluted in four components: C=C at 284.6 eV, C-O at 286.5 eV, C=O at 288.2 eV and O-C=O at 288.9 eV.

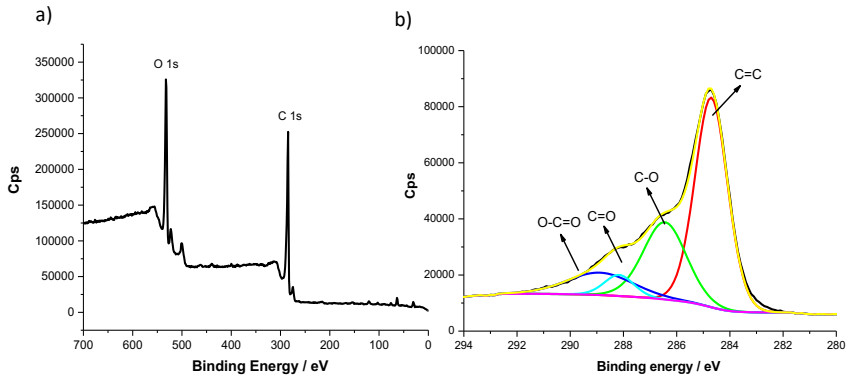

Figure 2.21. XPS analysis of GO. a) Survey spectrum. b) C 1s component deconvolution.

TGA analysis revealed a weight loss around a 36 % for the GO produced by the Kovtyukhova-Hummer's method due to the decomposition of the oxygen-containing groups attached to the surface (Figure 2.22).[150] However, the GO synthesized by the Staundemaier method presented a weight loss of a 13 %, which means that the GO produced by the Kovtyukhova-Hummer's method has a higher number of oxidized groups in the surface. Therefore, the high content in oxidized defects makes Kovtyukhova-Hummer's GO more appropriate than Staundemaier GO for the production of GQD by oxidative cutting.

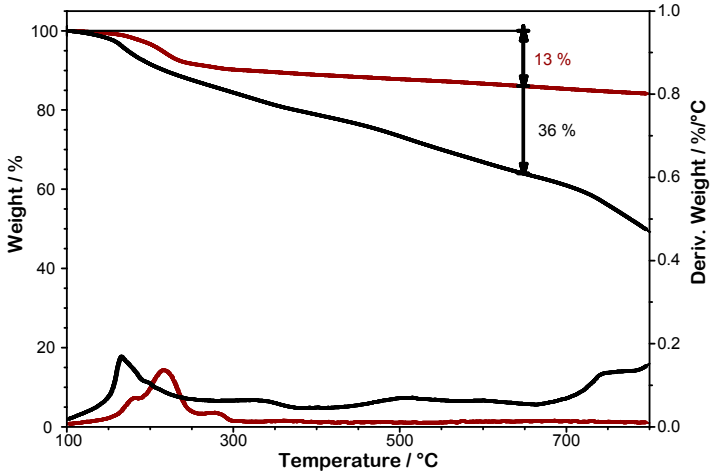

Figure 2.22. TGA and first derivative under inert conditions of Kovtyukhova-Hummer's GO (black) and Staundemaier GO (dark red).

Once obtained the GO, it was subsequently subjected to a similar procedure to the one reported by Haino *et al.*,[188] which consists in the oxidative cutting of GO sheets in a mixture of concentrated H_2SO_4 and HNO_3 (3/1 v/v) at 120 ^oC for 24 h, followed by neutralization of the excess of acid and a dialysis process (Scheme 2.2).

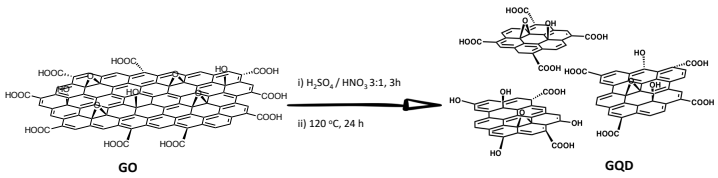

Scheme 2.2. Synthesis of GQD by Haino´s procedure.

First insights in the morphology of the as-prepared GQD were obtained from TEM and AFM. TEM analysis displays the presence of a mixture of few-layered GQD with sizes in the range from 4 to 18 nm, which confirmed the fragmentation of GO in small graphene layers. On the other hand, AFM analysis revealed the presence of individual GQD with an average height of 1.3 ± 0.3 nm. The lack of invidual GQD in the TEM could be due to aggregation of the GQD or/and due to the low contrast of the technique for the visualization of the single layered GQD.

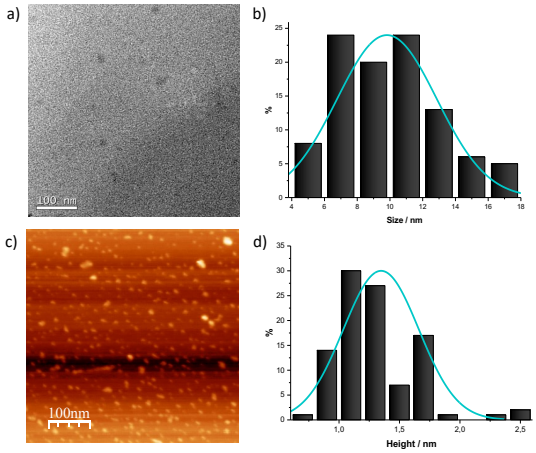

Figure 2.23. a) Representative TEM image of GQD. b) Size histogram with a curve fit of the data using a Gaussian model. Average size: 10.0 ± 3.1 nm. c) Representative AFM image of GQD. d) Height histogram with a curve fit of the data using a Gaussian model. Average height: 1.3 ± 0.3 nm.

Further structural information of the GQD was obtained from FTIR and NMR spectroscopies (Figure 2.24). In the FTIR spectrum was easy to identify the characteristic functional groups present in the GQD, highlighting the stretching vibrations of C=O and C-O at 1719 and 1150 cm^{-1}, respectively. In addition, the band due to the skeletal in-plane vibration of C=C was observed at 1611 cm^{-1}, which confirms that GQD retain the sp^2 lattice of the starting pristine graphite. Furthermore, in the region between 1000-1300 cm^{-1} there are signals due to the vibration of the hydroxy and epoxy functional groups. These results are in sound agreement with those obtained in the ^{13}C-NMR analysis, where it is important to stand out the presence of signals at 129.5-135.2 and 182.5 ppm which suggest the presence of sp^2 carbons and free carboxylic acids groups, respectively. By means of Raman spectroscopy (Figure 2.24b), additional information about the nature of GQD was obtained. The spectrum recorded for the as-prepared GQD showed the characteristic G band at 1600 cm^{-1} and the D band at 1390 cm^{-1}. The G band is related to the vibrations of the sp^2 carbons backbone, whereas the D band is due to the interruption of the sp^2 lattice by sp^3 defects arranged on the surface.

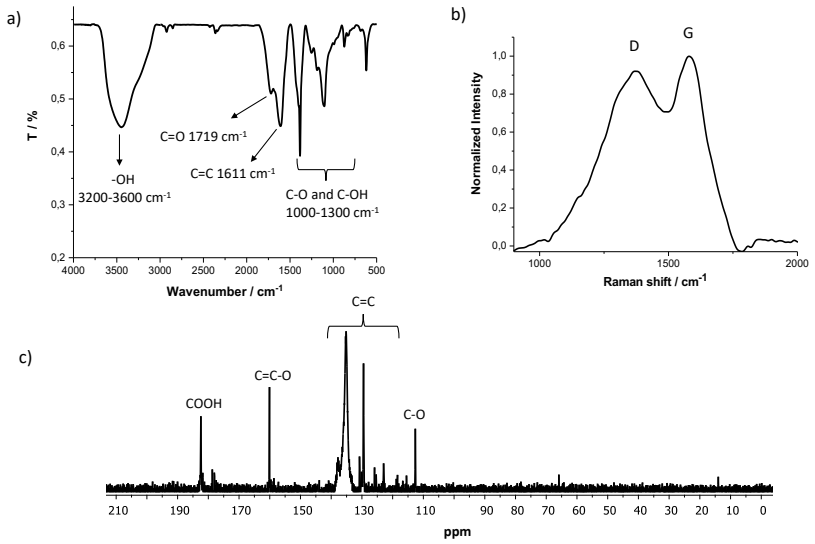

Figure 2.24. a) FTIR spectrum of GQD. b) Raman spectra of GQD recorded at room temperature and with a laser excitation wavelength of 532 nm. c) ^{13}C-NMR spectrum of GQD (175 MHz, D_2O, room temperature).

On top of that, in order to obtain more information about the features of the obtained GQD, their optical properties were investigated. The UV-Vis absorption spectrum showed an absorbance profile characteristic of GQD nanomaterials from 200 to 600 nm, where two different absorption peaks at 225 and 270 nm are appreciated. The former was attributed to the π-π* transition of aromatic C=C bonds, whereas the latter could be related with the n-π* transition of C=O bonds. Furthermore, upon light excitation (λ_{exc} = 350 nm), the as-prepared GQD display a strong emission at 525 nm responsible of the light-yellow color visible to the naked eye.

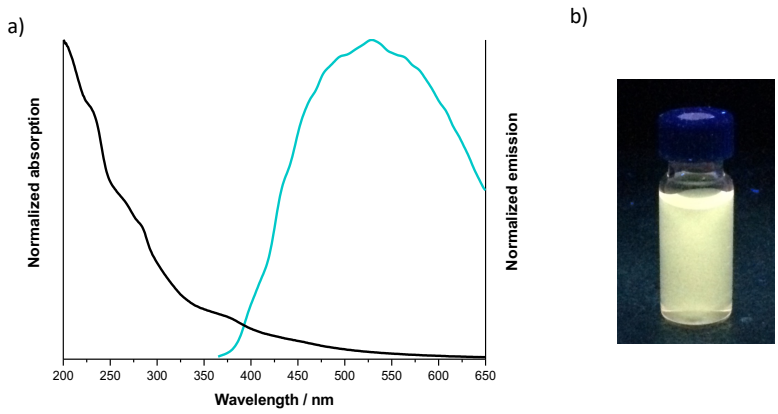

Figure 2.25. a) UV-Vis absorption spectrum (black) and emission spectrum under 350 nm excitation wavelength (blue) of a water solution of GQD. b) Water solution of GQD under 365 nm light irradiation.

2.3.2. Synthesis and characterization of CND

In this passage is discussed the synthesis and characterization of CND synthesized by bottom-up approaches. On one hand, it will be presented the synthesis of CND according to a single source approach, where further experiments have been performed in order to understand the graphitization process of these CND once subjected to an annealing treatment. On the other hand, it will be introduced the synthesis and characterization of CND by a multi-component approach in a microwave assisted synthesis controlling the pressure.

Synthesis of CND by a single source approach using L-glutamic acid as precursor (CND_{aGlu}). In this part CND have been synthesized by the pyrolysis of *L*-glutamic acid in a microwave reactor (Figure 2.26). Herein, *L*-glutamic acid was added into a microwave tube and heated to its decomposition temperature (210 ºC) in a microwave reactor for 10 min. A dark brown solid was obtained, which indicates the formation of CND. Afterwards, the larger aggregates were removed by filtration, and from the obtained solution the remaining starting material was removed by precipitation (more information in the experimental section).

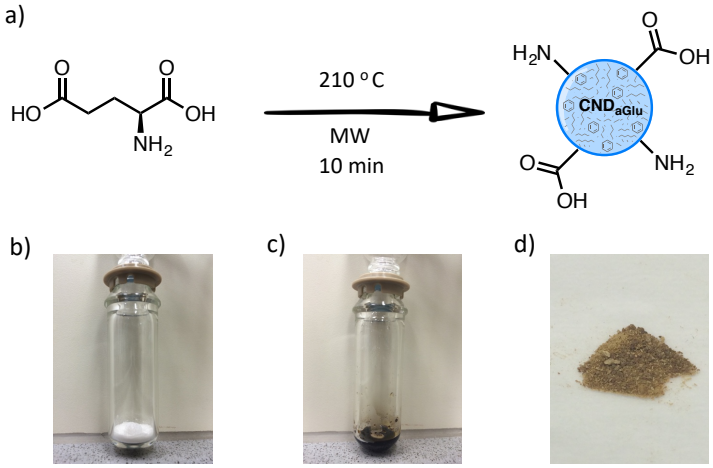

Figure 2.26. a) Schematic representation of CND_{aGlu} synthesis. b) *L*-glutamic acid before the microwave treatment, c) CND_{aGlu} obtained after microwave reaction, d) CND_{aGlu} powder.

The first step after the synthesis was to investigate the optical properties of this new nanomaterials by UV-Vis and emission spectroscopies (Figure 2.27). The UV-Vis spectrum of CND_{aGlu} in MeOH include an absorption maximum at 215 nm and an additional band at 334 nm (Figure 2.27a). Regarding to photoluminescence properties, first insights from the emission came after irradiating a solution of CND_{aGlu} in MeOH with 365 nm light resulting in a blue color emission at the naked eye. Moreover, in three-dimension excitation emission matrix fluorescence spectroscopy it was observed a strong fluorescence which maximizes at 410 nm (Figure 2.27b), with a quantum yield of 14.5 %. These CND_{aGlu} present a narrower emission band in comparison with GQD and the emission center is blue-shifted.

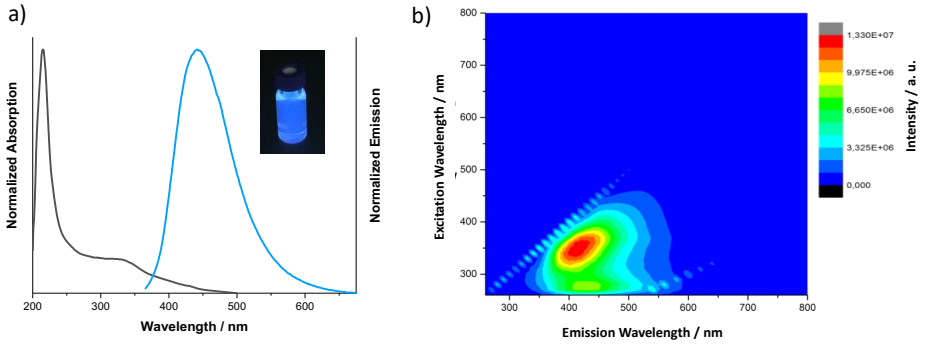

Figure 2.27. a) Normalized UV-Vis absorption spectrum (black) and emission spectrum under 350 nm excitation wavelength (blue) of CND_{aGlu} in MeOH. Inset: CND_{aGlu} solution in MeOH under 365 nm light irradiation. b) Excitation/emission 3D map of CND_{aGlu} in DMSO at room temperature with increasing intensity from blue to green and to red.

Conclusions about the morphology of the as-prepared CND_{aGlu} were drawn from TEM and AFM investigations. Through TEM analysis it was not possible to obtain clear information about the CND_{aGlu} morphology since only the large aggregates were discerned and it was not possible to detect individualized nanoparticles (Figure 2.28a). This fact could be related with the tendency to aggregate on the grid, or the too-low contrast of the individual CND. Nevertheless, from AFM images we derived rather uniform and monodisperse CND_{aGlu} with an average height of 1.6 ± 0.5 nm (Figure 2.28b and Figure 2.28c).

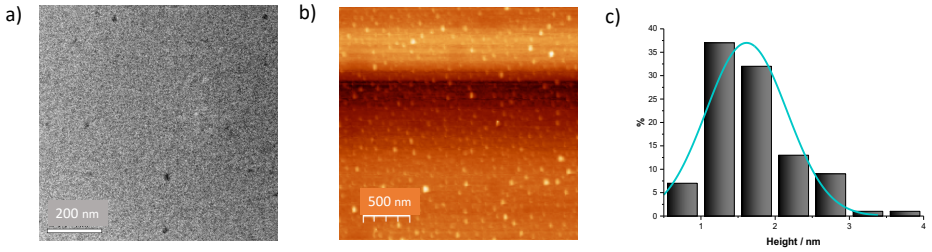

Figure 2.28. a) Representative TEM image of CND_{aGlu}. b) Representative AFM image of CND_{aGlu}. c) Height distribution histogram with a curve fit of the data using a Gaussian model. Average height: 1.6 ± 0.5 nm.

According to previous reports, mass spectrometry could be an interesting tool for obtaining information about the size and nature of the sample.[230] MALDI-TOF analysis showed a molecular weight dispersion, as expected from the random combination of different atoms, centred at 2000 Da (Figure 2.29b). Below this molecular weight only small oligomers were discerned and the presence of free *L*-glutamic acid was not detected (Figure 2.29a).

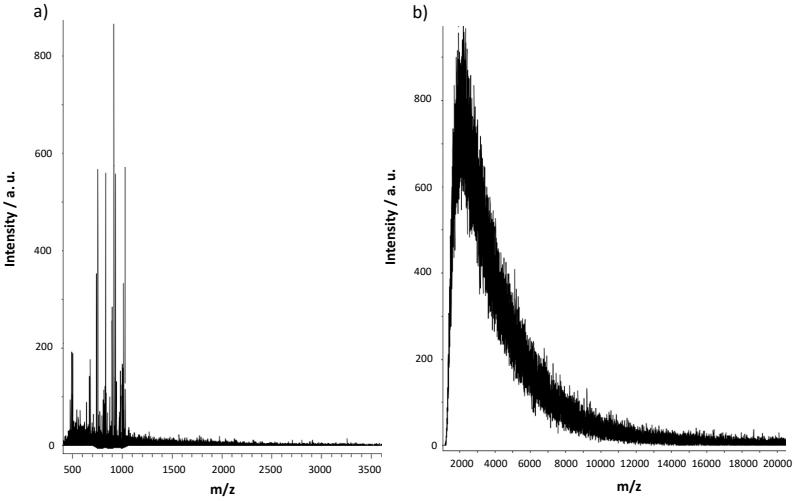

Figure 2.29. MALDI-TOF spectra of CND_{aGlu} obtained in reflector mode (a) and in lineal mode (b).

To gain structural insights, XPS and FTIR experiments were carried out. The XPS survey spectra, as illustrated in Figure 2.30a, showed three main features at 284.6, 399.6, and 531.6 eV related with the C 1s, N 1s and O 1s core-level contributions of CND_{aGlu}, as it was expected. Deconvolution of the C 1s core-level peak displays four species with binding energies of 284.8 eV (C-C/C=C), 285.7 eV (C-O/C-N), 286.4 eV (C=O) and 288.1 eV (O-C=O). Herein, it is important to mention the lack of the shake-up fingerprint characteristic contribution for graphitic systems which is in sound agreement with the results of TEM, where crystalline domains were not observed. Finally, in the deconvolution of N 1s and O 1s, the characteristic binding energies of carboxylic acids, amides and free amines present in the structure of CND_{aGlu} are obtained. Moreover, the content in graphitic-N is very low as it was expected due to the low number of sp^2 carbons in the structure of CND_{aGlu}.

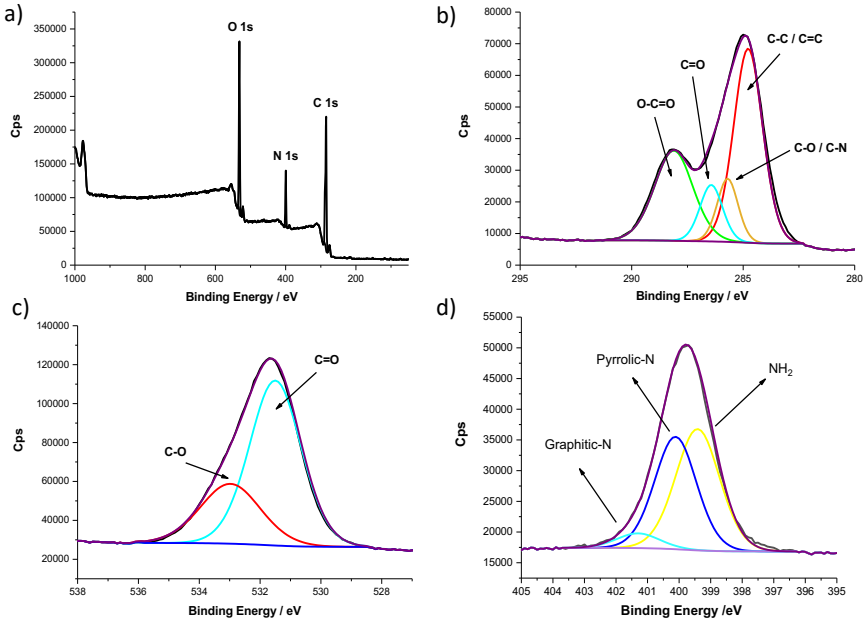

Figure 2.30. XPS analysis of CND_{aGlu} a) Survey spectrum. b) C 1s component deconvolution. c) O 1s component deconvolution. d) N 1s component deconvolution.

Independent proof for these functional groups came from FTIR spectroscopy. In Figure 2.31a, typical stretching vibration modes of C=O, C-N, and C-O are noted at 1725-1637, 1460-1383, and 1241-1085 cm^{-1}, respectively. In addition, the stretching vibrations of O-H and N-H evolve around 3300 cm^{-1}, while aliphatic C-H bond stretching vibrations are discernible at 2925-2833 cm^{-1}. However, the characteristic C=C stretching vibration is only observed in the form of a little shoulder included in the band of C=O groups.

Complementary information about the nature of the sample was obtained by XRD and Raman spectroscopy. The diffractogram of CND_{aGlu} is formed by several individual peaks which rather describe a crystalline polymeric phase instead of an amorphous graphitic system. Furthermore, in order to rule out that these peaks are due to remaining *L*-glutamic acid, the CND_{aGlu} diffractogram was compared with that of *L*-glutamic acid, and no coinciding diffraction peaks

were observed.[242] This analysis confirms the obtention on a novel nanomaterial with a crystalline phase not reported to date.[243]

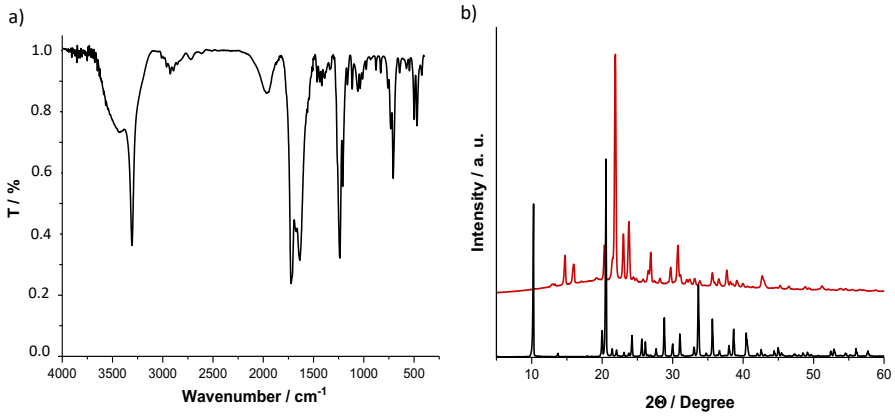

Figure 2.31. a) FTIR spectrum of $CND_{aGlu.}$ b) XRD diffractogram of: CND_{aGlu} (red) and *L*-glutamic acid (black).

Raman spectroscopy underlines the observations discussed atop for CND_{aGlu} samples where no features of graphitic systems (D and G bands) were discerned and only the typical fluorescence background was recorded during the experiments. These features are typical of polymeric-like carbon dots where incomplete carbonization may occur, resulting in polymeric structures rather than in pure graphitic structures.[244]

Taking into account all the structural characterization carried out on CND_{aGlu}, the methodology adopted in this PhD work seems to result in an incomplete carbonization giving rise to polymer-type materials with a prevalent ratio of sp^3 over sp^2 carbon domains, and a range of polar oxygenated and nitrogenated functionalities. For that reason, we decided to investigate if a post-treatment carbonization could result in materials with a higher degree of sp^2 domains. In these experiments, several CND_{aGlu} samples were heated in an oven during 72 h. at different temperatures, in the range from 100 to 220 ºC, and further characterized (Figure 2.32). In order to clearly distinguish the different

[242] H. Moshe, G. Levi, Y. Mastai, *CrystEngComm*, **2013**, *15*, 9203.
[243] http://webcsd.ccdc.cam.ac.uk
[244] F. Zhang, X. Feng, Y. Zhang, L. Yan, Y. Yang, X. Liu, *Nanoscale* **2016**, *8*, 8618.

samples, the as-prepared CND_{aGlu} were denominated CND_{aGlu} Ini, and the heated samples were designated according to the temperature of the heating process, i.e., the CND heated to 100 ºC are called CND_{aGlu} 100 and so on.

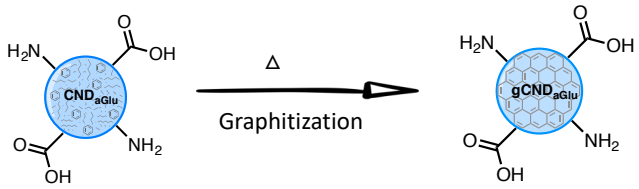

Figure 2.32. Schematic representation of graphitization experiments carried out with CND_{aGlu} samples.

The first property that was studied after the annealing experiments was the thermal stability of each sample by TGA (Figure 2.33). Until 140 ºC, no observable changes in the thermal stability of the samples are detected when compared with the CND_{aGlu} Ini reference material. Once the temperature is over 140 ºC, the material seems to start its graphitization process and, consequently, it is observed an increase in the thermal stability. This graphitization process reaches a maximum of thermal stability at 220 ºC, where the main weight loss is located around 400 ºC, which is almost 150 ºC above that observed for CND_{aGlu} Ini.

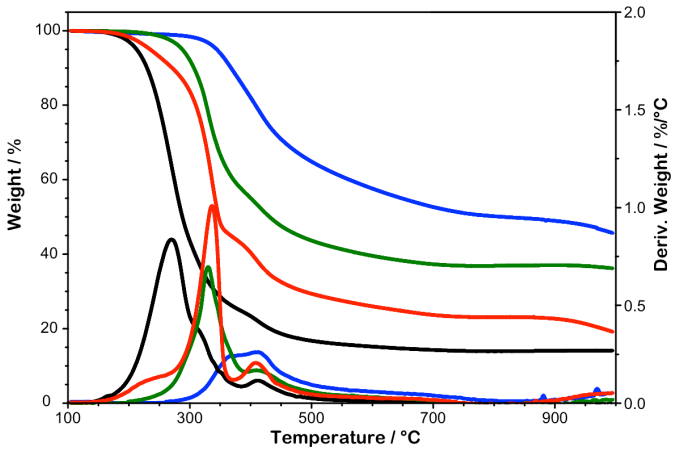

Figure 2.33. TGA and first derivative under inert conditions of CND_{aGlu} Ini (black), CND_{aGlu} 150 (red), CND_{aGlu} 180 (green) and CND_{aGlu} 220 (blue).

Furthermore, XRD analysis provided additional information about the structural evolution of CND_{aGlu} Ini after each heating step. XRD shows the transition of crystalline materials with clear diffraction peaks (Ini, 140 ºC and 160 ºC) to a broad diffraction at 220 ºC, consistent with an amorphous graphitic structure (Figure 2.34). Therefore, from the CND_{aGlu} Ini structure different crystalline phases are obtained up to 160 ºC, where a sudden graphitization starts to generate a new amorphous lattice, similar to that observed for graphite-based materials.[220,234]

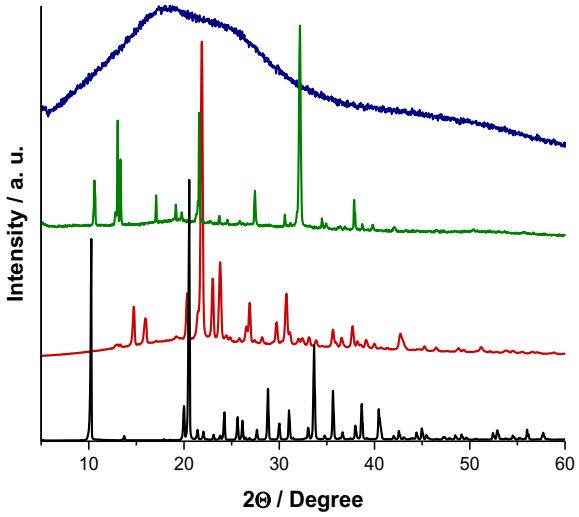

Figure 2.34. XRD diffractograms of CND_{aGlu} Ini, CND_{aGlu} 140 (red), CND_{aGlu} 160 (green) and CND_{aGlu} 220 (blue).

Raman spectra of the solid materials recorded with an excitation wavelenght of 785 nm were registered at the group of Prof. Juan Casado in Malaga University (Figure 2.35). This excitation falls in the longest wavelength tail of the fluorescence spectra of the samples, thus minimizing the interference effect of the strong photoluminescence noticed when excitations at 532 or 633 nm are used. Even in these conditions, the Raman spectra are unresolved for the samples treated at temperatures lower than 220 ºC as it is shown in Figure 2.35, where a typical fluorescence background is obtained.

Conversely, for the sample obtained at 220 ºC the Raman spectrum is resolved and presents the typical two bands pattern at 1300-1350 cm^{-1} and at 1560-1600 cm^{-1} owing to the characteristic D and G Raman bands, respectively, of

graphitic materials. At 220 ºC, the solid sample is not uniformly graphitized as it is seen in the spectra taken in zones of the sample with different brightness. The starting material together with those graphitized at 140 and 160 ºC display a spectral background, without vibrational resolution, consistent with their strong fluorescence. Nonetheless, the forms of the D and G bands start to get profiled in these samples at intermediate temperatures.

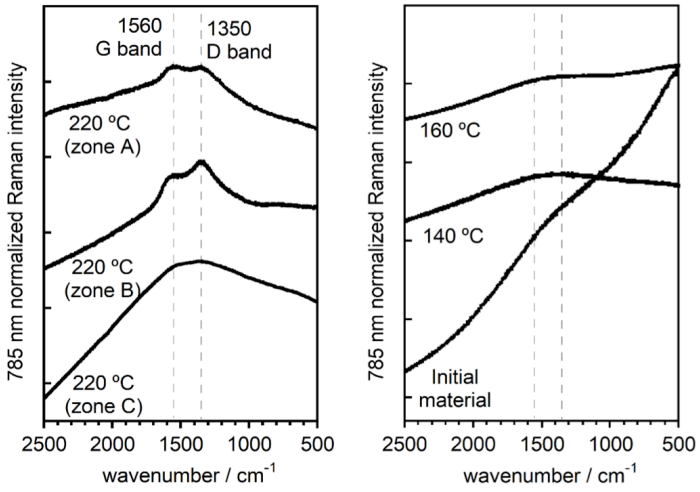

Figure 2.35. Room temperature Raman spectra of CND_{aGlu} Ini, CND_{aGlu} 140, CND_{aGlu} 160, and CND_{aGlu} 220, obtained with a laser excitation wavelength of 785 nm.

More information about the graphitization of CND_{aGlu} Ini was gathered from XPS. Table 2.1 shows the composition and deconvolutions of the different elements present in CND_{aGlu} Ini, CND_{aGlu} 160 and CND_{aGlu} 220. First insights in the composition of the samples point to an increase of the carbon content during the graphitization accompanied by a decrease of the oxygen content. Unlike carbon and oxygen, the nitrogen distribution experiences only a slight decrease during the graphitization process. One explanation for these results could be the decarboxylation of carboxylic acids during the heating steps, which would be the driving force for the formation of new sp^2 carbons, thus allowing the extension of the π-network. By this reason the content of oxygen would decrease, and the content of carbon would increase, as the obtained results show.

Looking inside the deconvolution of the C 1s core-level of the three samples, it is remarkable the increase of the C-C/C=C component whereas the component due to carboxylic acids (O-C=O) decreases when moving to samples heated at higher temperatures. Moreover, in the sample obtained at 220 ºC it was also discerned the presence of the distinctive π-π^* shake-up band of graphitic structures,[105] which confirms the increase of the sp^2 content with the increase in the annealing temperature. Moving to the deconvolution of the N 1s core-level contribution, herein it is noticeable a raise in the graphitic-N component as long as the temperature increases, resulting the higher content of this species for the CND_{aGlu} 220 sample. Finally, in the deconvolution of the O 1s, the drop in the C=O content, accompanied with the raise of the C-O content (see FTIR discussion below), perfectly match with the results observed for the C 1s core-level contribution.

Table 2.1. Atomic percentages of C, N and O in CND_{aGlu} Ini, CND_{aGlu} 160 and CND_{aGlu} 220 samples, as determined by XPS measurements.

	CND_{aGlu} Ini	CND_{aGlu} 160	CND_{aGlu} 220
C	**65.8**	**70.0**	**75.1**
C-C/C=C	48.1	57.5	65.6
C-O/C-N	11.3	15.7	24.7
C=O	11.0	9.0	8.7
O-C=O	29.7	17.8	-
π-π^*	-	-	1.0
N	**10.3**	**9.7**	**8.2**
Pyridinic-N	-	14.2	16.3
NH_2	50.0	35.0	30.7
Pyrrolic-N	44.1	37.0	33.6
Graphitic-N	5.9	13.9	19.5
O	**23.9**	**20.3**	**16.6**
C=O	70.3	40.9	30.8
C-O	29.7	59.1	69.2

More information about the different functional groups present in the CND_{aGlu} samples was obtained from FTIR and NMR spectroscopies. FTIR spectra are quite similar for the initial sample and that heated at 140 ºC (Figure 2.36). The peaks at 1723 and 1635 cm^{-1}, which resulted from the carboxylic acids C=O and amide C=O stretching vibrations, are observed. Moreover, the broad peak area from 3000-3700 cm^{-1} belongs to the carboxylic acids OH and to the amide NH stretching bands. The narrow and strong peak at 3304 cm^{-1} in both spectra indicates also the presence of primary amine groups.

Moving to the next sample (160 ºC) several changes are observed. On the one hand, two new peaks appear at 1775 and 1692 cm^{-1}, which could be the symmetric and asymmetric C=O stretching modes of anhydride groups. The presence of these groups could be a consequence of a condensation process between free carboxylic acids of the CND. This argument is in agreement with the presence of the new signals at 1355 and 1314 cm^{-1}, which might be the symmetric and asymmetric C-O stretching modes of the formed anhydrides.

On the other hand, the peak of the free amine groups at 3304 cm^{-1} completely disappear at 160 ºC. Bearing in mind these facts, the loss of carboxylic acid and amine groups could be the driving force for the graphitization of the CND surface with the introduction of sp^2 carbons, increasing its thermal stability, as shows the TGA analysis. In accordance with this assumption, the small peak between 1550-1600 cm^{-1} could be due to the newly formed C=C stretching bands.

Finally, in the 220 ºC sample, very few vibrations are observed, the most prominent is a broad peak centered at 1683 cm^{-1}, which is the result of the combination of the C=O peaks of the anhydrides, amides and the few remaining carboxylic acids stretching vibrations, it also contains as a shoulder the C=C stretching bands present in the CND. The lack of many signals in this spectrum could be due to a notable increase of the sp^2 carbons, giving rise to a more graphene-like material.

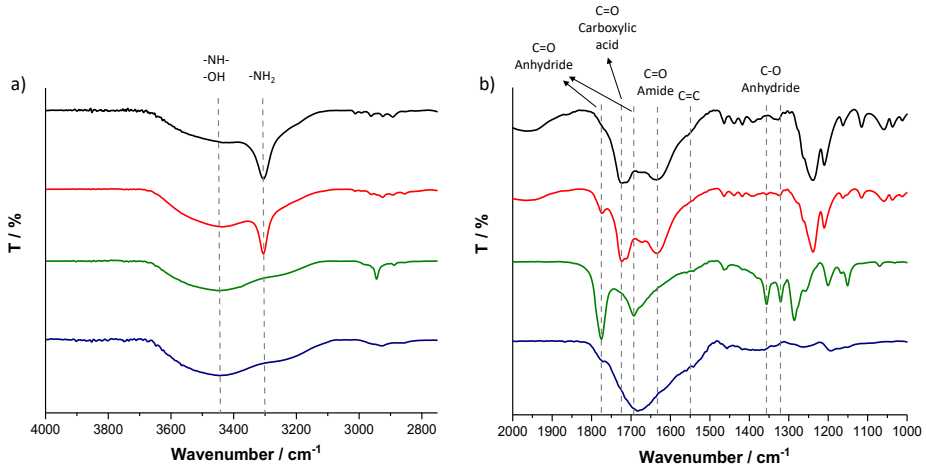

Figure 2.36. FTIR spectra of CND_{aGlu} Ini (black), CND_{aGlu} 140 (red), CND_{aGlu} 160 (green) and CND_{aGlu} 220 (blue). a) From 4000 to 2750 cm^{-1}. b) From 2000 to 1000 cm^{-1}

In regard to NMR experiments, in both ^{1}H and ^{13}C-NMR, no noticeable changes were detected in the registered resonance signals until 160 ºC, where first indications of the beginning of a graphitization process were noticed. Above 160 ºC new signals were discerned in the aliphatic region (red) of the spectra but, more important, new features raised up in the aromatic region (blue) as a result of the graphitization process which led to the formation of new sp^2 carbons. These carbon signals between 150 and 165 ppm are relatively upshifted due to the surrounding electron-withdrawing groups. Furthermore, it is important to mention the presence of new features stemming from the formation of additional carboxylic groups and amides.

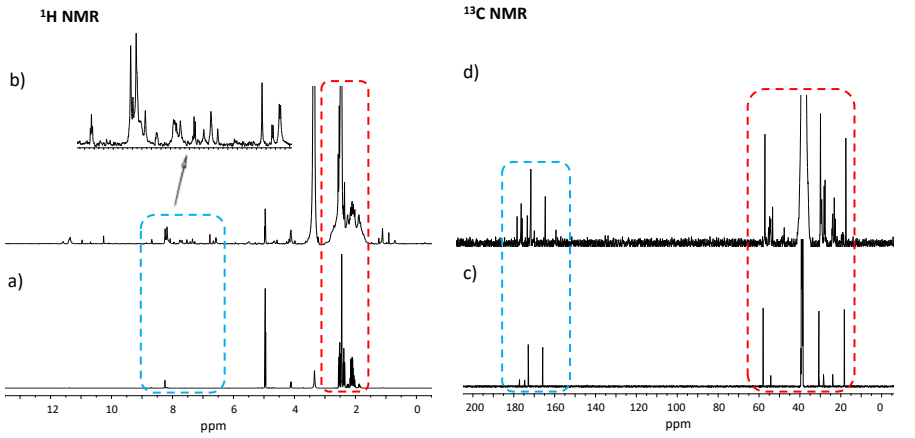

Figure 2.37. ^{1}H-NMR (700 MHz) spectra of CND_{aGlu} 160 (a) and CND_{aGlu} 220 (b) in -DMSO-d_6. ^{13}C-NMR (175 MHz) spectra of CND_{aGlu} 160 (c) and CND_{aGlu} 220 (d) in DMSO-d_6.

In addition to the structural changes mentioned above also morphological changes were detected by AFM microscopy. The most abrupt comparison was that of the CND_{aGlu} Ini with the sample obtained after annealing at 220 ºC. For this sample, a more heterogeneous distribution of nanoparticles is obtained, and the statistical analysis of the height of 100 of them by AFM allows to estimate an average height of 2.1 ± 0.6 nm for CND_{aGlu} 220. This height is slightly above that observed for CND_{aGlu} Ini, where an average height of 1.6 ± 0.5 nm was obtained. That is to say that during the annealing steps the particles grow-up as well as the number of sp^2 carbons increases due to the condensation of the polymer-like chains. In this process, the loose of functional groups such as amines and carboxyl acids takes places.

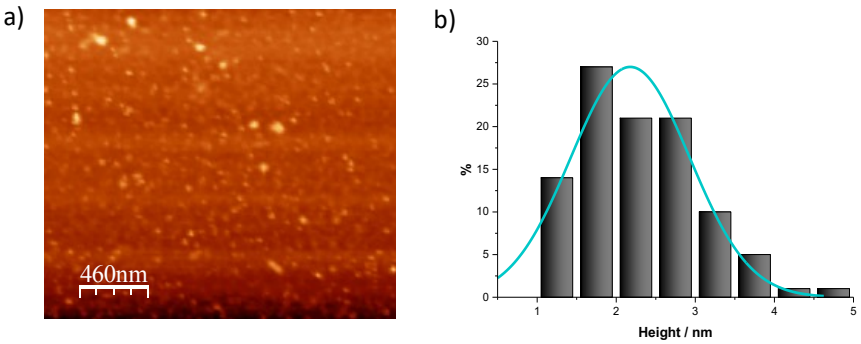

Figure 2.38. Representative AFM image of CND_{aGlu} 220. d) Height histogram with a curve fit of the data using a Gaussian model. Average height: 2.1 ± 0.6 nm.

Furthermore, MALDI-TOF experiments also confirmed that through the annealing processes the molecular weight of the samples slightly increases. Figure 2.39 shows the MALDI-TOF spectra of CND_{aGlu} 220 which present a polydisperse profile with most of the population located around 2500 Da, 500 Da above that observed for CND_{aGlu} Ini (2000 Da).

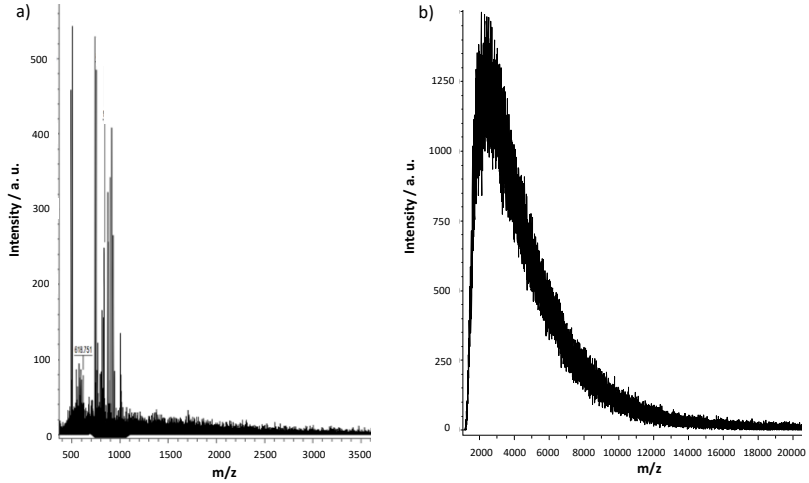

Figure 2.39. MALDI-TOF spectra of CND_{aGlu} obtained by reflector mode (a) and by lineal mode (b).

All CND are fluorescent and the fluorescence colour changes with the graphitization degree from blue to yellowish (Figure 2.40a).

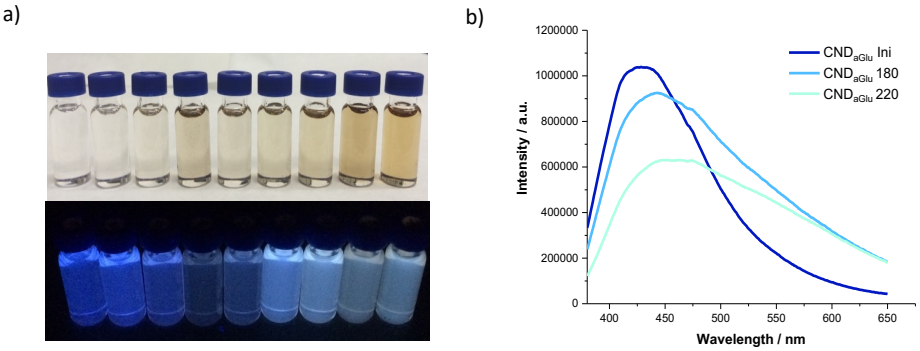

Figure 2.40. a) Top: 0.1 mg/mL solutions in DMSO of CND_{aGlu}, going from the initial sample (left) to samples heated at 100, 120, 140, 150, 160, 180, 200 and 220 ºC (right). Bottom: The same solutions under 365 nm illumination. b) Emission spectra of CND_{aGlu} Ini and the samples heated at 180 and 220 ºC in DMSO under 365 nm light irradiation.

The emission of selected CND_{aGlu} samples under the excitation wavelength of 365 nm is shown in Figure 2.40b. The emission band becomes broader with the increase of the temperature at the time that the maximum peak of each band is slightly red-shifted. This widening of the emission band gives rise to a profile very similar to that observed in GQD, which matches the previous evidences of the graphitization of the sample.

Investigations on the excitation-dependence in the emission of the different samples evidence that until samples heated at 180 ºC, the trend is the same for all the samples: a red-shift when the excitation wavelength increases, and the fluorescence intensity decreases as the peak red shifts (Figure 2.41a). Nevertheless, for the samples heated over 180 ºC a red-shift is noticed, but in this case, the intensity increases with the increasing excitation wavelengths (Figure 2.41b). These results, in principle, are consistent with photoluminescence mechanisms where trap states and assembled individual emitters are present (see section 2.1.4),[182] although are being subjected to further investigations.

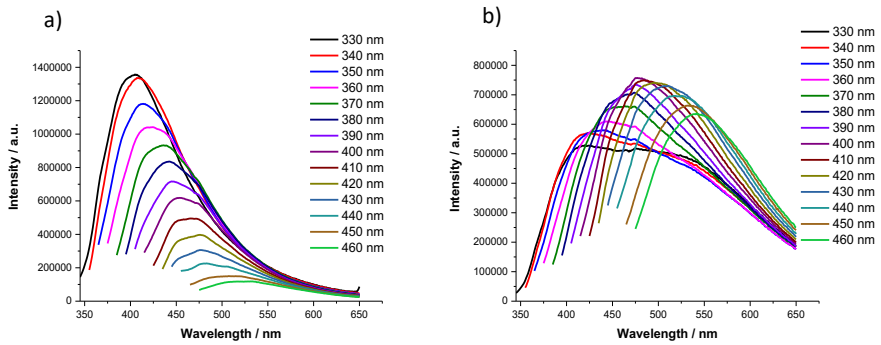

Figure 2.41. a) Emission spectra of CND_{aGlu} Ini in DMSO at different wavelengths. b) Emission spectra of CND_{aGlu} 220 in DMSO at different wavelengths.

Finally, it is necessary to comment that the graphitization of CND_{aGlu} not only affected the optical properties but also the solubility in water of these nanomaterials. As CND_{aGlu} starts to graphitize, its solubility in water tends to decrease significantly due to the loss of hydrophilic functional groups such as amines or carboxylic acids through condensation or decarboxylation processes, which trigger the formation of new sp^2 domains. The samples subjected to heating treatments above 180 ºC are practically insoluble in aqueous media unlike the samples heated below that temperature. Therefore, in the synthesis of these nanoparticles it is important to reach an equilibrium between the graphitization degree and the required solubility properties.

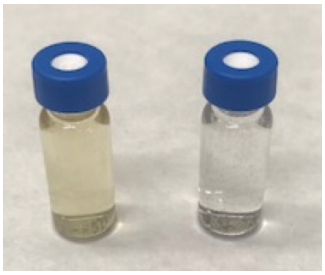

Figure 2.42. CND_{aGlu} Ini solution (left) and CND_{aGlu} 180 solution (right) in water.

In brief, we can conclude that the solvent-free pyrolysis of *L*-glutamic acid by microwave synthesis leads to an incomplete graphitization of the precursor resulting in polymer-like nanoparticles. Further experiments confirmed that it is possible to graphitize this CND_{aGlu} in a second heating step when using temperatures above 160 ºC, reaching the complete graphitization over 200 ºC.

Synthesis of CND by a multi-component approach using citric acid and urea as precursors under controlled pressure (pCND).

In the second part of this section is described a different approach employed for the preparation of CND. It consists in a multi-component methodology instead of a single-source precursor method, using as starting materials the widely employed citric acid and urea. Furthermore, to assure the complete carbonization of the precursors in only one step and to avoid further graphitization experiments, the methodology developed by Guldi and co-workers was implemented (Figure 2.43a).[205,209] In brief, a water solution of citric acid and urea was heated in a microwave reactor maintaining the pressure constant at 15 bar for 5 min. (more details can be found in the experimental section).

Pressure control limits the escape of gaseous byproducts from the solution, causing pCND formation to terminate at an early stage. The resulting polymeric structures formed at the beginning of the reaction serve as precursors in a carbonization step, where new extended π-systems (the CND cores) are formed. Furthermore, these conditions afforded deeply blue-colored solutions, which under UV illumination exhibit bright blue fluorescence (Figure 2.43c and Figure 2.44b). The water of the solution was evaporated and the solid was washed several times with acetone in order to remove small polymer by-products from the reaction. The obtained solid is a shiny black powder as shown in Figure 2.43d.

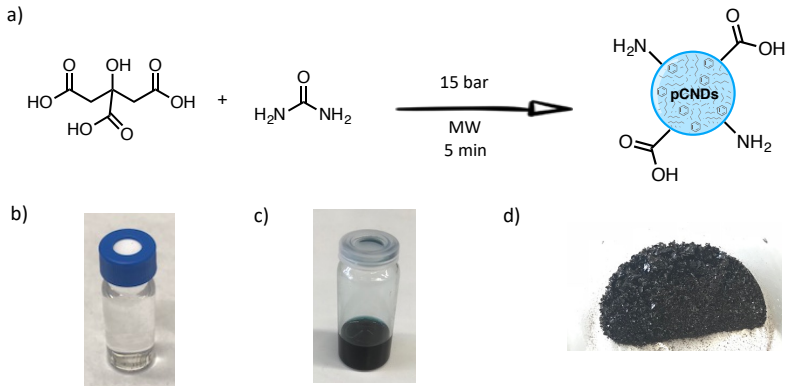

Figure 2.43. a) Schematic representation of the pCND synthesis, b) Water solution mixture of citric acid and urea. c) pCND solution obtained after microwave reaction. d) pCND powder.

Considering the optical properties, pCND exhibit an intense absorption band with a maximum at 350 nm and a shoulder at 376 nm. In addition, pCND present a single emission band, relatively narrow, located at 439 nm when the spectrum was recorded using a 350 nm excitation wavelength. Moreover, this type of carbon dots present a photoluminescence quantum yield around 20% in water,[232] which is higher than that observed for CND_{aGlu} Ini.

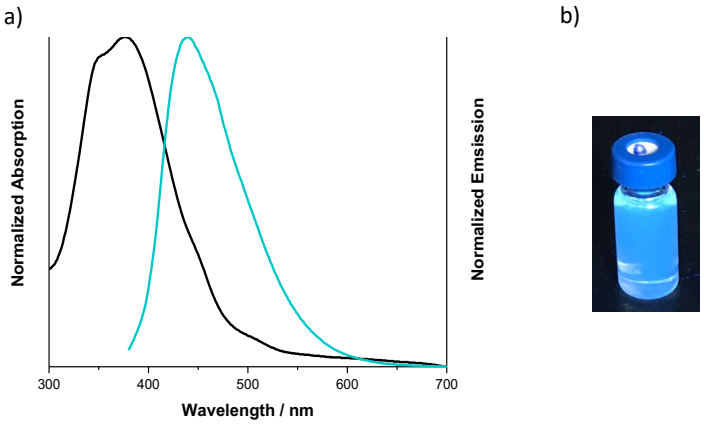

Figure 2.44. a) Normalized UV-Vis absorption spectrum (black) and emission spectrum under 350 nm excitation wavelength (blue) of pCND in DMSO. b) pCND water solution under 365 nm light illumination.

Morphological characterization by AFM reveals the presence of homogeneous particles with a mean height around 2 nm after the statistical evaluation of the height of 100 objects (Figure 2.45a and Figure 2.45b). TEM revealed the presence of amorphous particles where no diffraction of crystallites was observed. Moreover, the individual particles exhibit too little mass-thickness contrast to be detectable and only the larger aggregates were observed through this technique (Figure 2.45c and Figure 2.45d).

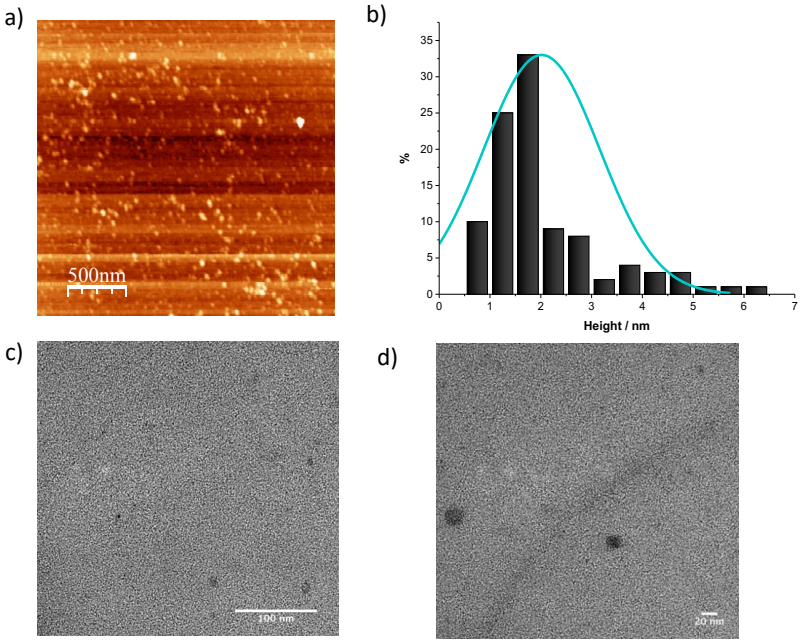

Figure 2.45. a) Representative AFM image of pCND. b) Height histogram with a curve fit of the data using a Gaussian model. Average height: 2.1 ± 1.1 nm. c) and d) Representative images obtained at two magnifications, 100 and 20 nm, respectively.

XRD analysis supported the information obtained from TEM, where non-defined crystalline phases were discerned resulting in a material weakly ordered. Furthermore, through XRD it was demonstrated the absence of starting materials or crystalline polymeric domains in the structure due to the lack of well-defined peaks in the XRD diffractogram (Figure 2.46a). This fact corroborated the thermolytic decomposition and complete carbonization of the precursors under this condition, unlike it happened in the above-mentioned synthesis of CND_{aGlu} where a further annealing treatment was required. The results obtained by Raman spectroscopy also pointed in this direction, as shown in Figure 2.46b, where a graphitic profile for pCND was observed with the characteristics D and G bands located at 1350 and 1569 cm^{-1}, respectively.

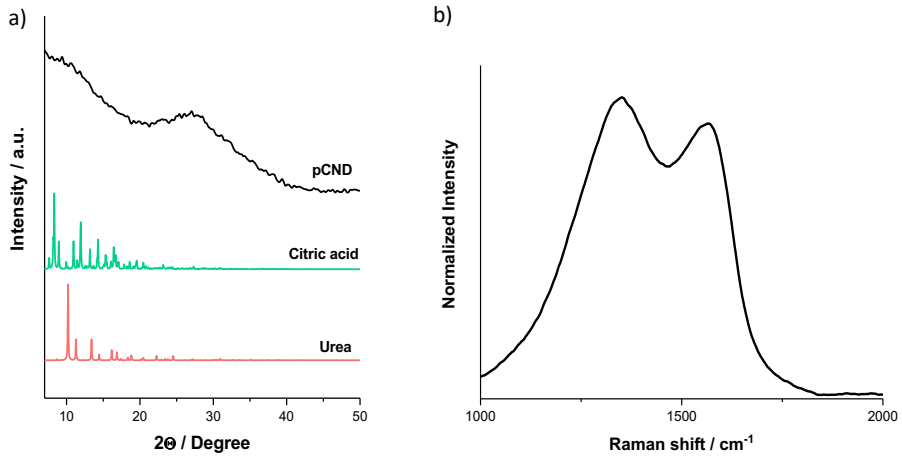

Figure 2.46. a) XRD diffractogram of urea (red), citric acid (green) and pCND (black). b) Room temperature Raman spectrum of pCND obtained with an excitation wavelength of 532 nm.

MALDI-TOF analysis revealed the polydisperse nature of pCND where most of the population exhibits a molecular weight around 2200 Da (Figure 2.47). This molecular weight distribution is very similar to those observed for CND_{aGlu} samples, so the different synthetic methodologies lead to particles with similar weights.

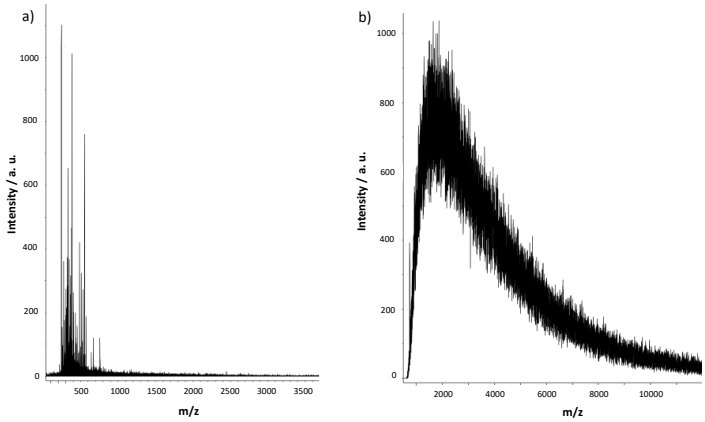

Figure 2.47. MALDI-TOF spectra of pCND obtained in reflector mode (a) and in lineal mode (b).

In order to gain information about the functional groups present in the sample FTIR and NMR experiments were carried out. The FTIR spectrum of pCND reveals the presence of abundant hydrophilic groups in their structure (Figure 2.48). In the region between 3200-3600 cm^{-1} a broad band, which involves the vibrations of OH and NH groups, reveals the presence of alcohols and amines in the surface. The next region that is important to point out is in the range between 1500-1750 cm^{-1}, where in a broad band converge the stretching vibrations of different C=O groups such as amides, esters, carboxylic acids and, C=C groups due to olefinic or aromatic groups. Finally, below 1500 cm^{-1} is important to mention the presence of signals originated from alcohols, ethers and C–O groups.

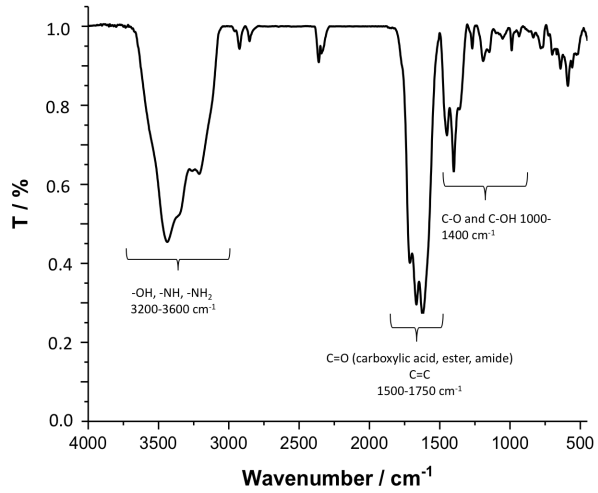

Figure 2.48. FTIR spectrum of pCND.

^{1}H and ^{13}C-NMR experiments were carried out in order to complete the information obtained by FTIR studies. The presence of carboxylic acids and amides was confirmed due to the signals located at 7-10 ppm (^{1}H-NMR) and 160-180 ppm (^{13}C-NMR), which fit with the data obtained by FTIR spectroscopy. In regard to the presence of sp^2 carbons, in the spectra of pCND the features belonging to aromatic signals at 6-8 ppm (^{1}H-NMR) and 150-160 ppm (^{13}C-NMR) are observed, confirming the presence of graphitic domains in the structure. Furthermore, several aliphatic signals are discerned in both ^{1}H and ^{13}C-NMR spectra, which point to the presence of sp^3 carbons in the structure of pCND.

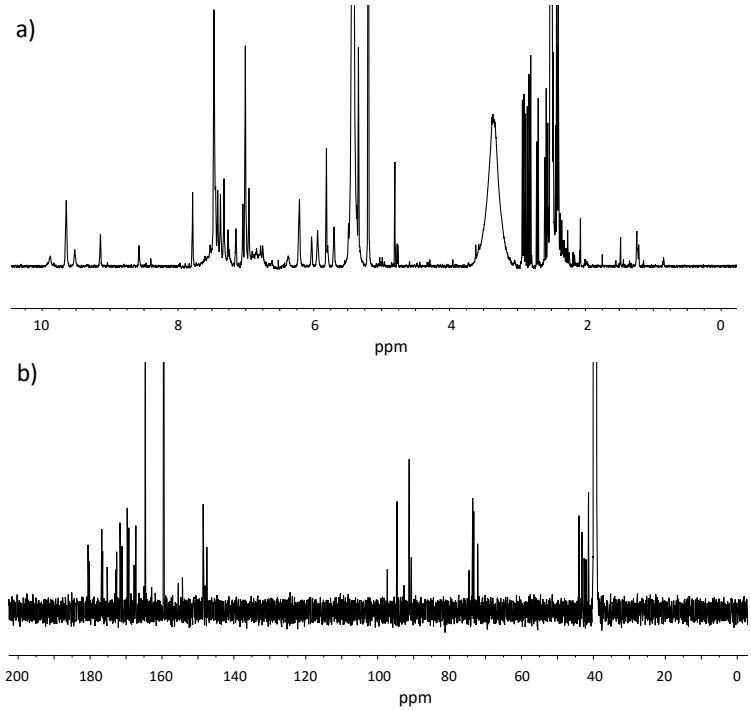

Figure 2.49. a) ^{1}H-NMR (700 MHz) spectrum of pCND in d_6-DMSO. b) ^{13}C-NMR (175 MHz) spectrum of pCND in d_6-DMSO.

XPS analysis was used to further investigate the composition of pCND. The survey spectrum (Figure 2.50a) shows three different elements: C 1s (285.1 eV), N 1s (399.9 eV), and O 1s (532.2 eV) as it was expected. Figure 2.50b represents the high-resolution spectrum of the C 1s core-level, which can be deconvoluted in six components, corresponding to C-C/C=C (284.6 eV), C-O/C-N (285.3 eV), C-O-C (286.6 eV), C=O (287.9 eV), O-C=O (288.7 eV) and π-π^* shake-up (290.2 eV).[245] Deconvolution of the N 1s core-level, on the other hand, shows four different chemical components located at 398.2 eV, 399.1 eV, 400.1 eV and 401.2 eV corresponding to pyridinic-N, amine-NH_2, pyrrolic-N and graphitic-N groups, respectively.[246] Finally, the O 1s deconvolution leads to two different components C=O (531.8 eV) and C-O (532.6 eV) groups.

[245] T. I. T. Okpalugo, P. Papakonstantinou, H. Murphy, J. McLaughlin, N. M. D. Brown, *Carbon* **2005**, *43*, 153.
[246] F. Arcudi, L. Đordević M. Prato, *Angew. Chem. Int. Ed.* **2017**, *56*, 4170.

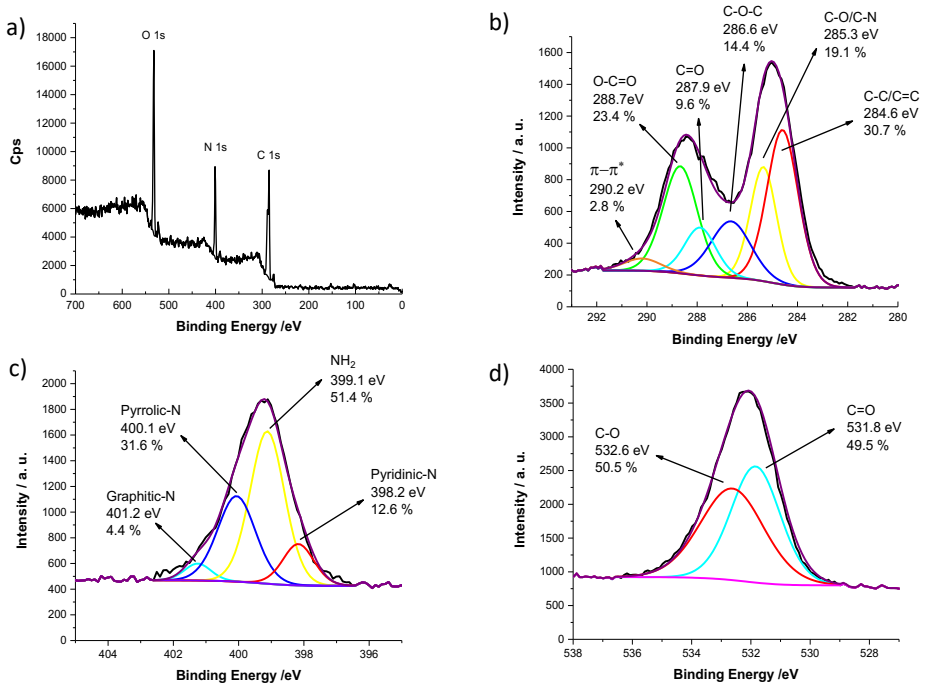

Figure 2.50. XPS analysis of pCND. a) Survey spectrum. b) C 1s component deconvolution. c) N 1s component deconvolution. d) O 1s component deconvolution.

All this characterization reveals a pCND structure with a carbon core containing a mixture of sp^3 and sp^2 domains with different hydrophilic functionals groups attached to its surface. For this reason, pCND nanoparticles are highly soluble in polar solvents. Furthermore, the homogeneous size of the obtained pCND yields a narrow excitation emission. From here, it can be deduced that the pressure controlled microwave method used for pCND production results in CND with enhanced properties compared with that of CND_{aGlu}. The production of the latter by solvent-free pyrolysis of *L*-glutamic acid needed further annealing treatments to obtain graphitic CND instead of polymer-like CND, and resulted in a more complex method with larger reaction times.

For that reasons, in the next section pCND will be the scaffold employed to form covalent D-A hybrids with organic electroactive molecules, and thus perform photophysical studies for exploring pCND in charge transfer processes.

2.3.3. Functionalization of GQD and pCND with exTTF molecules

Both CND and GQD exhibit interesting properties such as good UV/Vis light absorption, water solubility, and high stability, which make them interesting materials for their implementation as photosensitizers for solar-driven catalysis and in charge-transfer assays for artificial photosynthesis. For that reason, the study of these carbon nanoparticles in photoinduced charge transfer processes is an interesting topic for determining their role in D-A assemblies. Up to now, there are only a few examples of photoinduced charge transfer studies which involve CND or GQD in the formation of D-A complexes (see section 2.1.6). In this context, the supramolecular combination of CND or GQD with electroactive molecules has been more extensively used than the covalent approach.

With these precedents, in this PhD work we have considered the preparation of novel CND or GQD based electron donor–acceptor systems by using covalent approaches. In a first instance, we have linked photo- and redox-active exTTF molecules[247] to CND and GQD materials. These building blocks are pro-aromatic electron donors which undergo a remarkable gain of aromaticity and planarity upon oxidation, forming stable two-electron oxidized species at relatively low oxidation potentials. Considering these features, exTTFs have been widely used to form electroactive architectures when linked to fullerenes, carbon nanotubes, and graphene.[92, 93,248] They have been successfully used for preparing photoinduced electron transfer systems[249] as well as solar energy conversion devices.[250]

[247] F. G. Brunetti, J. L. López, C. Atienza, N. Martín, *J. Mater. Chem.* **2012**, *22*, 4188.
[248] N. Martín, L. Sánchez, M. A. Herranz, B. Illescas, D. M. Guldi, *Acc. Chem. Res.* **2007**, *40*, 1015.
[249] a) J. López-Andarias, M. J. Rodríguez, C. Atienza, J. L. López, T. Mikie, S. Casado, S. Seki, J. L. Carrascosa, N. Martín, *J. Am. Chem. Soc.* **2015**, *137*, 893. b) J. López-Andarias, J. L. López, C. Atienza, F. G. Brunetti, C. Romero-Nieto, D. M. Guldi, N. Martín, *Nat. Commun.* **2014**, *5*, 3763.
[250] S. Wenger, P.-A. Bouit, Q. Chen, J. Teuscher, D. Di Censo, R. Humphry-Baker, J.-E. Moser, J. L. Delgado, N. Martín, S. M. Zakeeruddin, M. Grätzel, *J. Am. Chem. Soc.* **2010**, *132*, 5164.

The carboxylic acids located in the surface of the carbon dots were used for the incorporation of the exTTF units, since they can act as anchoring points through esterification reactions.

2.3.3.1. Synthesis of exTTF electron donor units

In order to ensure the decoration of pCND or GQD with exTTF, it was synthesized an exTTF which contains a free benzylic alcohol for enabling the carboxylic acid esterification. The formation of the exTTF backbone was carried out by a Horner-Wadsworth-Emmons reaction between the dimethyl-(1,3-dithiol-2-yl)-phosphonate **16** (Scheme 2.3) and 2-hydroxymethyl-anthraquinone **18** (Scheme 2.4). To achieve this, it was necessary the synthesis of the phosphonate following the procedure showed in Scheme 2.3. In this route, vinylene trithiocarbonate **12** initiated a sequence of four reaction steps: *S*-methylation, reduction with $NaBH_4$, treatment with HBF_4 and phosphonylation with trimethylphosphite, to yield the desired phosphonate **16**.[251]

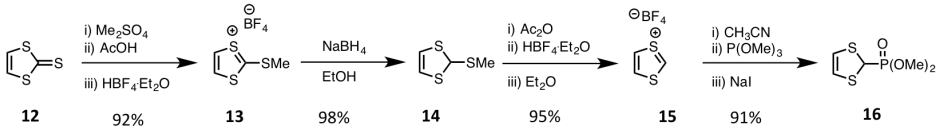

Scheme 2.3. Synthesis of phosphonate **16**.

Afterwards, the addition of *n*-BuLi over phosphonate **16** generated the corresponding carbanion that reacted with the protected 2-hydroxymethylanthraquinone **18**[252] to yield derivative **19** (Scheme 2.4). Finally, the benzylic alcohol of **19** was deprotected with tetra-n-butylammonium fluoride (TBAF) resulting in the desired exTTF derivative **20**.[253]

[251] A. J. Moore, M. R. Bryce*, Synthesis* **1991**, 26.
[252] G. J. Marshallsay, M. R. Bryce, *J. Org. Chem. Soc.* **1994**, *59*, 6847.
[253] S. González, N. Martín, D. M. Guldi, *J. Org. Chem.* **2003**, *68*, 779.

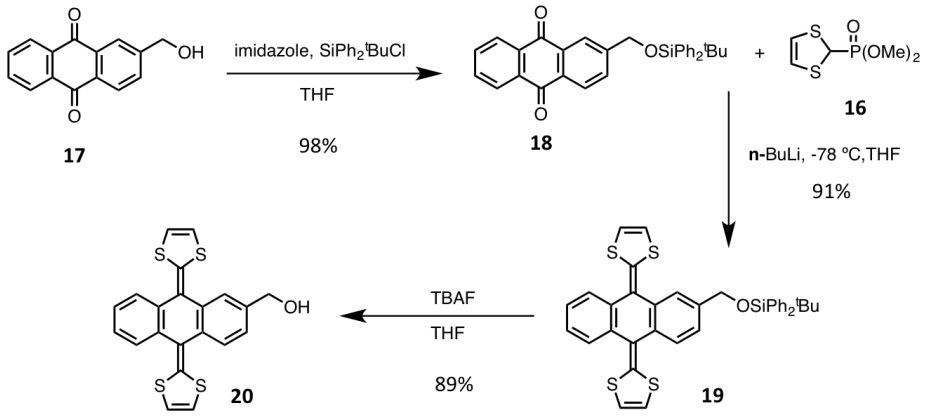

Scheme 2.4. Synthesis of exTTF **20**.

NMR spectroscopy was a convenient tool to confirm the synthesis of exTTF **20** (Figure 2.51). In the ^{1}H-NMR spectrum it is possible to distinguish the signals of the aromatic protons of the anthracene core between 7.3-7.8 ppm (blue), the doublet due to the 1,3-dithiole rings at 6.7 ppm (red), the methylene between the anthracene and the alcohol at 5.6 ppm (yellow) and the signal due to the alcohol as a triplet at 5.3 ppm (green).

In the ^{13}C-NMR spectrum, the signals of the anthracene core are discerned at 120.7–140.7 ppm (blue), the signals of the 1,3-dithiole rings at 118.0-118.2 ppm, and finally the methylene is located at 62 ppm.

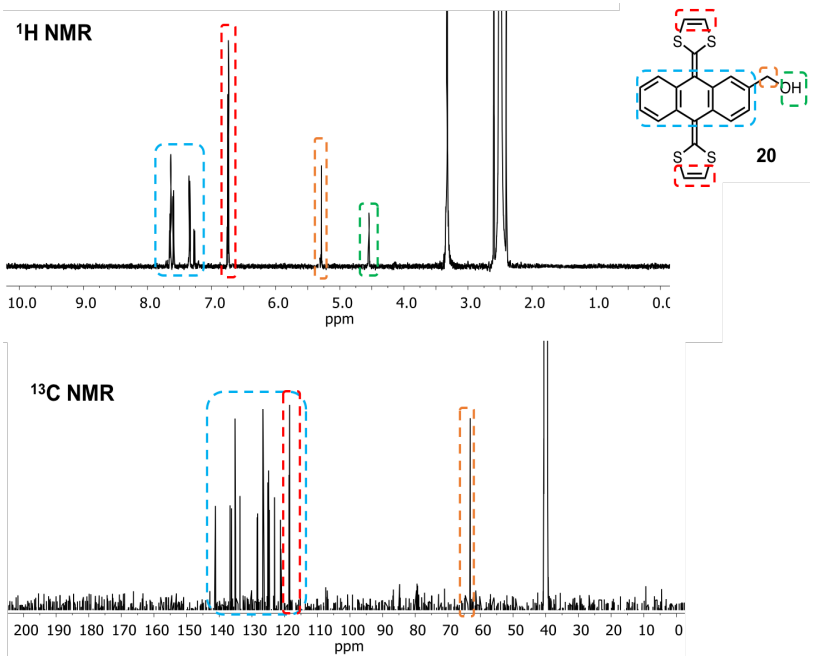

Figure 2.51. ^{1}H-NMR (700 MHz) and ^{13}C-NMR (175 MHz) spectra of compound **20** in d_6-DMSO.

The optical properties of **20** were studied by UV-Vis spectroscopy. Figure 2.52b shows the absorption spectrum of **20** where it is possible to see the characteristic absorptions of this compound responsible of its yellow colour. Two main peaks are observed, the less intense located at 366 nm and the maximum centered at 432 nm.

As mentioned above, exTTFs are good electron-donors suitable for charge-transfer investigations in combination with CND or GQD. In fact, exTTF moiety **20** is able to oxidize to its dicationic form at 0.01 V *vs.* Ag/$AgNO_3$ in DMSO (Figure 2.52c), in a quasi-reversible classic process in exTTFs.[254] During the oxidation, the geometry of the exTTF core changes from butterfly-shaped in its neutral form to a planar structure, where the aromatic dithiolium rings are perpendicular to the aromatic anthracene skeleton. The remarkable

[254] a) S.-G. Liu, I. Pérez, N. Martín, L. Echegoyen, *J. Org. Chem.* **2000**, *65*, 9092. b) M. A. Herranz, L. Yu, N. Martín, L. Echegoyen, *J. Org. Chem.* **2003**, *68*, 8379.

gain of aromaticity and planarity upon oxidation stabilizes the exTTF dicationic species (Figure 2.52a).

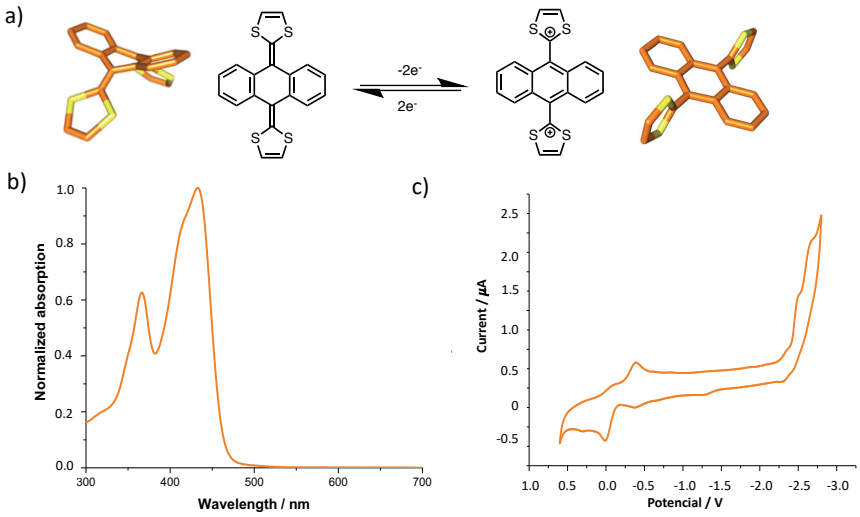

Figure 2.52. a) Geometrical change of exTTF upon oxidation. b) UV-Vis of compound **20** in DMSO. c) Cyclic voltammograms of **20** in a DMSO solution containing 0.1 mM $TBAPF_6$ as supporting electrolyte with a glassy carbon working electrode, a $Ag/AgNO_3$ reference electrode, and a Pt wire counter electrode.

2.3.3.2. Synthesis and characterization of pCND-exTTF hybrids

Once synthesized the donor exTTF molecules, the next step was their covalent anchoring to the pCND surface. As the structural characterization of pCND evidenced, the surface of this carbon dots is covered by carboxylic acids that can be employed as anchoring point for the attachment of the exTTF molecules. For that task, the as-prepared pCND were treated with $SOCl_2$ at 70 ºC to transform the carboxylic acids in acyl chlorides. Afterwards, the acyl chlorides reacted *in situ* with exTTF **20** in an esterification reaction to afford the **pCND-exTTF** hybrids.

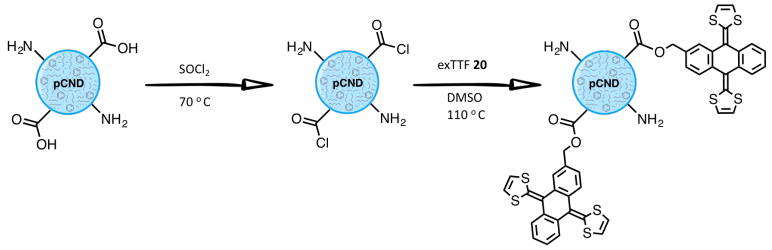

Scheme 2.5. Schematic representation of the synthesis of **pCND-exTTF**.

The obtained **pCND-exTTF** hybrids were fully characterized in order to confirm the covalent functionalization of **pCND**.

From TEM we concluded the presence of small individual **pCND-exTTF** coexisting with larger objects. However, by AFM a more homogeneous distribution with an average height of 5.3 ± 1.9 nm was found in the images taken on mica substrates. Only a few aggregates were discernable. From here, we can deduce that this increase in the dimensions of **pCND-exTTF** with regard to pCND (2.1± 1.1 nm) is due to the incorporation of the exTTF units on the pCND surface.

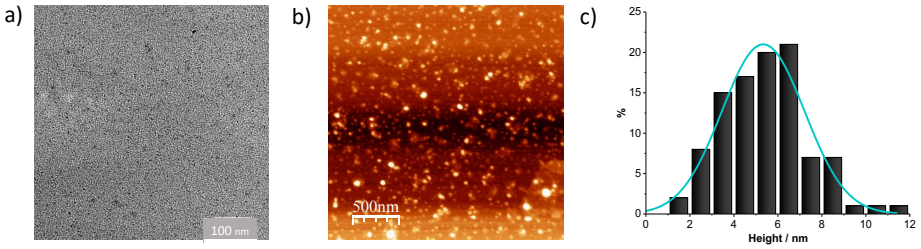

Figure 2.53. a) Representative TEM image of **pCND-exTTF**. b) Representative AFM image of **pCND-exTTF**. c) Height histogram with a curve fit of the data using a Gaussian model. Average height: 5.3 ± 1.9 nm.

Additional support of the covalent functionalization was extracted from ^{1}H and ^{13}C-NMR spectroscopy (Figure 2.54). Both spectra showed the signals corresponding to the 1,3-dithiole rings (red) at 6.7 ppm (^{1}H) and 118.0–118.2 ppm (^{13}C) as well as the anthracene core (blue) at 7.3–7.8 ppm (^{1}H) and 120.7–140.7 ppm (^{13}C), which confirmed the exTTF incorporation. As a result of pCND functionalization, the signal corresponding to the hydroxy group of **20** disappears in the covalent hybrid. Moreover, some of the pCND NMR signals

are not observed in the **pCND-exTTF** spectra. It is possible that the corresponding groups are entrapped within the pCND core or that their signals are either very broad or invisible owing to the restricted mobility of such groups in this environment.

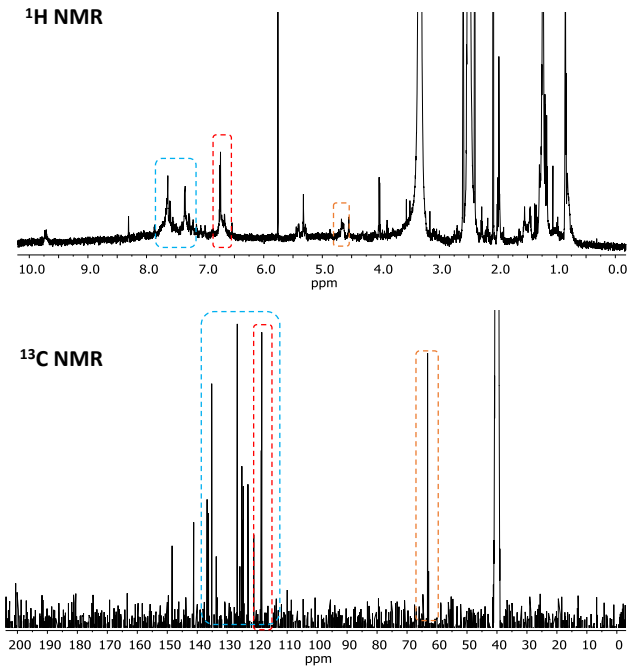

Figure 2.54. ^{1}H-NMR (700 MHz) and ^{13}C-NMR (125 MHz) spectra of **pCND-exTTF** in d_6-DMSO.

The next step was to perform TGA under inert atmosphere, where a similar weight loss is observed for both pCND and **pCND-exTTF**, although the stability of the pCND seems to increase upon esterification (Figure 2.55a). Furthermore, as we can see in the thermogram of **pCND-exTTF,** there is no trace of free exTTF, which suggests that the molecular units are covalently bonded. Regarding the **pCND-exTTF** structure, from powder XRD (Figure 2.55b) it was observed a broad diffraction related to an amorphous graphitic structure very similar to the starting pCND. The Raman spectrum of **pCND-exTTF** also reveals graphitic content and defects, since both G and D bands are observed (Figure 2.55d). The comparison with the spectrum of pCND showed minor changes such as an increase of the G band and a decrease of the D band

after the functionalization process, which might be an indication of the loss of sp^3 defects and the formation of new sp^2 bonds.

From FTIR spectroscopy (Figure 2.55c), the typical stretching vibrations of C=O, C-N, and C-O of **pCND-exTTF** are distinguished at 1715–1633, 1401, and 1090– 1018 cm^{-1}, respectively. Furthermore, stretching vibrations of O-H and N-H evolve around 3430–3182 cm^{-1}, while aliphatic C-H bond stretching vibrations are discernible at 2925–2852 cm^{-1}. Herein, it was difficult to see the formation of a new ester signal as a consequence of the functionalization, since the initial sample had ester groups in the structure. Nevertheless, changes in the shape of the broad band relative to the CO groups were observed, which could be indicative of the formation of new ester bonds. Finally, the C-S stretching of the exTTF molecule was detected at 647 cm^{-1}.

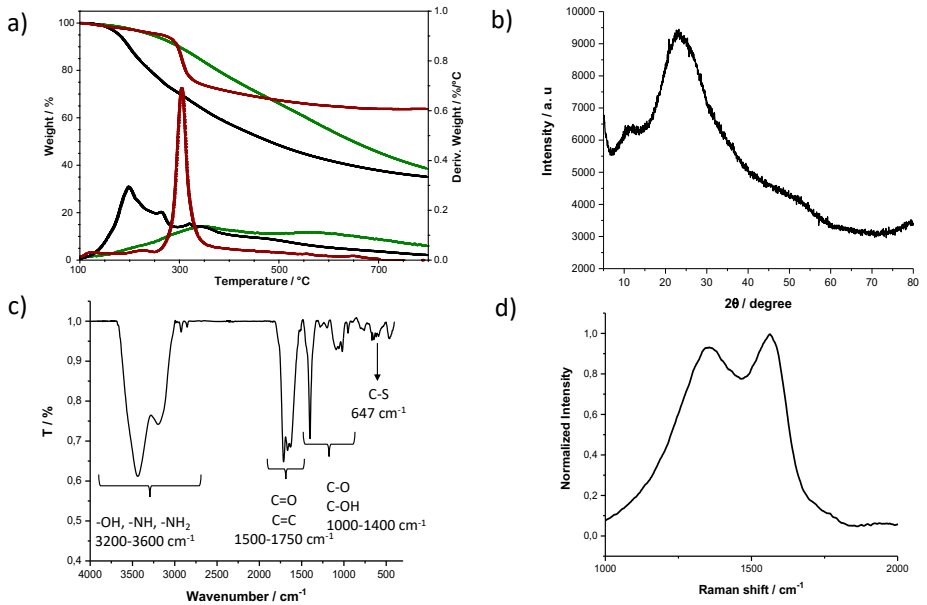

Figure 2.55. a) TGA and first derivative under inert conditions of pCND (black), exTTF **20** (dark red) and **pCND-exTTF** (green). b) XRD diffractogram of **pCND-exTTF**. c) FTIR spectrum of **pCND-exTTF**. d) Raman spectrum of **pCND-exTTF**.

XPS was also found to be useful in terms of deriving structural information for **pCND-exTTF** (Figure 2.56). Along with contributions stemming from the core-levels of C 1s, N 1s, and O 1s, evidence for the S 2p core-level was noted for **pCND-exTTF**. This confirmed the presence of sulfur in **pCND-exTTF**,

which was not found for the as-prepared pCND prior to the reaction with exTTF. Deconvolution of the C 1s core-level region of **pCND-exTTF** points to the same six species found for pCND, with binding energies of 284.1 (C-C/C=C), 284.9 (C-O/C-N), 286.2 (C-O-C), 287.4 (C=O), 288.2 (O-C=O), and 289.7 eV (π–π* shake up). The presence of the characteristic π–π* shake up of carbon atoms in graphene-like structures is in agreement with the TGA and Raman analyses and prompts to some graphitic character of the CND materials. TEM and AFM further support the notion of π–π* shake up bands, since the presence of small aggregates together with individual pCND are observed.

The fit of the N 1s line of **pCND-exTTF** shows four different chemical components centered at 398.5 (pyridinic N), 399.3 (amine), 400.0 (pyrrolic N), and 401.0 eV (graphitic N). The ratios of the same components in pCND suggest a slight increase of graphitic and pyridinic nitrogen after functionalization with exTTF and a decrease of the free amine groups, which goes along with the TGA results.

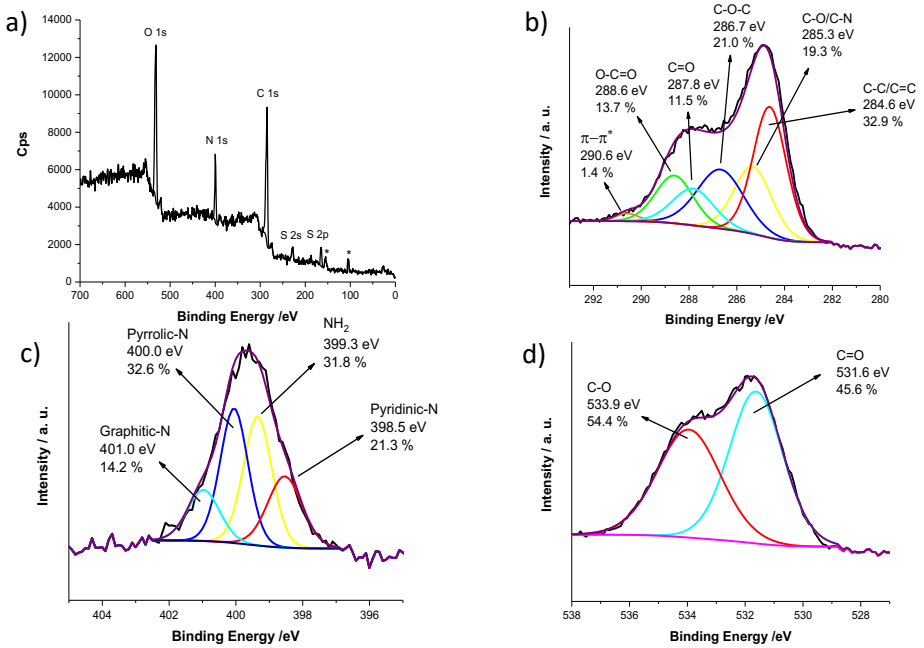

Figure 2.56. XPS analysis of **pCND-exTTF** a) Survey spectrum. b) C 1s component deconvolution. c) N 1s component deconvolution. d) O 1s component deconvolution.

All the different building blocks, that is, pCND and exTTF, are discernable in the absorption spectrum of **pCND-exTTF** (Figure 2.57a). The exTTF centered maxima are observed at 368 and 433 nm. Additionally, an absorption tails due to the presence of pCND throughout the visible range of the solar spectrum is also observed.

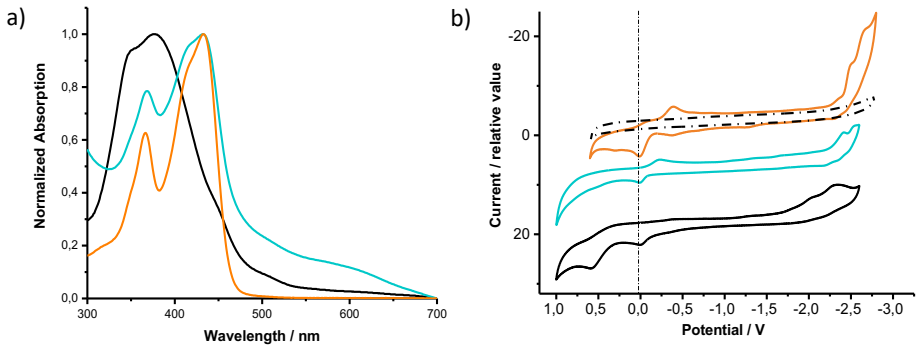

Figure 2.57. a) Normalized UV-Vis absorption spectra of pCND (black), exTTF **20** (orange) and **pCND-exTTF** (blue) in DMSO. b) Cyclic voltammograms of pCND (black), exTTF (orange) and **pCND-exTTF** (blue) in DMSO solutions containing 0.1 mM $TBAPF_6$ as supporting electrolyte with a glassy carbon working electrode, a $Ag/AgNO_3$ reference electrode, and a Pt wire counter electrode. The dashed line represents the background signal.

By means of cyclic voltammetry, the **pCND-exTTF** sample showed the characteristic quasi-reversible oxidation of exTTF (Figure 2.57b) at + 0.01 V *vs*. $Ag/AgNO_3$ in DMSO that is in accordance with that of exTTF **20**. After functionalization of pCND with exTTF units, the electrochemical features of pCND are not clearly discernible and mostly the exTTF oxidation (see above) and the reduction of its skeleton, in the form of two irreversible reductions close to the solvent window (-2.41 and -2.53 V), are observed. This fact could be due to the loss of amino groups in the pCND structure, responsible of most of the oxidations, and the extension of the sp^2 network during the functionalization process, which perfectly matches with the results obtained by TGA and XPS.

It is important to mention that these structural changes after functionalization also had an effect on the solubility of the new hybrids. The **pCND-exTTF** sample lose the initial solubility of the pCND in water and methanol and is

only soluble in DMSO or DMF due to the attachment of the exTTF on the pCND surface.

2.3.3.3. Synthesis and characterization of GQD-exTTF hybrids

A similar synthetic protocol to that described in the precedent section for pCND was used to incorporate exTTF units on GQD. That is, the activation of the carboxylic acids present onto the GQD surface via the *in situ* formation of acyl chlorides and their subsequent reaction with 2-hydroxymethyl-exTTF **20** through an esterification process to give rise to the **GQD-exTTF** nanoconjugates (Scheme 2.6).

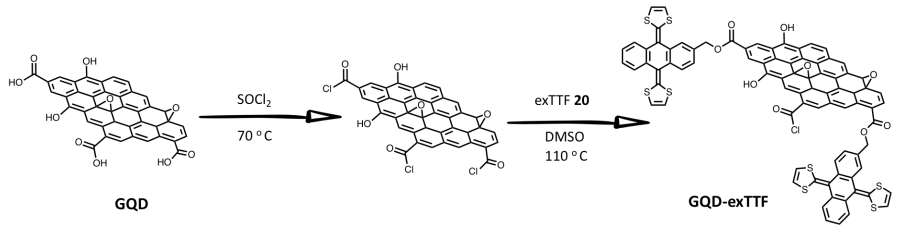

Scheme 2.6. Schematic representation of the synthesis of **GQD-exTTF**.

A first evidence of the covalent functionalization was gathered from TGA under inert atmosphere (Figure 2.58a). The thermogram shows an increased weight loss, of around a 28 %, after the functionalization process in **GQD-exTTF**, which is attributed to the incorporation of the exTTF units in the GQD. This behaviour was not clearly observed for pCND, since the weight loss due to exTTF was masked with the increase in the graphitization of the system.

The FTIR spectrum displayed the new functional groups that were introduced on the GQD (Figure 2.58b). Firstly, it is worth to point out the presence of the stretching vibration of C=O at 1740 cm^{-1} belonging to the new formed ester groups. Additionally, the C-S stretching vibrations was observed at 645 cm^{-1} although the intensity of this band is quite weak. The presence of the exTTF in the hybrid was also confirmed by ^{13}C-NMR spectroscopy, where some of the signals of the anthracene core and the 1,3-dithiole rings were discerned at 118-140 ppm. However, the low solubility of the sample prevents to register a spectrum with a good signal to noise ratio.

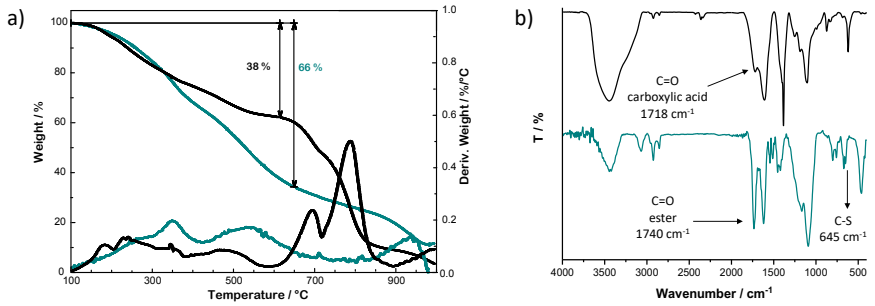

Figure 2.58. a) TGA and first derivative under inert conditions of GQD (black) and **GQD-exTTF** (blue). b) FTIR spectrum of GQD (black) and **GQD-exTTF** (blue).

XPS was another valuable tool to identify the surface groups, the chemical state of the atoms, and their relative abundance. For the **GQD-exTTF** nanoconjugates the element signals of C 1s, O 1s, and S 2p are obtained at 284.6, 531.6 and 163.6 eV, respectively (Figure 2.59a). In particular, the presence of sulphur, at a binding energy characteristic for C-S in tetrathiafulvalene (TTF) derivatives,[255] is an important evidence for the anchoring of the exTTF units to the GQD core. Moreover, deconvolution of the C 1s core-level region (Figure 2.59b) points to five species with binding energies of 284.1 eV (C=C/C-C), 284.8 eV (C-O), 285.7 eV (C-O-C), 286.2 eV (C=O), and 287.9 eV (O-C=O). Besides, it should be underlined the presence of the π-π* shake up component at 289-292 eV, characteristic of graphene-like materials.

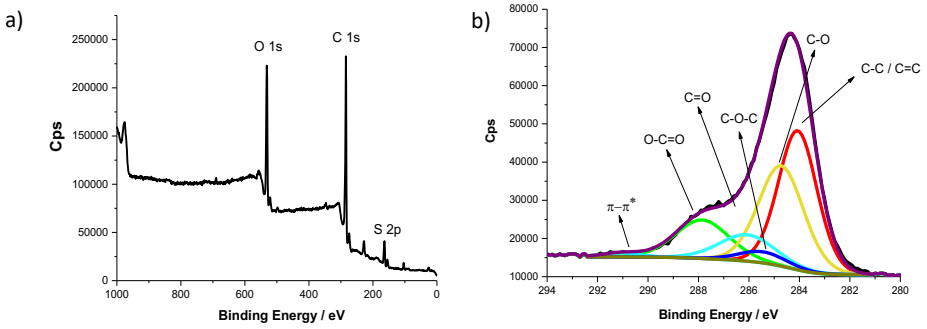

Figure 2.59. XPS analysis of **GQD-exTTF**. a) Survey spectrum. b) C 1s core-level component deconvolution.

[255] D. Choudhury, B. Das, D. D. Sarma, C. N. R. Rao, *Chem. Phys. Lett.* **2010**, *497*, 66.

AFM measurements provided information about the dimensions of the **GQD-exTTF** nanoconjugates. Overall, the images revealed roundish morphologies with average heights of 4.6 ± 1.6 nm, which are higher than those seen in the as-prepared GQD, although several agglomerated morphologies are observed (Figure 2.60b). In regard to the GQD structure after functionalization, no significant changes were observed by Raman spectroscopy, where the same characteristic D and G bands of graphitic materials are noted (Figure 2.60c). On the other hand, XRD showed an amorphous graphitic structure as it was expected (Figure 2.60d).

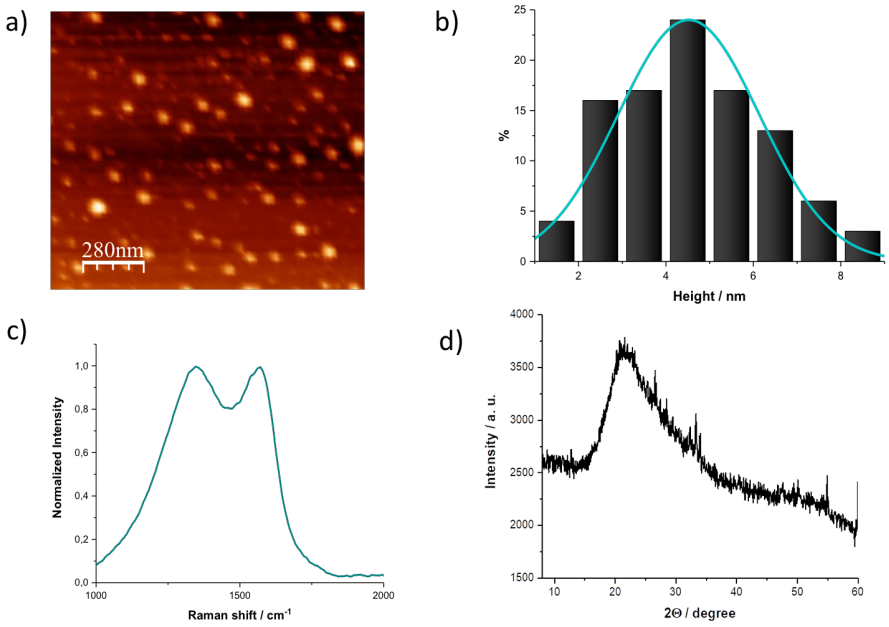

Figure 2.60. a) Representative AFM image of **GQD-exTTF**. b) Height histogram with a curve fit of the data using a Gaussian model. Average height: 4.6 ± 1.6 nm. c) Raman spectrum of **GQD-exTTF**. d) XRD diffractogram of **GQD-exTTF**.

The UV-Vis spectrum of **GQD-exTTF** showed the characteristic absorption profile of the starting GQD as well as the main absorption peaks of the exTTF units as two maxima at 367 and 432 nm.

The investigation of the electrochemical properties of **GQD-exTTF** by cyclic voltammetry (Figure 2.61), confirmed the presence of the exTTF due to the

presence of its characteristic quasi-reversible oxidation at +0.01 eV *vs.* $Ag/AgNO_3$. This result is along the lines of that observed in **pCND-exTTF**. In the solvent window provided by DMSO it is also noticeable the reduction of the exTTF skeleton, in the form of two irreversible reductions at -2.41 and -2.53 V.

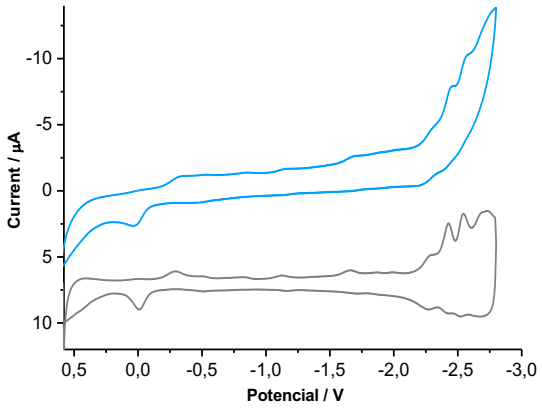

Figure 2.61. Cyclic voltammogram (blue) and deconvoluted voltammogram (grey) of **GQD-exTTF** in DMSO solutions containing 0.1mM $TBAPF_6$ as supporting electrolyte with a glassy carbon working electrode, a $Ag/AgNO_3$ reference electrode, and a Pt wire counter electrode.

2.3.3.4. Photophysical properties of pCND-exTTF and GQD-exTTF hybrids

The photophysical properties of the pCND and GQD nanomaterials functionalized with exTTF units where investigated in the laboratory of Prof. Dirk M. Guldi at the Friedrich-Alexander-Universität Erlangen-Nürnberg. Part of the results were obtained in a short stay during the last year of PhD work.

Photophysical study of pCND-exTTF. First insights into excited-state interactions came from fluorescence measurements. Herein, a fluorescence quenching of at least a 90% was observed for **pCND-exTTF** (Figure 2.62). Based on this finding, the existence of an additional pCND excited state deactivation in **pCND-exTTF** was postulated; the presence of photo- and electroactive exTTF activates either an energy or a charge transfer process.

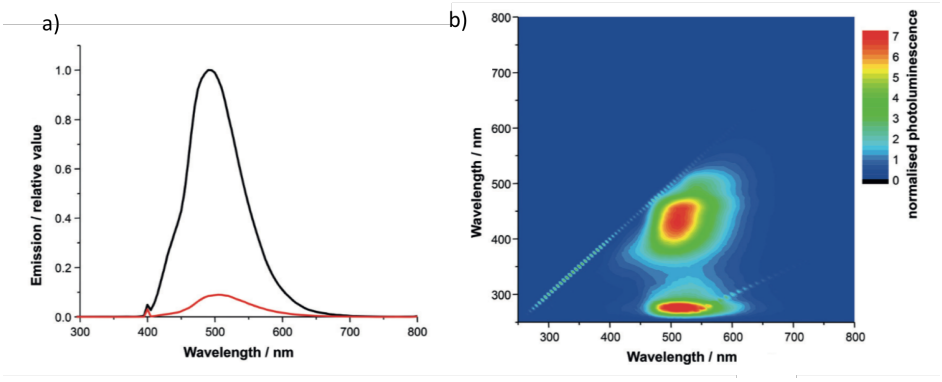

Figure 2.62. a) Steady state emission spectra of iso-absorbing pCND (black) and **pCND-exTTF** (red) obtained at an excitation of 400 nm in DMSO. b) Excitation/emission 3D map for **pCND-exTTF** obtained in DMSO.

Unambiguous confirmation for a charge-transfer rather than an energy-transfer deactivation stemmed from femtosecond transient absorption measurements with **pCND-exTTF**. In particular, 387 nm excitation leads to the instantaneous formation of an excited state with prominent maxima and minima at 612 and 438 nm, respectively. This converts, in contrast to which is observed for the exTTF and pCND references, within a few picoseconds into a new transient. The most notable fingerprints of this transient are maxima at 463, 549, and 660 nm as well as a 423 nm minimum, which are in sound agreement with pulse radiolytic findings focusing on the oxidation of exTTF.[256] In other words, a charge separation, in which exTTF are one-electron oxidized and pCND are one-electron reduced, evolves upon formation of the initial excited state. The ultimate fate of the **pCND$^{\bullet-}$-exTTF$^{\bullet+}$** charge separated state is charge recombination on the timescale of tens of picoseconds and the product is the ground state. Analyses, which were based both on multi-wavelength and global methods, provided the means to derive lifetimes of the charge separation and charge recombination processes.

Multi-wavelength analyses show that the charge separation as well as charge recombination in **pCND-exTTF** are fast with 1.3 and 13.3 ps, respectively. As

[256] a) D. M. Guldi, L. Sánchez, N. Martín, *J. Phys. Chem. B* **2001**, *105*, 7139. b) M. A. Herranz, C. Ehli, S. Campidelli, M. Gutiérrez, G. L. Hug, K. Ohkubo, S. Fukuzumi, M. Prato, N. Martín, D. M. Guldi, *J. Am. Chem. Soc.* **2008**, *130*, 66. c) V. Strauss, A. Roth, M. Sekita, D. M. Guldi, *Chem* **2016**, *1*, 531.

a consequence, we turned to global target analysis and employed a kinetic model based on an ultrafast chirp correction as well as monophasic charge separation and charge recombination (Figure 2.63). The spectral features of the species associated spectra (SAS) are in sound agreement with the proposed kinetic model, that is, a laser chirp (SAS1), an exTTF based excited state (SAS2), and a **pCND$^{\bullet-}$-exTTF$^{\bullet+}$** charge separated state (SAS3).

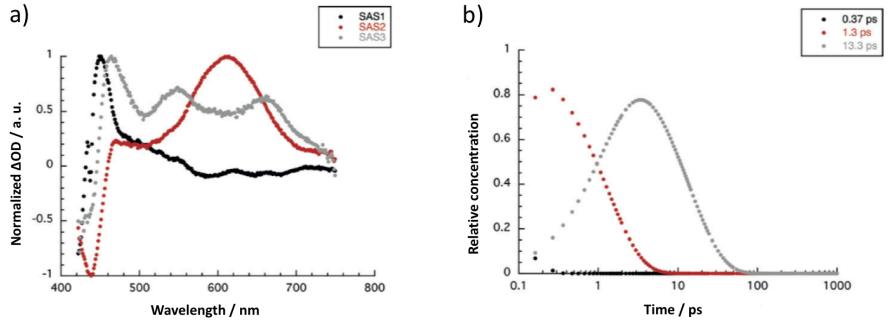

Figure 2.63. a) Normalized species associated transient absorption spectra (SAS1, SAS2, and SAS3) for **pCND-exTTF** obtained in DMSO using the kinetic model described above. b) Corresponding concentration profiles for **pCND-exTTF**.

Photophysical study of GQD-exTTF. Initial investigations by fluorescence spectroscopy reveal a nearly quantitative quenching of the GQD emission after their covalent funtionalization with exTTF units (Figure 2.64).

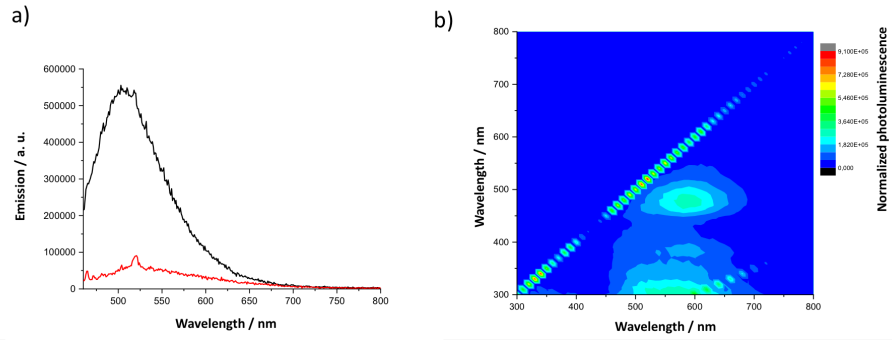

Figure 2.64. a) Steady state emission spectra of GQD (black) and **GQD-exTTF** (red) obtained at an excitation of 410 nm in DMSO. b) Excitation/emission 3D map for **GQD-exTTF** obtained in DMSO.

In order to prove the existence of a charge transfer process behind this quenching, transient absorption spectroscopic measurements with **GQD-exTTF** have been carried out. Excitation at 387 nm leads to the formation of an exTTF centered excited state with an absorption minimum at 440 nm and absorption maxima at 474, 610, and 710 nm. In contrast to the exTTF and GQD references, this transient converts into a new transient within two picoseconds. This new transient is characterized by maxima at 467, 546, 610, and 674 nm as well as a distinct 440 nm minimum, which are in sound agreement with pulse radiolytic findings regarding the oxidation of exTTF.[256] In other words, charge separation, in which exTTF are one-electron oxidized and GQD are one-electron reduced, evolves upon formation of the initial excited state.

Finally, the charge separated state recombines to the ground state on a timescale of tens of picoseconds. To gain deeper insights into the excited state dynamics, we conducted multi wavelength analyses. In Figure 2.65 the species associated spectra (SAS) and the corresponding concentration profiles are shown. The spectral features of the species associated spectra are in sound agreement with the proposed kinetic model, that is, an exTTF based excited state (SAS1) with a lifetime of 2.0 ps and a **GQD$^{\bullet-}$-exTTF$^{\bullet+}$** charge separated state (SAS2) with a lifetime of 52 ps. Notable is the lifetime of the **GQD$^{\bullet-}$-exTTF$^{\bullet+}$** charge separated state (SAS2), which is appreciable longer than that determined in the corresponding carbon nanodot (CND) conjugates. The less amorphous character of GQD compared to **pCND** is likely to facilitate a better delocalization of the electron.

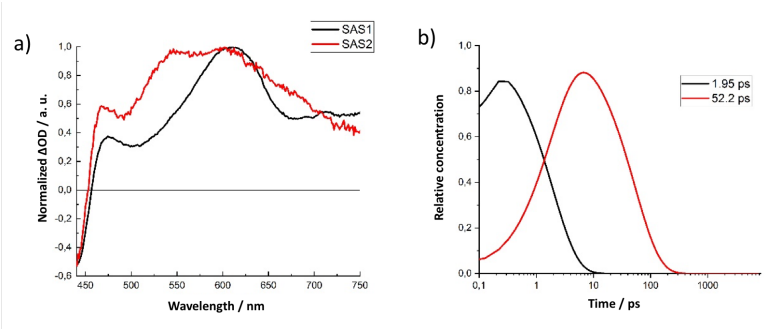

Figure 2.65. a) Normalized species associated transient absorption spectra (SAS1, SAS2, and SAS3) for **GQD-exTTF** obtained in DMSO using the kinetic model described above. b) Corresponding concentration profiles for **GQD-exTTF**.

2.3.4. Synthesis and characterization of pCND-TCAQ hybrids

In the last section were verified the acceptor features of pCND when combined with electron donor molecules (exTTF). The next step within this PhD work involves evaluating the capability of pCND to act as *p*-type nanomaterials when combined with acceptor molecules. In this regard, 11,11,12,12-tetracyano-9,10-anthraquinodimethane (TCAQ) has been chosen in the current study as the electron-acceptor owing to its remarkable electronic and geometrical characteristics.[257]

In particular, TCAQ exhibits a low reduction potential and a high stability of the reduced species because of the aromatization of the central quinoid moiety. (Figure 2.66). In the reduced form, the charge is efficiently spread over the two dicyanomethylenes and the central anthracene, affording highly stabilized radical anion and dianion species. Due to these interesting electronic properties, TCAQ has been widely used in the formation of D-A complexes in combination with conjugated polymers, CNT or fullerenes.[258]

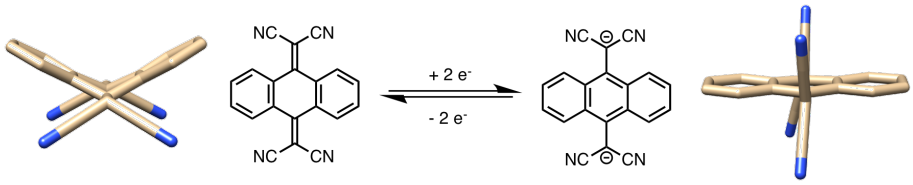

Figure 2.66. Geometrical change of **TCAQ** upon oxidation.

[257] N. Martín, R. Behnisch, M. Hanack, *J. Org. Chem.* **1989**, *54*, 2563.

[258] a) A. Wild, M. Strumpf, B. Häupler, M. D. Hager, *Adv. Energy Mater.* **2017**, *7*, 1601415. b) C. Romero-Nieto, R. García, M. A. Herranz, L. Rodríguez-Pérez, M. Sánchez-Navarro, J. Rojo, N. Martín, D. M. Guldi, *Angew. Chem. Int. Ed.* **2013**, *52*, 10216. c) E. M. Pérez, A. L. Capodilupo, G. Fernández, L. Sánchez, P. M. Viruela, R. Viruela, E. Ortí, M. Bietti, N. Martín, *Chem. Commun.* **2008**, 4567.

2.3.4.1. Synthesis of TCAQ electron-acceptor units

The TCAQ derivative **21** was synthesized in a well-known single-step reaction where 2-hydroxymethylanthraquinone was reacted with malononitrile in a Knoevenagel condensation reaction (Scheme 2.7).[259] However, the condensation of the quinoid system does not occur under standard conditions and it is necessary to use Lehnert's reagent ($TiCl_4$, piridinde).[260] Note that the obtained TCAQ derivative bears a hydroxymethyl group to facilitate the subsequent incorporation into the pCND by further esterification reaction.

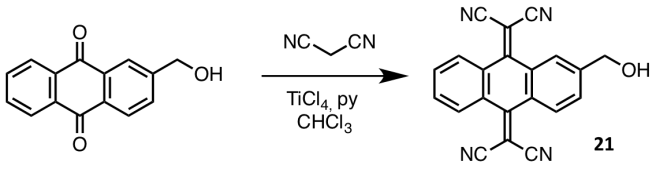

Scheme 2.7. Schematic representation of the synthesis of the TCAQ derivative **21**.

By means of ^{1}H-NMR spectroscopy are identified the main proton signals of **21**. The spectrum is composed by the two multiplets due to the anthracene core protons located at 8.22-8.14 ppm and 7.76-7.70 ppm and a singlet located at 4.82 ppm belonging to the methylene protons (Figure 2.67a). Nevertheless, since the starting anthraquinone presents the same signals, additional structural characterization is necessary to confirm the synthesis of the product. Therefore, the product was further characterized by FTIR spectroscopy and mass spectroscopy. The FTIR spectrum of **21** revealed the presence of the –C≡N groups by the stretching vibration band located at 2226 cm^{-1} (Figure 2.67b). Moreover, through mass spectrometry it was obtained a m/z of 334.1, which perfectly matches with the calculated mass of **21**. Regarding the optical properties, **21** absorbs in the UV region presenting a maximum located at 351 nm (Figure 2.67c)

[259] B. Illescas, N. Martín, C. Seoane, *Tetrahedron Lett*. **1997**, *38*, 2015.
[260] a) W. Lehnert, *Tetrahedron Lett.* **1970**, 4723. b) W. Lehnert, *Synthesis*, **1974**, 667.

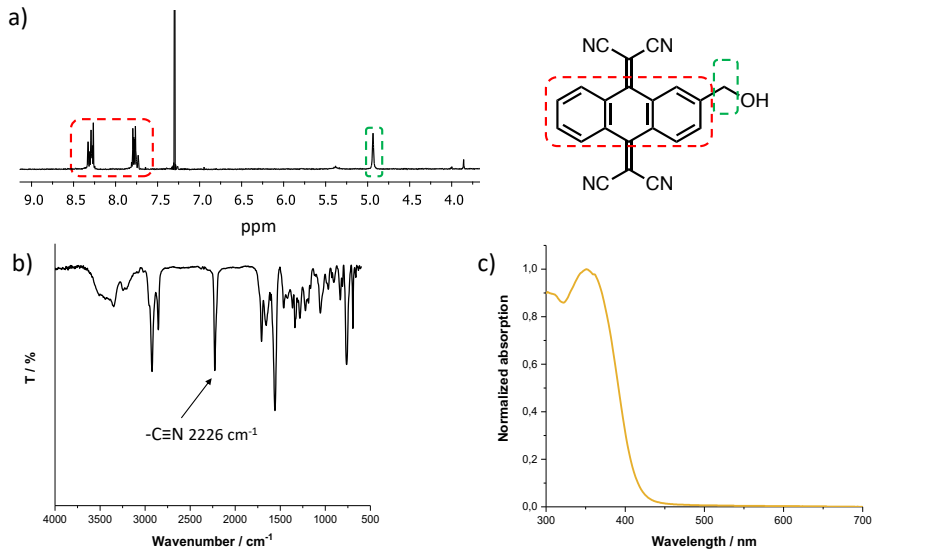

Figure 2.67. a) ^{1}H-NMR (300 MHz) spectrum of **21** in *d*$_6$-DMSO. b) FTIR spectrum of **21**. c) UV-Vis spectrum of **21** in DMSO.

2.3.4.2. Synthesis and characterization of pCND-TCAQ hybrids

The TCAQ derivative **21** was covalently linked to pCND following the same procedure used in the formation **pCND-exTTF**, which consisted in the previous activation of the carboxylic acids of pCND via acyl chloride formation and the subsequent attachment of **21** by an esterification reaction (Scheme 2.8).

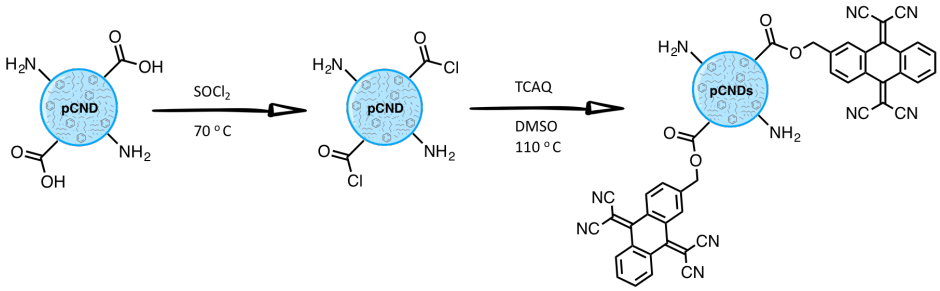

Scheme 2.8. Schematic representation of the synthesis of **pCND-TCAQ** hybrids.

First evidences of **pCND-TCAQ** formation came from the detection of the –C≡N groups in the hybrids by FTIR and XPS spectroscopies. On the one hand, the FTIR spectrum of **pCND-TCAQ** revealed the presence of the vibration belonging to the –C≡N groups, which was located at 2208 cm^{-1} (Figure 2.68a). On the other hand, the high-resolution N 1s core-level spectrum of **pCND-TCAQ** was composed of five components as depicted in Figure 2.68b. Four of these components were previously observed in the starting material (Graphitic-N, Pyrrolic-N, -NH_2 and Pyridinic-N) whereas the new component located at 398.1 eV corresponds to the –C≡N groups of the TCAQ units.[261]

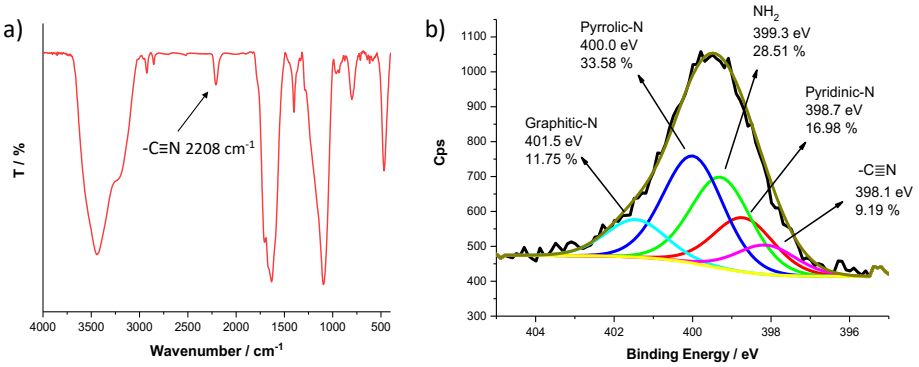

Figure 2.68. a) FTIR spectrum of **pCND-TCAQ**. b) N 1s component deconvolution spectrum of **pCND-TCAQ**.

The thermal stability of the obtained material was compared with that of the precursors, pCND and TCAQ derivative **21**. In Figure 2.69 is shown the thermogram of **pCND-TCAQ**, which presents a very similar behavior to that observed for **pCND-exTTF**, featuring a continuous weigh loss in the range of temperatures from 100 to 800 ºC. This result could be expected, since TCAQ and exTTF have a similar carbon framework.

[261] C. Urban, Y. Wang, J. Rodríguez-Fernández, R. García, M. A. Herranz, M. Alcamí, N. Martín, F. Martín, J. M. Gallego, R. Miranda, R. Otero, *Chem. Commun.* **2014**, *50*, 833.

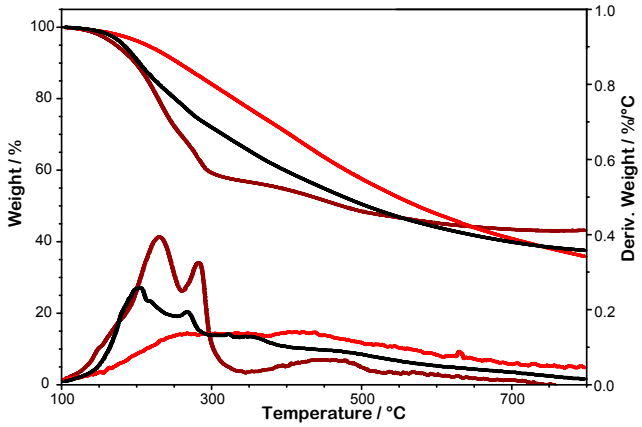

Figure 2.69. TGA and first derivative under inert conditions of pCND (black), TCAQ (dark red) and **pCND-TCAQ** (red).

The next step was to evaluate the morphology of the as-formed hybrids, where it is expected an increase of the size of pCND as it happened for the **pCND-exTTF** hybrids. The statistical analysis of **pCND-TCAQ** by AFM revealed the presence of particles with an average height of 4.3 ± 1.5 nm which are slightly smaller than **pCND-exTTF** (5.9 ± 1.9 nm) and bigger than the initial pCND (2.1 ± 1.1 nm). The increase in size after the introduction of exTTF and TCAQ might be amplified due to the π-π interactions between molecules of different hybrids resulting in larger aggregates.[262]

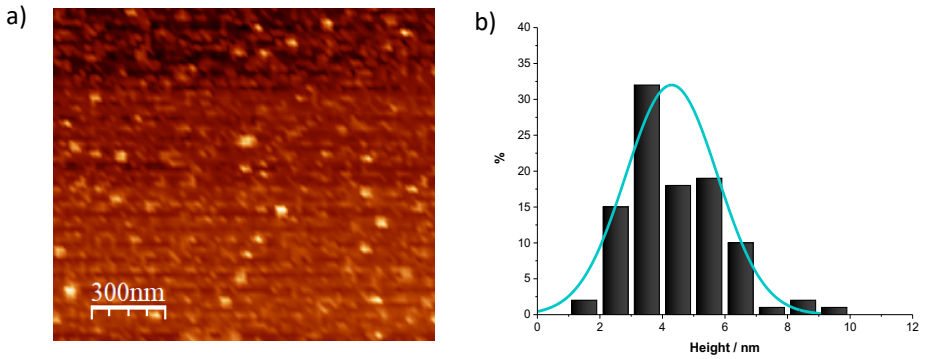

Figure 2.70. a) Representative AFM image of **pCND-TCAQ**. b) Height histogram with a curve fit of the data using a Gaussian model. Average height: 4.3 ± 1.5 nm.

[262] E. M. Pérez, N. Martín, *Chem. Soc. Rev.* **2008**, *37*, 1512.

The optoelectronic properties of **pCND-TCAQ** were investigated by UV-Vis spectroscopy and Square-Wave Voltammetry measurements (SWV) in methanol as solvent. The **pCND-TCAQ** spectrum (Figure 2.71) shows an absorption that covers the whole UV-Vis range with two maxima at *ca.* 340 and 420 nm, which are remarkably shifted from the maximum absorption peaks of the starting pCND and TCAQ derivative **21**. Considering the strong electron-accepting features of TCAQ, the underlying shifts could be rationalized to a redistribution of charge density and to a *p*-type doping of pCND.

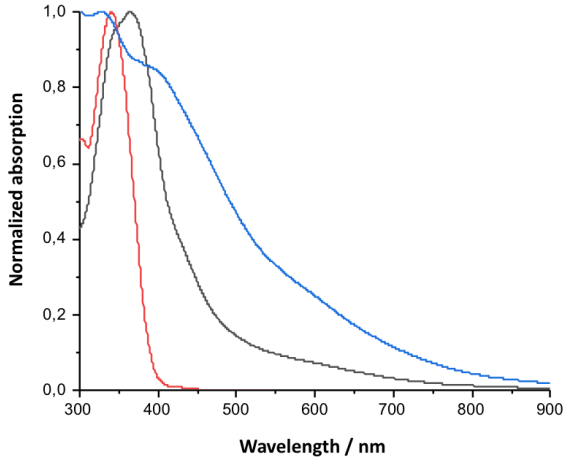

Figure 2.71. Normalized absorption spectra of pCND (black), **21** (red) and **pCND-TCAQ** (blue) in methanol.

Additional information for sizable ground state charge-transfer interactions in **pCND-TCAQ** came from electrochemical measurements. SWV were performed at room temperature and showed a first reduction potential of the TCAQ units at -0.23 V *vs.* and Ag wire, meanwhile the first oxidation of pCND appears at +0.62 V.[209] From these data, the lowest charge-separated state energy is estimated to be around 0.85 eV for **pCND$^{\bullet+}$-TCAQ$^{\bullet-}$**.

2.3.4.3. Photophysical properties of pCND-TCAQ hybrids

In preliminary investigations carried out, the photophysical properties of the **pCND-TCAQ** hybrids were studied by 3D fluorescence spectroscopy and femtosecond transient absorption spectroscopy. In fluorescence measurements (Figure 2.72), the most notable observation is the fact that the pCND centered fluorescence is quenched in the presence of TCAQ. The incorporation of TCAQ to pCND activates in the resulting **pCND-TCAQ** hybrids additional decay channels to those of the independent pCND and TCAQ derivative **21**.

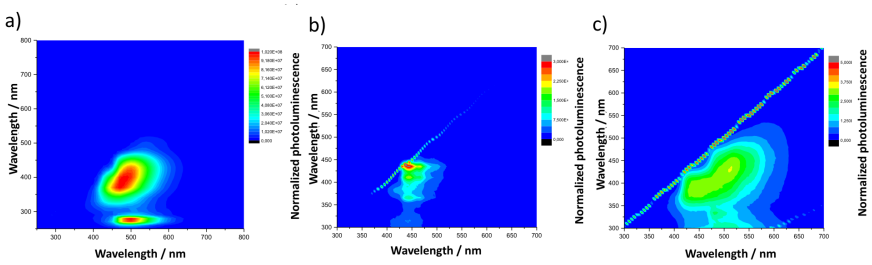

Figure 2.72. Excitation/emission 3D maps of pCND (a), **21** (b) and **pCND-TCAQ** (c) obtained in methanol.

To corroborate that photoinduced charge takes place rather than any other deactivation, femtosecond pump-probe experiments were performed. Instantaneously upon photoexcitation at 387 nm of **pCND-TCAQ**, the singlet excited state features of pCND and TCAQ are discernible. However, these features transform into new transients that are in agreement with the pulse-radiolysis generated $TCAQ^{\bullet-}$ radical anion.[263] With the help of global analyses the number of intermediate states, which participate in the decay cascades, were investigated together with their lifetimes and decay associated spectra. In Figure 2.73 the species associated spectra (SAS) and the corresponding concentration profiles are shown. The spectral features of the SASs are in accordance with a kinetic model, that considers a TCAQ based excited state (SAS1) with a lifetime of 6.98 ps and a **pCND$^{\bullet+}$-TCAQ$^{\bullet-}$** charge separated state (SAS2) with a lifetime of 5.85 ns. The lifetime of the **pCND$^{\bullet+}$-TCAQ$^{\bullet-}$** charge separated state (SAS2) is much longer than that determined in the

[263] J. Santos, B. M. Illescas, N. Martín, J. Adrio, J. C. Carretero, R. Viruela, E. Ortí, F. Spänig, D. M. Guldi, *Chem. Eur. J.* **2011**, *17*, 2957.

corresponding exTTF-based conjugates and further investigations are being carried out in order to confirm and rationalize these data.

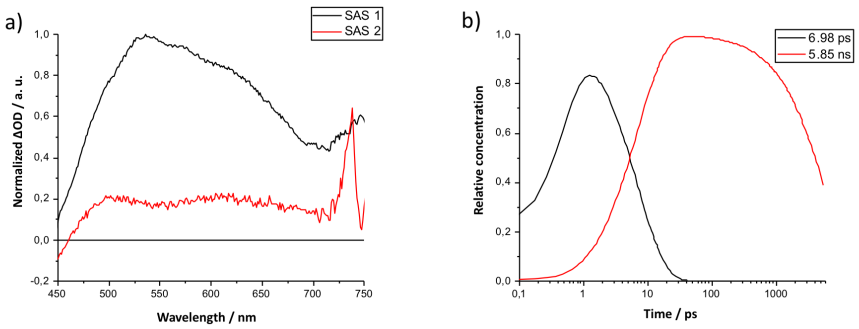

Figure 2.73. a) Normalized species associated transient absorption spectra (SAS1 and SAS2) for **pCND-TCAQ** obtained in methanol. b) Corresponding concentration profiles.

2.3.5. Synthesis and characterization of pCND-C_{60} and pCND-C_{70} hybrids

Following the work carried out in the previous sections, assembling pCND with derivatives of the electron-donor exTTF and the electron-acceptor TCAQ, the combination of two different carbon nanostructures (pCND and fullerenes) was explored. The merge of different carbon nanostructures has created nanohybrids with novel and improved properties for various technological applications.[264] One of the still unexplored class of nanohybrids is that resulting from the covalent attachment of C_{60} or C_{70} units onto pCND.

As it was briefly commented in the introduction of this thesis, C_{60} fullerene is a good electron-acceptor molecule which presents a low reorganization energy. The ability of C_{60} to accept up to six electrons as well as the capacity to provide long-lived load transfer states, made C_{60} fullerene really interesting for artificial photosynthetic systems.[265] Specifically, for the anchoring to pCND it was used a derivative of phenyl-C_{61}-butyric-methyl-ester ($PC_{60}BM$), widely

[264] V. Georgakilas, J. A. Perman, J. Tucek, R. Zboril, *Chem. Rev.* **2015**, *115*, 4744.
[265] M. J. Llansola-Portolesa, D. Gust, T. A.Moore, A. L.Moore, *C. R. Chimie* **2017**, 20, 296.

employed in the field of organic photovoltaics.[266] The chosen derivative is shown in Figure 2.74 and is decorated with an alcohol group (**PC_{60}BM-OH)** to facilitate the attachment to the pCND through an esterification reaction.

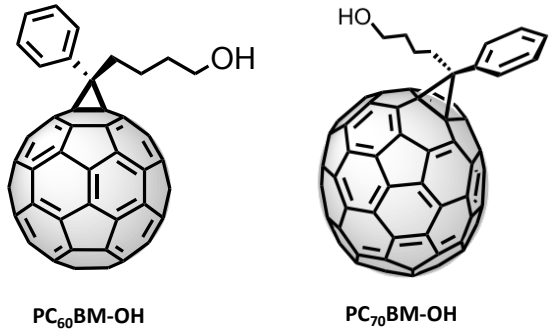

Figure 2.74. Representative structures of **PC_{60}BM-OH** and **PC_{70}BM-OH**.

Furthermore, it was also carried out the synthesis of **PC_{70}BM-OH**, structurally analogous, but having a C_{70} instead of C_{60}. Following to C_{60} fullerene, C_{70} is the next more stable fullerene. It is a cage formed by 12 pentagonal rings and 25 hexagonal rings with a structure resembling a rugby ball. Unlike C_{60}, the C_{70} molecule presents D_{5h} symmetry, absorbs strongly in the visible region of the electronic spectrum, and is constituted by four non-equivalent double bonds, namely: α, β, γ and δ.[267]

The formation of **pCND-PC_{60}BM** and **pCND-PC_{70}BM** hybrids provides the opportunity to compare and discuss the behavior and properties of both fullerenes coupled to **pCND** along this part of the chapter.

[266] J. C. Hummelen, B. W. Knight, F. LePeq, F. Wudl, J. Yao, C. L. Wilkins, *J. Org. Chem.* **1995**, *60*, 532.

[267] E. E. Maroto, A. de Cózar, S. Filippone, A. Martín-Domenech, M. Suárez, F. P. Cossío, N. Martín, *Angew. Chem. Int. Ed.* **2011**, *50*, 6060.

2.3.5.1. Synthesis of $PC_{60}BM$-OH and $PC_{70}BM$-OH derivatives

The first step in this section was the synthesis of $PC_{60}BM$ and $PC_{70}BM$ following a similar synthetic protocols to those previously reported.[266,268] For that task, it was firstly necessary the synthesis of the corresponding tosylhydrazone **24** (Scheme 2.9), which is a common precursor for the synthesis of both molecules. This compound was prepared from reaction of the commercially available 4-benzoylbutyric acid **22** with oxalyl chloride in refluxing methanol for 24 hours. Further treatment of **23** with *p*-toluenesulfonylhydrazine leads to hydrazone **24**.

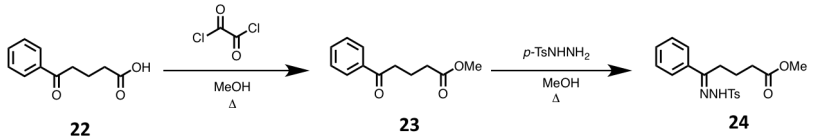

Scheme 2.9. Schematic representation of the synthesis of compound **24**.

Once formed the desired compound **24**, the next step was the synthesis of $PC_{60}BM$ and $PC_{70}BM$ (Scheme 2.10). These compounds were formed by direct reaction of compound **24** with C_{60} and C_{70}, respectively. The decomposition of tosylhydrazone **24** in basic media by following a Bamford-Stevens reaction,[269] allows the *in situ* generation of the corresponding diazocompound and its further reaction without any purification prior to the addition of C_{60} or C_{70}. The final step was the reduction of both, $PC_{60}BM$ and $PC_{70}BM$, with diisobutylaluminium hydride (DIBAL) to generate the final products **$PC_{60}BM$-OH**[270] and **$PC_{70}BM$-OH**. For simplicity only the major isomers (α-isomer, *ca.* 85% yield) of the four possible siteisomers[267] (α, β, γ, and δ) obtained for **$PC_{70}BM$** and **$PC_{70}BM$-OH** are shown. In this first approach towards pCND functionalizaton the work continued with the mixture obtained, without further purification of the different siteisomers.

[268] M. M. Wienk, J. M. Kroon, W. J. H. Verhees, J. Knol, J. C. Hummelen, P. A. van Hal, R. A. J. Janssen, *Angew. Chem. Int. Ed.* **2003**, *42*, 3371.
[269] W. R. Bamford, T. S. Stevens, *J. Chem. Soc.* **1952**, 4735.
[270] S. L. Fronk, C.-K. Mai, M. Ford, R. P. Noland, G. C. Bazan, *Macromolecules* **2015**, *48*, 6224.

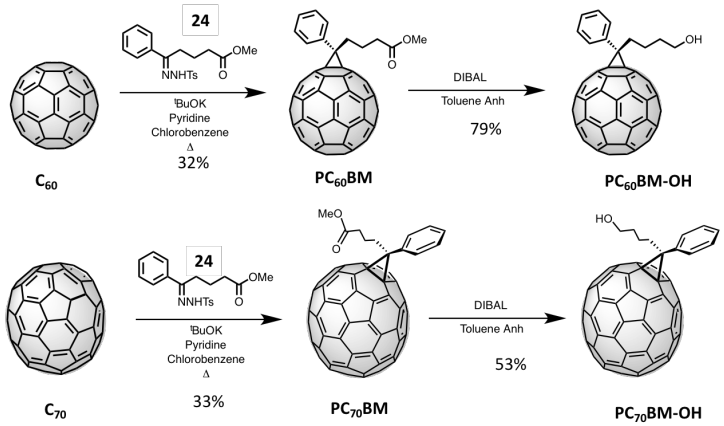

Scheme 2.10. Schematic representation of the synthesis of **$PC_{60}BM$-OH** and **$PC_{70}BM$-OH.**

The synthesis of **$PC_{60}BM$-OH** and **$PC_{70}BM$-OH** was perfectly tracked by ^{1}H-NMR spectroscopy (Figure 2.75 and Figure 2.76). In $PC_{60}BM$ and $PC_{70}BM$ are discerned the signals of the aromatic protons (red and green), the aliphatic signals of the butyric chain (blue) and the singlet due to the methoxy group (orange). Whereas, after the reduction of the ester group, it was observed the vanishing of these last signals for both derivatives, accompanied by the formation of a new triplet (purple) due to the new aliphatic (methylene) signal as a result of the reduction of the ester groups.

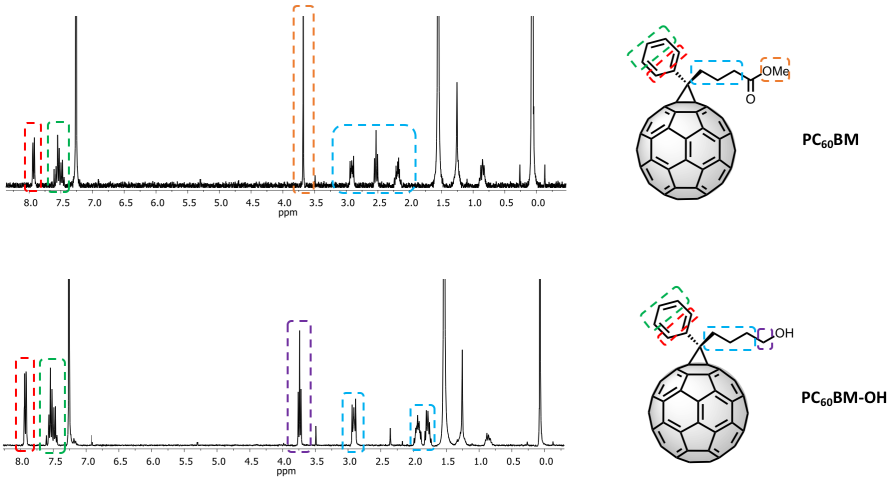

Figure 2.75. ^{1}H-NMR (700 MHz) spectra of $PC_{60}BM$ and **$PC_{60}BM$-OH** in $CDCl_3$.

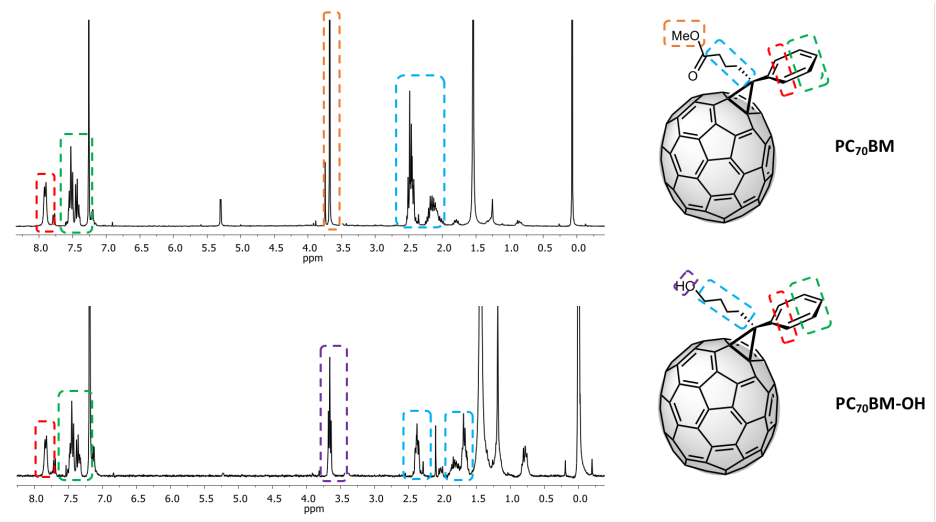

Figure 2.76. ^{1}H-NMR (700 MHz) spectra of $PC_{70}BM$ and **$PC_{70}BM$-OH** in $CDCl_3$.

Additional characterization of the obtained compounds was carried out by other techniques such as FTIR spectroscopy and UV-Vis spectroscopy.

2.3.5.2. Synthesis and characterization of pCND-$PC_{60}BM$ and pCND-$C_{70}BM$ hybrids

The attachment of **$PC_{60}BM$-OH** and **$PC_{70}BM$-OH** to pCND was carried out using the same strategy followed for the synthesis of **pCND-exTTF** and **pCND-TCAQ**. However, it was necessary to employ a mixture of DMSO/chlorobenzene 1/1 as solvent instead of only DMSO, due to the different solubilities that present pCND and PCBM derivatives (Figure 2.77).

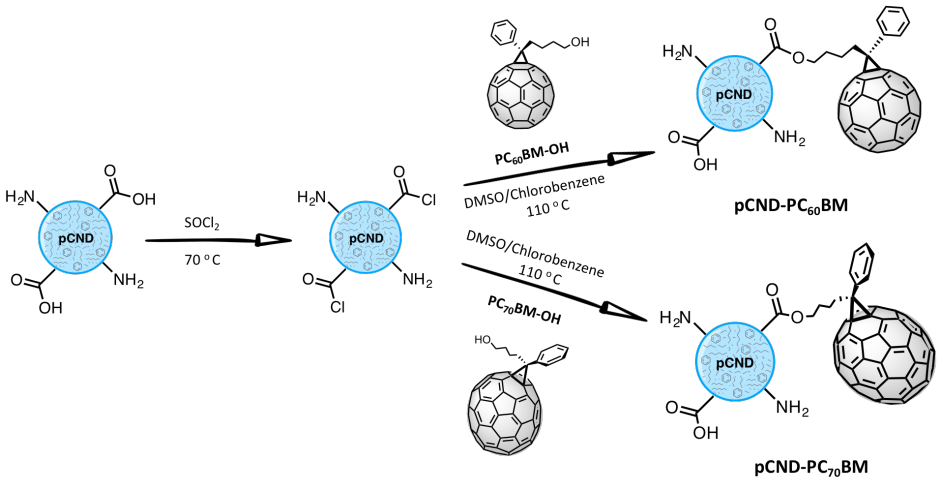

Figure 2.77. Schematic representation of the synthesis of **pCND-PC_{60}BM** and **pCND-PC_{70}BM.**

The isolated hybrids were initially characterized by UV-Vis-NIR spectroscopy in order to confirm the presence of the fullerenes in the different dyads. In Figure 2.78 are shown comparative spectra of pCND, PCBM molecules and pCND-PCBM hybrids. In the UV-Vis-NIR spectrum of **PC_{60}BM-OH** two local maxima at 330 and 435 nm are noticed. The signal at 435 nm is considered a fingerprint of saturated C–C bonds between two hexagons of the C_{60} sphere, regardless of the nature of the substituents involved.

In the synthesized hybrid material **pCND-PC_{60}BM**, it is observed a wider absorption range than that observed for the starting pCND. Furthermore, three additional shoulders are discerned (indicated in the graph with arrows), two of them being in the range of the main absorptions of **PC_{60}BM-OH**. These maxima appear at *ca.* 342 and 450 nm, which seem to indicate that the fullerene absorptions are batochromically shifted in the hybrids.

Similar results were found for **pCND-PC_{70}BM** where two small shoulders can be seen at 373 and 440 nm, both indicated by arrows in (Figure 2.78b). These two signals match with the absorption signals of **PC_{70}BM-OH**, but again, are quite shifted in comparison with its maxima visible at 374 and 460 nm. In principle, the obtained results might indicate some sort of electronic communication between the pCND and the fullerene derivatives in the ground state. However, further experiments are necessary to complement the

observations deduced from the featureless and broad spectra of the obtained nanohybrids.

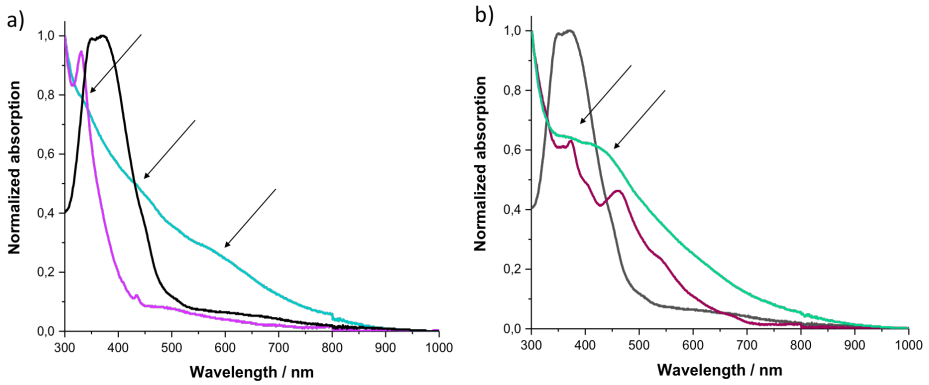

Figure 2.78. a) UV-Vis spectra of pCND (black), **PC_{60}BM-OH** (purple) and **pCND-PC_{60}BM** (blue) in DMSO. b) UV-Vis spectra of pCND (black), **PC_{70}BM-OH** (purple) and **pCND- PC_{70}BM** (green) in DMSO.

The pCND-fullerene hybrids were subsequently investigated by FTIR. C_{60} derivatives present a characteristic vibrational mode at 527 cm^{-1},[271] which is perfectly distinguished in both, the **PC_{60}BM-OH** and **pCND-PC_{60}BM** spectra (Figure 2.79) and is indicative of the successful synthesis of **pCND-PC_{60}BM**. Furthermore, in the starting pCND spectrum, no signal is observed in this region, which indicates that the signal observed in **pCND-PC_{60}BM** can be due only to the PC_{60}BM anchored to the pCND. In order to clearly indicate the position of this band, expanded Figures with a dashed line at 527 cm^{-1} are shown in the spectra of the three nanomaterials in Figure 2.79.

[271] J. P. Hare, T. J. Dennis, H. W. Kroto, R. Taylor, A. W. Allaf, S. Balm, D. R. M. Walton, *J. Chem. Soc., Chem. Commun.* **1991**, 412.

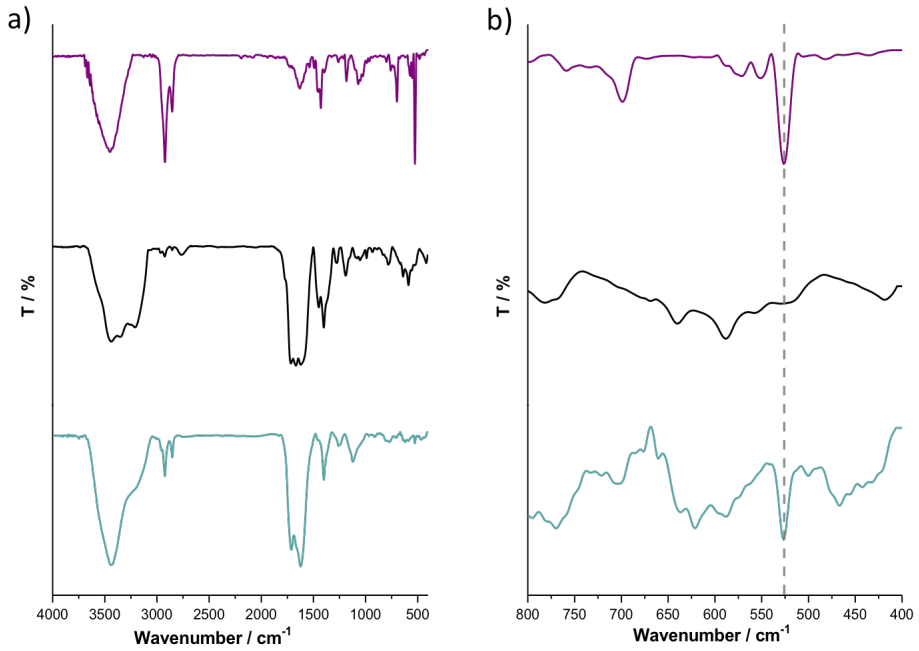

Figure 2.79. a) FTIR spectra of pCND (black), **$PC_{60}BM$-OH** (purple) and **pCND-$PC_{60}BM$** (blue). b) Expansion in the range of 800-400 cm^{-1} of the spectra showed in a).

In regard to C_{70} FTIR spectroscopy, this molecule presents more signals in its FTIR spectrum due to the loose of symmetry in comparison with the symmetric C_{60} molecule. Indeed, C_{70} exhibits five remarkable vibrational modes located at 533, 579, 645, 674 and 700 cm^{-1}.[271] These signals are perfectly recognized in the **$PC_{70}BM$-OH** and **pCND-$PC_{70}BM$** spectra as shown in Figure 2.80.

Moreover, these signals do not appear in the spectrum of the starting pCND, indicating that they come from the $PC_{70}BM$ in the functionalized pCND. In addition, the changes observed in the band at 1800-1600 cm^{-1} after the functionalization process could be indicative of the formation of new ester groups.

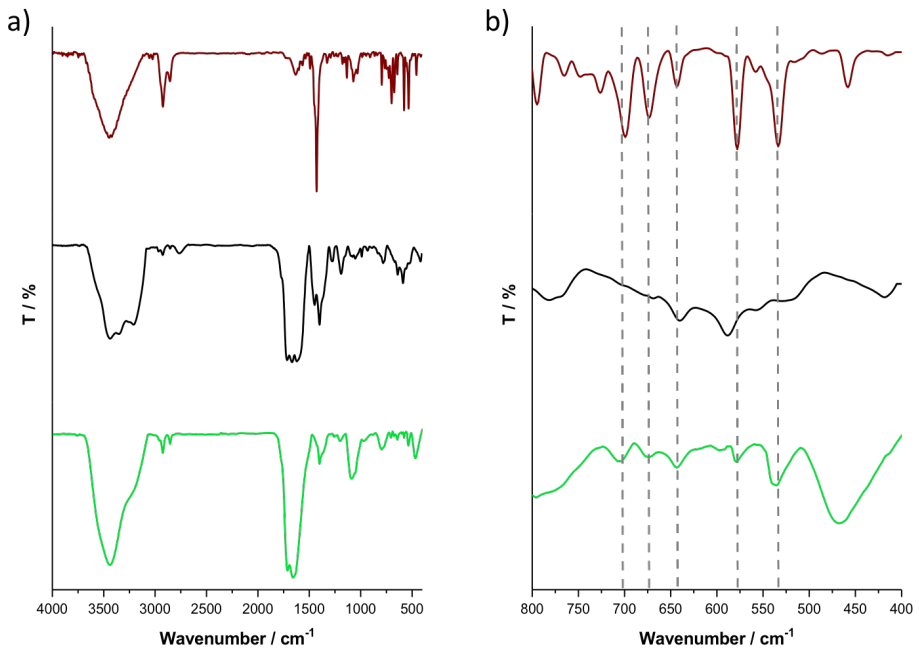

Figure 2.80. a) FTIR spectra of pCND (black), **$PC_{70}BM$-OH** (dark red) and **pCND-$PC_{70}BM$** (green). b) Expansion in the range of 800-400 cm^{-1} of the spectra showed in a).

The next step was to confirm that the signals observed in the FTIR spectra are due to the PCBMs attached to the pCND and not to molecules non-covalently bonded to the pCND. For that task, TGA analyses were performed with the starting pCND, the molecular fullerenes and the as-formed covalent hybrids (Figure 2.81).

In Figure 2.81a, it is observed the pCND accused weight loss around 200 ºC, and the more constant weight loss after this temperature. On the other hand, the **$PC_{60}BM$-OH** sample suffers a major loss at approximately 380 ºC and a second loss at 550 ºC. Both samples follow similar molecular decomposition pattern, since their weight losses occur in a narrow temperature range forming well-defined derivative peaks. Conversely, the **pCND-$PC_{60}BM$** sample decomposes in a soft and consistent way throughout the whole temperature range, with a pattern more similar to those observed in materials. In addition, it is important to highlight that the decomposition pattern of **pCND-$PC_{60}BM$**

does not have any abrupt weight loss which could match with the main decomposition temperature of the **$PC_{60}BM$-OH** sample.

In Figure 2.81b are observed several weight losses between 370-500 ºC for the **$PC_{70}BM$-OH** molecule. Whereas the **pCND-$PC_{70}BM$** hybrid exhibits a constant weight loss with the lack of any abrupt loss which can match with the features discerned in **$PC_{70}BM$-OH**. Therefore, from the TGA analyses can be concluded that the presence of free PCBM-OH molecules is not detected in the functionalized pCND hybrids. This information helps supporting the covalent coupling, ruling out the possibility that fullerenes are interacting by non-covalent forces with pCND.

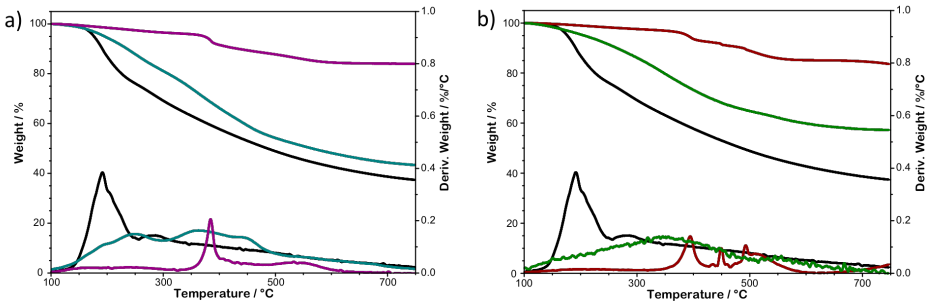

Figure 2.81. a) TGA and first derivative under inert conditions of pCND (black), **$PC_{60}BM$-OH** (purple) and **pCND-$PC_{60}BM$** (blue). b) TGA and first derivative under inert conditions of pCND (black), **$PC_{70}BM$-OH** (dark red) and **pCND-$PC_{70}BM$** (green).

The morphology of both pCND-PCBM hybrids was investigated by means of AFM (Figure 2.82). The measurements demonstrated the presence of quite homogeneous objects with heights between 2-6 nm and an increase in the height of pCND after the incorporation of the fullerenes onto their surface. To reach this outcome both samples were subjected to a statistical analysis where the height of one hundred elements of each sample were measured. For **pCND-$PC_{60}BM$** an average height of 3.2 ± 1.0 nm was obtained and for **pCND-$PC_{70}BM$** the calculated average height was of 3.3 ± 0.8 nm. Therefore, these hybrids have similar dimensions and are larger than those of the starting batch of pCND, with an average height of 1.9 ± 0.6 nm.

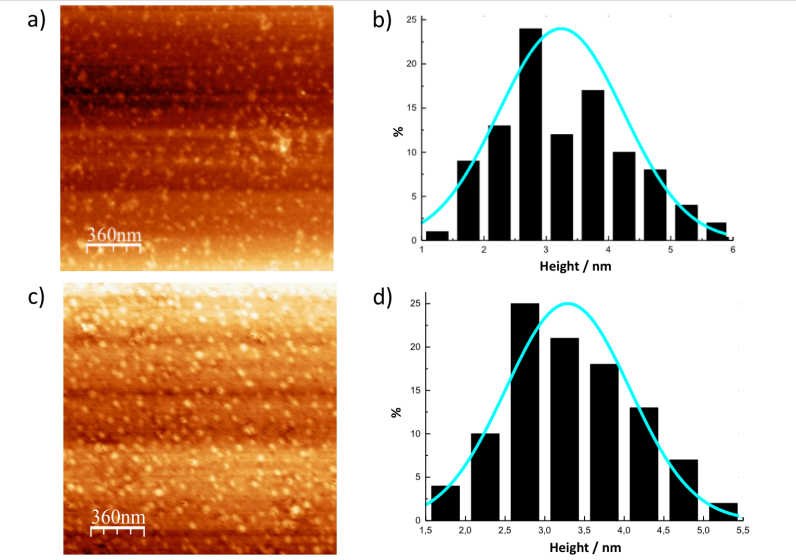

Figure 2.82. a) Representative AFM image of **pCND-PC$_{60}$BM**. b) Height histogram with a curve fit of the data using a Gaussian model. Average height: 3.2 ± 1.0 nm. c) Representative AFM image of **pCND-PC$_{70}$BM**. d) Height histogram with a curve fit of the data using a Gaussian model. Average height: 3.3 ± 0.8 nm.

Electrochemical measurements were carried out to evaluate the impact that the introduction of **PC$_{60}$BM-OH** and **PC$_{70}$BM-OH** units have on the electronic properties of pCND. The cyclic voltammograms (CVs) of the new pCND nanoconjugates are shown in Figure 2.83a. The CVs of the reference **PC$_{60}$BM-OH** and **PC$_{70}$BM-OH** molecules are depicted in Figure 2.83b. The measurements were carried out in DMSO containing 0.1 M $TBAPF_6$ and under an argon atmosphere.

pCND show two evident irreversible oxidations corresponding to the amino groups at -0.01 and +0.58 V and several irreversible reductions, the more prominent reductions are observed at -2.03 and -2.31 V (Figure 2.83a). After covalent modification with the **PC$_{60}$BM-OH** and **PC$_{70}$BM-OH** monoadducts, the electrochemical features of pCND are not clearly discernible. A continuum of diffusion-controlled cathodic current, with an onset at around -0.5 V is observed. This behavior could be attributed to the reductive charging of the **pCND-PC$_{60}$BM** and **pCND-PC$_{70}$BM** hybrids formed.

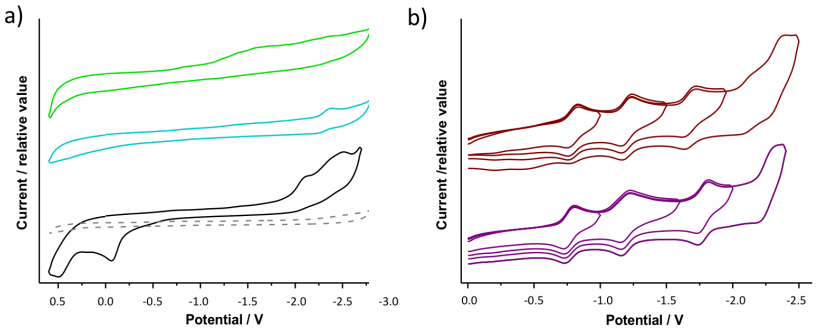

Figure 2.83. a) Cyclic voltammograms of pCND (bottom), **pCND-PC$_{60}$BM** (middle) and **pCND-PC$_{70}$BM** (top) in DMSO solutions. The dashed line represents the background signal. Scan rate 100 mV·s^{-1}. b) Cyclic voltammograms of **PC$_{60}$BM-OH** (bottom) and **PC$_{70}$BM-OH** (top) monoadducts in DMSO solutions. Scan rate 100 mV·s^{-1}.

The redox properties of the **PC$_{60}$BM-OH** and **PC$_{70}$BM-OH** monoadducts were also investigated by CV (Figure 2.83b). They show an electrochemical behavior close to that exhibited by the parent C_{60} and C_{70} on the cyclic voltammetry timescale. The CVs exhibit four reversible, monoelectronic, diffusion-controlled processes for both derivatives. These reduction processes are shifted to more negative values, relative to pristine C_{60} and C_{70} due to the saturation of a double bond in the fullerene core that raises the lowest unoccupied molecular orbital (LUMO) energy of the resulting monoadduct.[272]

A closer inspection to the reductive electrochemistry of the **pCND** nanoconjugates by Differential Pulse Voltammetry (DPV) reveals the presence of several reduction processes of variable intensity ranging from *ca.* -0.54 to -2.32 V (Figure 2.84, Table 2.2). Interestingly, the reductions corresponding to the C_{60} or C_{70} monoadducts could be identified within the multistep reductive processes of pCND nanoconjugates (see dashed lines in Figure 2.84). These fullerene reductions are not noticeable shifted when compared with the respective **PC$_{60}$BM-OH** or **PC$_{70}$BM-OH** monoadducts, which in principle rules out electronic interactions between pCND and the different fullerenes in the ground state.

[272] L. Echegoyen, L. E. Echegoyen, *Acc. Chem. Res.* **1998**, *31*, 593.

Table 2.2. Reduction peak potentials obtained from DPV (in DMSO, mV *vs.* $Ag/AgNO_3$) of pCND, **pCND-PC_{60}BM** and **pCND-PC_{70}BM** nanoconjugates and reference **PC_{60}BM-OH** and **PC_{70}BM-OH** monoadducts.

Material	E^1_{red}	E^2_{red}	E^3_{red}	E^4_{red}	E^5_{red}	E^6_{red}	E^7_{red}	E^8_{red}
pCND	-537 -685	-1015	-1315	-1392	–	-1871	-2043	-2322
PC_{60}BM-OH	-766	-1196	–	–	-1776	–	–	-2258
pCND-PC_{60}BM	-761	-928 -1195	-1333	-1505	-1765	–	-2015	-2286
PC_{70}BM-OH	-797	-1199	–	–	-1675	–	-2121	-2328
pCND-PC_{70}BM	-792	-1187	-1322	-1529	-1654	-1842	-1921 -2107	-2308

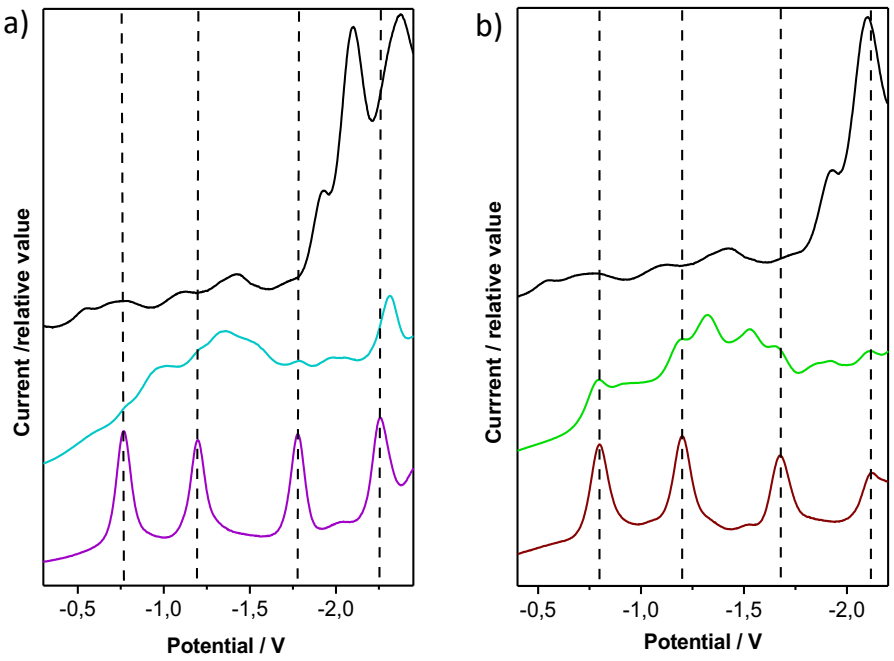

Figure 2.84. Differential pulse voltammograms of: a) From top to bottom pCND, **pCND-PC_{60}BM** and **PC_{60}BM-OH**, and b) From top to bottom pCND, **pCND-PC_{70}BM** and **PC_{70}BM-OH**.

Finally, both **pCND-PC$_{60}$BM** and **pCND-PC$_{70}$BM**, were analyzed by XPS. The high-resolution C 1s core-level spectra of both hybrids revealed the same species observed for pCND as well as the characteristic π- π* shake-up of the fullerenes[273] attached to the pCND surface. Herein, the shake-up of each compound was composed by two deconvolutions of low intensity, located at 288.4 and 289.6 eV for **pCND-PC$_{60}$BM**, and 287.1 and 290.5 eV for **pCND-PC$_{70}$BM**.

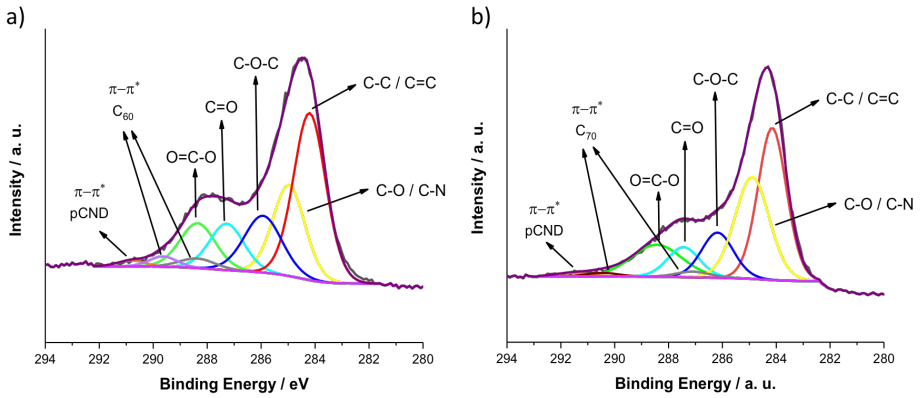

Figure 2.85. C 1s core-level component deconvolution spectra of **pCND-PC$_{60}$BM** (a) and **pCND-PC$_{70}$BM** (b).

All these results confirm the presence of fullerene derivatives in the hybrids and, therefore, that the functionalization process has worked as expected. Supplementary investigations will involve experiments in the excited state in order to see if a charge transfer occurs upon photoexcitation. These experiments are ongoing and there are no preliminary results yet available.

[273] a) G. Gensterblum, K. Hevesi, B. Han, L. Yu, J. Pireaux, P. A. Thiry, R. Caudano, A. Lucas, D. Bernaerts, S. Amelinckx, G. Van Tendeloo, G. Bendele, T. Buslaps, R. L. Johnson, M. Foss, R. Feidenhans'l, G. Le Lay, *Phys. Rev. B*. **1994**, *50*, 11981. b) B. Han, L. Yu, K. Hevesi, G. Gensterblum, P. Rudolf, J. Pireaux, P. A. Thiry, R. Caudano, P. Lambin, A. A. Lucas, *Phys. Rev. B.* **1995**, *51*, 7179.

2.4. EXPERIMENTAL SECTION

2.4. EXPERIMENTAL SECTION

General Methods

In this section the experimental details of techniques which have already been described in the experimental section of Chapter 1 are omitted. Only the new instrumentation or the different conditions used in this chapter are described below.

Atomic force microscopy (AFM): was performed under ambient conditions using SPM Nanoscope IIIa multimode working on tapping mode with a RTESPA tip (Veeco) at a working frequency of B235 KHz. Height and phase images were simultaneously obtained. The samples were prepared by drop-casting or spin coating an ethanol solution of the different nanomaterials on freshly cleaved mica. The substrate was dried under ambient conditions for 24 hours and, afterwards, in a vacuum oven for 48 hours.

X-ray difracction: was performed with a Panalytical X'Pert PRO diffractometer with Cu tube (λ = 1.5418 Å) in th-2th reflection symmetric mode. The divergence slit was used in automatic mode with 12 mm irradiated constant length. Samples were deposited on "zero background" silicon sample holders and measured in reflection geometry.

Electrochemistry: was carried out on a potentiostat/galvanostat AUTOLAB with PGSTAT30 equipped with a software GPES for windows version 4.8 in a conventional three compartment cell. Measurements were carried out using a GCE (glassy carbon) as working electrode, a $Ag/AgNO_3$ reference electrode, and a Pt wire as counter electrode. $TBAPF_6$ was used as supporting electrolyte and DMSO or methanol as solvent. Prior to each voltammetric measurement the cell was degassed under an argon atmosphere by *ca.* 10 min.

2.4.1. Synthesis of molecular precursors

2-(Methylthio)-1,3-dithiolium tetrafluoroborate (13)[251]

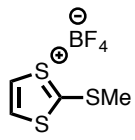

1,3-Dithiole-2-thione **12** (4 g, 29.8 mmol) was suspended in Me_2SO_4 (35.2 mL, 372.1 mmol), heated at 95 ºC for 30 min. and then left to cool to 0 ºC. At this temperature, glacial acetic acid (33 mL) was added and kept stirring for 10 min. $HBF_4 \cdot Et_2O$ (7.7 mL, 29.8 mmol) was added and the solution was stirred during 20 extra min., followed by the addition of diethyl ether (125 mL) to yield a precipitate that was filtered and washed with diethyl ether (92% yield).).

^{1}H-NMR (DMSO-d_6, 300 MHz), δ: 8.73 (s, 2H), 3.17 (s, 3H).

2-(Methylthio)-1,3-dithiole (14)[251]

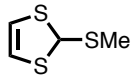

$NaBH_4$ (1.28 g, 26.8 mmol) was slowly added to a 0 ºC cooled solution of 2-(methylthio)-1,3-dithiolium tetrafluoroborate **13** (6 g, 26.8 mmol) in absolute ethanol under Ar atmosphere and the mixture was kept stirring for 2 h. The solvent was removed under reduced pressure, washed with water and extracted with DCM. The organic layer was dried over $MgSO_4$, filtered and taken to dryness to yield the desired product as a dark oil (98% yield).).

^{1}H-NMR ($CDCl_3$, 300 MHz), δ: 6.12 (s, 1H), 6.07 (s, 2H), 2.20 (s, 3H).

1,3-Dithiolium tetrafluoroborate (15)[251]

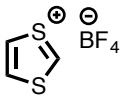

To a solution of 2-(methylthio)-1,3-dithiole **14** (4 g, 26.7 mmol) in acetic anhydride (70 mL) at 0 ºC, $HBF_4 \cdot Et_2O$ (6.3 mL, 29.4 mmol) was added dropwise. The solution was stirred for 15 min., afterwards diethyl ether (32 mL) was added. The mixture was stirred again for 30 min. to yield a white solid that was filtered and washed with diethyl ether (95% yield).).

^{1}H-NMR (DMSO-d_6, 300 MHz), δ: 6.79 (s, 1H), 9.37 (s, 2H).

Dimethyl-(1,3-dithiol-2-yl)-phosphonate (16)[251]

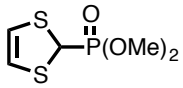

To a solution of 1,3-dithiolium tetrafluoroborate **15** (4.3 g, 22.6 mmol) in acetonitrile, $P(OMe)_3$ (2.7 mL, 22.6 mmol) and NaI (4.2 g, 22.6 mmol) were added successively, stirring the resultant mixture at room temperature for 2 h. The crude reaction solvent was then removed under reduced pressure, washed with water and extracted with DCM. The organic layer was dried over $MgSO_4$, filtered and the solvent was removed to yield the desired product as a dark oil (91% yield).).

^{1}H-NMR ($CDCl_3$, 300 MHz), δ: 5.98 (s, 2H), 4.73 (d, 1H, J = 4.5 Hz), 3.75 (d, 6H, J = 10.5 Hz).

2-(((*Tert*-butyldiphenylsilyl)oxy)methyl)anthraquinone (18)[252]

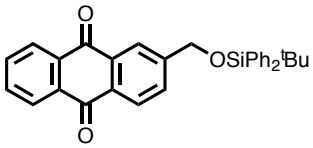

2-Hydroxymethylanthraquinone **17** (1.00 g, 4.20 mmol) was dissolved in 50 mL of anhydrous THF and, under Ar atmosphere, imidazole (1.43 g, 21.00 mmol) and *tert*-butyldiphenylsilane chloride (1.24 mL, 5.03 mmol) were added. The reaction mixture was kept stirring overnight. Then, the solvent was removed under reduced pressure and the residue was dissolved in DCM and washed with water. The organic layer was dried with $MgSO_4$ and filtered, the solvent was then evaporated to yield a crude that was purified by silica gel column chromatography, using a hexane/DCM (2/1) mixture as eluent. The final product was obtained as a pale yellow solid (98% yield).

^{1}H-NMR ($CDCl_3$, 300 MHz), δ: 8.33-8.25 (m, 4H), 7.83-7.79 (m, 3H), 7.73-7.70 (m, 4H), 7.47-7.38 (m, 6H), 4.92 (s, 2H), 1.16 (s, 9H).

2-(((*Tert*-butyldiphenylsylyl)oxy)methyl)-9,10-bis(1,3-dithiol-2-ylidene)-9,10-dihydroanthracene (19)[253]

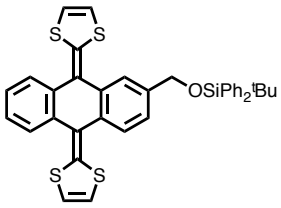

A volume of 1.1 mL of *n*-BuLi (2.5 M in hexane, 2.6 mmol) was added to a solution of dimethyl-(1,3-dithiol-2yl)-phosphonate **16** (0.50 g, 2.36 mmol) in anhydrous THF (100 mL) at -78 ºC and under Ar atmosphere. The mixture was kept stirring during 45 min. at the same temperature. Then, 2-(((*tert*-butyldiphenylsilyl)oxy)methyl)anthraquinone **18** (0.28 g, 0.59 mmol) was dissolved in anhydrous THF (100 mL) and added dropwise. The mixture was kept at -78 ºC for 1 h. and then was left to reach room temperature overnight. The solvent was removed under reduced pressure and the crude was washed with water (100 mL) and extracted with DCM (3 x 100 mL). The combined organic layers were washed with water (2 x 100 mL) and a saturated NaCl aqueous solution (2 x 100 mL), dried over $MgSO_4$ and filtered. The solvent was removed and the residue was purified by silica gel column chromatography using a hexane/DCM (2/1) mixture as eluent. The final product was obtained as a yellow solid (91% yield).).

^{1}H-NMR ($CDCl_3$, 300 MHz), δ: 8.25-8.14 (m, 7H), 8.03-7.72 (m, 10H), 6.79 (s, 4H), 4.83 (m, 2H), 1.16 (s, 9H).

2-(Hydroxymethyl)-9,10-bis(1,3-dithiol-2-ylidene)-9,10-dihydroanthracene (20)[253]

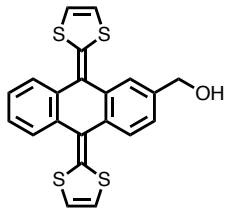

To a solution of 2-(((*tert*-butyldiphenylsilyl)oxy)methyl)-9,10-bis(1,3-dithiol-2-ylidene)-9,10-dihydroanthracene **19** (0.217 g, 0.33 mmol) in 40 mL of

anhydrous THF, a volume of 1.4 mL of TBAF (1.0 M in THF, 0.50 mmol) was added under Ar atmosphere. The mixture was kept stirring during 2 h. at room temperature. After this time, the reaction mixture was washed with water and extracted with DCM. The organic layer was dried over $MgSO_4$, filtered and the solvent was removed under reduced pressure. The residue was purified by silica gel column chromatography, using DCM as eluent, to yield a yellow solid (89% yield).

^{1}H-NMR ($CDCl_3$, 300 MHz), δ: 7.66-7.57 (m, 4H), 7.36-7.23 (m, 3H), 6.74-6.73 (m, 4H), 5.29 (t, 1H, J = 5.6 Hz), 4.54 (d, 2H, J = 5.6 Hz).

2-hydroxymethyl-11,11,12,12-tetracyano-9,10-anthra-*p*-quinodimethane (21)[259]

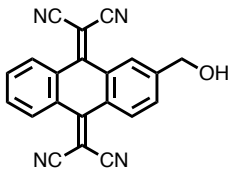

A solution of 2-hydroxymethylanthraquinone **17** (0.600 g, 2.5 mmol) and malonitrile (0.416 g, 6.3 mmol) in $CHCl_3$ (150 mL) was heated under Ar atmosphere at 65 ºC. Then, $TiCl_4$ and pyridine were added dropwise, keeping the solution stirring at this temperature 4 days. The same amounts of malonitrile, $TiCl_4$ and pyridine were added again every 24 h. After 4 days, the reaction mixture was left to reach r.t. and filtered over celite, washed with water, dry over Na_2SO_4, and filtered. The crude was taken to dryness and then purified by silica gel column chromatography using a hexane/ethyl acetate (3/1) mixture as eluent to yield a yellow solid (82 % yield).

^{1}H-NMR ($CDCl_3$, 300 MHz), δ: 8.22-8.14 (m, 4H), 7.76-7.70 (m, 3H), 4.82 4.82 (d, J = 5.1 Hz, 2H).

Methyl 4-benzoylbutyrate (23)[266]

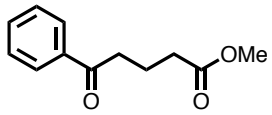

To a solution of 4-benzoylbutyric acid **22** (3 g, 15.6 mmol) in methanol (40 mL), oxalyl chloride (2.97 g, 23 mmol) was added and the reaction mixture was refluxed for 24 h. The solvent was partially evaporated under vacuum and the residue was extracted into DCM, washed with water/sodium bicarbonate, and dried with anhydrous $MgSO_4$. The solvent was removed under vacuum providing an oil (87% yield).

^{1}H-NMR ($CDCl_3$, 300 MHz), δ (ppm): 7.98 (d, J = 8.1 Hz, 2H), 7.65 (m, 2H), 7.45 (m, 1H), 3.69 (s, 3H), 3.07 (t, J = 7.1 Hz, 2H), 2.46 (t, J = 7.1 Hz, 2H), 2.09 (q, J = 7.1 Hz, 2H).

Methyl 4-benzoylbutyrate p-tosylhydrazone (24)[266]

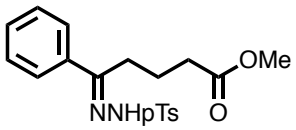

A mixture of methyl 4-benzoylbutyrate **23** (2.25 g, 11 mmol) and *p*-toluenesulfonyl hydrazide (3.17 g, 17 mmol) in ethanol (50 mL) was refluxed overnight. After that, the reaction mixture was allowed to reach room temperature and the solvent was partially removed under vacuum. The mixture was introduced into an ice bath and immediately a precipitate was formed. It was filtered and washed with cold ethanol several times to yield the final product (91% yield).

^{1}H-NMR ($CDCl_3$, 300 MHz), δ: 9.3 (s, 1H), 7.93 (d, J = 8.5 Hz, 2H), 7.66 (m, 2H), 7.34 (m, 3H), 7.28 (d, J = 8.5 Hz, 2H), 3.79 (s, 3H), 2.64 (m, 2H), 2.40 (s, 3H), 2.33 (t, J = 6 Hz, 2H), 1.69 (m, 2H).

1-(3-(MethoxycarbonyI)propyl)-1-phenyl-[6,6]-C_{61} ($PC_{60}BM$)[266]

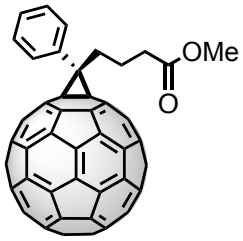

Methyl 4-benzoylbutyrate *p*-tosylhydrazone **24** (0.2 g, 0.53 mmol) and sodium *tert*-butoxide (0.111 g, 0.80 mmol) were mixed in 2 mL of dry pyridine under Ar atmosphere. After 20 min., C_{60} was added (0.385 g, 0.53 mmol) in chlorobenzene (250 mL) and the mixture was refluxed for 24 h. The solvent was removed under vacuum and the crude was purified by silica gel column chromatography using CS_2 as eluent to recover the unreacted C_{60}, and then a mixture of solvents (toluene/hexane 8/2) to collect the desired compound (32% yield).

^{1}H-NMR ($CDCl_3$, 300 MHz), δ: 7.93 (d, 2H, *J* = 8.0 Hz,), 7.54 (m, 3H), 3.68 (s, 3H), 2.91 (m, 2H), 2.53 (t, 2H, J = 7.5 Hz), 2.18 (m, 2H).

1-Hydroxybutyl-1-phenyl-[6,6]-C_{61} ($PC_{60}BM$-OH)[270]

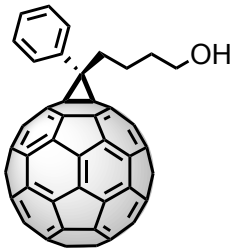

$PC_{60}BM$ (0.151 g, 0.17 mmol) was dissolved in dry toluene (100 mL) under Ar atmosphere. The solution was cooled to 0°C and after 20 min., DIBAL (1 M in hexane, 0.52 mL, 0.53 mmol) was added dropwise. The reaction was allowed to warm to room temperature and stirred for 24 h. The mixture was cooled to 0 ºC and the reaction was quenched adding water (0.073 mL) dropwise. After 10

min. NaOH was added (15% aqueous solution, 0.073 mL) and subsequently water (0.22 mL). The mixture was warmed to r.t. and stirred for 15 min., then it was added $MgSO_4$ and stirred for another 15 min. Finally, the salts were filtered in a celite pad and the collected filtrated was evaporated under reduced pressure. The product was purified using column chromatography on silica gel in a mixture of solvents (toluene/ethyl acetate 9/1) to provide the final compound (79% yield).

^{1}H-NMR ($CDCl_3$, 300 MHz), δ: 7.93 (m, 2H), 7.54 (m, 3H), 3.74 (m, 2H), 2.90 (m, 2H), 1.92-1.98 (m, 2H), 1.78 (m, 2H).

1-(3-(MethoxycarbonyI)propyl)-1-phenyl-[6.6]-C_{71} siteisomers mixture ($PC_{70}BM$)[268]

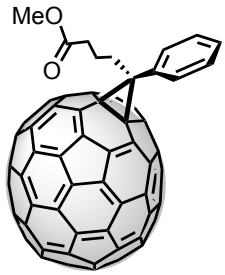

Methyl 4-benzoylbutyrate *p*-tosylhydrazone **24** (0.2 g, 0.53 mmol) and sodium *tert*-butoxide (0.111 g, 0.80 mmol) were mixed in 2 mL of dry pyridine under Ar atmosphere. After 20 min., C_{70} was added (0.450 g, 0.53 mmol) in chlorobenzene (250 mL) and the mixture was refluxed for 24 h. The solvent was removed under vacuum and the crude was purified by silica gel column chromatography using CS_2 as eluent to recover the unreacted C_{70}, and then, a mixture of solvents (toluene/hexane 8/2) to collect the desired compounds (33% yield).

^{1}H-NMR ($CDCl_3$, 300 MHz), δ: 7.91 (d, 2H), 7.54 (m, 3H), 3.68 (s, 3H), 2.49 (m, 4H), 2.17 (m, 2H).

1-Hydroxybutyl-1-phenyl-[6,6]-C_{71} siteisomers mixture ($PC_{70}BM$-OH)

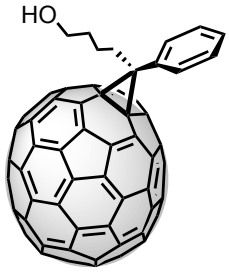

$PC_{70}BM$ (0.176 g, 0.18 mmol) was dissolved in dry toluene (25 mL) under Ar atmosphere. The solution was cooled to 0 °C and after 20 min., DIBAL (1 M in hexanes, 0.53 mL, 0.53 mmol) was added dropwise. The reaction was allowed to warm to room temperature and stirred for 24 h. The mixture was cooled to 0 ºC and the reaction was quenched adding water (0.073 mL) dropwise. After 10 min. NaOH was added (15% aqueous solution, 0.073 mL) and subsequently water (0.22 mL). The mixture was warmed to r.t. and stirred for 15 min., then it was added $MgSO_4$ and stirred for another 15 min. Finally, the salts were filtered in a celite pad and the collected filtrated was evaporated under reduced pressure. The product was purified using column chromatography on silica gel in a mixture of solvents (toluene/ethyl acetate 9/1) to provide the final compounds (53% yield).

^{1}H-NMR ($CDCl_3$, 300 MHz), δ: 7.90 (m, 2H), 7.47 (m, 3H), 3.73 (m, 2H), 2.45 (m, 2H), 1.90 (m, 2H), 1.74 (m, 2H).

2.4.2. Synthesis of carbon-based nanodots

Preparation of GO by the Kovtyukhova-Hummer's method[76,150]

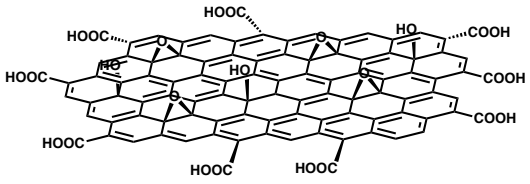

The modified Hummer's method reported by Kovtyukhova *et al.*[76] was adapted with some modifications.[150] The steps involved in the preparation of GO are described in detail below.

Pre-oxidation of graphite: graphite powder (4 g), $K_2S_2O_8$ powder (2 g), and P_2O_5 (2 g) were dry-mixed in a 250 mL round bottom flask followed by the addition of sulfuric acid (H_2SO_4, 98%, 10 mL). The mixture was refluxed at 80 °C for 6 h. The mixture was left to cool down to room temperature and then diluted in 250 mL of deionized water. The mixture was filtered over a hydrophilic PTFE membrane (0.1 μm) and then washed with water until the filtrate became neutral. The filter cake obtained was oven dried at 50 °C overnight affording a black-grey powder.

Low temperature stage: The dried pre-oxidized graphite powder (~ 4 g) and $NaNO_3$ (4 g) were dry-mixed in a 500 mL round bottom flask. Then H_2SO_4 (98%, 100 mL) was added and the mixture was kept stirring at 0 °C on an ice bath. When the powders were fully dispersed, $KMnO_4$ (12 g) was added slowly to the suspension. The addition rate was carefully controlled so that the temperature of the suspension was kept below 20 ºC. After the addition of $KMnO_4$ was completed, the suspension was stirred at 0 ºC for an additional 10 min.

Medium temperature stage: The ice bath was removed and the temperature was raised to 35 °C. The resulting mixture was allowed to stir at this temperature for 2 h. Afterwards, the brown pasty suspension was heated to 60 °C.

High temperature stage: Once the temperature reached 60 °C, 50 mL of deionized water were added to the mixture and stirred for 5 min. After this time, the temperature was set to 80 °C followed by the addition of 80 mL of deionized water and H_2O_2 (35 %, 10 mL). The mixture was stirred for 30 min. at 80 °C and then it was cooled to r.t. and stirred until the next day, where it was obtained a brown pasty mixture.

Washing and purification: The brown suspension of the previous step was filtered over a hydrophilic hydrophilic PTFE membrane (0.1 μm) and washed with an aqueous solution of HCl (1N) until the collected filtrate solution becomes nearly transparent. Afterwards, the brown solid was washed with an aqueous solution of NaOH (1N) until the collected filtrate solution becomes dark brown. Finally, the solid was resuspended in deionized water, sonicated

for 1 h. and centrifuged at 3000 rpm for 5 min. The obtained black solid was dried in an oven at 60 ºC for one week (5g).

FTIR (KBr), ν (cm^{-1}): 1719 (C=O stretching mode) and 1561 (C=C stretching mode).

TGA (N_2 atmosphere): weight loss and temperature desorption (organic anchoring groups): 36%, 650 °C.

UV-Vis (H_2O), λ_{max} (nm): 240.

XPS: % atomic: C (284.4 eV) = 70.1, O (532.3 eV) = 29.9.

Synthesis of GQD[26]

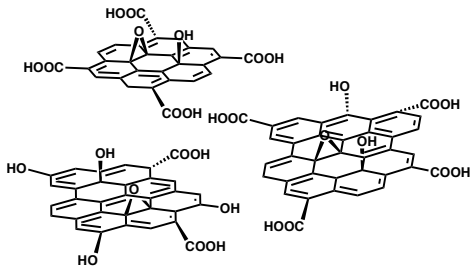

The GO (5g) obtained by the Kovtyukhova-Hummer method was added over a mixture of concentrated H_2SO_4 and HNO_3 (3/1, v/v, 250 mL). The solution was subjected to ultrasonic treatment for 3 h. and then it was stirred at 120 ºC for 24 h. After this period of time, the mixture was cooled to r.t. and was filtered over a hydrophilic PTFE membrane (0.1 μm). The collected filtrate was diluted with deionized water and neutralized with a saturated K_2CO_3 solution. The water was removed under reduced pressure until the solution reaches a final volume of around 100 mL. This solution was subjected to dialysis (bags of 2000 Daltons) for one week. Finally, water was removed under reduced pressure to afford GQD (265 mg).

FTIR (KBr), ν (cm^{-1}): 1719 (C=O stretching mode), 1611 (C=C stretching mode) and 1150 (C-O stretching mode).

TGA (N_2 atmosphere): weight loss and temperature desorption (organic anchoring groups): 38 %, 650 °C.

XPS: % atomic: C (284.6 eV) = 70.5, O (532.4 eV) = 29.4.

Raman, shift (cm^{-1}):1600 (G band), 1390 (D band). I_D/I_G = 0.92.

UV-Vis (H_2O), λ_{max} (nm): 270 (n-π^*), 225 (π-π^*).

Fluorescence (H_2O, λ_{exc} = 350 nm): λ_{max} = 525 nm.

Synthesis of the starting CND_{aGlu}

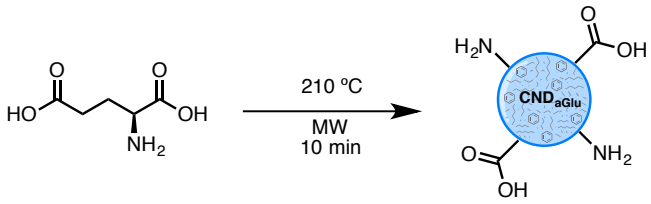

L-glutamic acid (1g) was added into a microwave tube and heated at 210 ºC in a microwave reactor for 10 min. A dark brown solid was obtained, which indicates the formation of CND. Then, a few mL of acetone were added, and the dispersion was filtered over a 0.2 µm syringe filter in order to remove the solid byproducts. The collected solution was stored in a freezer in order to precipitate the starting *L*-glutamic acid, which has not reacted. After 24 h. the solution was filtered over a 0.1 µm hydrophilic (PTFE) membrane to remove the excess of *L*- glutamic acid. Once filtered, the collected solution was evaporated under reduced pressure to give rise to the brown solid CND_{aGlu} (0.470 g).

FTIR (KBr), ν (cm^{-1}): 1703-1638 (C=O stretching mode), 1500 (C=C stretching mode), 1460-1383 (C-N stretching mode) and 1241-1085 (C-O stretching mode).

TGA (N_2 atmosphere): weight loss and temperature desorption (material stability): 90 %, 650 °C

XPS: % atomic: C (284.6 eV) = 65.8, O (531.6 eV) = 23.9, N (399.6 eV) = 10.3.

UV-Vis (MeOH), λ_{max} (nm): 215, 334.

Fluorescence (MeOH, λ_{exc} = 365 nm): λ_{max} = 450 nm.

Synthesis of annealed gCND$_{aGlu}$

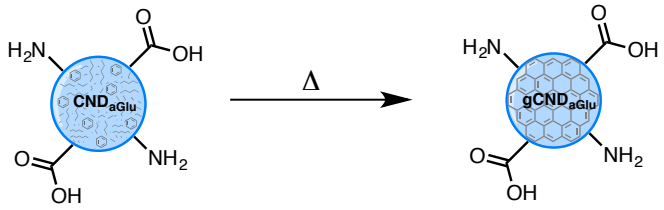

In these graphitization experiments, a sample of CND$_{aGlu}$ Ini (30 mg) was heated in an oven at different temperatures for 72 h. The temperatures used in each experiment were: 100, 120, 140, 150, 160, 180, 200 and 220 ºC generating the corresponding products CND$_{aGlu}$ 100, CND$_{aGlu}$ 120, CND$_{aGlu}$ 140. CND$_{aGlu}$ 150, CND$_{aGlu}$ 160, CND$_{aGlu}$ 180, CND$_{aGlu}$ 200 and CND$_{aGlu}$ 220. The changes observed in comparison with the starting CND$_{aGlu}$ Ini were commented and discussed in the "*Results and discussion*" section of this chapter.

Synthesis of pCND

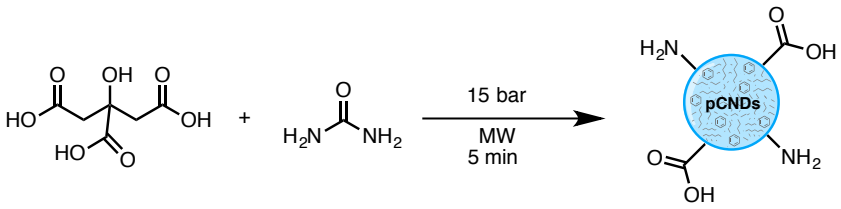

Citric acid (0.750 g) and urea (0.750 g) in 2.5 mL of deionized water were added into a microwave tube. This solution was heated in a microwave reactor for 5 min. maintaining the pressure at 15 bar during the 5 min. The resulting solution was poured into a 250 mL Erlenmeyer flask and was introduced in an

oven at 100 ºC one day in order to evaporate the water. The resulting black powder was washed with acetone with the aim of removing the polymeric residues formed during the synthesis. The solid was dried in an oven at 100 ºC obtaining a shiny black powder (0.460 g).

FTIR (KBr), ν (cm^{-1}): 1750-1500 (C=O stretching mode and C=C stretching mode).

TGA (N_2 atmosphere): weight loss and temperature desorption (material stability): 58 %, 650 °C.

XPS: % atomic: C (284.6 eV) =59.5, O (531.6 eV) =23.5, N (399.6 eV) =17.0.

Raman, shift (cm^{-1}):1569 (G band), 1351 (D band). I_D/I_G = 1.10.

UV-Vis (DMSO), λ_{max} (nm): 350, 375,

Fluorescence (DMSO, λ_{exc} = 350 nm): λ_{max} = 439 nm.

2.4.3. SYNTHESIS OF GQD and pCND DONOR-ACCEPTOR HYBRIDS

Synthesis of GQD-exTTF

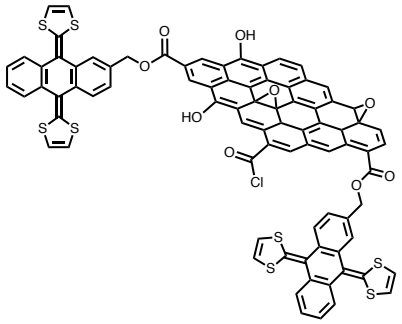

GQD (60 mg) were refluxed in $SOCl_2$ (10 mL) for 24 h. at 70 °C under Ar atmosphere, the excess of $SOCl_2$ was then evaporated using Ar as carrier gas. The GQD modified with acid chlorides were reacted *in situ* with 2-hydroxymethyl-exTTF **20** (60 mg), dissolved in 3.0 mL of DMSO at 110 °C for 24 h. and under Ar atmosphere. The resulting mixture was added over cold diethyl ether and was centrifuged at 6000 rpm for 10 min. Afterwards, the ether solution was removed and fresh cold ether was added and the mixture centrifuged again in the same conditions. This process was repeated several

times until the ether solution was colourless. The black solid was suspended in DCM and separated by filtration through a 0.1 µm hydrophilic PTFE membrane and subjected to consecutive washings with DCM, MeOH and water until the collected solution was colourless. The obtained black powder was dried in vacuum to obtain a dark brown solid (26 mg).

FTIR (KBr), ν (cm^{-1}): 1740 (C=O stretching mode), 1719 (C=O stretching mode), 1611 (C=C stretching mode) and 645 (C-S stretching mode).

TGA (N_2 atmosphere): weight loss and temperature desorption (material stability): 66 %, 650 °C

XPS: % atomic: C (284.6 eV) = 69.0, O (531.6 eV) =25.1, S (163.6 eV) = 5.9.

Raman, shift (cm^{-1}):1571 (G band), 1345 (D band). I_D/I_G = 1.00.

UV-Vis (DMSO), λ_{max} (nm): 363, 429.

Synthesis of pCND-exTTF

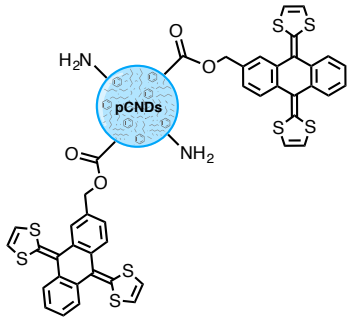

pCND (60 mg) were refluxed in $SOCl_2$ (10 mL) for 24 h. at 70 °C under Ar atmosphere, the excess of $SOCl_2$ was then evaporated using Ar as carrier gas. The pCND modified with acid chlorides were reacted *in situ* with 2-hydroxymethyl-exTTF **20** (75 mg), dissolved in 2.5 mL of DMSO at 110 °C for 24 h. and under Ar atmosphere. The resulting mixture was added over cold diethyl ether and was centrifuged at 6000 rpm for 10 min. Afterwards, the ether solution was removed and fresh cold ether was added and the mixture centrifuged again in the same conditions. This process was repeated several times until the ether solution was colourless. The black solid was suspended in DCM and separated by filtration through a 0.1 µm hydrophilic PTFE

membrane and subjected to consecutive washings with DCM, MeOH and water until the collected solution was colourless. The obtained black powder was dried in vacuum to obtain a dark brown solid (31 mg).

FTIR (KBr), ν (cm^{-1}): 1750-1500 (C=O stretching mode and C=C stretching mode) and 647 (C-S stretching mode).

TGA (N_2 atmosphere): weight loss and temperature desorption (material stability): 50 %, 650 °C.

XPS: % atomic: C (284.6 eV) = 57.8, O (531.6 eV) =26.3, N (399.6 eV) = 12.0, S (164.8 eV) = 3.9.

Raman, shift (cm^{-1}):1564 (G band), 1356 (D band). I_D/I_G = 0.93.

UV-Vis (DMSO), λ_{max} (nm): 366, 431.

Synthesis of pCND-TCAQ

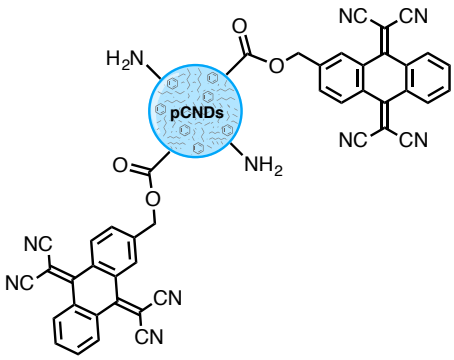

pCND (60 mg) were refluxed in $SOCl_2$ (10 mL) for 24 h. at 70 °C under Ar atmosphere, the excess of $SOCl_2$ was then evaporated using Ar as carrier gas. The pCND modified with acid chlorides were reacted *in situ* with 2-hydroxymethyl-TCAQ **21** (75 mg), dissolved in 2.5 mL of DMSO at 110 °C for 24 h. and under argon atmosphere. The resulting mixture was added over cold diethyl ether and was centrifuged at 6000 rpm for 10 min. Afterwards, the ether solution was removed and fresh cold ether was added and the mixture centrifuged again in the same conditions. This process was repeated several times until the ether solution was colourless. The black solid was suspended in

DCM and separated by filtration through a 0.1 μm hydrophilic PTFE membrane and subjected to consecutive washings with DCM, MeOH and water until the collected solution was colourless. The obtained black powder was dried in vacuum to obtain a dark brown solid (20 mg).

FTIR (KBr), ν (cm^{-1}): 2208 (C≡N stretching mode) and 1750-1500 (C=O stretching mode and C=C stretching mode).

TGA (N_2 atmosphere): weight loss and temperature desorption (material stability): 52 %, 650 °C.

XPS: % atomic: C (284.6 eV) = 49.0, O (531.6 eV) =36.2, N (399.6 eV) = 14.8.

UV-Vis (DMSO), λ_{max} (nm): 330, 411.

General procedure for the synthesis of pCND-$PC_{60}BM$ and pCND-$PC_{70}BM$

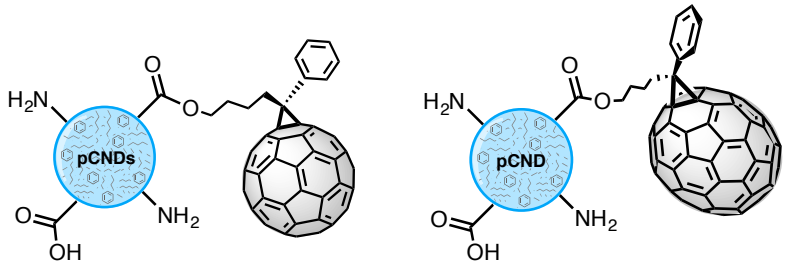

pCND (40 mg) were refluxed in $SOCl_2$ (10 mL) for 24 h. at 70 °C under Ar atmosphere, the excess of $SOCl_2$ was then evaporated using Ar as carrier gas. Over the modified pCND were added **$PC_{60}BM$-OH** or **$PC_{70}BM$-OH** (20 mg) dissolved in 10 mL of a DMSO/chlorobenzene (1:1) mixture, and the reaction flask was sonicated for 2 h. under argon atmosphere for ensuring the complete disolution of the reagents. Afterwards, the mixture was heated at 110 °C for 24 h. and under argon atmosphere. The resulting mixture was added over cold diethyl ether and was centrifuged at 6000 rpm for 10 min. Afterwards, the ether solution was removed and fresh cold ether was added and the mixture centrifuged again in the same conditions. This process was repeated several times until the ether solution was colourless. The black solid was suspended in

DCM and separated by filtration through a 0.1 μm hydrophilic PTFE membrane and subjected to consecutive washings with toluene, MeOH and water until the collected solution was colourless. The obtained black powder were dried in vacuum to obtain a dark brown solid.

pCND-PC_{60}BM

Obtained mass: 11.3 mg.

FTIR (KBr), ν (cm^{-1}): 1750-1500 (C=O stretching mode) and 527 (C_{60} stretching mode).

TGA (N_2 atmosphere): weight loss and temperature desorption (material stability): 54 %, 650 °C.

XPS: % atomic: C (284.6 eV) = 63.3, O (531.6 eV) =28.1, N (399.6 eV) = 8.6.

UV-Vis (DMSO), λ_{max} (nm): 342, 450, 563.

pCND-PC_{70}BM

Obtained mass: 16.6 mg.

FTIR (KBr), ν (cm^{-1}): 1750-1500 (C=O stretching mode and C=C stretching mode) and 533, 579, 645, 674 and 700 (C_{70} stretching modes).

TGA (N_2 atmosphere): weight loss and temperature desorption (material stability): 41 %, 650 °C.

XPS: % atomic: C (284.6 eV) = 63.4, O (531.6 eV) =27.9, N (399.6 eV) = 8.7.

UV-Vis (DMSO), λ_{max} (nm): 373, 440.

CONCLUSIONS

CONCLUSIONS

In the light of the results obtained during this thesis work, the next conclusions can be established.

Few-layer graphene (GR) and graphene oxide (GO) production

In the search of optimum conditions for the mechanical exfoliation of graphite in liquid phase for obtaining GR, two different solvents were tested: NMP and *o*-DCB. In both cases, under the same conditions of sonication and centrifugation, homogeneous dispersions without sedimentation were obtained. According to TEM studies, the aggregates obtained in *o*-DCB were formed with a higher number of layers than in the case of NMP, evidencing a lower exfoliation degree. The GR dispersions in NMP were further analyzed by Raman spectroscopy revealing that the material is composed by approximately three layers of graphene.

Regarding the GO production achieved by the Staundemaier method, the formation of GO was confirmed by the presence of new oxygenated species attached to the carbon sp^2 network. This information was revealed by the complete structural characterization of GO by TEM, TGA, FTIR and XPS. Herein, it is important to highlight the presence of carboxylic acids, and epoxy and hydroxy groups, among other species in the GO structure, which make GO perfectly dispersible in aqueous media.

The key point of this part was the understanding of the properties and the development of production methods for GR and GO, which were the scaffolds for the formation of new photo- and electroactive hybrids in combination with anionic heptamethine cyanines (Cy) in Chapter 1 of this dissertation.

Chemical functionalization of single-walled carbon nanotubes (SWCNTs) and graphene-based materials with Cy

In the first part of this section, was designed and synthesized an anionic hepthamethine cyanine with a pyrene fragment in its structure (CyPyr). This structure was subsequently used to form stable supramolecular assemblies with SWCNT and GR by π-π stacking forces (GR-CyPyr and SWCNT-CyPyr). The

formation of these complexes was monitored by steady-state absorption and by fluorescence titration experiments. On the one hand, the intercalation of CyPyr between the SWCNT bundles or GR layers allowed the individualization of SWCNT and the exfoliation of GR in methanol as demonstrated by TEM. Furthermore, it was noticed an increase in the stability of the GR-CyPyr and SWCNT-CyPyr dispersions in comparison with dispersions of pristine GR and SWCNT.

On the other hand, the electron-donating character of CyPyr enabled the *n*-doping of the carbon allotropes. This fact was confirmed by statistical Raman assays, where the downshifted of the 2D- and G-modes for SWCNT, as well as the up-shifted 2D- and downshifted G-modes for GR, revealed the *n*-doping of SWCNT and GR. Finally, further experiments in the excited state confirmed a metastable charge transfer process from the CyPyr to the carbon allotropes, accompanied by the formation of a radical-ion-pair state with a lifetime of several nanoseconds. Such a lifetime domain is quite remarkable for supramolecular assemblies where GR and Cy are so closely connected. To sum up, through this strategy we were able to achieve the exfoliation of GR or the individualization of SWCNT as well as the *n*-doping of these carbon materials in a single step.

In the second part of Chapter 1, imidazolium salts were grafted on GR and GO surfaces by covalent strategies (GR^{IL} and GO^{IL}). With regard to the functionalization of GO, the incorporation of the imidazole fragment was carried out by esterification reactions using the carboxylic acids of the GO surface. This reaction was confirmed by the formation of the amide bonds, which were identified by FTIR spectroscopy as well as by the appearance of a new component in the N 1s core-level contribution of the XPS analysis. Afterwards, the alkylation of the imidazole units was corroborated by the increase of the weight loss observed in TGA experiments, accompanied by the presence of Br 3d in the XPS survey spectrum, as result of the imidazolium salt formation. On contrary, the functionalization of GR was carried out by the addition of the imidazolium salt on the sp^2 lattice by radical addition (Tour reaction). In this case, the imidazolium salt was previously synthesized with an aniline group to allow the attachment to the GR surface. TGA experiments showed an increase of weight loss after the formation of GR^{IL} in comparison with the thermogram of the starting GR.

Finally, the bromide counter ions of the imidazolium salts attached onto GO and GR were exchanged by anionic heptamethine cyanines (Cy and CyC_{60}). The formation of the hybrid materials (GO^{IL}-Cy and GO^{IL}-CyC_{60}, GR^{IL}-Cy and GR^{IL}-CyC_{60}) was revealed by the presence of the Cy absorption bands in the UV-Vis-NIR spectra, as well as by the presence of the cyano groups around 2200 cm^{-1} in the FTIR spectra.

In conclusion, in this section we have proposed different synthetic strategies (covalent/supramolecular) for the functionalization of different carbon materials (GR, GO, SWCNT) with photoactive and electron-donating Cy.

Graphene quantum dots (GQD) and carbon nanodots (CND) production

The production of GQD was performed by the treatment of GO with a mixture of concentrated H_2SO_4/HNO_3 (top-down strategy). After this process the morphology of GQD was studied by TEM and AFM. Herein, we were able to see the presence of a mixture of isolated and few-layered GQD with sizes in the range from 4 to 18 nm and average heights of 1.3 ± 0.3 nm. Additional structural information came from FTIR spectroscopy, where the stretching vibrations of the OH, C=C, C=O and C-O bonds were discerned. The small size of GQD in combination with the polar groups attached in their structure resulted in nanoparticles soluble in aqueous media. Moreover, Raman spectroscopy revealed the graphitic nature of GQD due to the presence of the G and D bands in the spectrum. Turning to the optical properties of GQD, they exhibit absorptions in the range from 200 to 600 nm, and upon light excitation (λ_{exc} = 350 nm), present a strong emission at 525 nm responsible of the light-yellow color visible to the naked eye.

In subsequent investigations, CND were produced by a bottom-up methodology. For that task, in a first instance, it was carried out the microwave-assisted pyrolysis of *L*-glutamic acid. The obtained CND_{aGlu} presented quasi-spherical shapes with average heights of 1.6 ± 0.5 nm. Moreover, CND_{aGlu} provided a blue-shifted and narrower emission band than that of GQD. However, CND_{aGlu} exhibited a polymeric nature with a structure composed with mostly sp^3 domains unlike GQD, which presented a more defined graphitic structure. This fact was deduced by the observed crystalline polymeric phase in XRD experiments, the lack of π-π shake-up contributions in XPS and the absence of graphitic features in Raman experiments. For that reason, a post-treatment carbonization was performed with the aim of obtaining

a higher degree of sp^2 domains. These experiments confirmed that it is possible to graphitize CND_{aGlu} in a second heating step when using temperatures above 160 ºC, reaching the complete graphitization over 200 ºC. In this range of temperatures, it was observed an increase of the stability in TGA, a graphitic profile (D and G bands) in the Raman spectra, and an increase in the C=C and graphitic-N components in the XPS. Besides these structural changes, CND_{aGlu} subjected to thermal annealing with increasing temperatures, showed a broad emission band, which is slightly red-shifted when compared with the starting CND_{aGlu}, a similar profile to that observed in GQD. Finally, the CND_{aGlu} solubility in water tended to decrease significantly due to the loss of hydrophilic functional groups such as amines or carboxylic acids through condensation or decarboxylation processes, which trigger the formation of new sp^2 domains.

In a second instance, it was explored an alternative to this CND production: the multi-component synthesis of CND using citric acid and urea as precursors (pCND). This method consisted in the microwave heating of an aqueous solution of citric acid and urea maintaining the pressure constant at 15 bar. Through this methodology, it was assured the complete carbonization of the precursors in only one step, avoiding further graphitization experiments. Therefore, the obtained pCND were quasi-spherical nanoparticles with a mean height around 2 nm, composed by sp^2 and sp^3 domains, and soluble in polar solvents such us water, methanol or DMSO. Furthermore, the emission band was narrower than that observed for CND_{aGlu} Ini, and the obtained quantum yield higher (20 % for pCND, 14.5 % for CND_{aGlu}).

From these results, we can conclude that the last method is the best option for producing carbon dots (pCND), since it is faster than the others (GQD and CND_{aGlu}) and the obtained nanomaterials present enhanced emission properties.

Functionalization of GQD and CND with electroactive molecules

The second part of Chapter 2 was directly focused in the incorporation of electroactive molecules in the surface of GQD and pCND. For that task, it was established an efficient and easy methodology, which consisted in the previous activation of the carboxylic acids present in GQD and pCND with $SOCl_2$ and the *in situ* incorporation of the electroactive molecules, bearing hydroxy functional groups, by esterification reactions in DMSO.

According to this methodology, the first step was the decoration of GQD and pCND with electron donor exTTF molecules. Both, pCND-exTTF and GQD-exTTF, were fully characterized confirming the attachment of the exTTF by techniques such as XPS, NMR and electrochemistry experiments. Furthermore, for both systems was observed an almost quantitative quenching of GQD and pCND fluorescence, which suggested an electronic interaction with the electron donor exTTF in the excited state. Therefore, further photophysical experiments were carried out and revealed that, upon photoexcitation of the hydrids, a charge transfer process is triggered and results in the exTTF oxidation and the GQD or pCND reduction to for a charge-separated state. The observed lifetime for the charge recombination in $GQD^{\bullet-}$-$exTTF^{\bullet+}$ (54 ps) was slower than those observed in $pCND^{\bullet-}$-$exTTF^{\bullet+}$ (13 ps).

In conclusion, it has been proven the ability of pCND and GQD to act as an electron acceptors in combination with donor exTTF molecules. The difference observed in the charge recombination lifetime could be attributed to the structural differences found between GQD and pCND. The less amorphous character of GQD compared to pCND might be likely to facilitate a better delocalization of the electrons along the carbon network and, consequently, results in a higher recombination lifetime.

The next step was the formation of covalent hybrids by the combination of pCND with acceptor molecules, following the methodology described above. Firstly, it was chosen the acceptor TCAQ for the synthesis of the new hybrids. Through XPS and FTIR spectroscopies, it was detected the presence of the cyano groups in the pCND-TCAQ hybrid. More importantly, preliminary photophysical studies pointed out to a charge transfer process from the pCND to the TCAQ upon photoexcitation, revealing the donor ability of pCND in combination with acceptor molecules. Additional photophysical experiments are ongoing to corroborate these results.

Finally, pCND were functionalized with the acceptor fullerenes $PC_{60}BM$ and $PC_{70}BM$. In this case, due to the low solubility of both molecules in DMSO, the esterification reaction was carried out in a mixture of chlorobenzene/DMSO. The main evidences of the success of these reactions came from FTIR, due to the presence of the characteristic fullerene stretching modes, and from electrochemical experiments, where the characteristic reductions of the fullerenes were observed. Additional photophysical studies

are been carried out in order to determine the photophysical features of the all-carbon hybrid systems synthesized.

BIBLIOGRAPHY AND NOTES

BIBLIOGRAPHY AND NOTES

1. U.S. Energy Information Administration, International Energy Outlook, **2018**. https://www.eia.gov/analysis/
2. I. McConnell, G. Li, W. G. Brudvig, *Chem. Biol.* **2010**, *17*, 434.
3. K. Kalyasundaram, M. Graetzel, *Curr. Opin. Biotechnol.* **2010**, *21*, 298.
4. C. Liu, N. P. Dasgupta, P. Yang, *Chem. Mater.* **2013**, *25*, 415.
5. M. El-Khouly, E. El-Mohsnawy, S. Fukuzumi, *J. Photochem. Photobiol. C: Photochem. Rev*. **2017**, *31*, 36.
6. H. Van Amerongen, *Photosynthetic Excitons*, Singapore: World Scientific Publishing Co. Pte. Ltd. **2000**.
7. W. Zynth, J. Wachtveilt, *Chem.Phys.Chem.* **2005***,* 6, 871.
8. a) E. H. L. Falcao, F. Wudl, *J. Chem. Technol. Biotechnol*. **2007**, *82*, 524. b) J. L. Delgado, M. A. Herranz, N. Martín, *J. Mater. Chem*. **2008**, *18*, 1417.
9. a) H. W. Kroto, J. R. Heath, S. C. O'Brien, R. F. Curl, R. E. Smalley, *Nature* **1985**, *318*, 162. b) J. R. Heath, R. F. Curl, R. E. Smalley, *J. Chem. Phys*. **1987**, *87*, 4236.
10. N. Martín, L. Sánchez, B. Illescas, I. Pérez, *Chem. Rev.* **1998**, *7*, 2527.
11. H. Imahori, N. V. Tkachenko, V. Vehmanen, K. Tamaki, H. Lemmetyinen, Y. Sakata, S. Fukuzumi, *J. Chem. Phys*. *A*. **2001**, *105*, 1750.
12. R. Taylor, D. R. M. Walton, *Nature* **1993**, *363*, 685.
13. S. Iijima, *Nature* **1991**, *354*, 56.
14. a) S. Iijima, T. Ichihashi, *Nature* **1993**, *363*, 603. b) D. S. Bethune, C. H. Klang, M. S. de Vries, G. Gorman, R. Savoy, J. Vazquez, R. Beyers*, Nature* **1993**, *363*, 605.

15. K. S. Novoselov, A. K. Geim, S. V. Morozov, D. Jiang, Y. Zhang, S. V. Dubonos, I. V. Grigorieva, A. A. Firsov, *Science* **2004**, *306*, 666.

16. D. M. Guldi, N. Martín, *Carbon Nanotubes and Related Structures*, Wiley-VCH, Weinheim, **2010**.

17. R. H. Baughman, A. A. Zakhidov, W. A. d. Heer, *Science* **2002**, *297*, 787.

18. M. F. L. De Volder, S. H. Tawfick, R. H. Baughman, A. J. Hart, *Science* **2013**, *339*, 535.

19. a) K. S. Kim, Y. Zhao, H. Jang, S. Y. Lee, J. M. Kim, K. S. Kim, J.-H. Ahn, P. Kim, J.-Y. Choi, B. H. Hong, *Nature* **2009**, *457*, 706. b) A. H. Castro Neto, F. Guinea, N. M. R. Peres, K. S. Novoselov, A. K. Geim, *Rev. Mod. Phys*. **2009**, *81*, 109.

20. M. L. Mueller, X. Yan, B. Dragnea, L. S. Li, *Nano Lett*. **2011**, *11*, 56.

21. T. Ohta, A. Bostwick, T. Seyller, K. Horn, E. Rotenberg, *Science* **2006**, *313*, 951.

22. L. Jiao, L. Zhang, X. Wang, G. Diankov, H. Dai, *Nature* **2009**, *458*, 877.

23. H. Liu, Y. Liu, D. Zhu, *J. Mater. Chem*. **2011**, *21*, 3335.

24. a) X. Huang, Z. Yin, S. Wu, X. Qi, Q. He, Q. Zhang, Q. Yan, F. Boey, H. Zhang, *Small*. **2011**, *7*, 1876. b) X. Wan, Y. Huang, Y. Chen, *Acc. Chem. Res*. **2012**, *45*, 598.

25. a) L. Dai, *Acc. Chem. Res*. **2013**, *46*, 31. b) N. Martín, *Adv. Energy Mater*. **2017**, 7, 1601102.

26. R. Sekiya, Y. Uemura, H. Murakami, T. Haino, *Angew. Chem. Int. Ed*. **2014**, *53*, 5619.

27. K. P. Loh, Q. Bao, G. Eda, M. Chhowalla, *Nat. Chem*. **2010**, *2,* 1015.

28. M. Shamsipur, A. Barati, S. Karami, *Carbon* **2017**, *124*, 429.

29. N. V. Kozhemyakina, S. Eigler, R. E. Dinnebier, A. Inayat, W. Schwieger, A. Hirsch, *Fullerenes*, *Nanotubes and Carbon Nanostructures* **2013**, *21*, 804.

30. H. Lipson, A. R. Stokes, *Nature* **1942**, *149*, 328.

31. D. D. L. Chung, *J. Mater. Sci*. **2002**, *37*, 1475.

32. A. K. Geim, *Science* **2009**, *324*, 1530.

33. K. S. Novoselov, A. K. Geim, S. V. Morozov, D. Jiang, M. I. Katsnelson, I. V. Grigorieva, S. V. Dubonos, A. A. Firsov, *Science* **2005**, *438*, 197.

34. R. Peierls, Ann. Inst. *Henri Poincare* **1935**, *5*, 177.

35. J. Tolédano, P. Tolédano, *The Landau theory of phase transitions,* World Scientific Lecture Notes in Physics, **1987**.

36. J. C. Meyer, A. K. Geim, M. I. Katsnelson, K. S. Novoselov, T. J. Booth, S. Roth, *Nature* **2007**, *446*, 60.

37. S. Eigler, A. Hirsch, *Angew. Chem. Int. Ed*. **2014**, *53*, 7720.

38. A. K. Geim, K. S. Novoselov, *Nat. Mater*. **2007**, *6*, 183.

39. H. He, J. Klinowski, M. Forster, A. Lerf, *Chem. Phys. Lett*. **1998**, *287*, 53.

40. W. Cai, R. D. Piner, F. J. Stadermann, S. Park, M. A. Shaibat, Y. Ishii, D. Yang, A. Velamakanni, S. J. An, M. Stoller, J. An, D. Chen, R. S. Ruoff, *Science* **2008**, *321*, 1815.

41. W. Gao, L. B. Alemany, L. Ci, P. M. Ajayan, *Nat. Chem*. **2009**, *1*, 403.

42. A. Dimiev, D. V. Kosynkin, L. B. Alemany, P. Chaguine J. M. Tour, *J. Am. Chem. Soc.* **2012**, *134*, 2815.

43. S. Stankovich, D. A. Dikin, R. D. Piner, K. A. Kohlhaas, A. Kleinhammes, Y. Jia, Y. Wu, S. T. Nguyen, R. S. Ruoff, *Carbon* **2007**, *45*, 1558.

44. D. R. Dreyer, S. Park, C. W. Bielawski, R. S. Ruoff, *Chem. Soc. Rev*. **2009**, *39*, 228.

45. C. Gómez-Navarro, R. T. Weitz, A. M. Bittner, M. Scolari, A. Mews, M. Burghard, K. Kern, *Nano Lett*. **2007**, *7*, 3499.

46. X. Yang, X. Dou, A. Rouhanipour, L. Zhi, H. J. Räder, K. Müllen, *J. Am. Chem. Soc*. **2008**, *130*, 4216.

47. C. Berger, Z. Song, X. Li, X. Wu, N. Brown, C. Naud, D. Mayou, T. Li, J. Hass, A. N. Marchenkov, E. H. Conrad, P. N. First, W. A. de Heer, *Science* **2006**, *312*, 1191.

48. K. S. Kim, Y. Zhao, H. Jang, S. Y. Lee, J. M. Kim, K. S. Kim, J. Ahn, P. Kim, J. Choi, B. H. Hong, *Nature* **2009**, *457*, 706.

49. a) V. León, A. M. Rodriguez, P. Prieto, M. Prato, E. Vázquez, *ACS Nano* **2014**, *8*, 563. b) V. J. González, A. M. Rodríguez, V. León, J. Frontiñán-Rubio, J. L. G. Fierro, M. Durán-Prado, A. B. Muñoz-García, M. Pavone, E. Vázquez, *Green Chem*, **2018**, *20*, 3581.

50. Y. Hernandez, V. Nicolosi, M. Lotya, F. M. Blighe, Z. Sun, S. De, I. T. McGovern, B. Holland, M. Byrne, Y. K. Gun'Ko, J. J. Boland, P. Niraj, G. Duesberg, S. Krishnamurthy, R. Goodhue, J. Hutchison, V. Scardaci, A. C. Ferrari, J. N. Coleman, *Nat. Nanotechnol.* **2008**, *3*, 563.

51. A. Ciesielski P. Samorì, *Adv Mater*. **2016**, *28*, 6030.

52. J. N. Coleman, *Acc. Chem. Res*. **2013**, *46*, 14.

53. Y. Hernandez, M. Lotya, D. Rickard, S. D. Bergin, J. N. Coleman, *Langmuir* **2010**, *26*, 3208.

54. C. E. Hamilton, J. R. Lomeda, Z. Sun, J. M. Tour, A. R. Barron, *Nano Lett*. **2009**, *9*, 3460.

55. A. B. Bourlinos, G. Vasilios, Z. Radek, T. A. Steriotis, A. K. Stubos, *Small* **2009**, *5*, 1841.

56. Z. Sun, X. Huang, F. Liu, X. Yang, C. Rosler, R. A. Fischer, M. Muhler, W. Schuhmann, *Chem. Commun*. **2014**, *50*, 10382.

57. X. Zhang, A. C. Coleman, N. Katsonis, W. R. Browne, B. J. van Wees, B. L. Feringa, *Chem. Commun*. **2010**, *46*, 7539.

58. G. Bepete, E. Anglaret, L. Ortolani, V. Morandi, K. Huang, A. Pénicaud, C. Drummond, *Nat. Chem*. **2016**, *9*, 347.

59. K. Umar, O'Neill Arlene, L. Mustafa, D. Sukanta, J. N. Coleman, *Small* **2010**, *6*, 864.

60. M. Matsumoto, Y. Saito, C. Park, T. Fukushima, T. Aida, *Nat. Chem*. **2015**, *7*, 730.

61. M. Lotya, Y. Hernandez, P. J. King, R. J. Smith, V. Nicolosi, L. S. Karlsson, F. M. Blighe, S. De, Z. Wang, I. T. McGovern, G. S. Duesberg, J. N. Coleman, *J. Am. Chem. Soc*. **2009**, *131*, 3611.

62. M. Lotya, P. J. King, U. Khan, S. De, J. N. Coleman, *ACS Nano* **2010**, *4*, 3155.

63. S. Vadukumpully, J. Paul, S. Valiyaveettil, *Carbon* **2009**, *47*, 3288.

64. A. B. Bourlinos, V. Georgakilas, R. Zboril, T. A. Steriotis, A. K. Stubos, C. Trapalis, *Solid State Commun*. **2009**, *149*, 2172.

65. I. Uysal Unalan, C. Wan, S. Trabattoni, L. Piergiovanni, S. Farris, *RSC Adv*. **2015**, *5*, 26482.

66. D. Parviz, S. Das, H. S. T. Ahmed, F. Irin, S. Bhattacharia, M. J. Green, *ACS Nano* **2012**, *6*, 8857.

67. S. Das, F. Irin, H. S. Tanvir Ahmed, A. B. Cortinas, A. S. Wajid, D. Parviz, A. F. Jankowski, M. Kato, M. J. Green, *Polymer* **2012**, *53*, 2485.

68. S. Srinivasan, A. N. Basuray, K. J. Hartlieb, A. Taner, S. I. Stupp, S. J. Fraser, *Adv. Mater*. **2013**, *25*, 2740.

69. L. Zhang, Z. Zhang, C. He, L. Dai, J. Liu, L. Wang, *ACS Nano* **2014**, *8*, 6663.

70. C. Schafhaeutl, *J. Prakt. Chem*. **1840**, *21*, 129.

71. B. C. Brodie, *Ann. Chim. Phys*. **1855**, *45*, 351.

72. a) L. Staudenmaier, *Ber. Dtsch. Chem. Ges*. **1898**, *31*, 1481. b) L. Staudenmaier, *Ber. Dtsch. Chem. Ges*. **1899**, *32*, 1394. c) L. Staudenmaier, *Ber. Dtsch. Chem. Ges*. **1899**, *32*, 2824.

73. G. Charpy, C. R. Hebd. *Seances Acad. Sci*. **1909**, *148*, 920.

74. J. William, S. Hummers, R. E. Offeman, *J. Am. Chem. Soc*. **1958**, *80*, 1339.

75. W. S. Hummers, *Preparation of graphitic acid*, US2798878, **1957**.

76. N. I. Kovtyukhova, P. J. Ollivier, B. R. Martin, T. E. Mallouk, S. A. Chizhik, E. V. Buzaneva, A. D. Gorchinskiy, *Chem. Mater*. **1999**, *11*, 771.

77. A. M. Dimiev, S. M. Bachilo, R. Saito, J. M. Tour, *ACS Nano* **2012**, *6*, 7842.

78. S. Eigler, S. Grimm, F. Hof, A. Hirsch, *J. Mater. Chem. A*. **2013**, *1*, 11559.

79. O. C. Compton, S. W. Cranford, K. W. Putz, Z. An, L. C. Brinson, M. J. Buehler, S. T. Nguyen, *ACS Nano* **2012**, *6*, 2008.

80. a) A. Ganguly, S. Sharma, P. Papakonstantinou, J. Hamilton, *J. Phys. Chem. C*. **2011**, *115*, 17009; b) C. Botas, P. Álvarez, P. Blanco, M. Granda, C. Blanco, R. Santamaría, L. J. Romasanta, R. Verdejo, M. A. López-Manchado, R. Menéndez, *Carbon* **2013**, *65*, 156.

81. R. Rozada, J. I. Paredes, S. Villar-Rodil, A. Martínez-Alonso, J. M. D. Tascón, *Nano Res*. **2013**, *6*, 216.

82. C. K. Chua, M. Pumera, *Chem. Soc. Rev*. **2014**, *43*, 291.

83. A. C. Ferrari, J. C. Meyer, V. Scardaci, C. Casiraghi, M. Lazzeri, F. Mauri, S. Piscanec, D. Jiang, K. S. Novoselov, S. Roth, A. K. Geim, *Phys. Rev. Lett*. **2006**, *97*, 187401.

84. C. Vallés, C. Drummond, H. Saadaoui, C. A. Furtado, M. He, O. Roubeau, L. Ortolani, M. Monthioux, A. Pénicaud, *J. Am. Chem. Soc*. **2008**, *130*, 15802.

85. K. S. Novoselov, D. Jiang, F. Schedin, T. J. Booth, V. V. Khotkevich, S. V. Morozov; A. K. Geim, *Proc. Natl. Acad. Sci. U.S.A*. **2005**, *102*, 10451.

86. K. S. Subrahmanyam, S. R. C. Vivekchand, A. Govindaraj, C. N. R. Rao, *J. Mater. Chem*. **2008**, *18*, 1517.

87. P. Dorsa, I. Fahmida, S. A. Shah, D. Sriya, C. B. Sweeney, M. J. Green, *Adv. Mater*. **2016**, *28*, 8796.

88. M. Shtein, I. Pri-Bar, M. Varenik, O. Regev, *Anal. Chem*. **2015**, *87*, 4076.

89. D. R. Dreyer, S. Park, C. W. Bielawski, R. S. Ruoff, *Chem. Soc. Rev*. **2009**, *39*, 228.

90. For a recent overview see *Chem. Soc. Rev.* themed issue on *Graphene Chemistry*: T. Torres (Ed.), *Chem. Soc. Rev.* **2017**, *46*, 15, 4377-4810.

91. G. Luo, L. Liu, J. Zhang, G. Li, B. Wang, J. Zhao, *ACS Appl. Mater. Interfaces*. **2013**, *5*, 11184.

92. a) L. Rodriguez-Perez, M. A. Herranz, N. Martín, *Chem. Commun.* **2013***, 49*, 3721. b) K. Dirian, M. A. Herranz, G. Katsukis, J. Malig, L. Rodríguez-Pérez, C. Romero-Nieto, V. Strauss, N. Martín, D. M. Guldi. *Chem. Sci.* **2013***, 4*, 4335.

93. a) X. Gao, Y. Wang, X. Liu, T. L. Chan, S. Irle, Y. Zhao, S. B. Zhang, *Phys. Chem. Chem. Phys*. **2011**, *13*, 19449. b) G. Bottari, M. Á Herranz, L. Wibmer, M. Volland, L. Rodríguez-Pérez, D. M. Guldi, A. Hirsch, N. Martín, F. D'Souza, T. Torres, *Chem. Soc. Rev*. **2017**, *46*, 4464.

94. K. C. Knirsch, R. A. Schäfer, F. Hauke, A. Hirsch, *Angew. Chem. Int. Ed*. **2016**, *55*, 5861.

95. A. Savchenko, *Science* **2009**, *323*, 589.

96. R. R. Nair, R. Wencai, J. Rashid, R. Ibtsam, V. G. Kravets, B. Liam, B. Peter, S. Fredrik, A. S. Mayorov, Y. Shengjun, M. I. Katsnelson, Cheng Hui-Ming, S. Wlodek, L. G. Bulusheva, A. V. Okotrub, I. V. Grigorieva, A. N. Grigorenko, K. S. Novoselov, A. K. Geim, *Small* **2010**, *6*, 2877.

97. H. Liu, S. Ryu, Z. Chen, M. L. Steigerwald, C. Nuckolls, L. E. Brus, *J. Am. Chem. Soc.* **2009**, *131*, 17099.

98. E. Bekyarova, M. E. Itkis, P. Ramesh, C. Berger, M. Sprinkle, W. A. de Heer, R. C. Haddon, *J. Am. Chem. Soc*. **2009**, *131*, 1336.

99. A. Criado, M. Melchionna, S. Marchesan, M. Prato, *Angew. Chem. Int. Ed*. **2015**, *54*, 10734.

100. J. M. Englert, C. Dotzer, G. Yang, M. Schmid, C. Papp, J. M. Gottfried, H. Steinrück, E. Spiecker, F. Hauke, A. Hirsch, *Nat. Chem*. **2011**, *3*, 279.

101. J. M. Englert, K. C. Knirsch, C. Dotzer, B. Butz, F. Hauke, E. Spiecker, A. Hirsch, *Chem. Commun*. **2012**, *48*, 5025.

102. J. Mateos-Gil, L. Rodriguez-Perez, M. Moreno Oliva, G. Katsukis, C. Romero-Nieto, M. A. Herranz, D. M. Guldi, N. Martín, *Nanoscale* **2015**, *7*, 1193.

103. E. Choi, I. Jeon, S. Bae, H. Lee, H. S. Shin, L. Dai, J. Baek, *Chem. Commun*. **2010**, *46*, 6320.

104. M. Quintana, K. Spyrou, M. Grzelczak, W. R. Browne, P. Rudolf; M. Prato, *ACS Nano* **2010**, *4*, 3527.

105. D. García, L. Rodríguez-Pérez, M. A. Herranz, D. Peña, E. Guitián, S. Bailey, Q. Al-Galiby, M. Noori, C. J. Lambert, D. Pérez, N. Martín, *Chem. Commun*. **2016**, *52*, 6677.

106. a) S. Sarkar, E. Bekyarova, S. Niyogi, R. C. Haddon, *J. Am. Chem. Soc*. **2011,** *133*, 3324. b) S. Sarkar, E. Bekyarova, R. C. Haddon, *Acc. Chem. Res*. **2012**, *45*, 673.

107. T. A. Strom, E. P. Dillon, C. E. Hamilton, A. R. Barron, *Chem.Commun*. **2010**, *46*, 4097.

108. S. P. Economopoulos, G. Rotas, Y. Miyata, H. Shinohara, N. Tagmatarchis, *ACS Nano* **2010**, *4*, 7499.

109. A. Ciesielski, P. Samori, *Chem. Soc. Rev*. **2014**, *43*, 381.

110. D. Barun, K. E. Prasad, U. Ramamurty, C. N. R. Rao, *Nanotechnology* **2009**, *20*, 125705.

111. V. Rakesh, D. Barun, R. Chandra Sekhar, C. N. R. Rao, *J. Phys. Condens. Matter*. **2008**, *20*, 472204.

112. E. M. Pérez, N. Martín, *Chem. Soc. Rev*. **2015**, *44*, 6425.

113. A. Perry, S. J. Green, D. W. Horsell, S. M. Hornett, M. E. Wood, *Tetrahedron* **2015**, *71*, 6776.

114. N. V. Kozhemyakina, J. M. Englert, Y. Guang, S. Erdmann, C. D. Schmidt, H. Frank, A. Hirsch, *Adv. Mater*. **2010**, *22*, 5483.

115. Z. Liu, Y. Xu, X. Zhang, X. Zhang, Y. Chen, J. Tian, *J. Phys. Chem. B*. **2009**, *113*, 9681.

116. D. Yu, Y. Yang, M. Durstock, J. Baek, L. Dai, *ACS Nano*. **2010**, *4*, 5633.

117. I. A. Vacchi, C. Spinato, J. Raya, A. Bianco, C. Menard-Moyon, *Nanoscale* **2016**, *8*, 13714.

118. J. U. Lee, W. Lee, J. W. Yi, S. S. Yoon, S. B. Lee, B. M. Jung, B. S. Kim, J. H. Byun, *J. Mater. Chem. A*. **2013**, *1*, 12893.

119. Y. Yang, J. Wang, J. Zhang, J. Liu, X. Yang, H. Zhao, *Langmuir* **2009**, *25*, 11808.

120. X. Yang, X. Zhang, Z. Liu, Y. Ma, Y. Huang, Y. Chen, *J. Phys. Chem. C*. **2008**, *112*, 17554.

121. S. Qi, P. Shuping, A. Vajiheh, L. Chen, F. Xinliang, Müllen Klaus, *Adv. Mater*. **2009**, *21*, 3191.

122. M. Fang, K. Wang, H. Lu, Y. Yang, S. Nutt, *J. Mater. Chem*. **2010**, *20*, 1982.

123. H. Ismaili, D. Geng, A. X. Sun, T. T. Kantzas, M. S. Workentin, *Langmuir* **2011**, *27*, 13261.

124. M. Hsiao, S. Liao, M. Yen, P. Liu, N. Pu, C. Wang, C. M. Ma, *ACS Appl. Mater. Interfaces*. **2010**, *2*, 3092.

125. N. Armalori, V. Bolzoni, *Chem. Eur. J.* **2016**, *22*, 32.

126. a) N. Martín, *Adv. Energy Mater*. **2017**, *7*, 1601102. b) J. L. Delgado, S. Filippone, F. Giacalone, M. A. Herranz, B. Illescas, E. M. Pérez, N. Martín, *Top. Curr. Chem*. **2014**, *350*, 1. c) D. M. Guldi, N. Martín, *Carbon Nanotubes and Related Structures*, Wiley-VCH, Weinheim, **2010**.

127. A. Roth, M. Ragoussi, L. Wibmer, G. Katsukis, G. d. l. Torre, T. Torres, D. M. Guldi, *Chem. Sci*. **2014**, *5*, 3432.

128. A. Hirsch, C. Methfessel, M. Volland, K. Brunner, L. Wibmer, U. Hahn, T. Torres, D. Guldi, l. T. de, *Chem. Eur. J.* **2018**, *2*4, 18696.

129. M. Ragoussi, J. Malig, G. Katsukis, B. Butz, E. Spiecker, G. de la Torre, T. Torres, D. M. Guldi, *Angew. Chem. Int. Ed*. **2012**, *51*, 6421.

130. M. Supur, K. Ohkubo, S. Fukuzumi, *Chem.Commun*. **2014**, *50*, 13359.

131. S. K. Das, C. B. KC, K. Ohkubo, Y. Yamada, S. Fukuzumi, F. D'Souza, *Chem.Commun.* **2013**, *49*, 2013.

132. G. Kalita, S. Sharma, K. Wakita, M. Umeno, Y. Hayashi, M. Tanemura, *Phys. Chem. Chem. Phys*. **2013**, *15*, 1271.

133. M. Zhang, B. Yuan, S. Kang, L. Qin, G. Li, X. Li, *RSC Adv*. **2015**, *5*, 42063.

134. A. Mishra, R. K. Behera, P. K. Behera, B. K. Mishra, G. B. Behera, *Chem. Rev*. **2000**, *100*, 1973.

135. C. Wang, E. A. Weiss*, J. Am. Chem. Soc*. **2016**, *138*, 9557.

136. W. Sun, S. Guo, C. Hu, J. Fan, X. Peng, *Chem. Rev*. **2016**, *116*, 7768.

137. M. Guo, J. Huang, Y. Deng, H. Shen, Y. Ma, M. Zhang, A. Zhu, Y. Li, H. Hui, Y. Wang, X. Yang, Z. Zhang, H. Chen, *Adv. Funct. Mater*. **2015**, *25*, 59.

138. P. Bouit, E. Di Piazza, S. Rigaut, B. Le Guennic, C. Aronica, L. Toupet, C. Andraud, O. Maury, *Org. Lett*. **2008**, *10*, 4159.

139. P. Bouit, D. Rauh, S. Neugebauer, J. L. Delgado, E. D. Piazza, S. Rigaut, O. Maury, C. Andraud, V. Dyakonov, N. Martín, *Org. Lett*. **2009**, *11*, 4806.

140. C. Villegas, E. Krokos, P. Bouit, J. L. Delgado, D. M. Guldi, N. Martín, *Energy Environ. Sci*. **2011**, *4*, 679.

141. L. Rodríguez-Pérez, C. Villegas, M. Á Herranz, J. L. Delgado, N. Martín, *ACS Omega* **2017,** *2*, 9164.

142. J. L. Delgado, P. Bouit, S. Filippone, M. Á Herranz, N. Martín, *Chem. Commun*. **2010**, *46*, 4853.

143. Z. Li, S. Mukhopadhyay, S. Jang, J. Brédas, A. K. Jen, J. *Am. Chem. Soc*. **2015**, *137*, 11920.

144. S. Eigler, A. Hirsch, *Angew. Chem. Int. Ed*. **2014**, *53*, 7720.

145. M. Garrido, J. Calbo, L. Rodríguez-Pérez, J. Aragó, E. Ortí, M. Á Herranz, N. Martín, *Chem. Commun*. **2017**, *53*, 12402.

146. C. Casiraghi, A. Hartschuh, H. Qian, S. Piscanec, C. Georgi, A. Fasoli, K. S. Novoselov, D. M. Basko, A. C. Ferrari, *Nano Lett*. **2009**, *9*, 1433.

147. J. M. Englert, P. Vecera, K. C. Knirsch, R. A. Schäfer, F. Hauke, A. Hirsch, *ACS Nano* **2013**, *7*, 5472.

148. X. Dong, D. Fu, W. Fang, Y. Shi, P. Chen, L. Li, *Small* **2009**, *5*, 1422.

149. Q. Su, S. Pang, V. Alijani, C. Li, X. Feng, K. Müllen, *Adv. Mater.* **2009**, *21*, 3191.

150. a) Z. Ni, Y. Wang, T. Yu, Z. Shen, *Nano Res.* **2008**, 1, 273. b) L. M. Malard, M. A. Pimenta, G. Dresselhaus, M. S. Dresselhaus, *Phys. Rep*. **2009**, *473*, 51.

151. K. Mei, N. Rubio, P. M. Costa, H. Kafa, V. Abbate, F. Festy, S. S. Bansal, R. C. Hider, K. Al-Jamal, *Chem.Commun*. **2015**, *51*, 14981.

152. M. J. McAllister, J. Li, D. H. Adamson, H. C. Schniepp, A. A. Abdala, J. Liu, M. Herrera-Alonso, D. L. Milius, R. Car, R. K. Prud'homme, I. A. Aksay, *Chem. Mater*. **2007**, *19*, 4396.

153. W. Cai, R. D. Piner, F. J. Stadermann, S. Park, M. A. Shaibat, Y. Ishii, D. Yang, A. Velamakanni, S. J. An, M. Stoller, J. An, D. Chen, R. S. Ruoff, *Science* **2008**, *321*, 1815.

154. W. Gao, L. B. Alemany, L. Ci, P. M. Ajayan, *Nat. Chem*. **2009**, *1*, 403.

155. M. L. Toebes, van Heeswijk, Jürgen M. P, J. H. Bitter, v. D. Jos, K. de Jong, *Carbon* **2004**, *42*, 307.

156. H. P. Boehm, *Carbon* **1994**, *32*, 759.

157. S. Peng, C. Liu, X. Fan*, Integrated Ferroelectr*. **2015**, *163*, 42.

158. J. Chen, Y. Zhang, M. Zhang, B. Yao, Y. Li, L. Huang, C. Li, G. Shi, *Chem. Sci*. **2016**, *7*, 1874.

159. C. Romero, J. Guilleme, C. Villegas, J. L. Delgado, D. Gonzalez-Rodriguez, N. Martín, T. Torres, D. M. Guldi, *J. Mater. Chem*. **2011**, *21*, 15914.

160. G. A. Reynolds, K. H. Drexhage, *J. Org. Chem*. **1977**, *42*, 885.

161. G. Melikian, F. P. Rouessac, C. Alexandre, *Synth Commun*. **1995**, *25*, 3045.

162. L. Rodríguez-Pérez, R. García, M. Á Herranz, N. Martín, *Chem. Eur. J*. **2014**, *20*, 7278.

163. T. Tseng, C. Urban, Y. Wang, R. Otero, S. L. Tait, M. Alcamí, D. Ecija, M. Trelka, J. M. Gallego, N. Lin, M. Konuma, U. Starke, A. Nefedov, A. Langner, C. Wöll, M. A. Herranz, F. Martín, N. Martín, K. Kern, R. Miranda, *Nat. Chem*. **2010**, *2*, 374.

164. H. Terrones, A. M. Rao, M. Terrones, H. Qian, N. Anderson, A. Hartschuh, M. A. Pimenta, L. Novotny, A. Jorio, I. O. Maciel, J. Campos-Delgado, *Nat. Mater*. **2008**, *7*, 878.

165. R. Voggu, C. S. Rout, A. D. Franklin, T. S. Fisher, C. N. R. Rao, *J. Phys. Chem. C*. **2008**, *112*, 13053.

166. X. Dong, D. Fu, W. Fang, Y. Shi, P. Chen, L. Li, *Small* **2009**, *5*, 1422.

167. This photphysical study was carried out in the group of Prof. D. M. Guldi (Erlangen-Nuremberg University). Part of these results were also presented in the Thesis work of Alexandra Roth. (2017).

168. I. A. Vacchi, C. Spinato, J. Raya, A. Bianco, C. Menard-Moyon, *Nanoscale* **2016**, *8*, 13714.

169. N. Karousis, S. P. Economopoulos, E. Sarantopoulou, N. Tagmatarchis, *Carbon* **2010**, *48*, 854.

170. a) J. Guan, X. Chen, T. Wei, F. Liu, S. Wang, Q.Yang, Y. Lu, S. Yang, J. *Mater. Chem. A*. **2015,** *3*, 4139. b) M. Barrejón, M. Vizuete, M. J. Gómez-Escalonilla, J. L. G. Fierro, I. Berlanga, F. Zamora, G. Abellán, P. Atienzar, J.-F. Nierengarten, H. García, F. Langa, *Chem. Commun.* **2014**, *50*, 9053.

171. J. L. Bahr, J. M. Tour, *Chem.Mater*. **2001**, *13*, 3823.

172. W. L. F. Armarego, C L L Chai, *Purification of Laboratory Chemicals*, Elsevier **2003**.

173. J. J. Snellenburg, S. Laptenok, R. Seger, K. M. Mullen; van Stokkum, I H M, *J. Stat. Soft*. **2012**, 49, 1.

174. K. M. Mullen, I. H. M. van Stokkum, *J. Stat. Soft*. **2007**, *18*, 1.

175. F Mu, S L Coffing, D J Riese, R L Geahlen, P Verdier-Pinard, T E Hamel, J Johnson, M Cushman, *J. Med. Chem*. **2001**, *44*, 441.

176. A. I. Ekimov, A. A. Omushchenko, *J. Exp. Theor. Phys*. **1981**, *34*, 345.

177. X. Xu, R. Ray, Y. Gu, H. J. Ploehn, L. Gearheart, K. Raker, W. A. Scrivens, *J. Am. Chem. Soc*. **2004**, *126*, 12736.

178. Y. Sun, B. Zhou, Y. Lin, W. Wang, K. A. S. Fernando, P. Pathak, M. J. Meziani, B. A. Harruff, X. Wang, H. Wang, P. G. Luo, H. Yang, M. E. Kose, B. Chen, L. M. Veca, S. Xie, *J. Am. Chem. Soc*. **2006**, *128*, 7756.

179. a) S. E, Q. Mao, X. Yuan, X. Kong, X. Chen, J. Wang, *Nanoscale*, **2018**, *10*, 12788. b) W. Li, Z. Wang, S. Hao, L. Sun, M. Nisic, G. Cheng, C. Zhu, Y. Wan, L. Ha, S. Zheng, *Nanoscale* **2018**, *10*, 3744.

180. S. Y. Lim, W. Shen, Z. Gao, *Chem. Soc. Rev*. **2015**, *44*, 362.

181. L. Xiao, H. Sun, *Nanoscale Horiz.* **2018**, *3*, 565.

182. A. Cayuela, M. L. Soriano, C. Carrillo-Carrión, M. Valcárcel, *Chem. Commun*. **2016**, *52*, 1311.

183. G. A. M. Hutton, B. C. M. Martindale, E. Reisner, *Chem. Soc. Rev*. **2017**, *46*, 6111.

184. A. Narita, X.-Y. Wang, X. Feng, K. Müllen, *Chem. Soc. Rev.* **2015**, *44*, 6616.

185. X. Yan, X. Cui, L. Li, *J. Am. Chem. Soc*. **2010**, *132*, 5944.

186. P. J. Evans, J. Ouyang, L. Favereau, J. Crassous, I. Fernández, J. Perles, N. Martín, *Angew. Chem. Int. Ed*. **2018**, *57*, 6774.

187. X. T. Zheng, A. Ananthanarayanan, K. Q. Luo, P. Chen, *Small* **2015**, *11*, 1620.

188. R. Sekiya, Y. Uemura, H. Naito, K. Naka, T. Haino, *Chem. Eur. J.* **2016**, *22*, 8198.

189. J. Peng, W. Gao, B. K. Gupta, Z. Liu, R. Romero-Aburto, L. Ge, L. Song, L. B. Alemany, X. Zhan, G. Gao, S. A. Vithayathil, B. A. Kaipparettu, A. A. Marti, T. Hayashi, J. Zhu, P. M. Ajayan, *Nano Lett*. **2012**, *12*, 844.

190. X. Wu, L. Ma, S. Sun, K. Jiang, L. Zhang, Y. Wang, H. Zeng, H. Lin, *Nanoscale* **2018**, *10*, 1532.

191. L. Ling-Ling, J. Jing, F. Rong, W. Chong-Zhi, L. Qian, Z. Jian-Rong, J. Li-Ping, Z. Jun-Jie, *Adv. Funct. Mater*. **2012**, *22*, 2971.

192. K. P. Prasad, Y. Chen, M. A. Sk, A. Than, Y. Wang, H. Sun, K. Lim, X. Dong, P. Chen, *Mater. Horiz*. **2014**, *1*, 529.

193. J. Lu, J. Yang, J. Wang, A. Lim, S. Wang, K. P. Loh, *ACS Nano* **2009**, *3*, 2367.

194. X. Tan, Y. Li, X. Li, S. Zhou, L. Fan, S. Yang, *Chem. Commun*. **2015**, *51*, 2544.

195. R. L. Calabro, D. Yang, D. Y. Kim, *J. Colloid Interface Sci*. **2018**, *527*, 132.

196. C. X. Guo, D. Zhao, Q. Zhao, P. Wang, X. Lu, *Chem. Commun*. **2014**, *50*, 7318.

197. G. Huang, X. Chen, C. Wang, H. Zheng, Z. Huang, D. Chen, H. Xie, *RSC Adv*. **2017**, *7*, 47840.

198. F. Li, Y. Li, X. Yang, X. Han, Y. Jiao, T. Wei, D. Yang, H. Xu, G. Nie, *Angew. Chem. Int. Ed*. **2018**, *57*, 2377.

199. P. Hsu, Z. Shih, C. Lee, H. Chang, *Green Chem*. **2012**, *14*, 917.

200. A. Prasannan, T. Imae, *Ind. Eng. Chem. Res*. **2013**, *52*, 15673.

201. M. J. Krysmann, A. Kelarakis, P. Dallas, E. P. Giannelis, *J. Am. Chem. Soc*. **2012**, *134*, 747.

202. S. Tao, S. Zhu, T. Feng, C. Xia, Y. Song, B. Yang, *Mater. Today Chem*. **2017**, *6*, 13.

203. S. Zhu, Q. Meng, L. Wang, J. Zhang, Y. Song, H. Jin, K. Zhang, H. Sun, H. Wang, B. Yang, *Angew. Chem. Int. Ed*. **2013**, *52*, 3953.

204. B. C. M. Martindale, G. A. M. Hutton, C. A. Caputo, S. Prantl, R. Godin, J. R. Durrant, E. Reisner, *Angew. Chem. Int. Ed.* **2017**, *56*, 6459.

205. V. Strauss, J. T. Margraf, C. Dolle, B. Butz, T. J. Nacken, J. Walter, W. Bauer, W. Peukert, E. Spiecker, T. Clark, D. M. Guldi, *J. Am. Chem. Soc*. **2014**, *136*, 17308.

206. F. Arcudi, L. Đorđević, M. Prato, *Angew. Chem. Int. Ed*. **2016**, *55*, 2107.

207. M. K. Barman, B. Jana, S. Bhattacharyya, A. Patra, *J. Phys. Chem. C*, **2014**, *118*, 20034.

208. A. B. Bourlinos, G. Trivizas, M. A. Karakassides, M. Baikousi, A. Kouloumpis, D. Gournis, A. Bakandritsos, K. Hola, O. Kozak, R. Zboril, I. Papagiannouli, P. Aloukos, S. Couris, *Carbon* **2015**, *83*, 173.

209. V. Strauss, A. Kahnt, E. M. Zolnhofer, K. Meyer, H. Maid, C. Placht, W. Bauer, T. J. Nacken, W. Peukert, S. H. Etschel, M. Halik, D. M. Guldi, *Adv. Funct. Mater*. **2016**, *26*, 7975.

210. F. Rigodanza, L. Đorđević, F. Arcudi, M. Prato, *Angew. Chem. Int. Ed*. **2018**, *57*, 5062.

211. L. Đorđević, F. Arcudi, A. D'Urso, M. Cacioppo, N. Micali, T. Bürgi, R. Purrello, M. Prato, *Nat. Commun*. **2018**, *9*, 3442.

212. J. B. Essner, J. A. Kist, L. Polo-Parada, G. A. Baker, *Chem. Mater*. **2018**, *30*, 1878.

213. X. T. Zheng, A. Than, A. Ananthanaraya, D. Kim, P. Chen, *ACS Nano* **2013**, *7*, 6278.

214. X. Wu, F. Tian, W. Wang, J. Chen, M. Wu, J. X. Zhao, *J. Mater. Chem. C* **2013**, *1*, 4676.

215. J. Liu, S. Lu, Q. Tang, K. Zhang, W. Yu, H. Sun, B. Yang, *Nanoscale* **2017**, *9*, 7135.

216. X. Wang, L. Cao, S.-T. Yang, F. Lu, M. J. Meziani, L. Tian, K. W. Sun, M. A. Bloodgood and Y.-P. Sun, *Angew. Chem. Int. Ed.* **2010**, *49*, 5310.

217. H. Ding, S. Yu, J. Wei, H. Xiong, *ACS Nano* **2016**, 10, 484.

218. H. Liu, T. Ye, C. Mao, *Angew. Chem. Int. Ed*. **2007**, *46*, 6473.

219. N. Dhenadhayalan, K. Lin, R. Suresh, P. Ramamurthy, *J. Phys. Chem. C* **2016**, *120*, 1252.

220. L. Li, G. Wu, G. Yang, J. Peng, J. Zhao, J. Zhu, *Nanoscale* **2013**, *5*, 4015.

221. G. Eda, Y. Lin, C. Mattevi, H. Yamaguchi, H. Chen, I. Chen, C. Chen, M. Chhowalla, *Adv. Mater*. **2010**, *22*, 505.

222. J. Schneider, C. J. Reckmeier, Y. Xiong, M. von Seckendorff, A. S. Susha, P. Kasák, A. L. Rogach, *J. Phys. Chem. C*. **2017**, *121*, 2014.

223. M. O. Dekaliuk, O. Viagin, Y. V. Malyukin, A. P. Demchenko, *Phys. Chem. Chem. Phys*. **2014**, *16*, 16075.

224. S. Baker, G. Baker, *Angew. Chem. Int. Ed*. **2010**, *49*, 6726.

225. Y. Song, S. Zhu, S. Zhang, Y. Fu, L. Wang, X. Zhao, B. Yang, *J. Mater. Chem. C*. **2015**, *3*, 5976.

226. M. Righetto, A. Privitera, I. Fortunati, D. Mosconi, M. Zerbetto, M. L. Curri, M. Corricelli, A. Moretto, S. Agnoli, L. Franco, R. Bozio, C. Ferrante, *J. Phys. Chem. Lett*. **2017**, *8*, 2236.

227. S. H. Jin, D. H. Kim, G. H. Jun, S. H. Hong, S. Jeon, *ACS Nano* **2013**, *7*, 1239.

228. H. Ding, S. Yu, J. Wei, H. Xiong, *ACS Nano* **2016**, *10*, 484.

229. R. C. So, J. E. Sanggo, L. Jin, J. M. A. Diaz, R. A. Guerrero, J. He, *ACS Omega* **2017**, *2*, 5196.

230. D. Mazzier, M. Favaro, S. Agnoli, S. Silvestrini, G. Granozzi, M. Maggini, A. Moretto, *Chem. Commun*. **2014**, *50*, 6592.

231. G. A. M. Hutton, B. Reuillard, B. C. M. Martindale, C. A. Caputo, C. W. J. Lockwood, J. N. Butt, E. Reisner, *J. Am. Chem. Soc*. **2016**, *138*, 16722.

232. V. Strauss, J. T. Margraf, K. Dirian, Z. Syrgiannis, M. Prato, C. Wessendorf, A. Hirsch, T. Clark, D. M. Guldi, *Angew. Chem. Int. Ed*. **2015**, *54*, 8292.

233. S. Carrara, F. Arcudi, M. Prato, L. De Cola, *Angew. Chem. Int. Ed*. **2017**, *56*, 4757.

234. M. Vázquez-Nakagawa, L. Rodríguez-Pérez, M. A. Herranz, N. Martín, *Chem. Commun*. **2016**, *52*, 665.

235. Y. Choi, D. Jeon, Y. Choi, J. Ryu, B. Kim, *ACS Appl. Mater. Interfaces*. **2018**, *10*, 13434.

236. J. H. Liu, R. S. Li, B. Yuan, J. Wang, Y. F. Li, C. Z. Huang, *Nanoscale* **2018**, *10*, 17402.

237. A. Cadranel, V. Strauss, J. T. Margraf, K. A. Winterfeld, C. Vogl, L. Đorđević, F. Arcudi, H. Hoelzel, N. Jux, M. Prato, D. M. Guldi, *J. Am. Chem. Soc.* **2018**, *140*, 904.

238. T. Scharl, A. Cadranel, P. Haines, V. Strauss, S. Bernhardt, S. Vela, C. Atienza, F. Gröhn, N. Martín, D. M. Guldi, *Chem. Commun.* **2018**, *54*, 11642.

239. a) F. Arcudi, L. Đorđević, M. Prato, *Angew. Chem. Int. Ed*. **2016**, *55*, 2107. b) F. Arcudi, V. Strauss, L. Đorđević, A. Cadranel, D. M. Guldi, M. Prato *Angew. Chem. Int. Ed*. **2017**, *56*, 12097.

240. L. Vallan, R. Canton-Vitoria, H. B. Gobeze, Y. Jang, R. Arenal, A. M. Benito, W. K. Maser, F. D'Souza, N. Tagmatarchis, *J. Am. Chem. Soc*. **2018**, *140*, 13488.

241. J. Sun, Q. Xin, Y. Yang, H. Shah, H. Cao, Y. Qi, J. R. Gong, J. Li, *Chem.Commun*. **2018**, *54*, 715.

242. H. Moshe, G. Levi, Y. Mastai, *CrystEngComm*, **2013**, *15*, 9203.

243. http://webcsd.ccdc.cam.ac.uk

244. F. Zhang, X. Feng, Y. Zhang, L. Yan, Y. Yang, X. Liu, *Nanoscale* **2016**, *8*, 8618.

245. T. I. T. Okpalugo, P. Papakonstantinou, H. Murphy, J. McLaughlin, N. M. D. Brown, *Carbon* **2005**, *43*, 153.

246. F. Arcudi, L. Đordević M. Prato, *Angew. Chem. Int. Ed.* **2017**, *56*, 4170.

247. F. G. Brunetti, J. L. López, C. Atienza, N. Martín, *J. Mater. Chem.* **2012**, *22*, 4188.

248. N. Martín, L. Sánchez, M. A. Herranz, B. Illescas, D. M. Guldi, *Acc. Chem. Res.* **2007**, *40*, 1015.

249. a) J. López-Andarias, M. J. Rodríguez, C. Atienza, J. L. López, T. Mikie, S. Casado, S. Seki, J. L. Carrascosa, N. Martín, *J. Am. Chem. Soc.* **2015**, *137*, 893. b) J. López-Andarias, J. L. López, C. Atienza, F. G. Brunetti, C. Romero-Nieto, D. M. Guldi, N. Martín, *Nat. Commun.* **2014**, *5*, 3763.

250. S. Wenger, P.-A. Bouit, Q. Chen, J. Teuscher, D. Di Censo, R. Humphry-Baker, J.-E. Moser, J. L. Delgado, N. Martín, S. M. Zakeeruddin, M. Grätzel, *J. Am. Chem. Soc.* **2010**, *132*, 5164.

251. A. J. Moore, M. R. Bryce, *Synthesis* **1991**, 26.

252. G. J. Marshallsay, M. R. Bryce, *J. Org. Chem. Soc.* **1994**, *59*, 6847.

253. S. González, N. Martín, D. M. Guldi, *J. Org. Chem.* **2003**, *68*, 779.

254. a) S.-G. Liu, I. Pérez, N. Martín, L. Echegoyen, *J. Org. Chem.* **2000**, *65*, 9092. b) M. A. Herranz, L. Yu, N. Martín, L. Echegoyen, *J. Org. Chem.* **2003**, *68*, 8379.

255. D. Choudhury, B. Das, D. D. Sarma, C. N. R. Rao, *Chem. Phys. Lett.* **2010**, *497*, 66.

256. a) D. M. Guldi, L. Sánchez, N. Martín, *J. Phys. Chem. B* **2001**, *105*, 7139. b) M. A. Herranz, C. Ehli, S. Campidelli, M. Gutiérrez, G. L. Hug, K. Ohkubo, S. Fukuzumi, M. Prato, N. Martín, D. M. Guldi, *J. Am. Chem. Soc.* **2008**, *130*, 66. c) V. Strauss, A. Roth, M. Sekita, D. M. Guldi, *Chem* **2016**, *1*, 531.

257. N. Martin, R. Behnisch, M. Hanack, *J. Org. Chem.* **1989**, *54*, 2563.

258. a) A. Wild, M. Strumpf, B. Häupler, M. D. Hager, *Adv. Energy Mater.* **2017**, *7*, 1601415. b) C. Romero-Nieto, R. García, M. A. Herranz, L. Rodríguez-Pérez, M. Sánchez-Navarro, J. Rojo, N. Martín, D. M. Guldi, *Angew. Chem. Int. Ed.* **2013**, *52*, 10216. c) E. M. Pérez, A. L. Capodilupo, G. Fernández, L. Sánchez, P. M. Viruela, R. Viruela, E. Ortí, M. Bietti, N. Martín, *Chem. Commun.* **2008**, 4567.

259. B. Illescas, N. Martín, C. Seoane, Tetrahedron Lett. **1997**, *38*, 2015.

260. a) W. Lehnert, *Tetrahedron Lett.* **1970**, 4723. b) W. Lehnert, *Synthesis*, **1974**, 667.

261. C. Urban, Y. Wang, J. Rodríguez-Fernández, R. García, M. A. Herranz, M. Alcamí, N. Martín, F. Martín, J. M. Gallego, R. Miranda, R. Otero, *Chem. Commun.* **2014**, *50*, 833.

262. E. M. Pérez, N. Martín, *Chem. Soc. Rev.* **2008**, *37*, 1512.

263. J. Santos, B. M. Illescas, N. Martín, J. Adrio, J. C. Carretero, R. Viruela, E. Ortí, F. Spänig, D. M. Guldi, *Chem. Eur. J.* **2011**, *17*, 2957.

264. V. Georgakilas, J. A. Perman, J. Tucek, R. Zboril, *Chem. Rev.* **2015**, *115*, 4744.

265. M. J. Llansola-Portolesa, D. Gust, T. A.Moore, A. L.Moore, *C. R. Chimie* **2017**, 20, 296.

266. J. C. Hummelen, B. W. Knight, F. LePeq, F. Wudl, J. Yao, C. L. Wilkins, *J. Org. Chem.* **1995**, *60*, 532.

267. E. E. Maroto, A. de Cózar, S. Filippone, A. Martín-Domenech, F. P.Cossío, N. Martín, *Angew. Chem. Int. Ed.* **2011**, *50*, 6060.

268. M. M. Wienk, J. M. Kroon, W. J. H. Verhees, J. Knol, J. C. Hummelen, P. A. van Hal, R. A. J. Janssen, *Angew. Chem. Int. Ed.* **2003**, *42*, 3371.

269. W. R. Bamford, T. S. Stevens, *J. Chem. Soc,* **1952**, 4735.

270. S. L. Fronk, C.-K. Mai, M. Ford, R. P. Noland, G. C. Bazan, *Macromolecules* **2015**, *48*, 6224.

271. J. P. Hare, T. J. Dennis, H. W. Kroto, R. Taylor, A. W. Allaf, S. Balm, D. R. M. Walton*, J. Chem. Soc., Chem. Commun.* **1991**, 412.

272. L. Echegoyen, L. E. Echegoyen, *Acc. Chem. Res.* **1998**, *31*, 593.

273. a) G. Gensterblum, K. Hevesi, B. Han, L. Yu, J. Pireaux, P. A. Thiry, R. Caudano, A. Lucas, D. Bernaerts, S. Amelinckx, G. Van Tendeloo, G. Bendele, T. Buslaps, R. L. Johnson, M. Foss, R. Feidenhans'l, G. Le Lay, *Phys. Rev. B*. **1994**, *50*, 11981. b) B. Han, L. Yu, K. Hevesi, G. Gensterblum, P. Rudolf, J. Pireaux, P. A. Thiry, R. Caudano, P. Lambin, A. A. Lucas, *Phys. Rev. B.* **1995**, *51*, 7179.